Surface Alpha Interactions in P-Type Point-Contact HPGe Detectors: Maximizing Sensitivity of ^{76}Ge Neutrinoless Double-Beta Decay Searches

Julieta Gruszko

A dissertation
submitted in partial fulfillment of the
requirements for the degree of

Doctor of Philosophy

University of Washington

2017

Reading Committee:

Jason Detwiler, Chair

Ann Nelson

Grey Rybka

Program Authorized to Offer Degree:
UW Physics

University of Washington

Abstract

Surface Alpha Interactions in P-Type Point-Contact HPGe Detectors: Maximizing Sensitivity of ^{76}Ge Neutrinoless Double-Beta Decay Searches

Julieta Gruszko

Chair of the Supervisory Committee:
Assistant Professor Jason Detwiler
Physics

Though the existence of neutrino oscillations proves that neutrinos must have non-zero mass, Beyond-the-Standard-Model physics is needed to explain the origins of that mass. One intriguing possibility is that neutrinos are Majorana particles, i.e., they are their own anti-particles. Such a mechanism could naturally explain the observed smallness of the neutrino masses, and would have consequences that go far beyond neutrino physics, with implications for Grand Unification and leptogenesis.

If neutrinos are Majorana particles, they could undergo neutrinoless double-beta decay ($0\nu\beta\beta$), a hypothesized rare decay in which two antineutrinos annihilate one another. This process, if it exists, would be exceedingly rare, with a half-life over 10^{25} years. Therefore, searching for it requires experiments with extremely low background rates. One promising technique in the search for $0\nu\beta\beta$ is the use of P-type point-contact (P-PC) high-purity Germanium (HPGe) detectors enriched in ^{76}Ge, operated in large low-background arrays. This approach is used, with some key differences, by the Majorana and GERDA Collaborations.

A problematic background in such large granular detector arrays is posed by alpha particles incident on the surfaces of the detectors, often caused by ^{222}Rn contamination of parts or of the detectors themselves. In the Majorana Demonstrator, events have been observed that are consistent with energy-degraded alphas originating near the passivated surface of

the detectors, leading to a potential background contribution in the region-of-interest for neutrinoless double-beta decay. However, it is also observed that when energy deposition occurs very close to the passivated surface, high charge trapping occurs along with subsequent slow charge re-release. This leads to both a reduced prompt signal and a measurable change in slope of the tail of a recorded pulse. Here we discuss the characteristics of these events and the development of a filter that can identify the occurrence of this delayed charge recovery (DCR) effect, allowing for the efficient rejection of passivated surface alpha events in analysis.

Using a dedicated test-stand called the TUM Upside-down BEGe (TUBE) scanner, we have characterized the response of a P-PC detector like those used in the DEMONSTRATOR to alphas incident on the sensitive surfaces, developing a model for the radial dependence of the energy loss to charge trapping and determining the dominant mechanism behind the delayed charge effect. We have also used these measurements to demonstrate the complementarity of the DCR analysis with the drift-time analysis that is used to identify alpha background candidate events in the GERDA detectors. Using these two methods, we demonstrate the ability to effectively reject all alpha events (to within statistical uncertainty) with only 0.2% bulk event sacrifice.

Applying the DCR analysis to the events observed in the MAJORANA DEMONSTRATOR, we find that it reduces the backgrounds in the $0\nu\beta\beta$ region-of-interest by a factor of 29, increasing the expected experimental sensitivity by a factor of 3 over the lifetime of the DEMONSTRATOR. The results of the dedicated measurements in the TUBE scanner can be used to build a background model for alpha decays in the DEMONSTRATOR; here, we examine two simplified geometric models for the alpha source distribution and find that the observed spectral shape is consistent with alpha events originating in the plastics of the detector units.

TABLE OF CONTENTS

Page

List of Figures iii

List of Tables vi

Glossary vii

Chapter 1: Neutrino Physics and $0\nu\beta\beta$ Introduction 1
1.1 Neutrinos as a Key to New Physics 1
1.2 Neutrinoless Double Beta Decay 9
1.3 The Majorana Demonstrator 17

Chapter 2: Charge Collection and Surface Effects in HPGe Detectors 24
2.1 HPGe Detector Basics 24
2.2 P-Type Point Contact Germanium Detectors 28
2.3 Surface Effects and Other Charge Collection Anomalies 31
2.4 Alpha Interactions in Ge 34

Chapter 3: Delayed Charge Recovery Tagging 38
3.1 Potential Origins of the Delated Charge Recovery Effect 38
3.2 Current Implementation in the Majorana Demonstrator 40
3.3 Uncertainties Associated with DCR 47
3.4 Tested Improvements to the DCR Analysis 51
3.5 Results in the Majorana Analysis 59

Chapter 4: The TUBE Scanning System 64
4.1 Introduction 64
4.2 Experimental Setup 65
4.3 Measurements Taken 72

4.4 Data Processing Scheme . . . 73
4.5 Detector Performance . . . 79
4.6 Alpha Event Rate . . . 86

Chapter 5: Characterizing Surface Alpha Interactions with the TUBE Scanner . . . 89
5.1 Alpha Energy and Spectral Shape . . . 89
5.2 DCR Parameter Values and Peak Shape . . . 99
5.3 A/E and DCR: Complementary Pulse-Shape Discriminators . . . 115
5.4 Comparison to Models of Surface-Charge Collection . . . 125

Chapter 6: Alpha Backgrounds in the MAJORANA DEMONSTRATOR . . . 130
6.1 Introduction . . . 130
6.2 Standard MAJORANA Analysis . . . 130
6.3 DCR Cut Background Reduction . . . 133
6.4 Rate Analysis . . . 136
6.5 Detector-by-detector Backgrounds . . . 140
6.6 DCR Effect on $0\nu\beta\beta$ Sensitivity . . . 143
6.7 Identifying the Source of Alpha Events in the MAJORANA DEMONSTRATOR 145
6.8 Fitting to the MAJORANA DEMONSTRATOR Spectrum . . . 152

Chapter 7: Conclusions . . . 157
7.1 Summary of Results . . . 157
7.2 Proposed Improvements to the DCR Analysis . . . 158
7.3 Future Studies of Alpha Backgrounds . . . 159
7.4 The Future of Double-Beta Decay Searches . . . 160

Bibliography . . . 162

Appendix A: Background-Subtracted Efficiency . . . 175
A.1 Calculating Efficiency . . . 175
A.2 Uncertainty of Efficiency . . . 176

LIST OF FIGURES

Figure Number		Page
1.1	Feynman diagrams for the weak interactions	2
1.2	The two possibilities for the neutrino mass hierarchy	6
1.3	Feynman diagrams for double-beta decay processes.	10
1.4	$m_{\beta\beta}$ dependence on the neutrino mass and hierarchy	11
1.5	The experimental signature of $0\nu\beta\beta$ decay as it would appear in ^{76}Ge	12
1.6	The background requirements and exposure needed for 3σ discovery-level observation of $0\nu\beta\beta$ decay in the IH	18
1.7	The modular elements of the DEMONSTRATOR design	19
1.8	A diagram of the DEMONSTRATOR shielding configuration	20
2.1	p- and n-type HPGe detectors	26
2.2	Various geometries of HPGe detectors	26
2.3	Calculated signals in an n-type Ge(Li) detector	27
2.4	Weighting potential maps of a coaxial and BEGe-type detector	27
2.5	Simulations of the weighting potential in an p-type ORTEC-style point contact detector.	29
2.6	Sample single- and multi-site waveforms in a P-PC detector	30
2.7	A sample n^+ slow pulse	32
2.8	The ^{222}Rn decay chain	35
3.1	Simulated bulk and passivated surface waveforms	39
3.2	A sample MJD waveform, with indicated tail slope measurement points	41
3.3	The steps of the DCR parameter calculation	42
3.4	99% acceptance DCR cut efficiency and uncertainties	44
3.5	99% acceptance DCR cut continuum efficiency, averaged over all detectors	45
3.6	Comparison of DCR in singly-sampled and multi-sampled MJD data sets	48
3.7	DCR stability study results in DS3 high-gain channels	50
3.8	Sample waveforms demonstrating the effect of pulse-shape on DCR	52

3.9 The effect of bulk charge trapping on DCR in the ^{208}Tl DEP and surrounding continuum. 53
3.10 Comparing v1.0 and v1.1 DCR cut efficiency and uncertainties 55
3.11 The steps of the charge trapping tail slope correction 57
3.12 The results of DCR validation of the 90% bulk-acceptance cut 61
3.13 The rejection fraction of the 90% bulk-acceptance DCR cut as a function of energy 62

4.1 A diagram of the TUBE scanner 66
4.2 A photo of PONaMa-1 installed in the TUBE detector cup 68
4.3 A cartoon showing the accessible regions of the detector surface and the coordinate system of the TUBE scanner 69
4.4 A photo of the inside of the TUBE scanner 70
4.5 A sample TUBE waveform, with indicated tail slope measurement points . . 76
4.6 A comparison of v1.0 (`dcr90`) and v2.0 (`dcrpzc90`) of the DCR analysis in the TUBE system 77
4.7 The residuals of calibration peak positions 81
4.8 A comparison of A vs. E and A/E in calibration events 81
4.9 The TUBE Ge energy spectrum, before and after the muon veto is applied . 85
4.10 Observed alpha event rates in each TUBE data set, following background subtraction 87

5.1 The energy spectra and peak fits for various scanning positions. 90
5.2 Plots of A/E vs. E for small-magnitude radii scans. 92
5.3 The results of Gaussian fits to the alpha energy peaks 94
5.4 Energy fit results as a function of distance from the point contact 95
5.5 A polynomial fit describing the radial dependence on energy 97
5.6 The electron weighting potential at the passivated surface of a PPC detector 100
5.7 DCR parameter distributions and Gaussian fits for various peak positions . . 101
5.8 The results of Gaussian fits to the alpha peaks in `dcrpzc90` and `dcr90` . . . 104
5.9 The results of Gaussian fits to the alpha peaks in `dcrpzc99norm` 104
5.10 `dcrpzc90` and `dcr90` fit results as a function of distance from the point contact 105
5.11 `dcrpzc9norm` fit results as a function of distance from the point contact . . . 106
5.12 The energy of the collected delayed charge, as a fraction of the prompt alpha energy 107

5.13 DCR vs. energy in a data set, showing outlier events . . . 110
5.14 DCR scan results as a function of data set order, for all scanning positions . 112
5.15 DCR scan results as a function of data set order, for —r—¿12 mm, including rate information . . . 113
5.16 The change in DCR parameter values over time at repeated scan positions . 114
5.17 Sample A/E distributions and Gaussian peak fits to alpha events . . . 116
5.18 A comparison of A/E in p+ and near-p+ events. . . . 117
5.19 The results of fits to A/E in each data set . . . 118
5.20 The A/E vs. normalized DCR distribution at various scanning radii . . . 119
5.21 A plot of A/E and DCR alpha peak positions, showing the complementarity of the pulse shape discriminators . . . 120
5.22 The alpha rejection efficiency as a function of radius for each DCR parameter 124
5.23 Simulated waveforms under the two DCR models . . . 126
5.24 Simulation of the energy and DCR dependence on radius for the two charge loss models . . . 128

6.1 The high-energy spectrum in MAJORANA data sets 0-4 . . . 135
6.2 Background rates in MAJORANA Data Sets 0-4 . . . 138
6.3 M1 alpha background rates in MAJORANA Data Sets 0-3, as a function of time 139
6.4 Alpha background rates in all detectors . . . 140
6.5 The distribution of alpha background rates . . . 141
6.6 The predicted energy spectra for the uniform and point-contact contamination models . . . 149
6.7 The predicted energy spectra for the uniform distribution and point-contact contamination models, with incidence angle dependence . . . 152
6.8 The predicted energy spectra for the point-contact contamination model, as h varies . . . 153
6.9 A fit of the constant contamination model to the MAJORANA DEMONSTRATOR energy spectrum . . . 154
6.10 A fit of the point contact contamination model to the MAJORANA DEMONSTRATOR energy spectrum . . . 155

A.1 The energy regions used to calculate the alpha rejection efficiency . . . 176

LIST OF TABLES

Table Number Page

3.1 DCR optimization studies for the DEMONSTRATOR 46
3.2 $0\nu\beta\beta$ efficiency and uncertainties in the MAJORANA DEMONSTRATOR 60

4.1 Dimensions and operating parameters of the PONaMa-1 P-PC detector. . . . 65
4.2 Selected reconstructed data parameters, with brief descriptions. 75
4.3 Multi-site discriminator survival fractions in the ^{208}Th escape peaks and in the Compton continuum near the $0\nu\beta\beta$ region-of-interest. 84

5.1 The results of fits to the alpha energy peak at low-magnitude scanning radii 91
5.2 Estimated energy ranges of alpha interactions at small-magnitude radii . . . 92
5.3 The results of fits to the alpha energy peak for events occurring in the point contact 93
5.4 Average alpha rejection efficiencies for all evaluated DCR parameters. 125

6.1 MJD run quality bit definitions 132
6.2 A summary of open data used from the MAJORANA DEMONSTRATOR data sets. 134
6.3 Background rate results in MAJORANA DEMONSTRATOR data sets 0-4 . . . 137
6.4 The list of high-alpha activity detectors 142

GLOSSARY

$0\nu\beta\beta$: Neutrinoless Double-Beta Decay

$2\nu\beta\beta$: Two Neutrino Double-Beta Decay

SM: Standard Model

BSM: Beyond-the-Standard Model

ROI: Region-of-Interest

MJD: The Majorana Demonstrator

GERDA: GERmanium Detector Array

HPGE: High-purity Germanium

P-PC: P-type point contact detector

BEGE: Broad Energy Germanium

PONAMA: PPC from ORTEC made from Natural Material

TUBE: TUM Upside-Down BEGe Scanner

DCR: Delayed charge recovery

DS#: Majorana Demonstrator Data Set #

ACKNOWLEDGMENTS

I can barely scratch the surface of thanking all who had a hand in the many years of work that this document represents. The support of my advisor, Jason Detwiler, has been invaluable. His enthusiasm and positive outlook towards new problems and new ideas is a model I can only hope to emulate going forward. Thank you, Jason, for believing in my potential from the very beginning, for giving me the freedom to explore, and for your patience and guidance when those explorations lead to meandering paths or dead ends.

This work would not have been possible without David Radford's creativity in proposing this analysis approach, and Susanne Mertens' generosity in making my work at TUM possible and enjoyable. I am also very grateful to have benefited from the expertise and goodwill of the entire CENPA staff, particularly David Peterson, John Amsbaugh, and Doug Will. Thanks are also due to the E15 group at TUM, who welcomed me with open arms, and especially to Tobias Bode, who was always willing to bounce around ideas. The entire MAJORANA group has been an excellent first home in the world of physics – they made even 11-hour days underground in the depth of a South Dakota winter enjoyable at times (and bearable at others). I am so grateful to all of the faculty, led by John Wilkerson, for their commitment to teaching students well and giving them space to grow. All of the post-docs and graduate students, but particularly Clara Cuesta, Ian Guinn, and Micah Buucke, have made this work better than it would otherwise be, and indulged me when I needed a distraction from it.

I would not have reached this point without the help of some important mentors and friends. Laura Bodine, there is no way I can thank you enough for showing me how to be a "tough cookie" and a kind person who doesn't lose sight of the things that matter. Sarah Vorpahl, I am so glad we got to make it through these five years together, there is no one

else I would rather have shared it with. There are too many others to even think of naming them all, but thank you to all of my friends near and far: to Greg and Justin, for helping me become the physicist I am, and to Ben and Jon for commiserating with me when things didn't work, and celebrating with me when they did. Eric, thank you for always having something interesting to talk about that isn't physics, and for all of your support over these years. It means the world to me.

Finally, thank you to my family. Mariel, competing (in a friendly, sisterly way!) with you has taught me so many things that have ended up coming in handy, and I know talking to you will always give me a new perspective on things. Being your sister makes me a better scientist and a better person. Mom and Dad, thank you so much for supporting me even when you don't totally understand me, for teaching me curiosity, for indulging my love of planetarium shows so many years ago, and for sacrificing so much so that I could do something like this. There is no way I can thank you enough.

DEDICATION

Para mi Bobe y Zeide: cómo les hubiera gustado ver esto!

Chapter 1

NEUTRINO PHYSICS AND $0\nu\beta\beta$ INTRODUCTION

1.1 Neutrinos as a Key to New Physics

1.1.1 The "Desperate Remedy"

Since its introduction by Wolfgang Pauli in 1930, the neutrino has been allowing physicists to reconcile theories and experimental results that did not quite align. At the time, the theories in question were the conservation of energy and angular momentum; beta decay observations seemed to violate these key principles. Instead of carrying away the full Q-value of the decay, the observed electrons could carry off a range of energies up to that value. Total momentum did not seem to be conserved, and instead of exiting the interaction going back-to-back, as expected in a two-body decay under momentum conservation laws, the recoiling nucleus and electron could have any angle between them.

As a "desperate remedy," Pauli proposed the neutrino [62]– a light, neutral particle that is created in the decay, carrying off the missing energy and momentum. If it did not interact via the strong or electromagnetic forces, such a particle would be invisible to the beta decay experiments. In fact, the elusive neutrino escaped detection for over twenty years, until it was eventually observed in 1956 [35]. With the addition of this particle to the standard model, beta decay was explained as a three-body process, and the conservation laws were saved.

1.1.2 The Solar Neutrino Problem

Along with the neutrino, the concepts of lepton number and lepton number conservation were introduced. This value, in the standard model, is conserved in weak interactions, which proceed via two classes of vertex, called the neutral and charged currents. The Feynman diagrams for these processes are seen in Fig. 1.1. In the charged current interactions, charged leptons (i.e. the electron, muon, or tau, or their antiparticles) couple to the neutrinos via the W+ and W- bosons. In the neutral current interaction, any lepton couples to its corresponding anti-lepton via the Z boson.

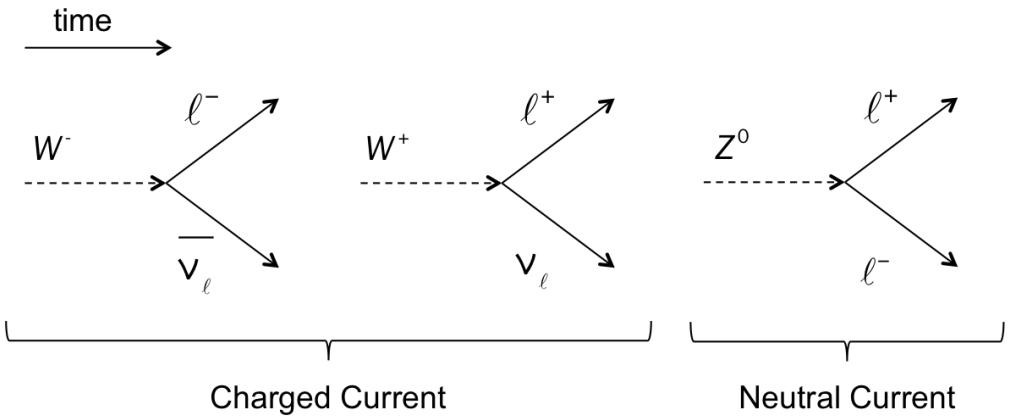

Figure 1.1: The primitive vertices of the Feynman diagrams for weak interactions between leptons in the standard model. Equivalent vertices exist for the quarks. [59]

There are three observed active neutrino flavors, corresponding to the three charged leptons, which form a basis of flavor eigenstates. They are created in these eigenstates; in a charged current interaction emitting an electron, for instance, the standard model requires that an electron anti-neutrino is also created. Originally, it was believed that neutrinos also followed lepton-flavor conservation. Since in the standard model, neutrinos are massless, that electron anti-neutrino would propagate in its flavor eigenstate, and remain an electron anti-neutrino.

With this assumption firmly in place, physicists attempted to detect the neutrinos created

in the sun. Ray Davis and his team, in the Homestake experiment (housed in the predecessor to today's Sanford Underground Research Facility), used a radiochemical technique based on the inverse beta decay $\nu_e + {}^{37}Cl \rightarrow {}^{37}Ar + e^-$ to measure the integrated flux of ν_e with energies over 0.518 MeV. Based on astrophysical models of solar fusion processes, over 6 SNU (Solar Neutrino Units, a unit equivalent to one interaction per 10^{36} target atoms per second) were expected [66] [21]. Measurements from Davis's and other solar neutrino experiments, however, consistently found about a third the flux that these models predicted [31]. Once again the theory and the experimental results did not agree.

As in the 1930s, the unexpected physics of the neutrino saved the day. If the neutrino was not massless, as the Standard Model seemed to assert, but instead had a small mass, it would not propagate in its flavor eigenstate. Instead it would propagate in a mass eigenstate, and if these eigenstates were not equivalent, it would change from one flavor to another as it traveled from the sun to detectors on earth. Experiments like Davis's, which were sensitive only to electron-type neutrinos, would see fewer events than expected, but the deficit would appear as a surplus in the muon- and tau-type neutrino fluxes.

Testing this theory required experiments that could detect the other neutrino flavors, instead of just the solar flux of ν_e. With the construction of the Super-Kamiokande and SNO, atmospheric neutrino disappearance [44] and flavor transformation [18] could be detected. These two observations could only be reconciled by the theory of neutrino oscillations, and the KamLAND experiment directly confirmed that oscillations were occurring [41].

1.1.3 Measuring Neutrino Properties

The mixing of the mass eigenstates in a given flavor eigenstate is described by the unitary Pontecorvo-Maki-Nakagawa-Sakata (PMNS) matrix,

$$\begin{bmatrix} \nu_e \\ \nu_\mu \\ \nu_\tau \end{bmatrix} = \begin{bmatrix} U_{e1} & U_{e2} & U_{e3} \\ U_{\mu 1} & U_{\mu 2} & U_{\mu 3} \\ U_{\tau 1} & U_{\mu 2} & U_{\mu 3} \end{bmatrix} \begin{bmatrix} \nu_1 \\ \nu_2 \\ \nu_3 \end{bmatrix} \tag{1.1}$$

where ν_1, ν_2, and ν_3 are the three distinct neutrino mass eigenstates and the U_{ij} are the mixing parameters. The matrix is generally parameterized using three mixing angles $\theta_{12}, \theta_{23}, \theta_{13}$ and three phase angles, δ_{CP}, α_1, and α_2. In that case, the PMNS matrix can be expressed as:

$$U = \begin{bmatrix} 1 & 0 & 0 \\ 0 & c_{23} & s_{23} \\ 0 & -s_{23} & c_{23} \end{bmatrix} \begin{bmatrix} c_{13} & 0 & s_{23}e^{-i\delta_{CP}} \\ 0 & 1 & 0 \\ -s_{23}e^{-i\delta_{CP}} & 0 & c_{13} \end{bmatrix} \begin{bmatrix} c_{12} & s_{12} & 0 \\ -s_{12} & c_{12} & 0 \\ 0 & 0 & 1 \end{bmatrix} \begin{bmatrix} 1 & 0 & 0 \\ 0 & e^{i\frac{\alpha_1}{2}} & 0 \\ 0 & 0 & e^{i\frac{\alpha_2}{2}} \end{bmatrix} \quad (1.2)$$

where $c_{ij} = \cos\theta_{ij}$ and $s_{ij} = \sin\theta_{ij}$.

This is the parametrization generally used to describe the results of neutrino oscillation experiments. In general, the neutrino oscillation angles θ_{ij} have been observed to be large, unlike the equivalent mixing angles in the quark sector [59]. The only phase observable in neutrino oscillations is δ_{CP}, which describes the quantity of charge-parity symmetry violation. The other two phases, α_1 and α_2, are the Majorana CP-violation phases, which are discussed in Sec. 1.1.4.

The probability of neutrino oscillation from one flavor, α, to another, β, is:

$$P_{\alpha\beta} = \left| \sum_i U^*_{\alpha i} U_{\beta i} e^{-im_i^2 L/2E} \right|^2$$

where L is the baseline length of the oscillations (i.e., the distance traveled by the neutrino), E is the energy of the neutrino, and m_i is the mass of the each mass eigenstate.

To see the the salient features of the mixing, we can examine the simplified case of two-flavor mixing:

$$P_{\alpha\beta} = \sin^2(2\theta) sin^2 \left(\frac{\Delta m^2 L}{4E} \right)$$

where θ is the mixing angle between the two mass eigenstates, and $\Delta m^2 \equiv m_2^2 - m_1^2$. As seen here, the mixing between the flavors depends only on the mass-squared difference between the states, and not on the state masses themselves, or on the sign of the differences between the masses.

The same holds true in the full 3-flavor case. Therefore, in spite of the fact that the mixing parameters and mass-splittings (the Δm_{ij}) have been measured to fairly high accuracy by oscillation experiments, we still have limited information about the other neutrino properties.

The sign of Δm^2_{ij} does appear in the oscillation probability when the neutrino passes through matter, instead of through vacuum, during its travel. The amount of matter needed for the sign determination at current oscillation measurements' sensitivity levels is large. At the moment, only the sign of Δm^2_{21}, also called Δm^2_{sol}, is known. In this case, the neutrino's travel through the sun can be leveraged. From solar neutrino oscillation experiments like SNO and SuperK it is known that $m_2 > m_1$ [59].

Many experiments plan to determine the sign of Δm^2_{atm} (i.e. Δm^2_{23} or Δm^2_{32}, as the case may be) in the coming decade [28], by measuring the effect of the earth's matter on neutrinos. Some plan to detect laboratory-produced beams of neutrinos at long baselines, like DUNE [10], others plan to measure reactor neutrinos at middling baselines, like JUNO [19] and RENO50 [51], and yet others plan to use atmospheric neutrinos, like PINGU [67] and HyperK [4]. At the moment, however, the sign of Δm^2_{23} is unknown, leading to what are called the "normal" and "inverted" possible cases of the neutrino mass hierarchy, as seen in Fig. 1.2 [48].

The normal hierarchy (NH) is referred to as such by analogy to the masses of the charged leptons, since the small splitting between the two lightest species mimics the similar masses of the e and μ, with the τ being significantly heavier. However, both hierarchies are considered to be equally natural under the SM.

The overall mass of each of the eigenstates is also unknown. Direct mass measurements studying the shape of β decay spectra are sensitive to the mix of mass eigenstates of the electron-flavor neutrino:

$$m^2_{\nu_e} = \sum_i |U_{ei}|^2 \, m_i^2$$

The most sensitive such limits come from the Mainz [54] and Troitsk [20] measurements of tritium (^{3}He) decay, which have set upper limits of 2.3 and 2.05 eV, respectively, on $m(\nu_e)$. The KATRIN experiment plans to directly probe masses down to $m(\nu_e) \sim 0.20\,\text{eV}$ [63].

More stringent limits, below 0.29 eV, have been derived from cosmic microwave background observations [39], which are sensitive to the sum of the neutrino masses $\sum m_i$. These

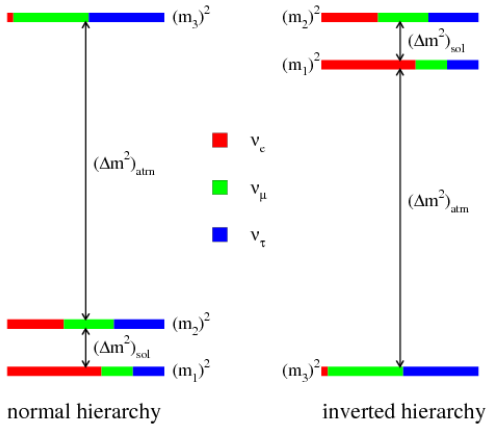

Figure 1.2: The two possible cases of the neutrino mass hierarchy [48]. The sign of Δm^2_{21} is known, but the sign of Δm^2_{23} (or, equivalently, Δm^2_{13}) is not known.

measurements, however, are highly model-dependent.

The CP symmetry-violation phase δ_{CP} is also unknown. This parameter drives the potential difference between the oscillation of the left-handed active neutrinos, and the right-handed active antineutrinos. If charge parity (CP) symmetry is conserved, their oscillation probabilities will be identical; any deviation indicates $\delta_{CP} \neq 0$. Current measurements from neutrino beam experiments like T2K [3] and NOνA [56] weakly disfavor CP conservation.

1.1.4 The Origins of Neutrino Mass

Because neutrino oscillations have been observed, at least two of the neutrino mass eigenstates are required to be non-zero. The Standard Model description of how particles get their mass, however, cannot be straightforwardly applied to the neutrino.

The Dirac Mass Mechanism

In the SM, fermions are described by a combination of four independent fields. Electrons, for instance, are described with the fields (e_L, $\overline{e_L}$, e_R, $\overline{e_R}$), where L and R refer to left- and right-chiral fields and the bar refers to charge-conjugation, i.e., the positron e^+. Such Dirac

particles receive their masses through interaction with the Higgs field, which couples the left- and right-chiral fields of the same charge to one another. In other words, the Higgs interaction changes the particle's chirality, but not its charge.

In the SM, however, the right-chiral neutrino field ν_R and the left-chiral antineutrino field $\overline{\nu_L}$ do not exist; since the weak-interaction is maximally parity-violating, such fields would be sterile. In other words, the $W^{+(-)}$ and Z bosons would not couple to them, and they would be non-interacting. Unlike the charged particles of the SM, they are not needed to fully describe the interactions we observe.

These fields can be added to the SM, making the neutrino a Dirac particle and granting it mass via the Higgs mechanism. This mass mechanism, however, leaves a fine-tuning problem. Current limits indicate that the neutrino mass is at least five to six orders of magnitude smaller than the masses of the other standard model particles, and the theory provides no justification for this large difference.

The Majorana Mass Mechanism

Since the neutrino is neutral, the four independent Dirac fields are not needed to fully describe it. Instead, the neutrino could be described by just two fields, ν_L and ν_R. The left-chiral field, in this case, corresponds to the particle we observe as the neutrino, and the right-chiral field to the one we observe as the antineutrino. This would make the neutrino a Majorana particle.

In this case, the particle would receive its mass from the the left-handed Majorana mass term, which couples $\overline{\nu_R}$ to ν_L. In other words, the Majorana mass term changes the particle's chirality and its charge. On its own, however, it is not renormalizible; some sort of Beyond-the-Standard-Model physics is needed to act as a cut-off or to cancel the infinite terms. The right-handed Majorana mass term (and therefore the sterile neutrino fields ν_R and $\overline{\nu_L}$) or some other massive particle could perform this function.

The Majorana mass mechanism violates lepton-number conservation and allows for the possibility of additional CP-violation. In the PMNS matrix, parametrized as in Eqn. 1.2,

the Majorana phases α_1 and α_2 can now be observed.

Since the mass mechanism is completely different than that of the other SM particles, the size of the neutrino mass is no longer unnatural. In fact, the Majorana mass mechanism can be used to explain its smallness, through what is known as the "see-saw mechanism."

The See-Saw Mechanism and Other Remedies

An intriguing possibility for the origin of the neutrino mass is the see-saw mechanism, in which the neutrino has both Dirac and (left- and right-handed) Majorana masses. In this case, the 4 degenerate-mass Dirac fields of the neutrino are split into two lighter and two heavier fields by the addition of the Majorana mass term.

When both of these terms are included, the Lagrangian for the neutrino mass becomes:

$$L_{mass} = \frac{1}{2} \left(\overline{\nu_L}\ \overline{\nu_R}^c\right) \begin{bmatrix} M_L & m_D \\ m_D & M_R \end{bmatrix} \begin{bmatrix} \nu_L^c \\ \nu_R \end{bmatrix} + h.c.$$

where M_L and M_R are the left- and right-handed Majorana mass terms, m_D is the Dirac mass term, and *h.c.* indicates the Hermitian conjugate of the first term.

If $M_L \to 0$, diagonalizing this matrix gives two effective fields:

$$L_{mass} = \left(\overline{\nu}\ \overline{N}\right) \begin{bmatrix} \frac{m_D^2}{M_R} & 0 \\ 0 & M_R \end{bmatrix} \begin{bmatrix} \nu \\ N \end{bmatrix}$$

where we have identified the particle with the correct handedness (i.e. a left-handed particle and a right-handed antiparticle) as the neutrino ν, and the new particle as N.

The ν then has mass $\frac{m_D^2}{M_R}$, and the new opposite-handed particle N has mass M_R. If m_D is about 100 GeV, similar to the other Dirac masses, and m_R is of the same order as the GUT scale, about 10^{15} GeV, then the neutrino mass would be about 10 meV, similar to the neutrino mass implied by current limits and oscillation experiments. The new particle N would be a heavy right-handed neutrino that is only present in the early universe.

Thus, the see-saw mechanism provides a natural explanation for the smallness of the observed neutrino mass. The Majorana mass mechanism also allows leptogenesis, which

in combination with the new heavy right-handed neutrino N could provide a mechanism for baryogenesis in the early universe, explaining the matter/anti-matter imbalance in the observable universe [24]. The unexpected physics of the neutrino could once again provide a remedy to some of the problems of our current understanding of fundamental physics.

1.2 Neutrinoless Double Beta Decay

1.2.1 $0\nu\beta\beta$ Theory

The most promising process by which to discover the nature of the neutrino is neutrinoless double beta decay.

In standard-model two neutrino double-beta decay ($2\nu\beta\beta$), a nucleus that contains an even number of nucleons is energetically forbidden from decaying via single beta-decay. Therefore, $2\nu\beta\beta$, a far rarer, second-order process, can be observed. Two beta decays occur, leading to the emission of two electrons and two electron anti-neutrinos:

$$X(A, Z) \rightarrow X(A, Z + 2) + 2e^{-} + 2\ \overline{\nu_e}$$

as shown in Fig. 1.3a. $2\nu\beta\beta$ has a very long half-life ($t_{1/2} > 10^{18}$ yrs), but is predicted under the Standard Model and has been observed in about a dozen different nuclei [22].

If the neutrino is Majorana, an even rarer process could occur: instead of emitting two antineutrinos, the antineutrino could be exchanged within the nucleus as a virtual particle. In other words, it functions as an outgoing antineutrino for one of the β decays, and as an incoming neutrino for the other decay, as shown in Fig. 1.3b. Thus, no neutrinos are seen in the final state:

$$X(A, Z) \rightarrow X(A, Z + 2) + 2e^{-},$$

and all of the energy of the decay is carried by the electrons. Due to momentum conservation, the nucleons carry a negligible amount of the energy.

This decay relies on the non-conservation of lepton number, on the Majorana nature of the neutrino, and on the fact that the emitted neutrino is in a mixed helicity state. Because

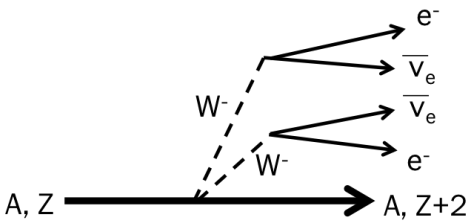

(a) Standard Model-allowed $2\nu\beta\beta$.

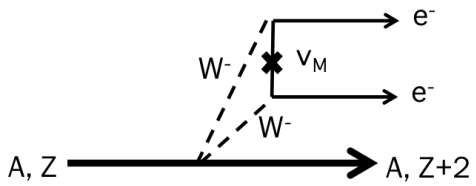

(b) $0\nu\beta\beta$, which can only occur if the neutrino is Majorana. The cross indicates the appearance of a Majorana mass term.

Figure 1.3: Feynman diagrams for double-beta decay processes.

of the last consideration, the effective size of the Majorana mass term,

$$\langle m_{\beta\beta} \rangle = |\sum_{i=1}^{3} U_{ei}^2 m_i|,$$

appears in the $0\nu\beta\beta$ rate:

$$(T_{1/2}^{0\nu})^{-1} = G^{0\nu} |M_{0\nu}|^2 \left(\frac{\langle m_{\beta\beta} \rangle}{m_e} \right)^2 . \tag{1.3}$$

$G^{0\nu}$ is a phase space factor, $M_{0\nu}$ is the nuclear matrix element, and m_e is the electron mass.

The half-life in Eqn. 1.3 only holds for double-beta decay via the exchange of a light Majorana neutrino, the minimal model by which it can occur. However, this observed decay could also occur via a variety of other, more exotic mechanisms, all of which would imply that the neutrino is a Majorana particle and that lepton number is not conserved [65].

Because they contribute to $m_{\beta\beta}$, both the overall neutrino mass scale and the mass hierarchy can contribute to the observed rate, as seen in Fig. 1.4. Here we see that if the neutrino masses are large compared to the size of the mass splittings, the mass hierarchy does not significantly affect $m_{\beta\beta}$. If, on the other hand, the neutrino masses are similar in scale to the mass splittings, having two heavier neutrinos and only one lighter neutrino, as in

the IH, leads to a higher $m_{\beta\beta}$ and a higher $0\nu\beta\beta$ rate than the NH at an equivalent lightest neutrino mass.

Additionally, in the NH, unlike in the IH, the two Majorana phases α_1 and α_2 can lead to complete cancellation of $m_{\beta\beta}$ at certain neutrino masses, seen in Fig. 1.4 as the region in which the allowed band extends to $m_{\beta\beta} = 0$. In Bayesian models of the discovery potential of future $0\nu\beta\beta$ experiments, the probability of such a combination of parameters depends strongly on the prior used to model the neutrino masses. It has been discussed extensively in recent analyses [15] [29].

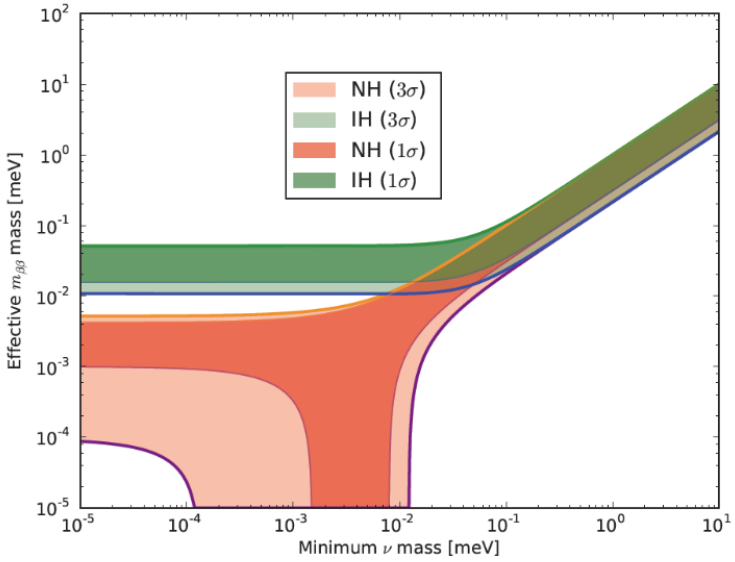

Figure 1.4: $m_{\beta\beta}$, and therefore the $0\nu\beta\beta$ rate, depend on the neutrino mass hierarchy and the overall mass scale [70]. The shaded bands indicate 1 and 3σ uncertainties on the neutrino oscillation parameters.

The well-understood behavior of $m_{\beta\beta}$, and therefore $(T^{0\nu}_{1/2})^{-1}$, makes $0\nu\beta\beta$ an exciting prospect for experimental study. One hopes to detect $0\nu\beta\beta$, of course, but even a null signal provides information about the nature of the neutrino, particularly when combined with other experiments that could determine the neutrino mass and mass hierarchy.

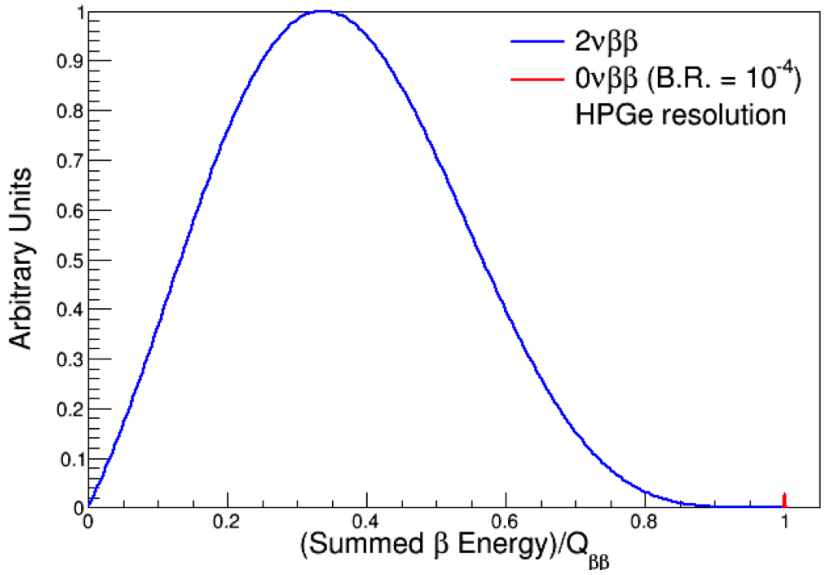

Figure 1.5: The experimental signature of $0\nu\beta\beta$ decay as it would appear in ^{76}Ge. Plot courtesy of Jason Detwiler.

Conversely, a measurement of $(T^{0\nu}_{1/2})^{-1}$ would provide information about the neutrino mass and possibly determine the neutrino mass hierarchy. There would be some uncertainty in these determinations, since experimental results must be translated from a measurement of $(T^{0\nu}_{1/2})^{-1}$ to a value of $m_{\beta\beta}$, which involves the uncertain matrix element for the nucleus in question. If $0\nu\beta\beta$ were detected in multiple isotopes, however, the effects of this uncertainty would be mitigated.

1.2.2 Observing $0\nu\beta\beta$

Since no energy is carried away by neutrinos, the entire energy difference Q between the initial- and final-state nucleus undergoing double-beta decay is carried by the outgoing electrons. Since double-beta decay experiments measure the sum of the electron energies, the experimental signature of such a decay would be a delta peak in energy at the endpoint of the two-neutrino mode spectrum, as in Fig. 1.5.

The challenge in detecting $0\nu\beta\beta$ comes from its extremely low rate. Current limits set the $0\nu\beta\beta$ half-life to greater than 10^{25} years [32]. To observe such a rare decay, backgrounds of $0\nu\beta\beta$ experiments must be extremely low, and the mass of source material must be as large as possible.

Several strategies are commonly used by the $0\nu\beta\beta$ community. Some are determined solely by the choice of source material:

- Q Value: The higher the Q-value of the $0\nu\beta\beta$ decay in some material, the less background contamination will occur in the signal region. While incomplete energy collection, Compton scattering, and other processes can cause background events to appear at energies below the peak value of the decay, events generally cannot gain energy by any process.

- Enrichment: Source materials often have to be enriched in the $0\nu\beta\beta$ isotope to allow for higher source masses without increasing backgrounds. The ease and expense of this process varies widely depending on the material, as does the need for enrichment.

- Favorable Matrix Elements: $M_{0\nu}$ varies between isotopes; a favorable rate could increase the $0\nu\beta\beta$ rate. However, different calculation strategies lead to variation in these values that is on the order of the difference between isotopes. See [50] for further discussion.

- Low $2\nu\beta\beta$ Rate: The resolution of any detector is imperfect, so events from the high-energy tail of the $2\nu\beta\beta$ will contribute to the background. The 2ν rate is unrelated to the 0ν rate, so a lower $2\nu\beta\beta$ rate reduces backgrounds without affecting the $0\nu\beta\beta$ rate.

Unfortunately, there is no "magic bullet" isotope for $0\nu\beta\beta$ that has all the favorable properties [64].

Other strategies for background reduction are affected by the detector technology used and the design of the experiment:

- Source as Detector: Using the same material for both source and detector increases efficiency and makes it easier to increase source mass without increasing backgrounds.

- Surface Event Rejection and Fiducial Volume Cuts: Generally, the bulk of the source/detector material is low in background, and most background events are from surface contamination, external sources or other components of the experiment. Detection strategies that allow surface events to be removed from the data set can often reduce backgrounds by taking advantage of self-shielding.

- Multi-Site Rejection and Particle Identification: Many backgrounds are from γ and α particles. The former often lead to multi-site interactions, while $0\nu\beta\beta$ is by its nature a single-site process, since electrons have much a shorter mean-free-path than photons in detector materials. If the detector can distinguish between multi-site and single-site interactions, backgrounds can be reduced. α backgrounds can be distinguished from e/γ interactions in many two-energy-channel detectors, like time projection chambers and scintillating bolometers, and similarly reduced.

- High Resolution: Higher resolution makes background events easier to identify and shrinks the region of interest (ROI) for $0\nu\beta\beta$ decay, making background requirements less stringent.

- Low Thresholds: Low energy thresholds are not required, but can allow better identification of high-energy backgrounds through timing cuts that search for L- and K-shell decay peaks of short-lived intermediate states of certain background decays.

- Large Overburden: All competitive $0\nu\beta\beta$ decay experiments are housed underground, to decrease the rate of cosmic-ray-induced backgrounds and cosmogenic activation of detector materials.

This work focuses on improving an existing $0\nu\beta\beta$ experiment via the development of pulse-shape based identification of surface α events, a strategy that falls under two of these bullet points.

1.2.3 Backgrounds and $0\nu\beta\beta$ Sensitivity

The coming generation of $0\nu\beta\beta$ searches will attempt to explore the entire inverted hierarchy region of $m_{\beta\beta}$, i.e. the bottom edge of the green region in Fig. 1.4. A plot showing the required exposure needed to achieve a discovery at this level in a given isotope, as shown in the case of ^{76}Ge in Fig. 1.6, demonstrates the stringent background requirements of such an experiment. For an experiment that could discover $0\nu\beta\beta$ in inverted-hierarchy neutrinos with any neutrino mass, $1\,\mathrm{cnt/(ROI\,t\,y)}$ is the maximum allowable background at all reasonable exposures. The background requirements of experiments using other isotopes are comparable.

1.2.4 $0\nu\beta\beta$ Searches in ^{76}Ge

^{76}Ge has several advantages as a choice of isotope for $0\nu\beta\beta$ searches, both in its innate properties and when used to create semiconductor diode detectors.

Its Q-value, at 2.039 MeV, is above the energies of most gamma background events. The only potentially significant environmental gamma background contributions are from ^{208}Th and ^{214}Bi decay in the ^{232}Th and ^{238}U chains, respectively. Other potential gamma background contributions come from cosmogenic activation of the detector and other materials in the experiment, in the form of ^{68}Ge and the sum-peak of ^{60}Co decay. Finally, muon-induced neutron spallation in the materials surrounding the detector could also lead to scattering of fast neutrons or high-energy gamma cascades, though these events are rare for experiments with large overburdens.

Natural-abundance Ge, which is 7.75% ^{76}Ge, can be enriched to over 87% ^{76}Ge. Though this process is expensive, it is well-understood, and both the facilities and raw material exist to enrich the large quantities needed for current and future experiments.

The biggest advantages of ^{76}Ge $0\nu\beta\beta$ searches come from the detector technologies that can be used with this isotope. High-Purity Ge (HPGe) detectors are intrinsically very pure, giving them low internal backgrounds. They have a long history in nuclear physics and rare-event searches, so the techniques needed to operate them reliably are well-developed. The detector operating conditions are also relatively undemanding, another major advantage; they run at liquid nitrogen temperatures and biases below 5 kV. Both ultra-low temperatures, like those needed to operate bolometers, and high voltages, like those needed to operate time-projection chambers, can be difficult to achieve while maintaining low environmental background rates.

P-type point-contact HPGe detectors are particularly appropriate for $0\nu\beta\beta$ searches. They can be operated with extremely high resolution, giving a $0\nu\beta\beta$ region-of-interest of 3 keV. Compared to other detectors that are deployed in granular arrays, P-PC detectors have low susceptibility to surface backgrounds. Their energy thresholds are low, and can be below 1 keV, allowing the possibility of additional rare-event searches using the same $0\nu\beta\beta$ detector, such as direct light-WIMP and solar axion searches [7]. The properties of P-PC detectors also allow for multi-site event rejection. These aspects of HPGe detector physics and operation are discussed more extensively in Ch. 2.

Past experiments have searched for $0\nu\beta\beta$ in ^{76}Ge, and two large experiments using this isotope are currently underway. The two currently-operating experiments are the Majorana Demonstrator, described at length in Sec. 1.3, and the GERmanium Detector Array (GERDA), a similarly-sized experiment at LNGS. The two projects differ mainly in their approach to background reduction. Unlike the Demonstrator, GERDA relies on active shielding from a liquid-Argon veto system to identify and reject background events[11]. The P-PC detectors used in the two experiments also have different geometries, as discussed in Ch. 2. The work described in this thesis applies, at least in part, to both experiments.

A controversial claim of observed $0\nu\beta\beta$ in ^{76}Ge was published by Klapdor-Kleingrothaus et. al in 2001[52]. The current generation of experiments aims to evaluate this claim and establish techniques for future experiments. Already, the GERDA results have disproven

this claim at high confidence and demonstrated background-free operation of a large-scale array of HPGe detectors [33].

Additional low-background techniques, developed for the MAJORANA DEMONSTRATOR, should allow the next generation of experiments to probe the entire inverted-hierarchy region, which requires $\mathcal{O}$(1 tonne) of source material, given reasonably achievable backgrounds. See Fig. 1.6. The LEGEND Collaboration, formed in October 2016, plans to pursue this via a scaled approach, building first a 200 kg-scale detector, and then moving to a tonne-scale detector.

1.3 The MAJORANA DEMONSTRATOR

1.3.1 The DEMONSTRATOR *Apparatus*

The MAJORANA DEMONSTRATOR, the $0\nu\beta\beta$ decay search that is the focus of much of this thesis, is an experiment made up of 44.8 kg of PPC detectors. 29.7 kg of this mass is enriched to 88% ^{76}Ge, and 15.1 kg is in natural-abundance detectors. In addition to making a measurement of the $0\nu\beta\beta$ half-life comparable to that of other currently-operating experiments, its main experimental goals are:

- to demonstrate backgrounds low enough to justify construction of a tonne-scale experiment
- to establish the feasibility of and techniques needed to construct and field modular arrays of Ge detectors
- to search for additional physics beyond the Standard Model

The DEMONSTRATOR established a background goal of 3 cnts/(ROI t y) assuming a 4 keV ROI at the $0\nu\beta\beta$ Q-value. Accounting for self-shielding effects, this rate scales to 1 cnt/(ROI t y) in a tonne-scale experiment, the maximum allowable background needed to fully explore the IH region with such an experiment.

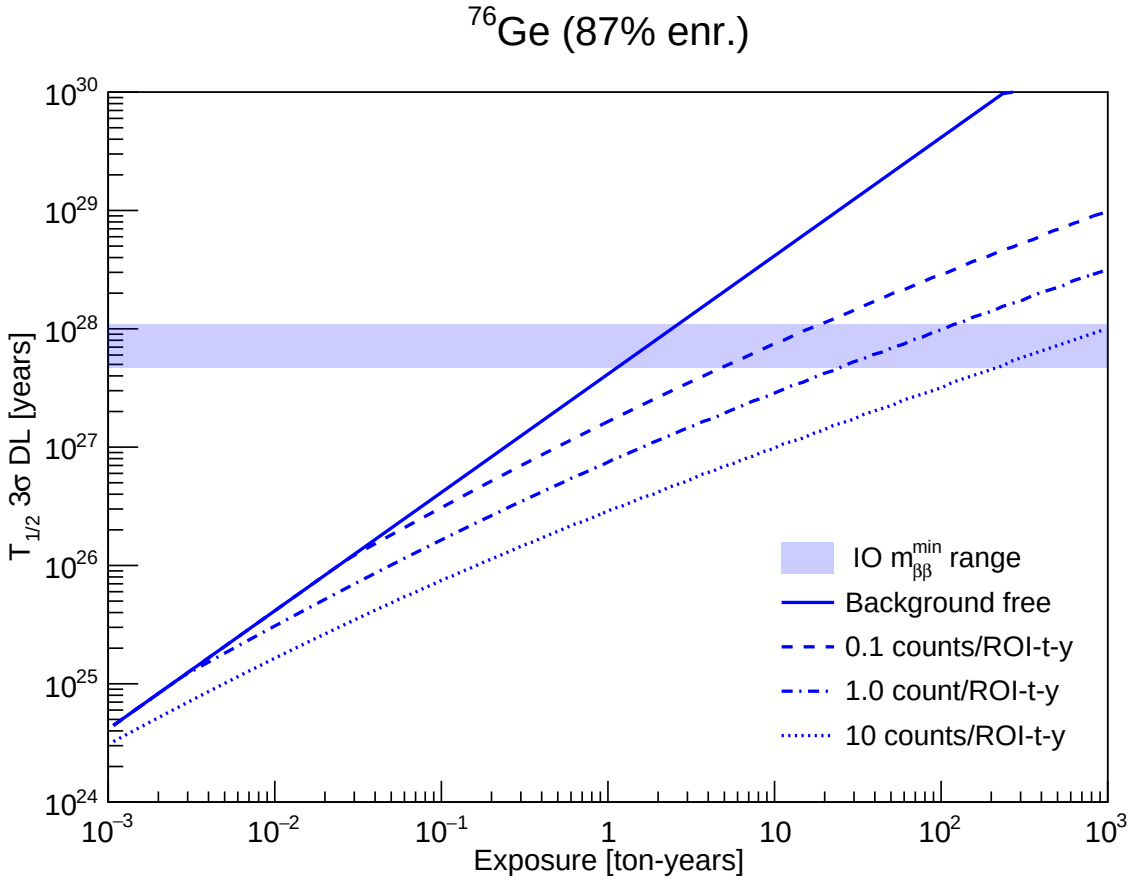

Figure 1.6: The background requirements and exposure needed for 3σ confidence-level discovery of $0\nu\beta\beta$ decay (in over 50% of an ensemble of identical experiments), assuming the inverted hierarchy. The various blue lines indicate the increase in sensitivity with increasing exposure for different background levels, and the shaded band indicates the bottom of the inverted hierarchy band in Fig. 1.4 under various nuclear matrix element calculation approaches. Plot courtesy of Jason Detwiler.

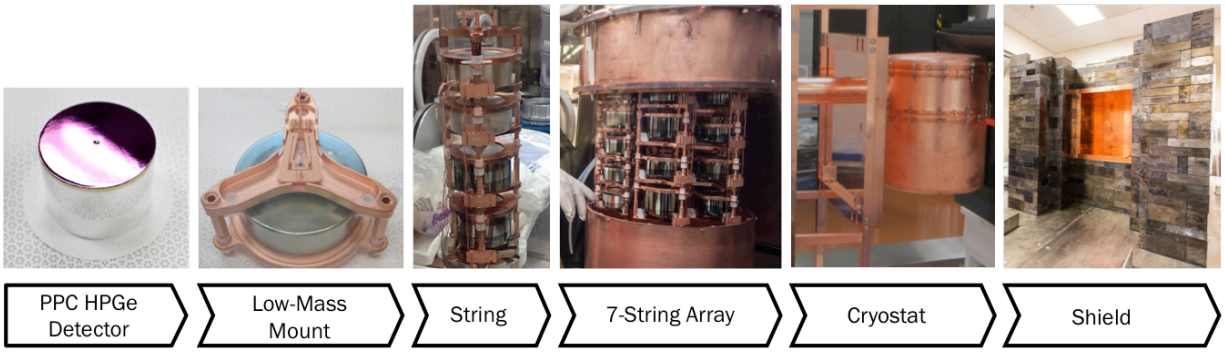

Figure 1.7: The MAJORANA DEMONSTRATOR uses a modular design approach. The P-PC detector shown is similar, though not identical, to those used in the DEMONSTRATOR. Photos by James Loach and Matt Kapust.

The DEMONSTRATOR uses a staged, modular approach to construction (as seen in Fig. 1.7), making its techniques naturally scalable to a tonne-scale experiment. All of the detectors in the DEMONSTRATORare P-PC HPGe detectors, produced by ORTEC and Canberra. The detectors themselves are discussed in Ch 2. Each of the 58 detectors is placed in a low-mass copper mount that holds the detector and a low-mass front-end (LMFE) board that provides the first stage of signal amplification. The mount provides contact to the detector for thermal cooling, high-voltage biasing, and signal readout. These detector mounts are stacked into "strings" of three to five detectors, and each string is suspended from the cold-plate of a copper cryostat. Seven strings are housed in each of the two MAJORANA cryostats. Each cryostat has its own cooling and vacuum system; the cryostat together with its dedicated systems is called a "module."

The two cryostats are inserted in a compact Cu and Pb shield and surrounded by a nitrogen-purged radon exclusion enclosure. Plastic scintillator veto panels surround the shield, detecting through-going cosmic muons, and the modules are enclosed in high density polyethylene (HDPE) shielding to limit neutron backgrounds. The inner layers of the poly shielding are made of borated HDPE to provide further neutron capture. See Fig. 1.8.

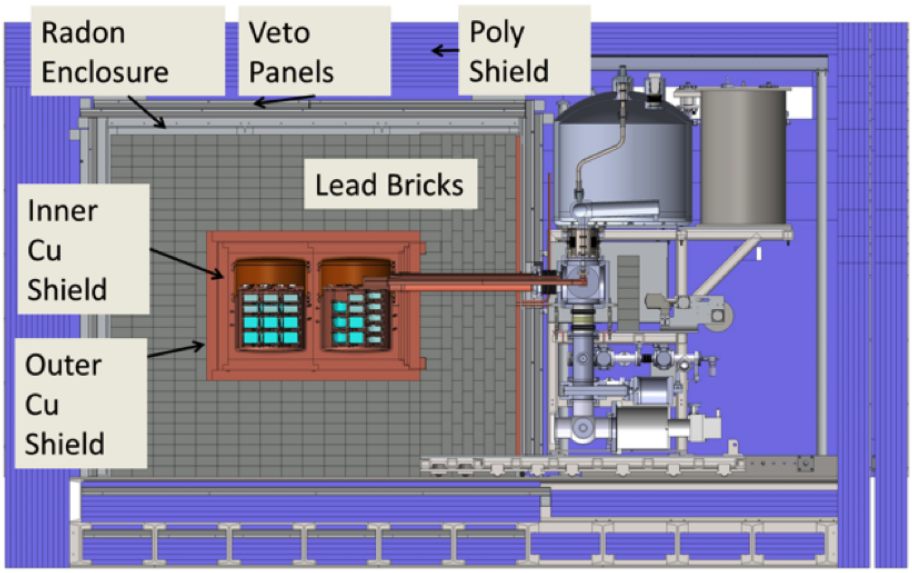

Figure 1.8: A diagram of the DEMONSTRATOR showing the placement of the two cryostats, one of the two modules, the veto panels, and the shielding structure. The inner copper shield is made from underground electroformed copper, with the outer copper shield made from OFHC commercial copper. Diagram taken from [5].

The DEMONSTRATOR is housed at the Davis Campus, at the 4850' level of the Sanford Underground Research Facility (SURF) [5].

The DEMONSTRATOR relies on ultra-low-background material selection and construction for its background reduction approach, with passive shielding to limit radioactive background events from the surrounding environment. The DEMONSTRATOR's main innovations in this area are the use of ultra-clean underground electroformed copper and the development of extremely low-background and low-noise front-end electronics.

Electroforming copper effectively removes impurities, limiting the U and Th chain contamination of the material. By performing the electroforming and machining of the parts underground, the material's exposure to cosmic rays is also minimized. This prevents the formation of ^{60}Co, another problematic long-lived isotope. The over-2000 kg of copper made

underground by the MAJORANA Collaboration has U and Th chain contamination levels of less than 0.1 μBq/kg each. This upper limit is better than the 0.3 μBq/kg goal set by the Collaboration [8]. This clean copper is used for almost all the parts found in the DEMONSTRATOR, from the mounts holding each detector to the cryostats and inner shielding layer. The use of this material, along with extensive clean material selection and assay programs, has led to an assay-based prediction of < 3.5 cnts/(ROI t y) of background events in the DEMONSTRATOR[8].

The LMFE developed for the DEMONSTRATOR has excellent noise performance [5] while maintaining high radiopurity. This allows the LMFE to be mounted directly onto each detector, reducing capacitative noise in the system, and improving the DEMONSTRATOR's overall noise performance. In the search for $0\nu\beta\beta$, there are two main benefits to this design. First of all, the extremely good resolution of the DEMONSTRATOR allows the use of a 3 keV ROI [30], rather than the planned 4 keV window. This reduces the background for $0\nu\beta\beta$ detection by 75% for an equivalent contamination level in the experiment. Second of all, the fast rise-times and low noise of the LMFE and other developed electronics allow for good performance of multi-site event discrimination, described in Ch. 2.

The electronics design and low backgrounds of the DEMONSTRATOR, even at low energies, also allow the MAJORANA Collaboration to pursue additional BSM physics observations. In the search for low-mass WIMP dark matter candidates, solar axion scattering off of electrons, and a slew of other proposed new physics, the DEMONSTRATOR has shown sensitivity comparable to that of many dedicated experiments [7]. The DEMONSTRATOR's sensitivity to these processes will continue to increase as its exposure increases and as the analysis techniques used for near-threshold events are improved.

1.3.2 Construction of the DEMONSTRATOR

To maintain material cleanliness, the DEMONSTRATOR was constructed in a class-1000 cleanroom. All parts internal to the shielding were placed under nitrogen purge immediately after surface cleaning to reduce Rn implantation. The detectors themselves were only exposed in

nitrogen-purged spaces, and never to the air of the underground laboratory. The assembly of all elements internal to the cryostat, where the materials have line-of-site exposure to the detectors, was conducted in a class-10 continuously-purged glovebox.

These efforts reduced the chance of the detectors being exposed to humidity and dust, which increases their leakage current, degrading their resolution, and of all the materials being contaminated with U- and Th-containing dust, increasing backgrounds in the DEMONSTRATOR. The use of nitrogen-purged environments reduces the chance of contamination by ^{222}Rn or other isotopes in its decay chain, which pose problematic backgrounds for $0\nu\beta\beta$ detection. This source of background events is the focus of this thesis.

To ensure that cleanliness standards were maintained and that the many detectors and strings were assembled in a repeatable and reliable way, extensive administrative controls were developed. These work-logging and quality control procedures allowed the DEMONSTRATOR to be successfully assembled by a rotating workforce, with many new researchers being trained in construction over the course of more than two years. Every part and procedure used in the experiment was also tracked in the Majorana Parts Tracking Database [6], allowing the origin of any observed backgrounds to be investigated.

1.3.3 Operations

The DEMONSTRATOR operations took a phased approach, allowing the start of low background data taking with Module 1 while Module 2 was being assembled. Module 1 began operations in May 2015, with Module 2 beginning data taking in May 2016. The MAJORANA DEMONSTRATOR's official transition to operations occurred in March 2017.

The DEMONSTRATOR uses a statistical blinding approach, in which 1/4 of the data is open, and the remaining 3/4 is blinded. Blinded data-taking has been ongoing since Dec. 31, 2015. The results discussed in Ch. 6 are from the open part of Data Sets 0 through 4, summarized in Table 6.2.

Initial results from the DEMONSTRATOR, covering only the open portions of data sets 0 and 1, were reported at the XXVII International Conference on Neutrino Physics and

Astrophysics in 2016 [42]. Using a background estimate window of 400 keV surrounding $Q_{\beta\beta}$, these results reported a background index of $(7.5^{+4.5}_{-3.4}) \times 10^{-3}$ cnts/(keV kg y), corresponding to 23^{+13}_{-10} cnts/(ROI t y) in a 3.1 keV ROI.

Recent simulations by the MAJORANA Collaboration have shown that the 400 keV background estimate window used to report these results includes several expected gamma peaks from background sources, and over-estimates the flat background rate in the $0\nu\beta\beta$ ROI. The change to a 350 keV window that excludes these peaks, along with other improvements in analysis and the DEMONSTRATOR's increased exposure, result in a background index of $(2.6^{+4.0}_{-1.6}) \times 10^{-3}$ cnts/(keV kg y). This corresponds to $7.7^{+11.0}_{-4.8}$ cnts/(ROI t y) in the now-appropriate 3.0 keV ROI [30]. These preliminary results, which are discussed in Ch. 6, are consistent to within 1σ with the DEMONSTRATOR assay- and simulation-based upper limit of the expected backgrounds.

Chapter 2

CHARGE COLLECTION AND SURFACE EFFECTS IN HPGE DETECTORS

2.1 HPGe Detector Basics

High-purity Germanium (HPGe) detectors are made from one large semiconductor crystal of low impurity-concentration germanium, forming a diode (i.e. p-n junction). Two electrical contacts, the p^+ and n^+ contacts, are made on the crystal's surface, and the entire crystal is reverse-biased, resulting in a depleted region between the contacts. When the detector is biased to its operating voltage (generally between 1 and 5 kV), its entire volume is fully depleted, and the charge drift speeds in the interior are fully saturated. In other words, applying a higher bias voltage will not change the current produced at the contacts. The electric field (and therefore, the pattern of charge drift paths) in the interior of the detector is fixed, set by the shape of the electrical contacts at the surface and, in some cases, the doping of the crystal.

In normal operation, currents in the detector are produced when some form of radiation penetrates the active volume, moving electrons in the crystal from the valence band to the conduction band. This leaves a vacancy in the valence band called a "hole," which behaves as a positive charge in the electric field. The amount of energy needed to create such an "electron-hole pair" depends on the size of the band gap in the crystal.

In germanium, the band gap is very small, at 0.7 eV [26]. Therefore, thermal excitations at room temperature can easily create electron-hole pairs. To reduce this "dark current," the detector must be cooled, generally to between 77 and 100 K using liquid nitrogen. The main advantage of semiconductor detectors like HPGe detectors is in the small amount of energy needed to create an electron-hole pair. In Ge at 77 K, only 2.96 eV is needed for each

pair. This gives the detectors intrinsically high resolution, or at least, the potential for high resolution.

Once in the conduction band, the electrons and holes drift to the n^+ and p^+ contacts, respectively, inducing a current on the contacts. The integral of the current induced is proportional to the energy of the interaction that originally created the cloud of electron-hole pairs. Currents from both charge carriers sum to give the observed signal; the fraction contributed by each type of carrier depends on the position where the charges originate and on the electric field, which in turn depends on the doping of the detector.

HPGe detectors are made in *p*- and *n*-types, as determined by their doping. *n*-type detectors are doped with electron donor impurities, so called because they leave one loosely-held valence electron available after bonding to the surrounding Ge atoms. The net effect of these impurities, even at low concentrations, is to give an excess of conduction electrons and a deficit of holes compared to the un-doped material. This means that for almost all charge origin positions in *n*-type detectors the majority of the observed current is made by the electrons, with a small contribution from the holes. To take advantage of this fact, *n*-type detectors have their electrical contacts arranged as in Figs. 2.1 and 2.2, with the geometry giving a large field gradient near the n^+ contact, where the signal is read out.

The reverse is true of *p*-type detectors, which are doped with electron acceptor impurities. In this case, the holes provide most of the current, and the signal is read out at the p^+ contact.

In both types of detectors, the fractional contribution of the two types of carriers also varies as a function of the event origin position (i.e. where in the volume of the crystal the charge cloud is created). In an *n*-type coaxial detector, as shown in Fig. 2.3, signals from events near the central (n^+) contact, like event 2, will have a small fast electron-fraction, and a large slower hole fraction. Near the outer (p^+) contact (i.e. event 0), the reverse will be true, with the signal having a small fast hole fraction, and a large slower electron fraction. Event 1 occurs at a halfway position, where the effect of the detector doping dominates the carrier fractions. Since the detector shown is *n*-type, its signal has a large electron fraction, and a small slower hole fraction. In all three cases, the opposite behavior is seen in *p*-type

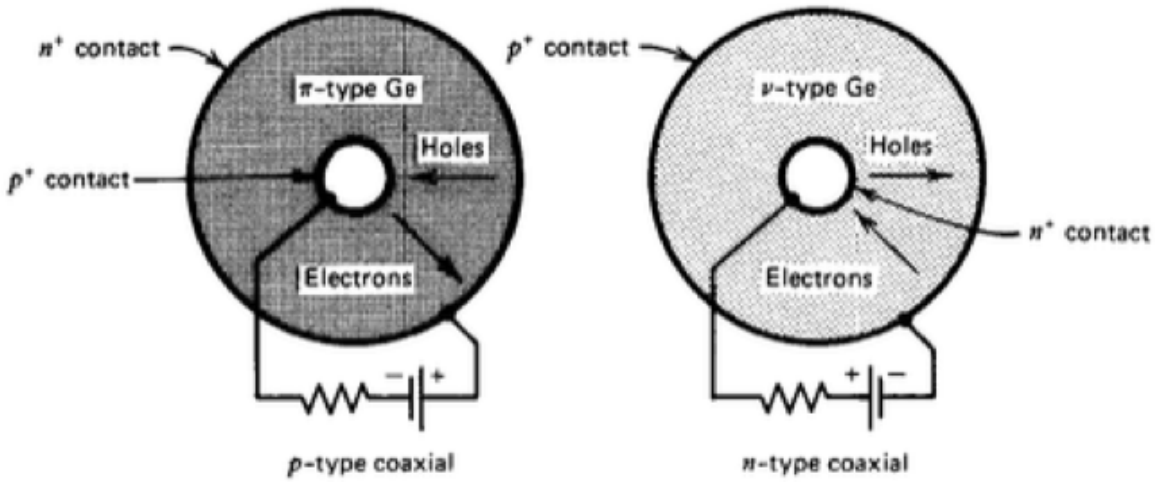

Figure 2.1: Diagrams of coaxial detector cross-sections for *p- (left)* and *n- (right)* type HPGe detectors. From [53].

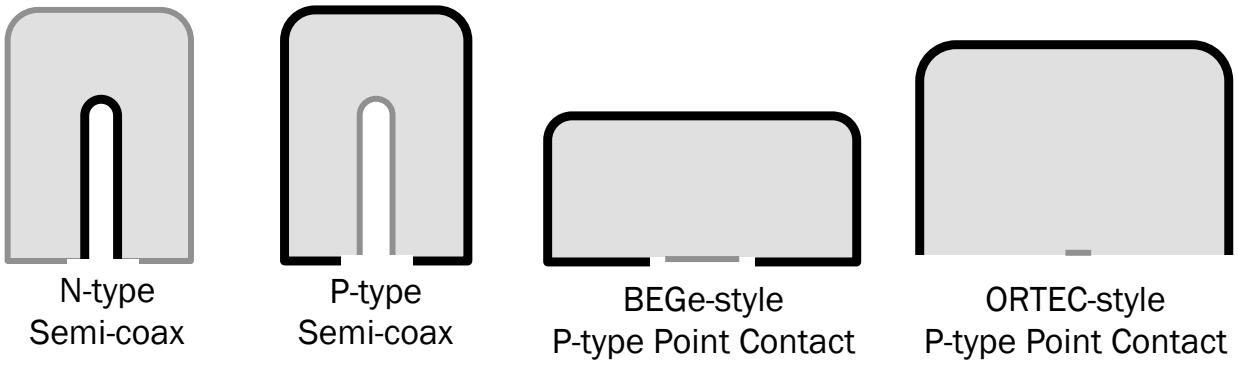

Figure 2.2: Cartoon showing the geometries and electrode arrangements of semi-coaxial and point-contact detectors. The black line indicates the n^+ contact, the grey line is the p^+ contact, and the gap in the outline indicates passivation to create an insulating surface. Dimensions not to scale.

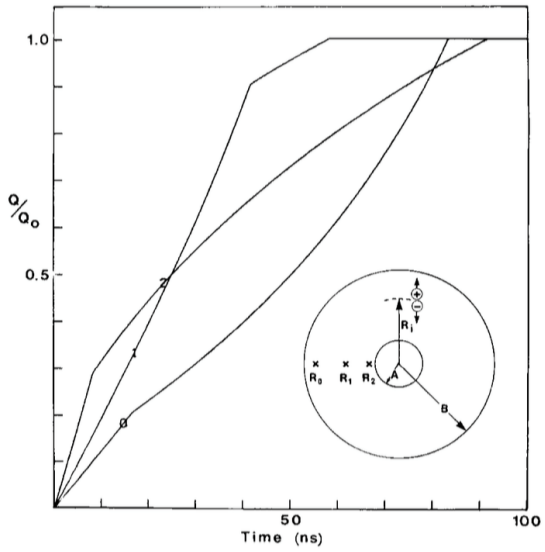

Figure 2.3: Calculated pulse shapes for several interaction positions in an n-type Ge(Li) detector. Three different interactions points are indicated as 0, 1, and 2. From [45].

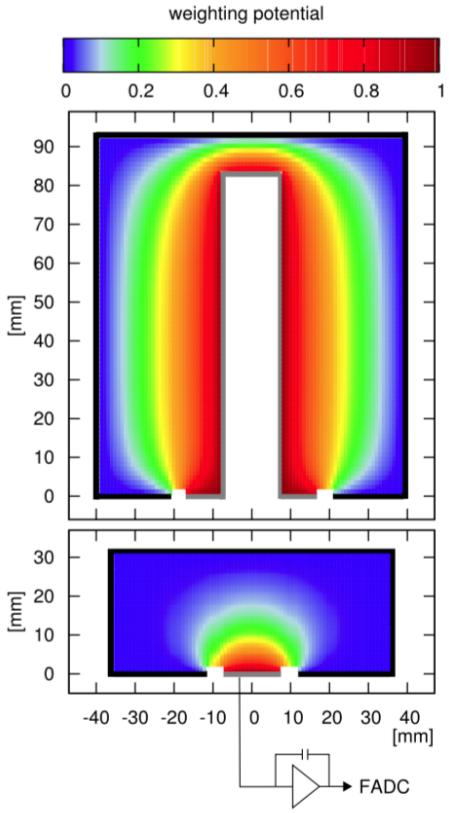

Figure 2.4: Cross section of the weighting potential of a p-type semi-coaxial detector *(top)* and a p-type BEGe-style point contact detector *(bottom)*. The p^+ contact is drawn in grey, with the n^+ contact in black. The gap between the contacts is an insulating passivated groove. The BEGe is shown with a charge sensitive amplifier like the LMFEs used to read out the MAJORANA detectors. Image from [13].

detectors.

The varying contributions of the carrier types with event position can be visualized in a weighting potential diagram, like those shown in Figs. 2.4 and 2.5. In Figs. 2.4 and 2.5a, a cross-section of the detector shows the fraction of the total signal contributed by the electrons as a function of radius r and height z. In Fig. 5.6, the weighting potential is drawn as a function of r at a chosen height (in this case, $z = 0$) in a p-type point-contact detector. As seen in these plots, signals in p-type detectors are dominated by the hole contribution over most of their volume.

Until recently, large (1 kg and above) HPGe detectors were made in semi-coaxial (seen in Fig. 2.2), coaxial, well, or segmented geometries. These designs ensured that no low-field regions, which lead to incomplete charge collection, remained in the corners of the detector. As seen in the upper image in Fig. 2.4, these detectors have nearly constant weighting potential profiles at all heights. The drift path lengths of charge carriers from all positions in the crystal bulk are also similar.

2.2 P-Type Point Contact Germanium Detectors

It has long been known that reducing the capacitance of HPGe detectors would reduce their noise and energy thresholds. This could done by using a small "point-like" central contact, instead of the deep well used by coaxial detectors. The first attempts to make germanium detectors with point-contact geometries were made in 1989 by Luke et. al [55]. Though these detectors had much smaller capacitance than coaxial detectors, they suffered from severe charge-trapping effects, degrading the detector resolution.

The breakthrough improvement that made this geometry useful in 2007 came with the switch from n-type to p-type detectors. i.e., in switching from drifting electrons to drifting electron holes through the crystal [23]. Since the holes are less susceptible to trapping, p-type point-contact (P-PC) detectors can achieve resolutions similar to those of coaxial detectors, with electric fields created primarily through careful control of the charge impurity gradient in the bulk of the crystal.

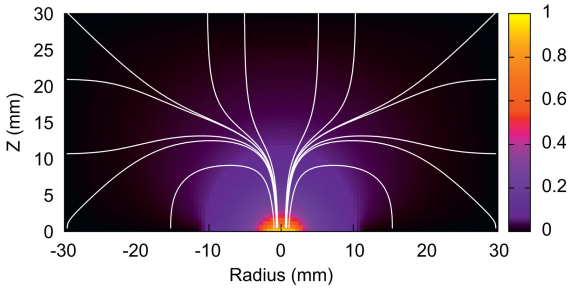

(a) The charge drift paths (in white) are long and highly position-dependent. Image from [2].

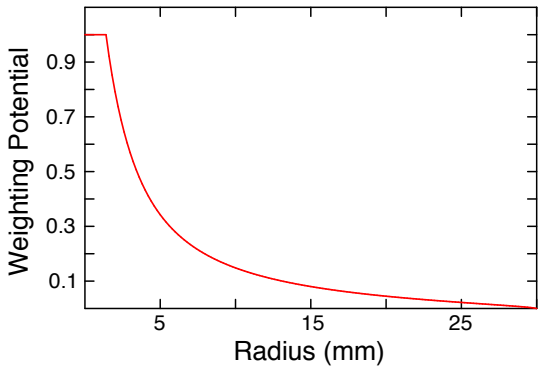

(b) The weighting potential at $z = 0$. Plot courtesy of David Radford.

Figure 2.5: Simulations of the weighting potential in an p-type ORTEC-style point contact detector.

Due to their geometry, P-PCs have capacitance of about 1 pF, far lower than that of similarly-sized coaxial detectors. This leads to far lower noise than is found in coaxial detectors, and therefore lower thresholds. While P-PCs have masses up to 1 kg, the thresholds that can be achieved are comparable to those of small ($\sim$ 1 g) x-ray detectors [23].

2.2.1 Multi-site Pulse Shape Discrimination

The most significant advantage of P-PC detectors for $0\nu\beta\beta$ decay searches is in their pulse shape characteristics. Unlike in coaxial detectors, the distance that must be traveled by a charge cloud varies strongly with the location in the detector at which it is produced, as is clear in Fig. 2.5a. Therefore, multi-site events, in which a γ ray deposits energy at multiple points in the crystal, have clearly "step-like" rise times, and can be identified and cut to reduce backgrounds. Double-beta decay, on the other hand, is intrinsically single-site since electrons have small mean free paths in germanium. Therefore the sacrifice of signal events

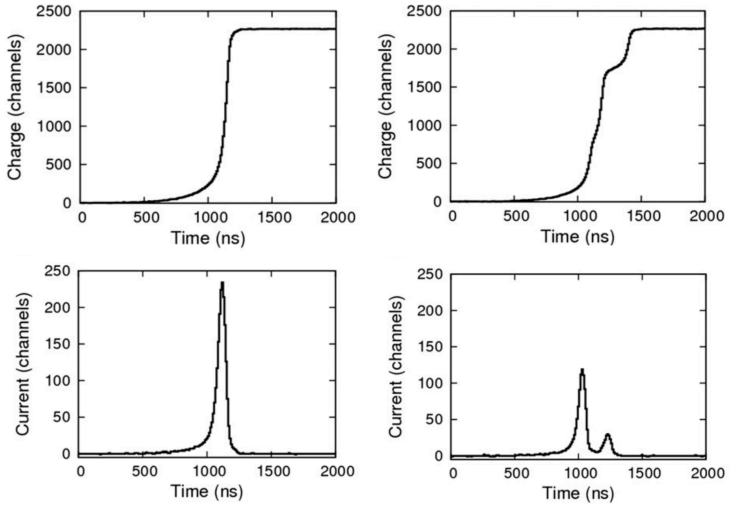

Figure 2.6: Sample 1332 keV single-site *(left)* and multi-site *(right)* waveforms in a P-PC detector. The charge read out from the detector *(top)* shows the appearance of multiple steps in multi-site interactions, which leads to a reduced maximum current *(bottom)* in these events. Image adapted from [34].

in an analysis employing multi-site discrimination is minimal.

As seen in Fig. 2.6, one reliable way to identify these events is through the difference in their maximum current A. For a given energy E of an event, which is proportional to the integral of the total current, multi-site events have lower-than-expected value of A. The pulse shape discrimination parameter used can be constructed from these parameters in a variety of ways. In this work, I use both their ratio A/E, with a correction for the energy dependence of A [27] (called `aenorm`), and the energy-corrected current "A vs. E" (called `avse`)[37].

The cut level in the parameter is set to accept 90% of the ^{208}Th double-escape peak, a sample of known single-site events, and reject events with `aenorm` or `avse` below the cut value. The effectiveness of the multi-site discrimination is evaluated by counting the remaining events in the single-escape peak (SEP), a sample of known multi-site events. Generally,

the SEP and Compton continuum are reduced to approximately 5-10% and 30-40% of their original amplitudes, respectively.

Since the gamma background in the $0\nu\beta\beta$ ROI is dominated by Compton scattering events, the use of multi-site event discrimination in P-PC detectors provides a major improvement in sensitivity. This is the main reason P-PC detectors were chosen by both the GERDA and MAJORANA Collaborations.

2.3 Surface Effects and Other Charge Collection Anomalies

2.3.1 n^+ Surface Events

Most of the surface of P-PC detectors is covered by the n^+ contact, a ruggedized layer of lithium that is diffused into the detector surface. Dedicated measurements have shown that this surface is characterized by two differently-behaving regions: a fully-dead conducting surface layer, in which there is no electric field and charge recombination occurs before the free charge carriers can enter the bulk, and a transition layer where incomplete charge collection occurs, and the energies of the observed events are degraded. Together, these have been measured to be 0.5 to 2 mm thick, depending on the detector's fabrication techniques and thermal history.

These measurements have also shown that events originating in the transition layer have a distinct "slow-pulse" shape, with increased rise-time (and degraded values of A) compared to bulk events at the same energy. See Fig. 2.7. Based on simulations of charge transport, this is thought to be due to slow charge diffusion from the transition layer into the bulk [17]. This process affects the entire rising edge of the pulse, slowing the rise time from the usual 1 to 2 μs of events in the bulk of P-PC detectors, to approximately 3 μs.

2.3.2 p^+ Surface Events

The p^+ contact of a P-PC detector is formed by implanting boron ions into the surface, resulting in a contact that is 0.3 μm thick. The size and shape of the p^+ contact region

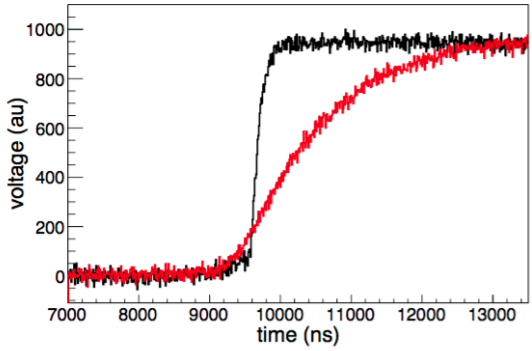

Figure 2.7: Sample bulk *(black)* and n^+ *(red)* surface events, both with energies of approximately 20 keV, in the MALBEK P-PC detector. The n^+ surface event shows a distinctive slow pulse shape, with a 3 μs rise-time, compared with bulk rise-times of 1 to 2 μs. Image from [46]

varies depending on the detector design. In BEGe-syle detectors, the contact has a radius of 5 to 6 mm. In ORTEC-style detectors, the radius is 1.5 to 2 mm.

Events originating on or near the point-contact have distinct pulse shapes, with very fast rising edges and resulting anomalously high values of A. GERDA has therefore used an additional upper limit on A/E to reject alpha events occurring on this surface [33]. Additional discussion of this approach is found in Ch. 5. No charge trapping is expected in this region, and the only expected energy loss is due to the thin dead layer.

2.3.3 Passivated Surface Events

The remainder of the detector surface is passivated, generally with amorphous germanium, to isolate the contacts from one another. In the BEGe-style design, the passivated area is limited to only the interior of the "ditch" surrounding the point-contact, a toroidal groove less than 3 mm in width. In the ORTEC-style detectors, the passivated area covers the entire bottom face of the cylindrical crystal, as shown in Fig. 2.2.

The passivation layer itself is very thin, formed of just a few monolayers. Previous

measurements, however, have shown that the charge collection in the passivated surface region is often incomplete, with high trapping observed in BEGe-type and segmented Ge detectors [14] [9]. Based on the data taken with the MAJORANA DEMONSTRATOR and simulations of charge transport on the surface [57], it was suspected that these events also featured distinctive pulse shapes caused by delayed charge collection. As further discussed in Ch 3, two potential processes were thought to drive the trapping and re-release: slow charge transport on the surface of the crystal, particularly of electrons, and bulk trapping and re-release at crystal dislocation or impurity sites near, but not on, the passivated surface.

The effects observed near the passivated surface region are thought to depend on the technique used to passivate the surface and the electric field of the detector in that region, two factors that differ widely from one detector style and manufacturer to another. Therefore, it is key that the characteristics of these events be measured in each type of detector being used, particularly for ultra-low background experiments like GERDA and MAJORANA.

2.3.4 Bulk Charge-Trapping

Charge-trapping in the bulk of the crystal, which causes low-energy tailing in gamma calibration peaks, has been observed in the MAJORANA DEMONSTRATOR. This trapping correlates linearly with drift path length. The charge loss is of a constant fraction of the total charge in the event, meaning that it is also proportional to energy. This effect is corrected for in the MAJORANA analysis using an "effective pole-zero correction" [30].

The rising edges of events with trapped charge are not noticeably affected, and the A/E and/or A vs. E of these events is normal. The charge trapping does, however, have a small but noticeable effect on our attempts to distinguish pulses from the passivated surface region, as discussed in Ch. 3.

2.4 Alpha Interactions in Ge

2.4.1 Alpha Energy Loss

Alpha particles (i.e. ^{4}He nuclei) primarily interact with matter through Coulomb interactions with the electrons of the absorber material. At high energies (above about 0.5 MeV), their energy loss is described by the Bethe formula:

$$-\frac{\mathrm{d}E}{\mathrm{d}x} = \frac{4\pi e^4 z^2}{m_0 v^2} NB \tag{2.1}$$

where

$$B \equiv Z\left[\ln\frac{2m_0v^2}{I} - \ln\left(1-\frac{v^2}{c^2}\right) - \frac{v^2}{c^2}\right] \tag{2.2}$$

v and ze are the velocity and charge of the primary particle, N and Z are the number density and atomic number of the absorber atoms, m_0 is the electron rest mass, and e is the electron charge. The parameter I is the average excitation and ionization potential of the absorber, and is experimentally determined [53].

Using this formula, 5.0 to 5.5 MeV alpha particles in germanium are expected to lose 205 to 215 keV/μm. Their expected range is between 17.6 and 20.0 μm. In copper, their expected range is between 10.1 and 11.5 μm [69].

2.4.2 Sources of Alpha Backgrounds

Given the very low range of alpha particles in matter, any observed alpha backgrounds must originate inside the detector (though such events have not yet been observed in any HPGe experiment), or within a line-of-sight of the sensitive detector surfaces. They may be from emitters on the detector surface itself, on the surfaces of parts near the detector, or from a very thin skin-depth of the materials' bulk.

The most highly concerning source of alpha backgrounds in experiments like the DEMONSTRATOR is the decay of radon isotopes and their progeny, particularly ^{222}Rn. Radon, a radioactive noble gas that is naturally created by the decay of uranium and thorium, is found in particularly high concentrations inside underground laboratories. Though many isotopes

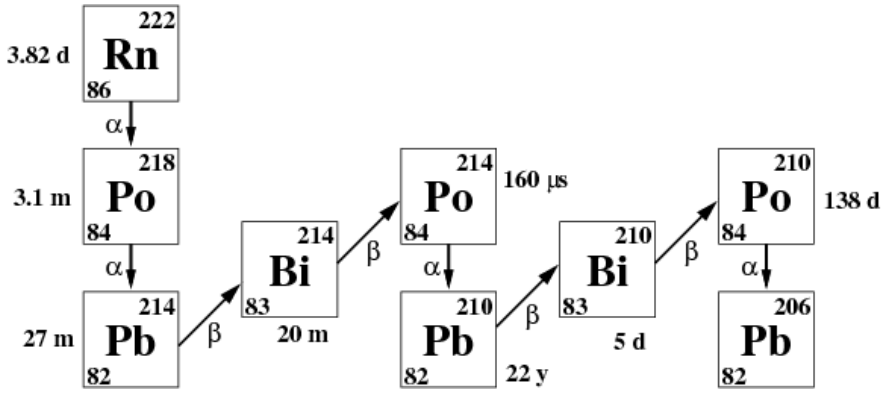

Figure 2.8: The ^{222}Rn decay chain, with the rare branchs to ^{218}At and ^{210}Tl removed for clarity. Image from [47]

are created by the decays of ^{232}Th and ^{238}U, only ^{222}Rn has a long-lived radioactive isotope in its subsequent decay chain.

Radon is particularly insidious in that as a noble gas, it easily permeates most materials. To reduce the impact of radon backgrounds, the MAJORANA Collaboration developed extensive cleaning procedures, particularly a method by which to surface-etch and passivate copper after machining [49] that reduces the problem of ^{210}Po re-deposition observed with other etching methods [71]. Plastics were leached in nitric acid to reduce their surface contamination [60].

Following cleaning, parts are stored and assembled under continuous nitrogen flow from liquid nitrogen boil-off, which is naturally low in radon. The resulting dry environment, however, can also lead to buildup of electrostatic charge, particularly on plastic parts. In its radioactive decay, radon creates charged progeny that can then be attracted to these surfaces. Deposition models are highly dependent on the environment, requiring dedicated studies in cleanroom and glovebox environments [47].

The ^{222}Rn decay chain is pictured in Fig. 2.8. The longest-lived isotopes are ^{210}Pb, with a half-life of 22 years, and ^{210}Po, with a half-life of 138 days. The short half-lives of all the isotopes occurring earlier in the chain imply that their decays are irrelevant to

the backgrounds of the DEMONSTRATOR: as the experiment runs under vacuum and in a radon-purged environment, the short-lived isotopes from the upper half of the decay chain will quickly decay, leading to a build-up of ^{210}Pb.

Of the subsequent decays, the most concerning is that of ^{210}Po, which emits an alpha particle with 5.407 MeV in 100% of its decays. The other decays are either lower in energy than $Q_{\beta\beta}$, like the β decays, or have very low branching ratios, like the alpha decay of ^{210}Bi. The alpha decay of ^{210}Po, on the other hand, can appear in the $0\nu\beta\beta$ ROI if its energy is degraded, whether by interactions in the material from which it is emitted, by charge loss in dead regions of the detector, or by charge-trapping effects in the detector.

This scenario, in which the parts or detectors are exposed to radon directly or to one of the isotopes falling between ^{222}Rn and ^{210}Pb in the decay chain, is called *lead-supported* ^{210}Po contamination. In this case, the 22 yr half-life of ^{210}Pb implies that the alpha background rate will remain roughly constant over the life of the experiment.

An alternative scenario, in which the chain is broken at ^{210}Bi or ^{210}Po, can also occur. In this case, the rate of alpha background events will fall with the 138 day half-life of ^{210}Po, leading to an improvement in the backgrounds over the life of the experiment. This is the case seen in the GERDA experiment [16].

2.4.3 Alpha Backgrounds in P-PC Detectors

The small range of alpha particles in germanium implies, first of all, that all alpha events not originating inside the crystal itself should be considered potential "surface events" in P-PC detectors. It also implies that the n^+ contact is entirely dead to alpha particles, and that alphas normal to the p^+ contact should be absorbed with energy loss of just 60 keV, given the thickness of the contact cited by the detector manufacturer. Therefore, alpha particles impinging on the n^+ surface will never pose a problematic background for $0\nu\beta\beta$ searches, and those on the p^+ surface will only contribute in the ROI if the alpha particle is emitted from the bulk of some material, and is therefore highly degraded before reaching the detector.

5.3 MeV alphas incident on the passivated surface, on the other hand, could contribute to

the backgrounds in the $0\nu\beta\beta$ ROI if there were significant energy degradation and/or charge trapping in this region. Indeed, as discussed in Ch. 6, these decays appear to dominate the background rate of the DEMONSTRATOR above 2 MeV. Therefore, an offline technique to reliably identify these events based on their pulse shape has been developed, as discussed in Ch. 3.

To validate this technique, dedicated measurements were conducted of surface alpha events on the passivated surface of an ORTEC-style detector. These measurements and results are described in Ch. 4 and Ch. 5. These results can be used create a model for the charge loss in the passivated surface region that can subsequently be used in fits to the MAJORANA background spectrum. Analytic examples of this technique are used in Ch. 6 to estimate the position of the source of the alpha background events, and will be incorporated into full Monte-Carlo simulations of the MAJORANA backgrounds in future work.

Chapter 3

DELAYED CHARGE RECOVERY TAGGING

3.1 Potential Origins of the Delated Charge Recovery Effect

As discussed in Sec 2.3, P-PC response to events near the passivated surface is difficult to predict. High charge trapping has been observed on similar surfaces in BEGe-type and segmented Ge detectors [14] [9], but the charge collection properties near this surface can differ for different detector models. In the MAJORANA DEMONSTRATOR, events have been observed in which alphas originating on this surface are significantly degraded in energy, leading to a potential background contribution in the region-of-interest for neutrinoless double-beta decay.

However, it is also observed that charge mobility is drastically reduced on or near the passivated surface, and is slowly released on the timescale of waveform digitization, leading to a measurable increase in the slope of the tail of a recorded pole-zero-corrected pulse. The same effect has been observed in the TUBE alpha source scans (see Ch 5).

There are two potential models for charge collection in the passivated surface region. One possibility is that this effect is due to surface propagation of the electron contribution to the signal, with the holes being collected normally. This matches the model developed in [57]. In an alternative model, some fraction of the holes are trapped when they originate in a few-micron-thick region at the passivated surface, and then slowly re-released.

In both cases, part of the the energy of the event appears as a normal, fast pulse, and the remainder of the charge is collected slowly. See Fig. 3.1 for sample waveforms, simulated using the `siggen` software package [1]. These waveforms are generated using the electron surface drift model, but the waveforms appear similar regardless of the cause of the delayed charge.

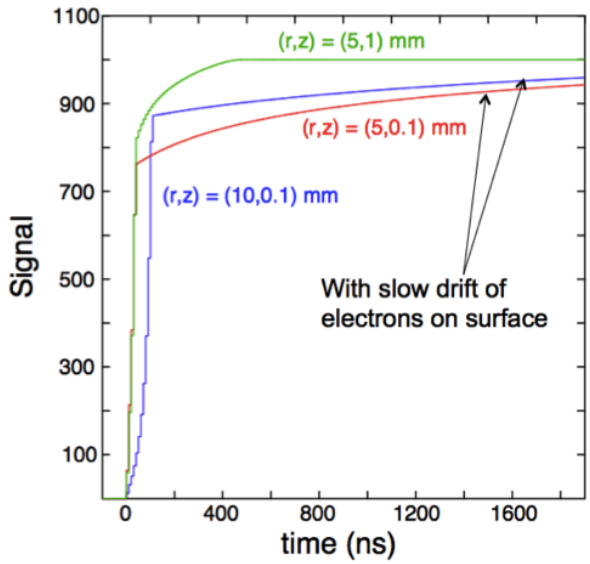

Figure 3.1: Bulk and passivated-surface waveforms, created using `siggen`, a dedicated software package used to simulate signals in semiconductor detectors. Surface charge transport of electrons is induced by incorporating an arbitrary small amount of passivated-surface charges in the model of the detector's electric field, which leads to field lines that carry charge to the passivated surface. Figure courtesy of David Radford.

The models do behave differently as the position of the alpha interaction on the passivated surface changes, so they can be distinguished using the TUBE scan results (see Sec. 5.4). The bulk trapping and slow surface drift effects could also appear simultaneously, with the radial behavior governed by the dominant effect.

For the purpose identifying alpha events, the cause of the delayed charge is irrelevant. Using a filter that can identify the occurrence of this delayed charge recovery (DCR), these events can be identified, allowing for the efficient rejection of passivated surface alpha events in offline analysis. The goal of such a filter is to detect the presence of slow charge collection occurring after the bulk charge collection has been completed. In a waveform that has been fully corrected for the electronic response function, this appears as a positive slope of the

tail. In an uncorrected pulse, it appears as a tail which has a less-negative slope than is expected for that particular channel's electronics response.

3.2 Current Implementation in the Majorana Demonstrator

For all versions of the DCR analysis cut, the relevant parameters are found using calibration data, since these runs contain a negligible fraction of surface events. Version 1.0 (v1.0) is the version of the analysis currently in use in the Majorana Demonstrator analysis chain, and does not require knowledge of the electronics response function. The cut optimization procedure and error estimates are fully described for v1.0 of the analysis.

Tested improvements are described in Sec. 3.4: Version 1.1 (v1.1) is identical to v1.0, but with an added term that corrects for charge trapping in the bulk of the detector, reducing systematic uncertainties. It is currently under development. Version 2.0 (v2.0) is a proposal to be implemented in future analysis of Majorana Demonstrator data, which uses a full correction for the electronics response function.

Samples of the current implementation steps and results are given using detectors from Data Set 3 (DS3) in the Majorana Demonstrator, defined as in Table 6.2. All of the standard Majorana analysis cuts (see Sec. 6.2) are applied to the data used, except for the granularity cut, which is not used when working with calibration data. The cut is not needed, since the high-multiplicity waveforms passing all other analysis cuts have normal single-site bulk pulse shapes, and its use in calibration runs leads to large dead-time losses. The granularity cut is applied when analyzing the low-background data.

3.2.1 Calculation of the DCR Parameter

The DCR parameter is found by first calculating the slope of the waveform tail for each event in a channel. 1 μs of the waveform is averaged (corresponding to 100 waveform samples in non-multisampled data) at each of two points on the waveform. First, the 97% rise point of the waveform is determined by finding the maximum height of the pulse, and stepping forward from the start of the digitization window until 97% of that maximum value is reached.

The first region lies between 2 and 3 μs after this 97% rise point, and the second is the final μs of the waveform (in the non-multisampled data, this is between 19 and 20 μs). See Fig. 3.2. These values were chosen to avoid introducing unwanted sensitivity to the shape of the waveform turnover and to decrease sensitivity to noise. Waveforms for which no valid tail slope can be found, i.e. those in which the 97% time point occurs too late to leave a usable tail, are flagged and automatically accepted by the DCR analysis.

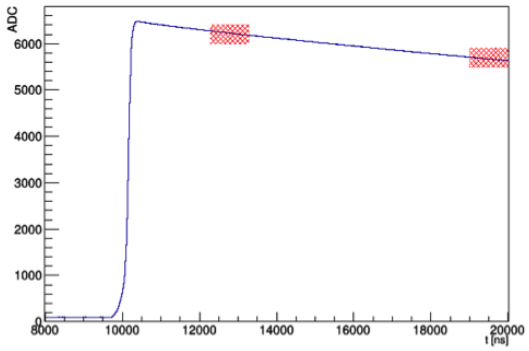

Figure 3.2: A sample MJD waveform. The ADC values are averaged in each of the two shaded regions. The slope between those average points is taken to be δ.

Assuming that the tail of bulk-event waveforms has an exponential form, the slope δ is:

$$\delta = \frac{y_1 - y_2}{t_1 - t_2} = h\frac{e^{\frac{-t_1}{\tau}} - e^{\frac{-t_2}{\tau}}}{t_1 - t_2}$$

where y_1, y_2, t_1 and t_2 correspond to the average values and times for each of the two regions, h is the waveform amplitude, and τ is the decay constant of the tail. To first order in t_n/τ,

$$\delta = \frac{h}{\tau}$$

for bulk events.

The tail slope is plotted with respect to energy for each channel. The energy estimator used is `trapENMCal`, the maximum of the optimized trapezoidal filter for the channel. Using single-site events with energies between 1 MeV and 2.38 MeV (the Compton shoulder of the

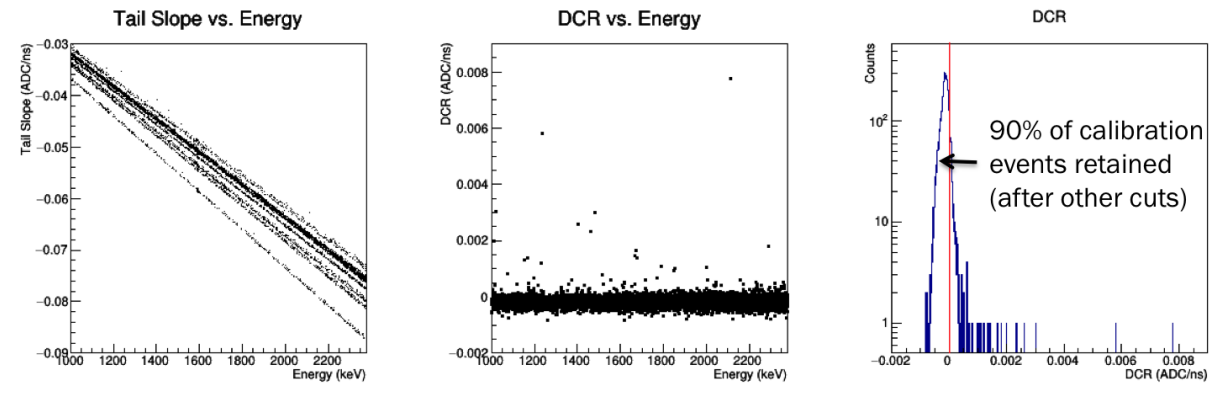

Figure 3.3: The steps of the DCR parameter calculation, plotted for all high gain channels in DS3 detectors. *Left:* δ vs. Energy is plotted and fit with a line for each channel. *Center:* The fit parameters are used to calculate the raw DCR value, which is then shifted such that 90% of single-site calibration events in this energy range fall below 0. *Right:* The DCR distribution displays a Gaussian distribution with a high-DCR tail.

^{208}Th 2614 keV peak), a line is fit to the resulting distribution, and the parameters of that fit are used to project δ on to the energy axis. This is equivalent to finding the average decay constant for the pulses in a channel and doing a first-order pole-zero correction of the waveforms prior to measuring their tail slope.

The resulting value is defined as the raw DCR parameter for the waveform:

$$DCR_{raw} = \delta - \left(\frac{a}{\tau}E + b\right)$$

where a is a scaling constant that converts between pulse amplitude and energy for the channel. b, which is generally positive, is a constant determined by the fit that corrects for the fact that a waveform with signal height 0 will have a positive estimated energy when the maximum value of a trapezoidal filter is used as the energy estimator.

The calibration run events have a median raw DCR of 0, with low tail slope events (like events occurring near the passivated surface) having larger DCR values. The width of the Gaussian part of the DCR distribution in the calibration data is primarily determined by the

noise and energy nonlinearity of the channel. The high-DCR tail is due to passivated-surface events, transition-layer multisite events (see Fig. 3.8) and other multi-site events that go untagged by A vs. E and pile-up cuts, and an additional contribution that depends on the bulk charge trapping of the detector (see Sec. 3.4.1 for details).

The cut value c is set to reject 1% of the single-site events with energies between 1 MeV and 2.38 MeV in the calibration data set used to determine the cut parameters. Single-site events are selected using A vs. E analysis [37] and additional pile-up cleaning cuts. To set the "corrected DCR" ($\mathrm{DCR_{corr}}$) value (hereafter referred to simply as "DCR"), the raw DCR value is shifted such that the rejected events have $\mathrm{DCR_{corr}} \geq 0$:

$$\mathrm{DCR_{corr}} = \delta - \left(\frac{a}{\tau}E + b\right) - c$$

This value is then calculated for all background events, and the cut is applied by selecting events with $\mathrm{DCR} < 0$.

3.2.2 Energy Non-linearity Effect

The non-linearity of the waveform digitization has a significant effect on the efficiency of the cut at a given energy. Though much of the variation in efficiency is removed by applying channel-specific nonlinearity corrections to each waveform [30], a systematic variation with energy remains, as seen in the oscillatory variation of the Compton continuum acceptance in Fig. 3.4 or in the left-hand plot of Fig. 3.10. This effect differs from channel to channel, with low-gain channels displaying higher variation. The variation due to this effect is highly dependent on the chosen bulk acceptance efficiency; at high acceptance levels, the impact of the non-linearity is drastically reduced.

This cannot be correctly termed an uncertainty of the cut, since the energy of a given event is well-known, as is the DCR efficiency at a given energy. A gain uncertainty of 0.4 keV, larger than that observed in any data set [30] leads to a DCR efficiency change of less than 0.2%, which is negligible compared to the other DCR uncertainties. Therefore, the resulting uncertainty is neglected.

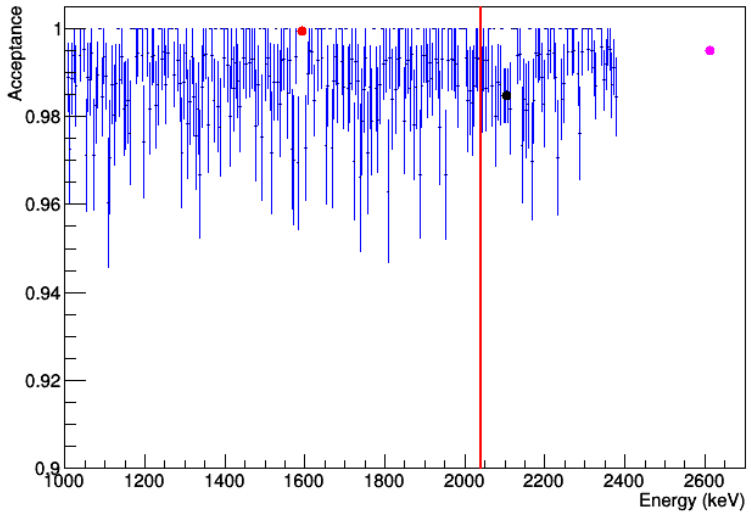

Figure 3.4: Efficiency plot for the 99% acceptance DCR cut in P42665A, a typical detector in DS3. The acceptance in the ^{208}Th DEP, SEP, and FEP are indicated by the red, black, and magenta points, respectively. The blue points indicate the acceptance in each 5 keV bin of the Compton continuum. The red line indicates the 3 keV $0\nu\beta\beta$ ROI. The errors shown assume binomial statistics.

The non-linearity effect will change the spectral shape of the remaining events, however, which could pose a challenge for spectral shape fitting. Choosing a high bulk acceptance (like the 99% acceptance used here) reduces this effect, and combining the data from all channels further limits the spectral shape distortion by averaging it away. The remaining non-linearity effect, seen in Fig. 3.5, is of order 0.5%, similar to the other uncertainties of the cut (see Sec. 3.3).

When estimating an integral rate over some region, the DCR acceptance should be calculated for that particular region, so that bias is not introduced. For the $0\nu\beta\beta$ limit calculation, the DCR efficiency is calculated in a 3 σ-window around the $0\nu\beta\beta$ Q-value.

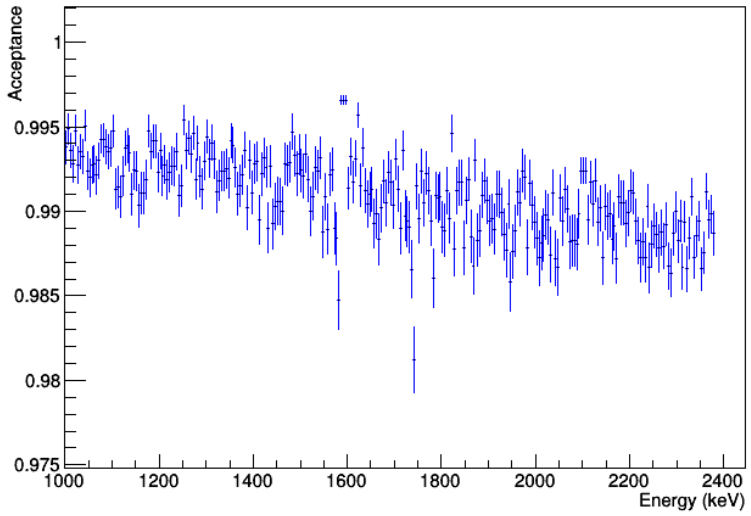

Figure 3.5: Efficiency plot for the 99% acceptance DCR cut in all DS3 detectors, for the Compton continuum events. The non-linearity effect remaining is about 0.5%. The decrease in efficiency at high energy is more troubling, and indicates that the correction for charge trapping, as discussed in Sec. 3.4, should be implemented to correct for this effect. The errors shown assume binomial statistics.

3.2.3 Optimization

As described in [40], the sensitivity to the $0\nu\beta\beta$ decay half-life, in the presence of high backgrounds, is proportional to $\frac{\epsilon}{\sqrt{N_b}}$, where ϵ is the cut acceptance and N_b is the number of background events. In this case, the energy range used to find the number of background events is a disjoint 350 keV window around the $0\nu\beta\beta$ Q-value that is used to estimate the background level in the ROI. The event energies included those from 1950 to 2350 keV, with the exception of the regions from 2094 to 2127 keV and 2195 to 2212 keV, where the MAJORANA background model predicts the presence of gamma background peaks from the uranium and thorium decay chains.

An optimization study was conducted using the open data from MAJORANA DEMON-

DS	ϵ (%)	N_b (counts)	$\frac{\epsilon}{\sqrt{N_b}}$ (arb.)	$N_{b,enr}$ (counts)	$\frac{\epsilon}{\sqrt{N_{b,enr}}}$ (arb.)
0	100	79	0.113±0.056	69	0.120±0.060
	99	14	0.265±0.13	10	0.313±0.157
	95	14	0.254±0.13	10	0.300±0.150
	90	14	0.241±0.12	10	0.285±0.142
1	100	49	0.143± 0.071	46	0.147±0.074
	99	6	0.0404±0.020	3	0.0572±0.029
	95	6	0.0388±0.019	3	0.0548±0.027
	90	6	0.0367±0.018	3	0.0520±0.026
2	100	7	0.378±0.19	6	0.408±0.20
	99.9	0	-	0	-
	99.5	0	-	0	-
	99	0	-	0	-
	95	0	-	0	-
	90	0	-	0	-
3	100	25	0.200±0.10	21	0.218±0.11
	99	2	0.700±0.35	0	-
	95	2	0.672±0.34	0	-
	90	2	0.636±0.32	0	-
4	100	17	0.243±0.12	16	0.250±0.13
	99	1	0.990±0.50	0	-
	95	1	0.950±0.48	0	-
	90	1	0.900±0.45	0	-

Table 3.1: DCR optimization studies in DS0 to 4 show that the sensitivity of the cut is optimized at 99%. Results in DS2 suggest that higher acceptances, up to 99.9%, may be optimal when multi-sampling is used.

STRATOR Data Sets (DS) 0 to 4. See Table. 6.2 for descriptions and exposures of each data set, and Sec. 6.2 for a discussion of the standard analysis steps applied. DS5 was excluded from this study due to the known elevated noise rate in its first half, which distorts the DCR distribution and reduces the effectiveness of the analysis. Improvements that would mitigate the effect of this noise are discussed in Sec. 7.2. Only enriched detectors were included in the optimization study, since these detectors dominate the DEMONSTRATOR's sensitivity to $0\nu\beta\beta$.

For this study, the sensitivity was optimized by maximizing the figure-of-merit $\epsilon/\sqrt{N_b}$ over a range of DCR calibration-event acceptance levels, varying from 90% to 100%. See Table 3.1. Based on the results, the DCR acceptance level was chosen to be 99%.

Higher acceptance levels are being considered for multi-sampled data (described in Sec. 6.2), since the longer duration of the waveform tail leads to a more-sharply peaked DCR distribution for bulk events. See Figure 3.6. Though the open exposure in this data set is low, and higher statistics are needed to make a definitive recommendation, studies of DS2, which used multi-sampling, suggest that a 99.9% acceptance DCR cut may be the optimal choice for multi-sampled data.

3.3 Uncertainties Associated with DCR

3.3.1 Stability

To study DCR stability over time, calibration skim files are chained together and analyzed. DCR values for every event are plotted as a function of time, with time presented as the number of minutes elapsed since the beginning of the first calibration, with non-calibration periods removed from the timeline. See Fig. 3.7, *top*. Only calibrations from the Module 1 source are used in the DS0-DS3 analysis, and only calibrations from the Module 2 source are used in the DS4 analysis. Calibrations from both sources are used in the DS5 analysis. Calibration runs with timing or quality issues are removed from all analyses.

Only single-site (as determined by A vs. E [37] and pile-up [58] cuts) events that pass

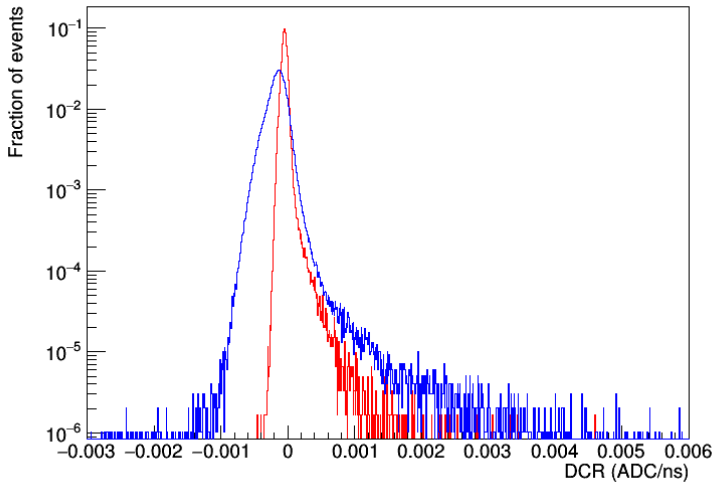

Figure 3.6: DCR of single-site Compton continuum events in calibration data, in multisampled data (DS2, in red) and singly-sampled data (DS3, in blue). In DS 2, DCR is more sharply peaked for bulk events, allowing for a higher-acceptance DCR cut that retains the same sensitivity to alpha events.

data-cleaning cuts, from detectors that are included in the energy spectrum analysis, are included in the analysis. The energy window used for the $0\nu\beta\beta$ analysis is 2028 keV - 2050 keV. A second analysis of the ^{208}Tl DEP (1590 keV - 1595 keV) is also conducted. A 40-minute moving average of the DCR values within the closed range [-0.003,0.035] is calculated. The larger upper bound was chosen to identify events with a high DCR due to failure of the energy calibration of the max-pickoff energy `trapENMCal`. The mean DCR value is then plotted at the central time value within each forty-minute window (see Fig. 3.7, *middle*). Data points from the first and last forty minutes are excluded to eliminate bias due to window effects.

The DCR cut efficiency (i.e. the percentage of events within the window with DCR< 0) over time is plotted using the same moving-average algorithm, as in Fig. 3.7, *bottom*. Note

that this method of calculating efficiency differs from the standard efficiency calculation, which weights each detector's efficiency by its active mass. A one-dimensional histogram is created out of the efficiency values over time, and the standard deviation of this distribution is taken to be the uncertainty in the efficiency of DCR over time, σ_{stab}.

Results are given in Table 3.2. If the efficiency deviates by more than $2\sigma_{stab}$ in a set of calibration runs, the DCR parameters are re-evaluated using the relevant runs and a stability correction is applied. Stability corrections to DCR are also applied when a stability correction is needed in the A vs. E analysis [37]. Generally, instability in the DCR acceptance is caused by a small change in the pole-zero constant of the channel, but changing noise conditions can also change the efficiency. Proposed improvements that would minimize the instability due to these effects are described in Sec. 3.4.2.

The current version of the analysis employs one to two long (8 to 12 hour) energy calibrations to set the cut in each Data Set, save for when additional stability corrections are applied.

3.3.2 Statistical Uncertainty

In each channel, the statistical uncertainty of the cut efficiency is $\sigma_{stat} = \sqrt{\frac{(\epsilon)(1-\epsilon)}{N}}$, where N is the number of events rejected by the DCR cut in the set of calibration runs used to set the cut, in the energy window being used. See Table 3.2 for the uncertainties in the $0\nu\beta\beta$ efficiency window.

3.3.3 Pulse-Shape Bias

Irregularities in the pulse shapes of events, particularly charge-trapping re-release and multi-site effects, can have an effect on the calculated DCR acceptance. Events with a transition layer multi-site component, multi-site events occurring very near the point contact, and events with high charge trapping, like those seen in 3.8, may be untagged by A vs. E and data cleaning analyses, but will be accepted by the DCR cut with lower-than-average

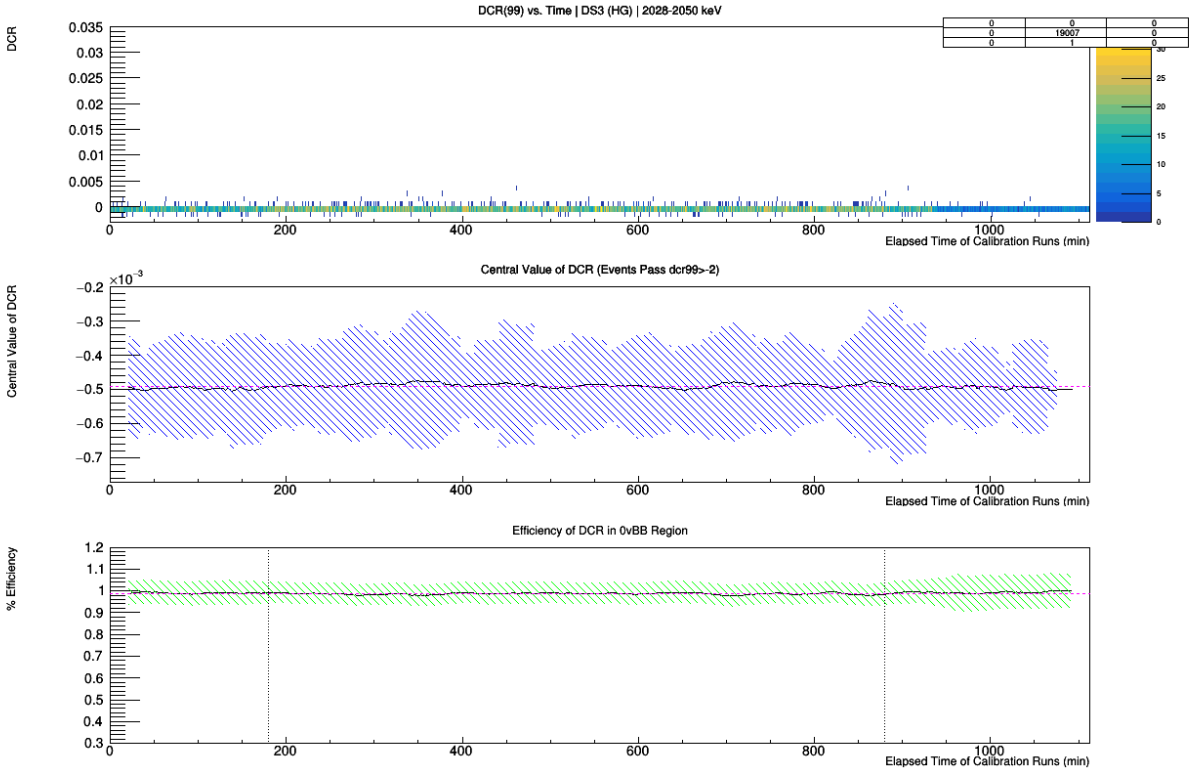

Figure 3.7: Stability study results for DS3 high-gain channels. The middle and bottom figures are calculated using a 40-minute moving average; in these plots the filled dashed region indicates the uncertainty in each value, taken as the standard deviation of the value's distribution in a given time window. The magenta lines indicate the mean of the plotted values. *Top:* DCR values for all events passing cuts. *Middle:* The central value of DCR over time. *Bottom:* The bulk acceptance of the DCR cut over time. The vertical lines indicate the runtime boundaries of the long calibration run used to set the DCR cut, and the blue line indicates the average efficiency in this time window. Plots courtesy of Chris Haufe.

efficiency. A visual examination of the calibration events rejected based on their DCR values shows many of them to be of this type.

To quantify the uncertainty introduced by these effects, we compare the DCR acceptance in a 3σ window centered on the ^{228}Th double-escape peak (DEP), a known sample of single-site events, to the average acceptance in the left- and right-hand sidebands of the peak. The difference is cited as the pulse shape-dependent bias (σ_{PS}) for each channel. This value is generally positive, indicating that the acceptance in the DEP is higher than the acceptance in the ROI, and therefore that we have taken a conservative estimate of the DCR efficiency. The overall bias is given by an exposure-weighted average of the bias in each channel, since σ_{PS} is assumed (conservatively) to be fully correlated among the detectors.

The pulse shape bias indicates that the DCR analysis is effectively tagging some fraction of the multisite gamma events that go untagged by the A vs. E analysis. This implies that the DCR analysis has power for rejecting background gamma events in addition to alpha events.

3.4 Tested Improvements to the DCR Analysis

3.4.1 DCR Version 1.1

V1.1 of the DCR analysis, which corrects for the effect of bulk charge trapping in the detectors on the tail slope, has been developed and tested. It was developed with the goal of reducing the pulse-shape systematic uncertainty of the cut acceptance. Correcting for this effect will also reduce the overall width of the DCR distribution, allowing for a more effective cut at the same level of bulk-event sacrifice, and correct the slight broadening of the DCR distribution with increasing energy.

Bulk Charge Trapping and the DCR Distribution

The bulk charge trapping in a given detector can be measured by its energy resolution improvement when the effective pole-zero charge trapping correction is applied. Using this

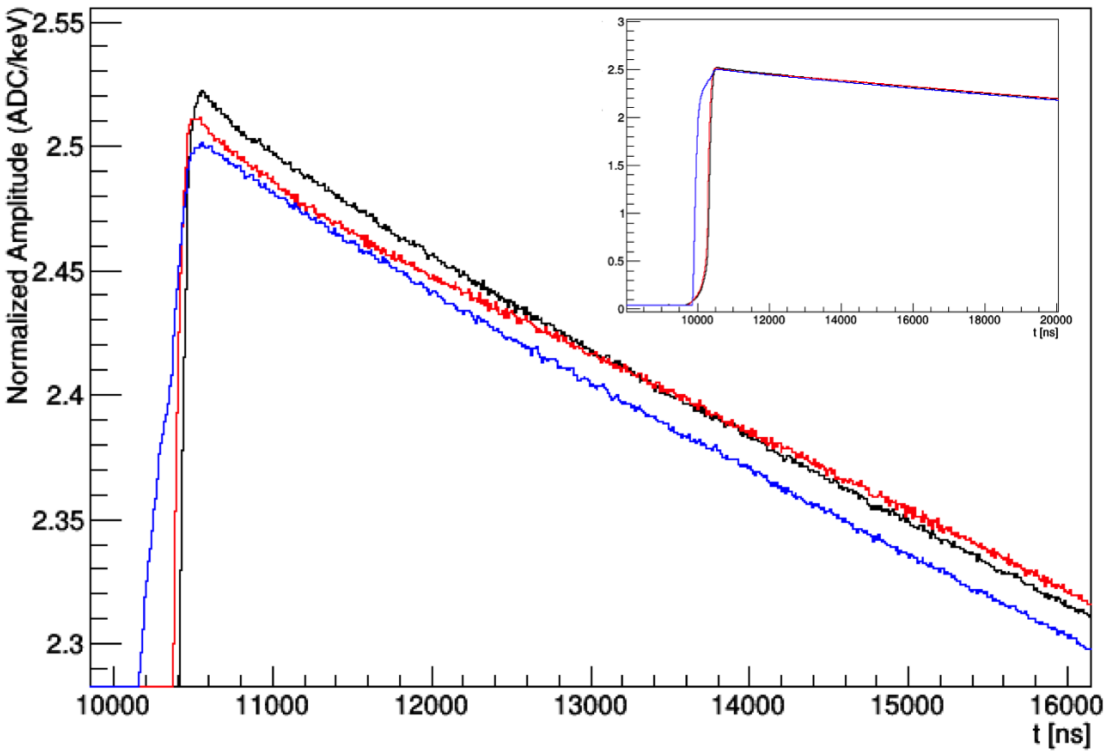

Figure 3.8: The effect of pulse-shape on DCR, in one channel. The event drawn in black passes the DCR cut, those in blue and red fail the cut. The event in blue is thought to be a near-point-contact multi-site event, where the late charge arrival from the second site gives it an "incorrect" energy for its tail slope. The one in red is thought to be a transition-layer multisite event or an event with high bulk charge trapping, either of which would contribute the additional slow component that changes its tail slope. All events are normalized by(`trapENMCal`).

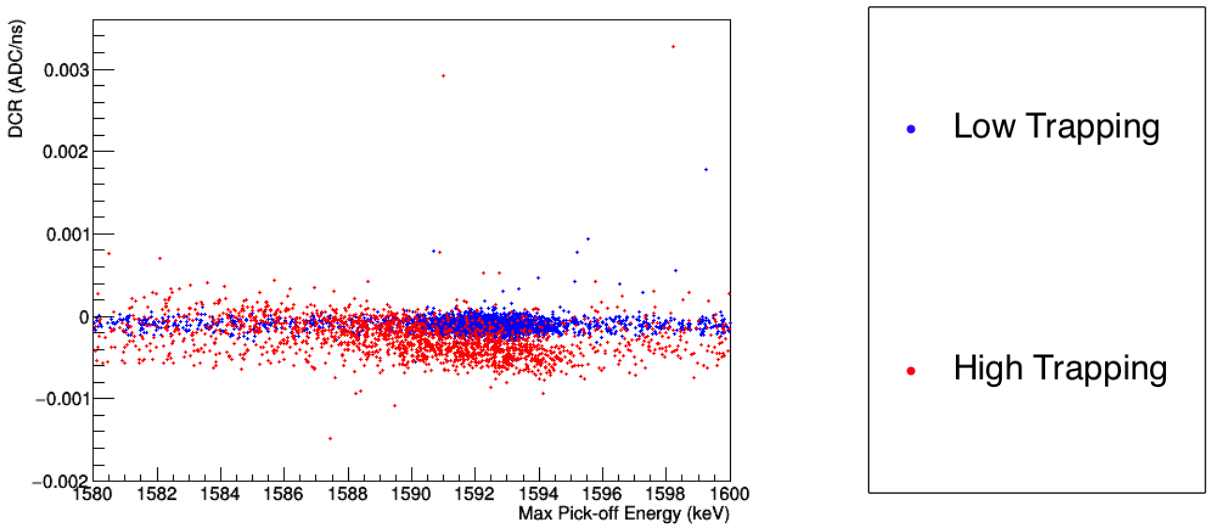

Figure 3.9: The effect of bulk charge trapping on DCR in the ^{208}Tl DEP and surrounding continuum. The points in red are from detector P42537A, which exhibits a 3 keV FWHM improvement in the 2614 keV peak when charge-trapping is corrected. The points in blue are from detector P42661A, which exhibits a 0.4 keV improvement. The energy shown here, which is used to calculate the DCR value, is `trapENMCal`.

method we can comparing the DCR vs. energy distributions for high charge-trapping detectors and low charge-trapping detectors, as in Fig. 3.9. It is clear that for detectors with minimal charge trapping, the DCR distribution is narrower and that all portions of a peak, like the ^{208}Tl double escape peak (DEP) shown, have consistent DCR acceptance. For a detector with high charge-trapping, on the other hand, the low-energy tail, which contains the events in which charge-trapping has occurred, has higher DCR values than the bulk of the peak. This matches the effect that would be expected if bulk trapped charge were being released on a 2-3 μs timescale, adding a slow additional component to the tail slope and making it less negative.

Each energy peak shape in the spectrum is made up in part by a Gaussian peak, where

events with normal charge collection appear, and an exponentially-modified Gaussian low energy tail, which contains events in which bulk trapping has occurred [30]. Since the Gaussian portion of the DEP is made up of events that are particularly likely to be single-site and unlikely to have been affected by bulk charge trapping (since if they were affected by trapping, they would be shifted into the low-energy tail of the peak), the acceptance of these events will be higher than that of the surrounding continuum events. This increases σ_{PS}. In detectors that have high bulk charge-trapping, this peak will therefore have higher DCR acceptance than the Compton continuum in the $0\nu\beta\beta$ ROI, which is made up of events with a normal incidence of charge trapping, making σ_{PS} large for that detector.

The presence of bulk charge trapping also broadens the overall DCR distribution, increasing the tail of the distribution with high values of DCR. The amount of trapped charge in an event at a given position in the crystal is expected to be a constant fraction of the total energy, so the broadening due to this effect will increase with energy. This causes the fall in DCR cut efficiency with increasing energy observed at higher-sacrifice cuts, as seen in the left-hand plot of Fig. 3.10.

Correcting DCR for Charge Trapping

The charge trapping effect on DCR can be corrected because the distinctive trapping and re-release timescales can be calculated from calibration data. Therefore, for a known level of charge trapping in an event, its re-release effect on the waveform tail can be subtracted from the tail slope δ, and then the DCR parameter can be calculated in the usual fashion from the remaining slope.

In addition to `trapENMCal`, the standard MAJORANA analysis also includes another calibrated energy, `trapENFCal`, which corrects for charge-trapping through the use of an effective pole-zero constant and a fixed-time pickoff of the trap filter relative to the start of the drift of the pulse [30]. The amount of charge trapping in a given event can be quantified; it is

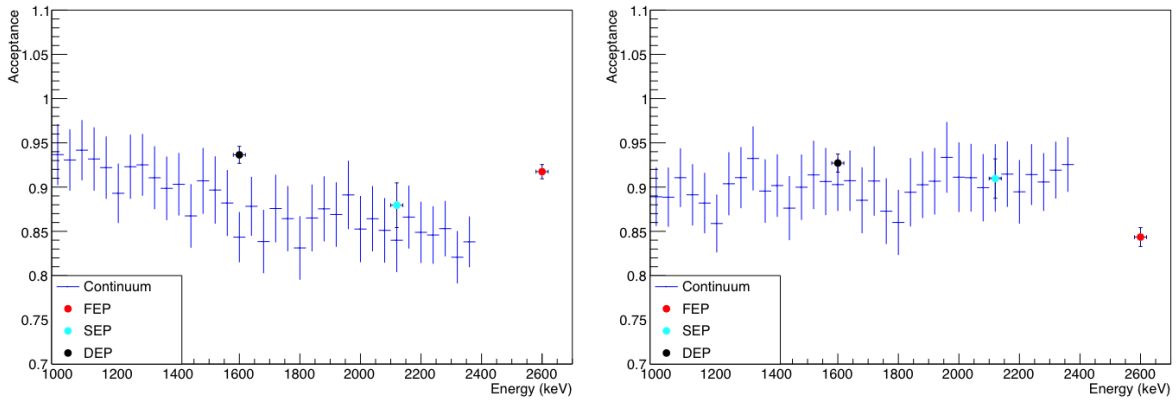

Figure 3.10: Efficiency plots for the 90% acceptance DCR cut in P42537A, DS3, using v1.0 and v1.1 of the analysis. *Left:* DCR v1.0 cut efficiency with respect to energy, in 40 keV bins. σ_{PS} is large and the efficiency falls with increasing energy. *Right:* The charge-trapping-corrected (v1.1) DCR efficiency. The correction has reduced σ_{PS} and the overall energy dependence has been corrected, but the efficiency is lower than expected in the full-energy 2614 keV peak. This requires further study.

given by the difference between the charge trapping-uncorrected and corrected energies, ΔE:

$$\Delta E = \texttt{trapENFCal} - \texttt{trapENMCal}$$

The dependence of δ on the trapping is found by plotting δ vs. Δ_E and fitting with a line of slope ℓ_E, as Fig. 3.11a. The energy dependence of this slope is then fit with an exponential function, shown in Fig. 3.11b. Then, for a given event, the charge trapping-corrected tail slope δ_{CTC} is:

$$\delta_{CTC} = \delta - (Ae^{\lambda E})\Delta E$$

where A and λ are the parameters found in the exponential fit.The DCR parameters are then calculated as in v1.0, leading to a narrower DCR distribution, with less of a high-DCR tail, as in Fig. 3.11c.

Preliminary tests show that the use of the charge trapping correction improves σ_{PS} and

the energy-dependence of the DCR cut in detectors with significant charge trapping, but further study is needed to understand its effect in the full-energy peak. See Fig. 3.10.

These tests have also shown that the calibration of `trapENM` is not reliable enough to use as an indicator of the amount of trapped charge in every detector, since the large low-energy tails make the mean of the Gaussian part of the peak difficult to identify reliably. Depending on how the calibration of the energy is conducted, the peak positions may be offset by up to several keV in some channels, leading to unphysical negative estimates of trapped charge. Though v1.1 of the analysis is a good proof-of-concept, demonstrating that charge trapping is leading to significant broadening of the DCR distribution and to the large observed pulse-shape uncertainty, it is not the best path forward to reliably correcting for this effect, since it requires very accurate energy calibrations and high statistics to determine the correction.

3.4.2 DCR Version 2.0

True Pole-Zero Correction

Future versions of the DCR analysis could be improved by applying de-convolution of the full channel-specific electronic response function before searching for a remaining slow component. This component could be identified either using a two-point slope estimator, like the one used in v1.0 and v1.1, or some other method.

Preliminary work on the TUBE scanning system, using a two-point slope estimator after pole-zero correction, shows that since this approach uses the full pole-zero decay function, instead of first-order approximation, it gives a narrower distribution for bulk events. This is particularly true at energies over 3 MeV, where muons and multisite events dominate. This approach leads to improved discrimination of passivated surface events in this system, which has a high background rates. See Fig. 4.6.

If a true pole-zero correction were employed in the DCR algorithm, the stability uncertainty of the DCR parameters could be reduced by re-tuning the decay constant for each detector with each weekly energy calibration of the DEMONSTRATOR. In the effective correc-

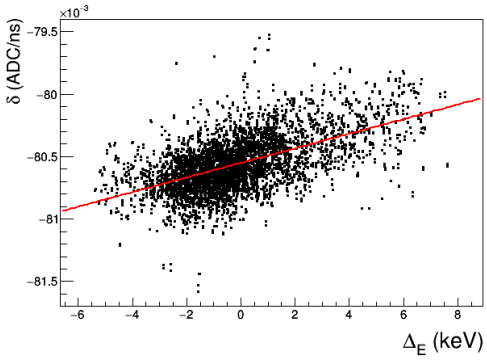

(a) δ vs. ΔE is plotted and fit with a line of slope ℓ_E, in red, for each energy peak.

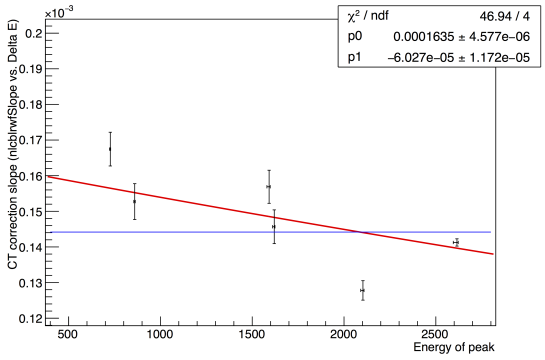

(b) ℓ_E is plotted with respect to E and fit with an exponential, in red. The assumption of constant ℓ_E, in blue, is a poor model of the observed behavior.

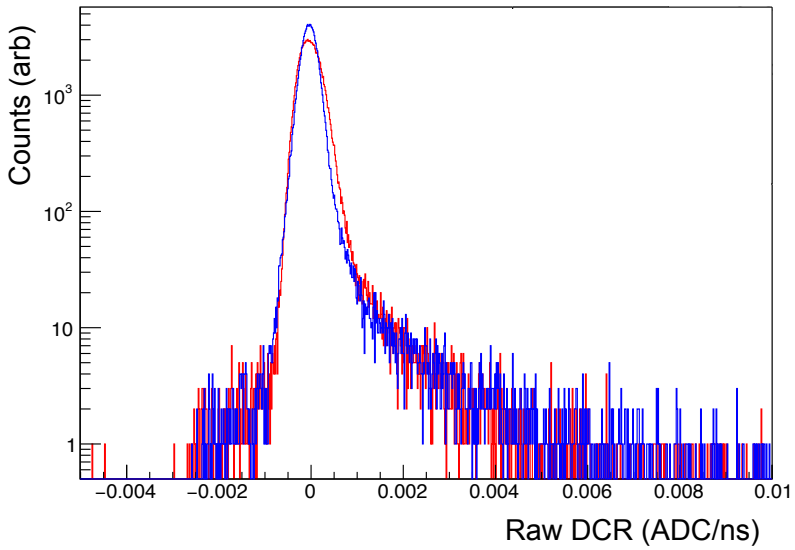

(c) When corrected using the resulting parameters, the charge-trapping-corrected DCR distribution in the 1 to 2.38 MeV range, in blue, is narrower than the uncorrected distribution, in red.

Figure 3.11: The steps of the charge trapping tail slope correction, in P42537A, a high charge trapping detector in DS3.

tion used in v1.0 and v1.1 of the analysis, multi-hour calibration runs are needed to re-tune the parameters; therefore, physics live time considerations prevent regular re-tuning. A true pole-zero correction, on the other hand, can be determined using very few (less than 500) events, allowing it to be re-tuned using the already-established weekly energy calibrations.

Waveform Filtering

During a portion of Data Set 5, which is not used in this analysis, ground loops are known to have been responsible for problematic noise in the system. Studies of these runs have shown that in spite of the $1\,\mu$s averaging window used to measure the tail slope δ, the addition of this noise drastically broadens the DCR v1.0 distribution. This noticeably reduces the efficacy of alpha rejection for any given bulk acceptance efficiency.

Initial work has begun on applying waveform filtering prior to DCR parameter estimation; notch, wavelet, and bandpass filtering approaches are all being considered. Since it is high-frequency noise that cases bulk DCR distribution broadening, and the low-frequency components of the waveform that indicate that delayed charge recovery is occurring, filtering is expected to be quite effective.

Charge Trapping Correction

Further work is also being done on a waveform-by-waveform charge-trapping correction, which uses the drift time of the pulse to calculate the expected amount of charge lost in the bulk. Early results indicate that this approach is more reliable than the estimate of ΔE used in v1.1, and dramatically reduces the width of the DCR distribution, allowing for more effective surface event discrimination.

3.5 *Results in the* MAJORANA *Analysis*

3.5.1 Efficiencies

In each channel, the average acceptance for single-site events (after standard MAJORANA analysis cuts are applied, as described in Sec. 6.2) in the Compton continuum region, taken to be from 1 MeV to 2.38 MeV, is set to match the quoted acceptance of the cut. For instance, `dcr99` has average bulk acceptance of 99%, as nearly as is allowed by the finite statistics of the sample used to set the cut.

The true acceptance for the $0\nu\beta\beta$ region is calculated from that energy region directly, also using calibration data, due to the energy non-linearity effect, as discussed above. It is given in Table 3.2 for each of the data sets.

3.5.2 Uncertainties

As discussed, the pulse shape systematic uncertainty and uncertainty due to cut instability dominate, with the statistical uncertainties contributing about 0.2% and the energy scale uncertainty contributing negligibly. The uncertainties for each data set are given in Table 3.2.

3.5.3 DCR Validation in Low-Background Data

The DCR in each low-background skimmed data set is checked using a dedicated validation script, which is used to check for channels in which the DCR parameters are not being applied correctly, unexpected energy dependence, and other errors in the DCR parameters. The validation script is applied first to the open data, and then, after unblinding, to the remaining data. Standard MAJORANA analysis cuts are applied (see Sec 6.2). The energy range used is from 100 keV to 9 MeV. This script produces the following plots:

- The DCR distribution in each channel: It should have a roughly Gaussian shape, with a high-DCR tail extending to the right. The peak should be centered at a DCR value less than 0. See Fig. 3.12a. If a channel does not have a DCR cut available, a sharp

Data Set	ϵ_{ROI} (%)	σ_{PS} (%)	σ_{stab} (%)	σ_{stat} (%)	σ_{tot} (%)
DS0	98.1	0.8	0.3	0.1	0.9
DS1	95.6	1.1	0.8	0.1	1.4
DS2	98.6	0.9	0.5	0.2	1.1
DS3	99.1	0.9	0.4	0.1	0.9
DS4	98.9	1.2	0.5	0.1	1.3
DS5a	92.1	0.7	2.5	0.3	2.6
DS5b	95.8	1.4	1.7	0.2	2.2

Table 3.2: $0\nu\beta\beta$ efficiency and uncertainties, given for high gain channels in each data set. DS5 was split into DS5a and DS5b because the presence of elevated electronic noise in DS5a (due to known ground loop problems) drastically reduced the effectiveness of the DCR cut in these runs. The addition of waveform filtering should allow the DCR analysis in DS5a to be improved.

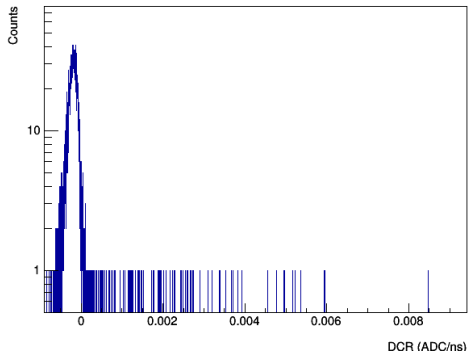

(a) The DCR distribution.

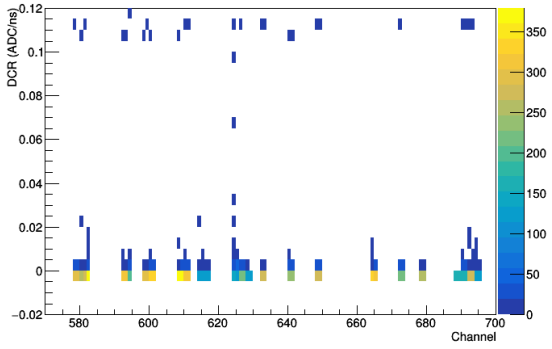

(b) The DCR distribution for each channel.

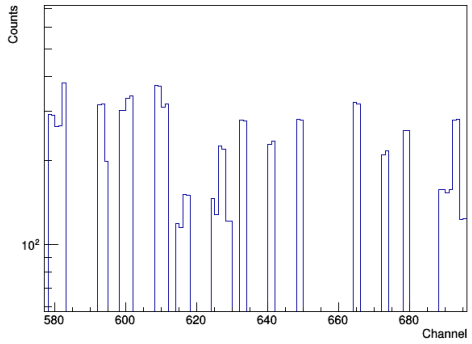

(c) The number of events remaining after the DCR cut, in each channel.

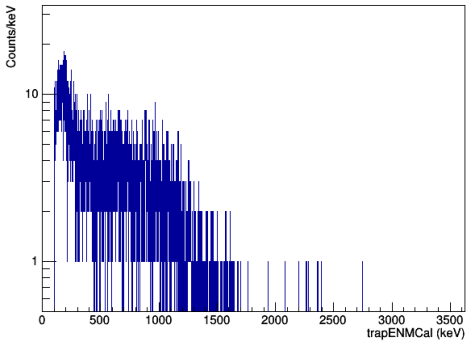

(d) The spectrum after the DCR cut is applied.

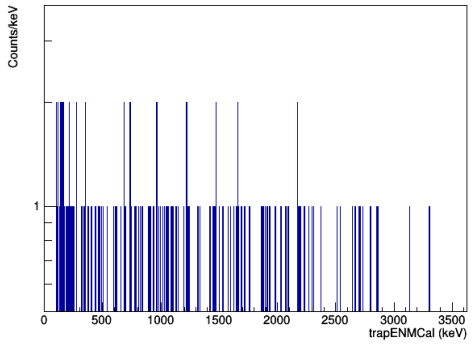

(e) The spectrum of events cut by DCR.

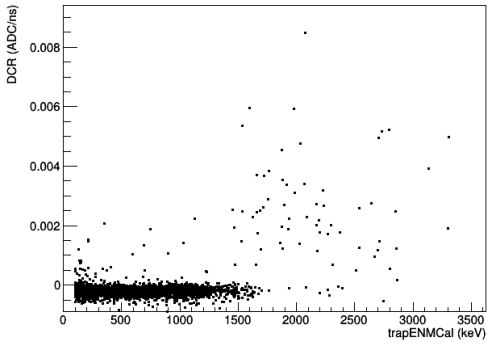

(f) The DCR vs. energy distribution.

Figure 3.12: The results of DCR validation of the 90% bulk-acceptance cut for DS 3 high gain channels.

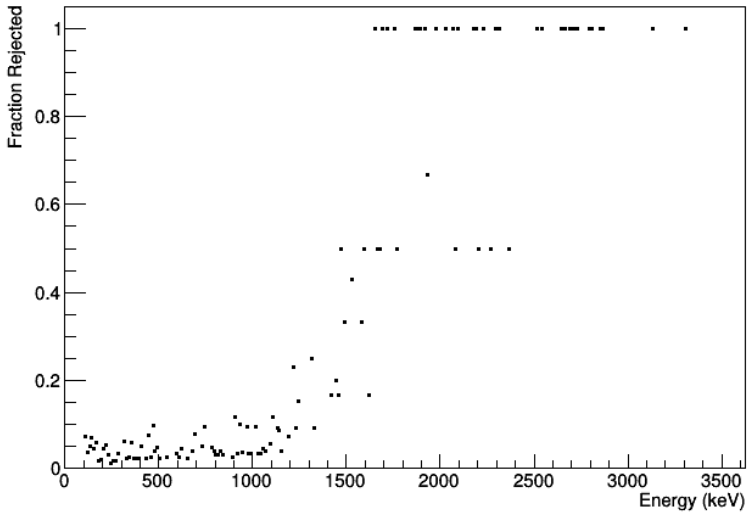

Figure 3.13: The rejection fraction of the 90% bulk-acceptance DCR cut as a function of energy, in DS 3 high gain channels.

(single-bin-width) spike will appear at 0 along with the Gaussian for the correctly calculated parameters.

- The DCR distribution for all channels: Each distribution should be peaked just below 0, with a tail extending to high-DCR values. All events appearing at 0, or a peak appearing in a different location, are indications of errors in the DCR parameters. See Fig. 3.12b.

- The number of events retained by the DCR cut in each channel: All bins should be similar in height, since the event rate in the low-background data is dominated by $2\nu\beta\beta$ decay (in the enriched detectors) and by low-energy gamma events. See Fig. 3.12c.

- The energy spectrum after the DCR cut is applied: It should resemble the $2\nu\beta\beta$ spectrum at energies above 500 keV, with no large dips at any particular energies. There should be few events remaining above 1.8 MeV. See Fig. 3.12d.

- The energy spectrum of the events removed by the DCR cut: It should be roughly flat, with a small rise at low energy. See Fig. 3.12e.

- The DCR vs. energy distribution of events: Most events above 1.8 MeV should have visibly high DCR. Below 1.5 MeV, most events should have DCR below 0. See Fig. 3.12f.

- The DCR rejection efficiency as a function of energy, in 10 keV bins: It should be at or near 1 in most bins above 1.8 MeV, and fall to approximately the chosen cut bulk-rejection (in this case, 90%) at energies below 1 MeV. See Fig. 3.13.

Additionally, stability studies are conducted of each data set, and the necessary stability corrections are applied. If no anomalies or significant instabilities are found, the DCR cut is ready to be used in spectral analysis. Other checks, like a verification that the $2\nu\beta\beta$ decay rate is consistent in all enriched detectors, are also applied at that stage.

Chapter 4

THE TUBE SCANNING SYSTEM

4.1 Introduction

As previously discussed in Ch. 3, alpha particle backgrounds originating on or near the passivated surface of P-PC detectors are a major contributor to the MAJORANA DEMONSTRATOR background spectrum, but can be identified effectively via a delayed-charge recovery (DCR) pulse-shape discriminator. While ^{228}Th source calibrations and $2\nu\beta\beta$ events can be used to estimate the DCR acceptance of bulk events, a sample of known passivated-surface alpha events is needed to estimate the alpha rejection efficiency of the analysis. Such measurements can also be used to estimate the alpha background spectral shape both before and after the DCR cut, allowing the construction of an accurate background model for the DEMONSTRATOR.

Given that the weighting potential near the passivated surface varies with radius (see Fig. 5.6), the energy lost to delayed charge in these events, and therefore the reconstructed energy of the events, is also expected to vary with radius. Similarly, the rate of charge re-release and amount of charge released, which combine to produce the DCR parameter value, are also expected to vary with radius. These variations lead to an radially- (and therefore energy-) dependent alpha rejection efficiency. The signs of the DCR and energy correlations with radius depend on the mechanism of charge delay and/or loss, including whether only electrons or both holes and electrons are affected, and whether surface-charge transport or charge-trapping (followed by re-release into the bulk) near the passivated surface is primarily responsible for the observed delayed-charge effect.

To study these effects, a collimated ^{241}Am source was used to scan PONaMa-1, a P-PC detector with the same geometry as the enriched detectors currently operating in the

PONaMa-1 Properties	
Diameter	68.9 mm
Height	52.0 mm
Dimple Diameter	3.2 mm
Dimple Depth	2.0 mm
Capacitance	1.8 pF
Depletion Voltage	1850 V
Leakage Current	10 pA
Resolution at 1332 keV	1.99 keV
(Measured at ORTEC)	

Table 4.1: Dimensions and operating parameters of the PONaMa-1 P-PC detector.

Majorana Demonstrator. Data was taken at with the source incident at positions spanning nearly the entire diameter of the passivated surface.

4.2 Experimental Setup

4.2.1 PONaMa-1

The detector chosen to be scanned was PONaMa-1 (serial number TP42486A), a test-run detector produced by ORTEC using natural-abundance germanium. Its production process was identical to that used for the enriched detectors in the Demonstrator, and its geometry is similar to that of those detectors. Its properties are given in Table 4.1.

4.2.2 The TUBE Scanner

The TUM (Technical University of Munich) Upside-down BEGe (TUBE) scanner is a custom-built cryostat first made to study the backgrounds in GERDA due to surface interactions on the p+ electrode and groove of Canberra BEGe P-PC detectors [14]. It allows a P-PC

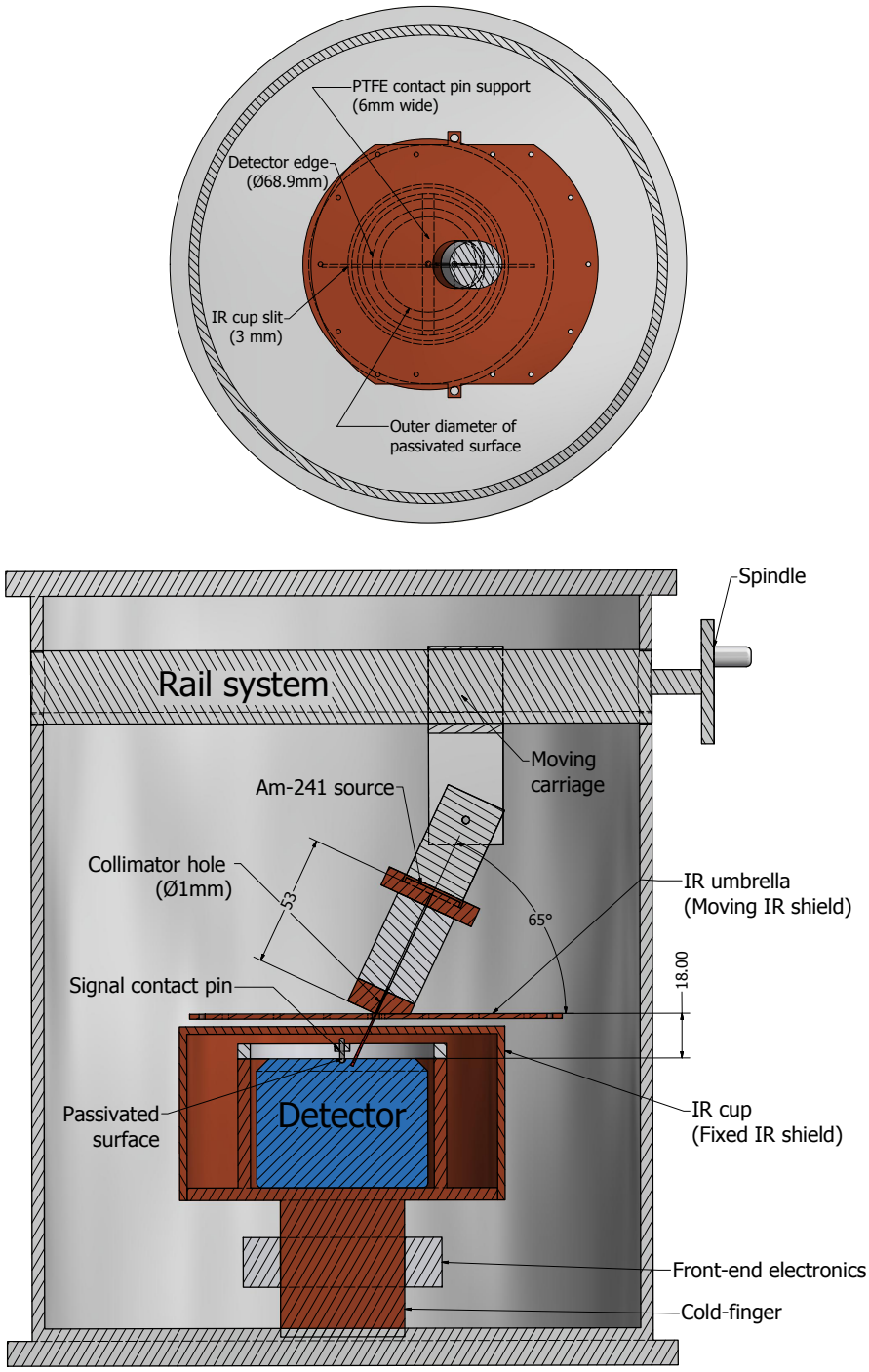

Figure 4.1: Simplified top *(top)* and bisected views *(bottom)* of the TUBE scanner, showing key dimensions. The thermal braids connecting the IR umbrella to the IR cup and the mylar covering of the IR umbrella are not shown. Details of the detector cup, front-end electronics, and cold-finger are also removed for clarity.

detector to be installed "upside-down," with the passivated surface facing upwards, so that the surface may be scanned with a collimated source. The scanner consists of three main parts, seen in Fig. 4.1: the cryostat, detector holder, and collimator assembly.

The cryostat is made from a stainless steel tube with top and bottom flanges, with a vacuum feed-through that allows the cryostat cold-finger and signal electronics (from a Canberra vendor cryostat) to be inserted. A rail system is mounted at the top of the vessel, with a rotational feedthrough on the sidewall that allows the collimator radial position to be changed while the system is under vacuum. The collimator assembly is mounted to the carriage of this rail system, which has a pitch corresponding to 1.5 mm of travel for every turn of the spindle. Ultra-high vacuum in the vessel is achieved using a turbomolecular pumping stand with a diaphragm forepump, connected to the system by Viton-sealed flanges. The measurements described here were taken with the pump in continuous operation, though the cooled system can retain pressures of around 1E-5 mbar even after eight hours without pumping.

The detector is mounted in a modified version of the original TUBE copper holder, adapted for the dimensions of PONaMa-1 by the addition of teflon shims. This holder was made by adapting the vendor-cryostat detector mount, and houses the front-end electronics. Contact with the p+ electrode is made via a spring-loaded contact pin, held in a narrow Teflon® holder that also provides routing for the signal cable, which runs from the contact pin to the front-end electronics. This holder creates a 6-mm "blind spot" on the detector surface that cannot be scanned. See Figs. 4.3 and 4.4.

This assembly is housed inside a copper infrared (IR) shield (called the "IR cup") with a 3 mm-wide slit running along its diameter. This slit defines the axis that is scanned along, as the source beam shines through it onto the detector surface. See Fig. 4.1.

Further IR-shielding, required due to the high IR-shine susceptibility of the large passivated surface of ORTEC P-PC detectors, was added for use with PONaMA-1. It is provided by a copper "IR umbrella" shield, mounted on the tip of the collimator and moving along with the source. This shield, which minimizes the IR-shine onto the passivated surface through the

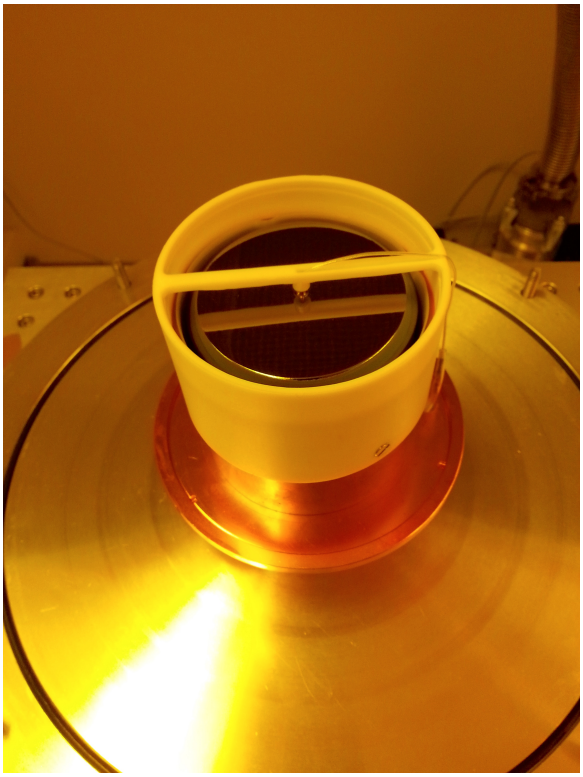

Figure 4.2: A photo of PONaMa-1 installed in the TUBE detector cup. The contact pin, visible at the center of the detector, is held by the Teflon® crossbar, with the signal cable running along the top.

slit of the IR cup, is thermally grounded to the cup via two flexible high-thermal-conductivity copper braids. The dimensions of the IR umbrella were subject to the existing constraint of the TUBE cryostat chamber diameter; therefore, it does not completely cover the IR cup slit at all scanning positions. This leads to variation in the detector leakage current as the collimator is moved along the surface. The top face of the IR umbrella is covered with several layers of insulator-backed Mylar®, to minimize its radiative heat-load. The IR umbrella and mylar sheets have a 3 mm diameter hole to allow the source beam to penetrate.

A photo of the TUBE scanning system (Fig. 4.4) shows the IR umbrella, thermal grounding braids, and Mylar®insulation.

4.2.3 ^{241}Am *Source and Collimator Properties*

The collimator has an overall length of 53 mm, and is suspended from the carriage of the rail system. The source is housed in a copper holder with a 1 mm-diameter collimating hole.

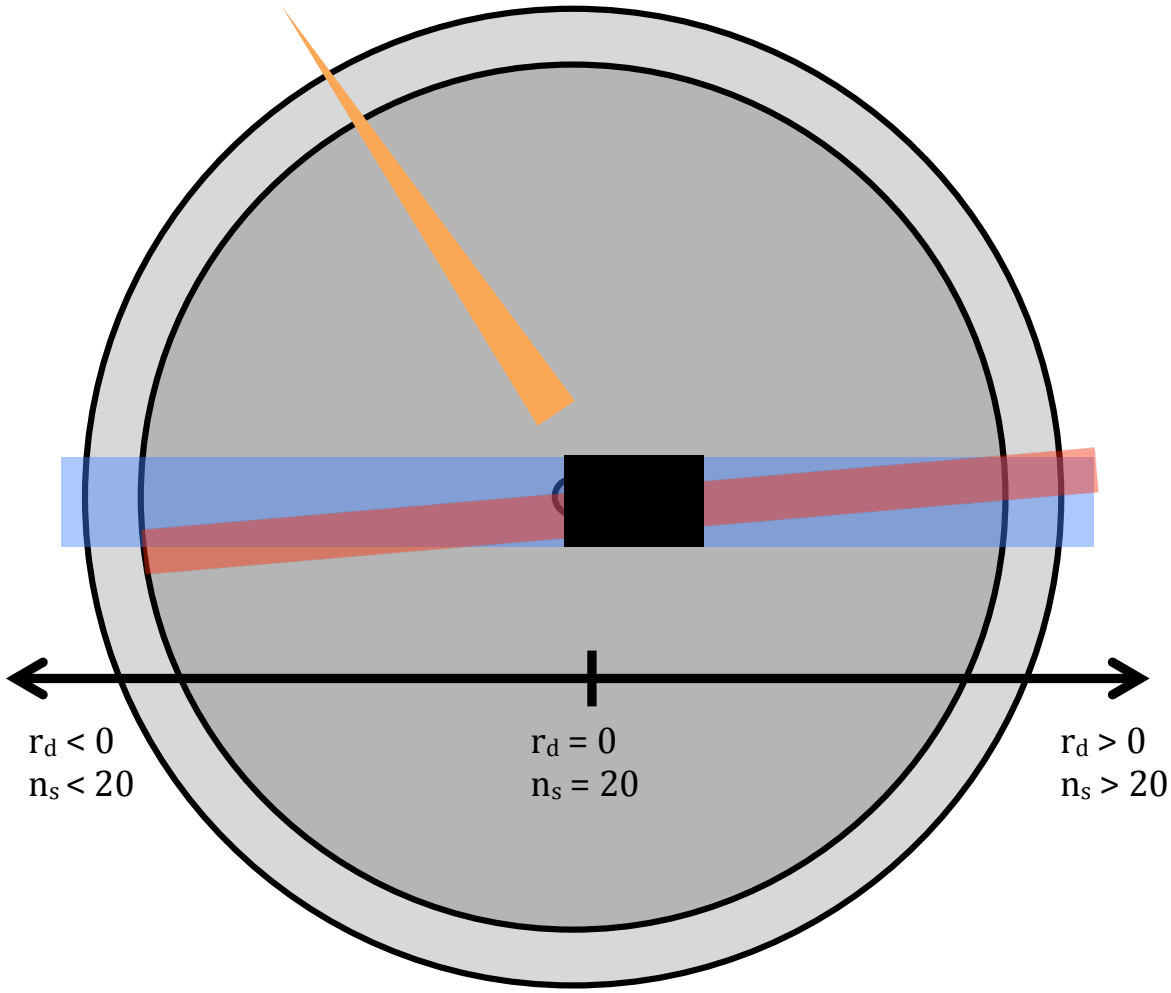

Figure 4.3: A diagram showing the accessible scanning regions and the coordinate systems used to describe the source position. The dark gray and light gray regions represent the passivated surface and edge of the n+ contact surface, respectively. The gold triangle represents the source beam, which forms a 65° angle to the negative r axis. The blue region represents the portion of the detector visible through the IR cup slit, and the red region is the path traced out by the source beam. Notice that due to the misalignment of the two axes, only the region of their overlap can be scanned. The black region is the inaccessible "blind spot" due to the contact-pin holder. It occludes all but one edge of the p+ contact region, which spans the region from $r_d = -1.6\,\text{mm}$ to $r_d = 1.6\,\text{mm}$. The misalignment is estimated as described in Sec. 4.3.1. Dimensions not to scale.

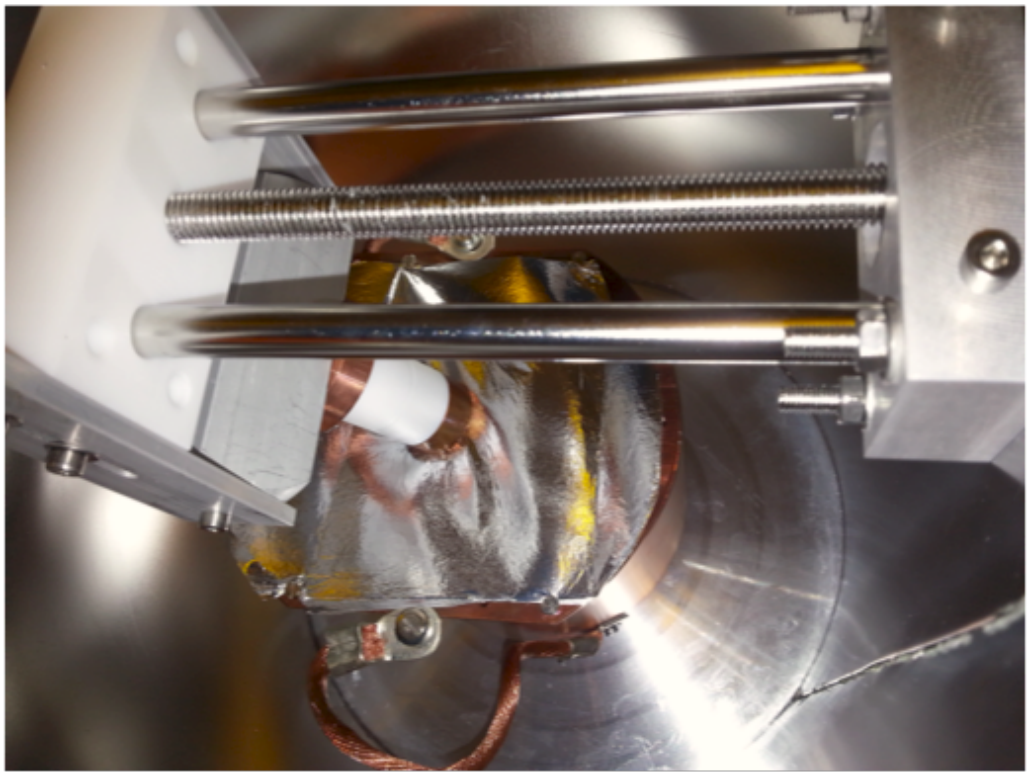

Figure 4.4: A photo of the inside of the TUBE scanner. The moving carriage and rail system is at the top, with the source and collimator suspended from it. The IR umbrella is suspended from the collimator tip, and is cooled via the thermal grounding braids, one of which is visible at the bottom of the photo.

The beam then passes through a teflon and aluminum tube, with a collimating hole of 3 mm in diameter, that thermally isolates the source holder, carriage, and rail system from the IR umbrella. The collimator assembly ends in a copper tip with a 1 mm diameter collimator hole, which is chamfered to create a source-beam incidence angle of 66.8° to the horizontal plane. In the course of mounting the collimator to the rail system, this angle may change by up to 2.3° in either direction without impeding the movement of the source. For these measurements, the incidence angle is taken to be 65°, as discussed in Sec. 4.3.1. The spot size of the source on the detector surface is estimated to be 1.8 mm in diameter.

The ^{241}Am source used was a 40 kBq alpha spectrometry source provided by Eckert & Ziegler Nuclitec GmbH, with product code AMR14. It is an open source, with the radionuclide deposited onto a 7 mm-diameter spot of a stainless steel disc. This minimizes energy degradation, giving an expected full width at half maximum for the 5.486 MeV alpha peak of less than 20 keV. In the expected event rate calculation, we assume that the radionuclide is deposited with equal density over the entire 7 mm-diameter spot.

Given the source strength and collimator geometry, an activity of 18 mBq (65 events/hour) is expected at the detector surface. 84.8% of events, corresponding to an activity of 15 mBq (54 events/hour) should include a 5.486 MeV alpha emission. Another 13.1% of events include a 5.443 MeV alpha emission [25]. If the energy resolution of the detector is sufficiently reduced by interactions in the passivated surface, these peaks will be indistinguishable, and 98% of the total activity will lie in the observed peak.

4.2.4 Muon Veto System

The expected vertical flux of cosmic ray muons with energy over 1 GeV is 1 $\mathrm{cm}^{-2}\,\mathrm{min}^{-1}$ at sea level for a horizontal detector [59]. Therefore the expected rate of high energy muons in the TUBE system detector is approximately 620 mBq (2240 events/hour), far overwhelming the expected alpha event rate. An active muon veto system is used to reduce the cosmic muon background rate. The veto system used consists of a 82 cm by 60 cm BC-408 plastic scintillator panel that is 5.5 cm thick and 2-inch photomultiplier tube (PMT), placed on top of the cryostat.

4.2.5 Data Aquisition

High voltage to PONaMa-1 was suppled by a CAEN N1471HA module. The detector was first operated at 950 V of bias, 100 V above the observed depletion voltage; ultimately, the bias was raised to 1050 V to eliminate pinch-off. A Canberra Model 2002 Spectroscopy Preamplifier was used, with the low gain (100 mV/MeV) setting in place.

The veto system PMT was operated at a 1000 V bias, and amplified using a Canberra Model 2025 AFT Research Amplifier, with a gain of x20 and a shaping time of .5μs.

Data from both PONaMa-1 and the muon veto system were recorded with a Struck SIS3302 digitizer, sampling at 100 MHz. The digitizer and readout are controlled using ORCA (Object-oriented Real-time Control and Acquisition) [36].

4.3 Measurements Taken

4.3.1 As-Built Geometry

Several aspects of the TUBE scanner geometry are determined at the moment of assembly, and are subject to human error. In particular, both the total vertical distance between the collimator tip and detector surface and the source beam incidence angle are approximate. Given the observed positions of the detector edges, the vertical spacing is thought to be 22 mm (rather than the expected 18 mm), and the angle of incidence is thought to be 65° (rather than the expected 66.8°).

With these as-built dimensions, the mapping from number of turns of the spindle, which is used to describe the data sets, to source spot position on the detector surface is given by $r_d = (n_s - 20)(1.5\,\text{mm})$, where n_s is the number of turns and r_d is the distance from the point contact on the surface of the detector. Negative and positive radii are defined as shown in Fig. 4.3, with 0 at the center of the p+ contact. The region between $r_d = -1\,\text{mm}$ and $r_d = 7\,\text{mm}$ is occluded by the contact-pin and PTFE contact-pin holder, and cannot be scanned.

In the course of the measurements, it was discovered that the IR cup slit and scanning axis were misaligned. This led to a falling source rate at large-magnitude negative scanning radii, as seen in Fig. 4.10. An additional slight sideways shift in the collimator mounting position (i.e. when aligned with the P-contact, the source shines slightly to one side of the IR-slit center line, rather than into the center of the P-contact), leads to a difference in the source obstruction at negative and positive radii. Based on the observed source rates

and known geometry, the angular misalignment must be less than 2.5°, and the sideways misalignment must be less than 1 mm.

Hysteresis effects were observed in the source position, so an uncertainty of 0.75 mm (corresponding to a 1/2 turn of the spindle) is assigned to all source positions.

4.3.2 Data Sets

Data were taken at all integer-turn positions for at least 24 hours. Each of these run sets, taken without changing the source position or operating conditions, is grouped into a data set. Several multi-day runs were also taken to study the stability of the system. In those cases, multiple data sets cover the span of time, with each data set corresponding to approximately one day of run time. Scanning positions were repeated non-contiguously to study the effect of the source position hysteresis and the long-term stability of the DCR parameters. Measurements were taken at half-turn positions in the vicinity of the p+ contact and at the edges of the passivated surface.

4.4 Data Processing Scheme

4.4.1 Analysis Chain

The data were analyzed using a modified version of the MAJORANA processing stream. Runs are limited to half an hour in duration and 2 GB in file size. In practice, alpha source and background runs are half an hour long, and thorium calibration runs (whether taken with a ^{228}Th or ^{232}Th source) are shorter.

Each half-hour run is processed independently until the final step of processing. Using the Majorana-OrcaRoot (MJOR) and OrcaRoot software packages, the raw ORCA output files are converted into ROOT output files, which contain `TTree`s of ORCA output parameters encapulated in MAJORANA GERDA Data Objects (MGDO) classes. Included in each run's `TTree` are the raw waveforms collected by the digitizer. These waveforms are 30 μs long and sampled at 100 MHz, with the trigger appearing about 10 μs after the start of the

waveform. These waveforms are packaged into "events," which contain all waveforms that triggered within a 10 μs window. If a cosmic ray muon triggers both the veto panel PMT and germanium detector, for instance, the event will contain two waveforms. The resulting files are referred to here as "built" data files.

The built data is then processed using the Germanium Analysis Toolkit (GAT) software package. At this processing step, each waveform has a variety of filters (such as baseline removal, pole-zero correction, etc.) and parameter calculators applied to it. Multiple waveforms in a given event are also processed together to give parameters such as multiplicity. The energy calibration (determined as described below) is applied during this stage of processing. All of the resulting values are saved to the "reconstructed" data files, which do not contain the waveforms themselves.

A summary of the parameters saved at this stage is given in Table 4.2. Baseline removal is applied by subtracting the average value of the first 500 waveform samples from each sample of the waveform. The pole-zero correction applied uses the decay constant $\tau = 44.224\,\mu$s, found by fitting to the decay of 1000 pulses in a calibration run from the first calibration data set taken. The trapezoidal filter used for energy reconstruction has an integration time of 8 μs and a collection time of 3 μs. A second trapezoidal filter, with integration time of 0.5 μs and collection time of 0.3 μs, is used to tag pile-up events. A one-sided trapezoidal filter, with integration time of 200 ns and peaking time of 10 ns, is used to calculate the current 'A' used in the determination of A vs. E [37].

Three varieties of the waveform tail slope, which will be used to determine the DCR parameters, are saved. The values are the result of a two-point slope calculation, using the average value (in ADC) of the waveform in a 1 μs region for each of the points. All three varieties use the region starting 2 μs after the 97% rise point of the waveform as the first point. The `blrwfSlope` and `blrpzcwfSlope` use the final 1 μs of the baseline-removed waveform as their second point. The former uses the effective pole-zero correction strategy described in Sec. 3.2. For the latter, true pole-zero correction is applied before measuring the slope. The `mjdblrwfSlope` parameter emulates the waveforms collected in MAJORANA

Selected Reconstructed Data Parameters	
Name	Description
`run`	Run number
`channel`	Channel (Ge or PMT)
`timestamp`	Digitizer timestamp at time of trigger (in 10 ns units)
`startTime`	Start time of run (in UTC)
`stopTime`	Stop time of run (in UTC)
`m`	Multiplicity of event
`pileUpWFsnRisingX`	Number of rising threshold crossings of pile-up trap. filter
`trapEMPZ`	Maximum of baseline-removed, pole-zero corrected, trapezoidal-filtered waveform.
`trapEMPZCal`	Calibrated version of the above, used for Ge energy determination.
`onboardE`	Digitizer trap. filter energy, optimized for PMT energy determination
`blrwfSlope`	Tail slope of baseline-removed waveform
`mjdblrwfSlope`	Tail slope of MJD-emulating baseline-removed waveform
`blrpzcwfSlope`	Tail slope of baseline-removed pole-zero-corrected waveform
`TSCurrent200Max`	Current filter maximum

Table 4.2: Selected reconstructed data parameters, with brief descriptions.

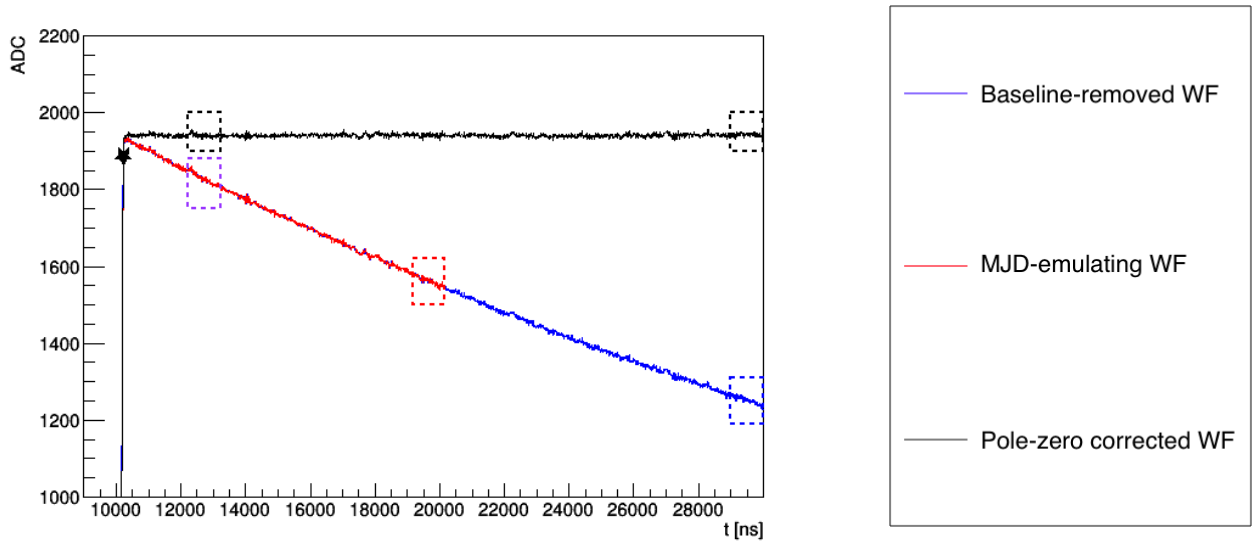

Figure 4.5: Sample 2614 keV waveform, with the points needed to calculate various tail slope parameters. The star indicates the 97% rise point of the pulse. The blue waveform has had its baseline removed; the slope between the averages in the violet and blue dotted regions is the `blrwfSlope`. The red waveform has had its final 10 us chopped following baseline removal to emulate singly-sampled MJD waveforms; the slope between the averages in the violet and red dotted regions is the `mjdblrwfSlope`. The black waveform has had pole-zero correction applied after baseline removal; the slope between the averages in the black dotted regions is the `blrpzcwfSlope`.

data sets that do not use multi-sampling (MJD Data Sets 0, 1, and 3-5). For this parameter, the baseline-removed waveform is cut to have only 2016 samples, removing the final 10 μs of decay tail. Then the final 1 μs of the shortened waveform is used as the second region. See Fig. 4.5.

In the final step of processing, GAT is used to combine about 24 hour's worth of consecutive runs into a skimmed data set. An offline energy threshold is applied to both the germanium and PMT data to reduce the number of noise events in the data set, and these

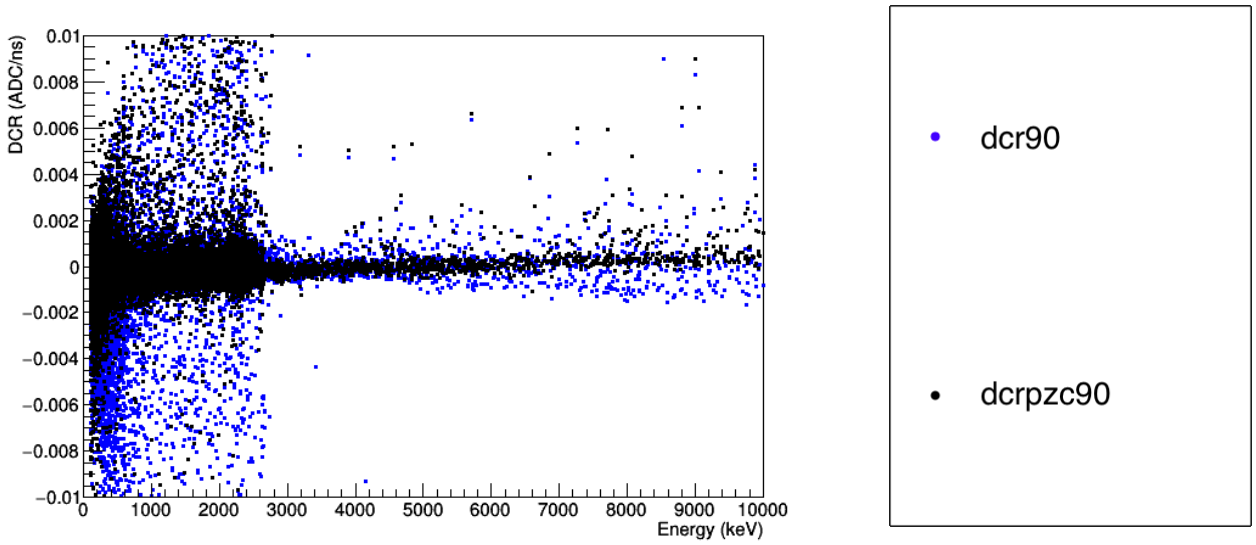

Figure 4.6: A comparison of `dcr90` (in blue) and `dcrpzc90` (in black) in single-site calibration events (from calibration Data Set 8) after the muon veto is applied. `dcr90` falls and degrades in resolution at energies over 4 MeV. Though `dcrpzc90` rises slightly with increasing energy, likely due to a small change in the pole-zero decay constant τ between calibration Data Set 1 and 8, the effect is minimal compared to the broadening of `dcr90`.

thresholds are used to calculate a "clean" multiplicity that excludes events below the analysis threshold.

Other high-level parameters (i.e. those that require calibrated energy as an input value) are also calculated at this stage. These include A vs. E, which is the multi-site event discriminator used in this work [37], A/E, a multi-site discriminator that is used to identify near-point-contact events, and the DCR parameters, described below.

4.4.2 DCR Parameters

For a detailed discussion of the procedure used to calculate DCR parameters, see Ch 3.

Four types of DCR parameters are calculated for each PONaMa-1 waveform. For each

of the parameters, versions are saved with 99% and 90% bulk acceptance. The `dcr90` and `dcr99` parameters are calculated using the waveforms after baseline-removal, with no other filters applied. The `mjddcr90` and `mjddcr99` parameters are derived from the MJD-emulating waveforms, which have only a 10 μs decay tail, instead of a 20 μs one. They are provided as a point of comparison to study the effectiveness of the DCR analysis in the MAJORANA Data Sets that do not use multisampling. Both of these sets of DCR parameters are calculated using the procedure described in Sec. 3.2

The final 2 sets of DCR parameters, the DCRPZC and DCRPZCnorm parameters, are calculated using the baseline-removed waveform after pole-zero correction. This eliminates the need for the step in which the tail slope parameter is projected onto the energy axis, and creates a DCR parameter that has no dependence on energy for high-DCR events, unlike the other DCR parameter values. The DCRPZC parameters are a measure of the amount of delayed charge collected in the first 20 μs after the fast, bulk charges are collected.

The `dcrpzc90` (`dcrpzc99`) parameter is calculated by finding the 90% (99%) acceptance value of `blrpzcwfSlope` for single-site non-muon events with energies between 1 MeV and 2380 keV, and subtracting this value from `blrpzcwfSlope`. Therefore, 90% (99%) of bulk events should have `dcrpzc90` (`dcrpzc99`) < 0.

The DCRPZC parameters are the most appropriate set to use when comparing TUBE results to waveform simulations, which do not include pole-zero decay. This version of the DCR analysis also performs better with respect to muon events; bulk events have consistent average DCRPZC even at high energy, while DCR degrades in resolution and falls off at energies above 4 MeV. See Fig. 4.6. Except for cases in which a direct comparison of TUBE results to MAJORANA data is required, DCRPCZ is used in this work. Ultimately, we plan to move to a similar analysis for the MAJORANA data as well, as described in Sec. 3.4.2.

Additionally, normalized versions of DCRPZC, `dcrpzc90norm` and `dcrpzc99norm`, are calculated to correct for small instabilities in gain, PZ-decay constant, and noise in the system. To create these parameters:

- The `blrpzcwfSlope` distribution of single-site calibration events with 1 MeV$< E <$ 2380 keV is fit with a Gaussian peak, the fit range of which is set to exclude the high-DCR tail).

- The centroid of the fit is subtracted from `blrwfSlope`.

- The 90% (99%) acceptance value is found as described above.

- The shifted `blrpzcwfSlope` values are normalized by the cut value.

Therefore, the mean value of `dcrpzc90norm` (`dcrpzc99norm`) is 0, and 90% (99%) of bulk events should have `dcrpzc90norm` (`dcrpzc99norm`) < 1. The value of these parameters is insensitive to changes in the gain of the system, unlike the unnormalized DCRPZC parameters. The DCRPZC parameters also allow for a simple evaluation of how well-separated a given alpha event peak is from the bulk events.

4.5 Detector Performance

PONaMa-1 was first installed in the TUBE scanning system in September of 2016. In January of 2017 it was remounted to correct a significant misalignment and to install a spectral-grade source, which replaced the closed energy-degraded source that had original been installed. Data were taken from February 2nd to July 10th, 2017. Over these months, the detector's performance was consistent and stable.

4.5.1 Energy Calibration

Energy calibration using the GAT Multipeak Fitter [30] is applied to each data set. Fourteen peaks in the spectrum ranging in energy from 295 keV to 2614 keV are fit with a Gaussian peak, a low energy tail, a high energy tail (which fits to small values, in general), a step (which is centered at the Gaussian centroid), and a linear or quadratic background (depending on the expected shape of the continuum in the vicinity of the peak).

Comparing the resulting fit to a fit in which the peak positions were allowed to float, it was found that a linear calibration curve gave a poor fit to the peak positions in the spectrum. The residuals appeared to lie on a quadratic curve, with the 2614 keV peak position being underestimated by up to 0.8 ADC (corresponding to approximately 1 keV).

The fit was improved by the addition of a quadratic component to the peak position function (see Fig. 4.7). I.e., the uncalibrated peak position is given by:

$$E_{ADC} = p_0 + p_1 E_{keV} + p_2 E_{keV}^2,$$

where p_2 is positive. With this change, the peak position residuals are generally less than 0.4 ADC and are evenly distributed about 0, though some non-linearity remains, likely due to digitization effects.

4.5.2 Energy Stability

Given the high room background rates, it is possible to calibrate every data set independently, without relying on dedicated calibration runs. The energy stability within data sets is measured by calculating the position of the 2614 keV peak in ADC for each data set by applying the appropriate calibration constants, and then calculating the absolute value of the shift between consecutive data sets. The average shift is found to be 0.68 ± 0.60 ADC, corresponding to 0.92 ± 0.81 keV at the 2614 keV peak.

All shifts in the energy scale had less than a 2 ADC effect on the position of the 2614 keV peak save for one, between runs 1638 and 1639, which led to a shift of 4 ADC. This shift was large enough to require that a stability correction be applied in the pulse-shape discriminating parameters, as discussed below.

4.5.3 Energy Resolution

The average FWHM at the 2614 keV peak is 3.2 ± 0.6 keV. The Gaussian component of the peak has an average standard deviation of 1.1 ± 0.1 keV, which would correspond to a FWHM of 3.0 ± 0.3 keV. The remaining contribution is due primarily to the low-energy tail,

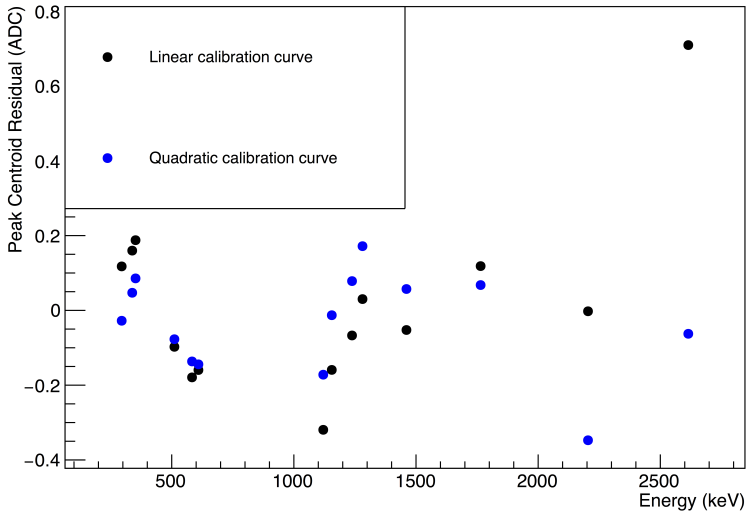

Figure 4.7: The residuals of calibration peak positions. The entire spectrum was first fit with the peak positions (in ADC) restricted to lie either on a linear (in black) or quadratic (in blue) function of energy (in keV), and then fit with the peak positions allowed to float.

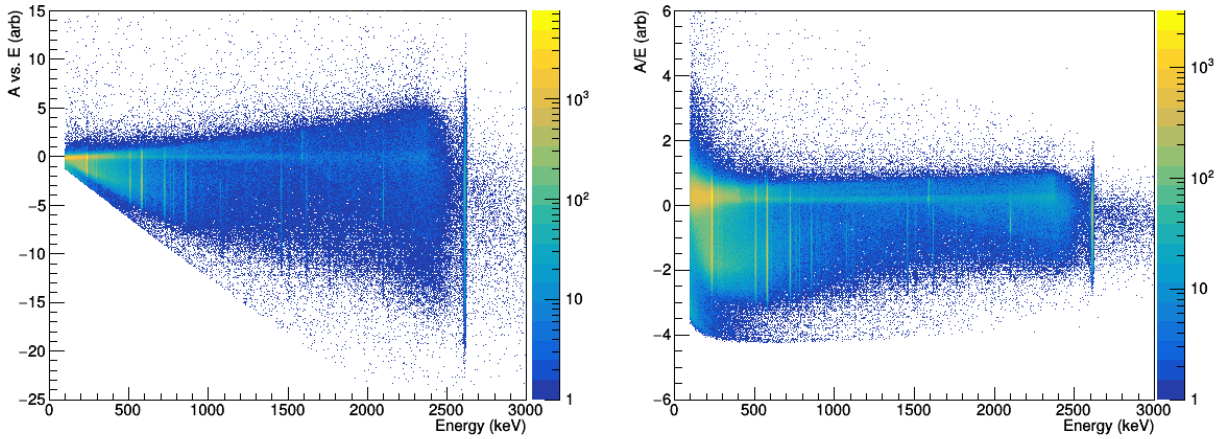

Figure 4.8: A comparison of A vs. E *(left)* and A/E *(right)* in calibration events (from calibration Data Set 8) after the muon veto is applied. The color scale indicates the number of events. Near point-contact events have energy-dependent values of A vs. E, as seen in the sloped upper edge of the A vs. E distribution when it is drawn with respect to energy, but have energy-independent values of A/E. Therefore, A/E is used to identify near-point-contact events.

with a minimal contribution from the high-energy tail. The average resolution curve of the gaussian component is given by:

$$\sigma = \sqrt{2.79 \times 10^{-1} + 3.21 \times 10^{-4}\, E_{keV} + 2.84 \times 10^{-9}\, E_{keV}^2}$$

The resolution suffers due to the continuous operation of the turbopump attached to the TUBE cryostat, since microphonic noise is introduced into the system. However, it was determined that the resolution was satisfactory for these measurements, and that gaining added duty cycles by avoiding pumping between measurements was a higher priority than optimizing the energy resolution.

4.5.4 A vs. E

The "A vs. E" pulse shape discriminator is used to tag and eliminate multi-site events, as described in [37]. The parameters for the cut are set using ^{228}Th calibration runs, since the ^{228}Th spectrum has no other spectral peaks near the 2614 keV double-escape peak (DEP), at 1592 keV. The ^{232}Th spectrum, on the other hand, has a gamma peak at 1588 keV from the decay of ^{228}Ac; this peak is not well-separated from the DEP, and can contribute multi-site events that lead to an inaccurate A vs. E cut calibration.

The current is estimated using a 200 ns `TSCurrent` filter, which estimates the derivative of the pulse from a running linear fit over a small range of the waveform. The energy estimator used, `trapEMPZCal`, is described above. The process used to determine the correct parameters and calculate the efficiencies and uncertainties is exactly that used for the MAJORANA analysis [37].

To correct for the gain and noise change that occurred following run 1639, the A vs. E parameters and results are calculated separately for these two run periods. See Table 4.3. These cuts are set using calibration Data Sets 1 and 8, which are 17.9 and 2.9 hrs in duration, respectively.

4.5.5 A over E

Since the width of the distribution of "A vs. E" estimator values depends on energy (see Fig. 4.8), it is a poor choice of parameter to describe the shape of the pulses from near-point-contact alpha events. For that, we use "A/E," the current discriminator normalized by the energy. Using this estimator, near-point-contact events appear in an energy-independent band at higher values than single-site events.

The A/E parameters are determined following a similar procedure to that outlined in [27]:

- "A," the maximum current, is taken to be the maximum value of a 200 ns `TSCurrent` filter.
- The ratio A/E is calculated for all events.
- For each of eight spectral peaks with energies from 1000 to 2220 keV, the mean A/E value is calculated.
- A linear function in energy is fit to the mean A/E values. This energy correction is applied to all A/E values.
- The A/E cut value is chosen such that 90% of events in the DEP are accepted, following statistical background subtraction using the sidebands of the peak.
- The cut value is subtracted from the energy-corrected A/E value to give the "multi-site corrected A/E" ($A/E_{corr,MS}$).
- The 99% acceptance value of of $A/E_{corr,MS}$ is determined. This is the value that 99% of events (whether multisite or single-site) with energies between 1 MeV and 2630 keV lie below. $A/E_{corr,MS}$ is normalized by this value to give the parameter hereafter referred to as 'A/E.'

PSD	Run Range	DEP (%)	SEP (%)	ROI CC (%)
A vs. E	1 - 1639	90.4 ± 2.7	20.0 ± 4.0	70.6 ± 1.1
A vs. E	1639 - 6189	90.1 ± 1.0	11.4 ± 0.8	50.9 ± 0.6
A/E	1 - 1639	90.2 ± 3.0	11.9 ± 1.0	48.7 ± 1.3
A/E	1639 - 6189	89.6 ± 1.9	12.6 ± 0.7	53.7 ± 0.8

Table 4.3: Multi-site discriminator survival fractions in the ^{208}Th escape peaks and in the Compton continuum near the $0\nu\beta\beta$ region-of-interest.

Therefore, multi-site events are expected to have A/E < 0, and single-site events will have $A/E > 0$. The final normalization corrects for gain instability and changes in the noise of the system, and 99% of calibration-run gamma events will have $A/E < 1$. Near point-contact events will have $A/E \gg 1$.

As for A vs. E, the A/E acceptance in the DEP and SEP is calculated using statistical background subtraction. The region from 1989 keV to 2089 keV, termed the $0\nu\beta\beta$ region, provides an estimate of the Compton continuum reduction provided by the cut. Again, a stability correction is applied after run 1639. See Table 4.3.

4.5.6 Muon Veto

The energy in the muon veto panel is estimated using the digitizer onboard trapezoidal energy filter, with integration time of 2.63 μs and collection time of 2.5 μs. An offline threshold is applied to avoid cutting on noise events in the PMT. Events in the P-PC detector that occur within 10 μs of a muon panel event are vetoed. After the cosmogenic muon cut, the germanium detector event rate in the 3 to 10 MeV energy window is reduced from 1245 events/keV/hr to 823 events/keV/hr.

The muon system efficiency is not expected to be 100%, since particles with high zenith angles can hit the germanium detector without passing through the muon veto panel. Addi-

tionally, the background reduction provided by the veto system is likely reduced by the poor noise performance of the PMT, amplifier, and energy filters. The system was not extensively tuned to optimize the energy threshold. In spite of this, the germanium spectrum of vetoed events has the expected features (see Fig. 4.9). The reduction of the muon rate achieved is sufficient to allow measurements of the alpha source peak.

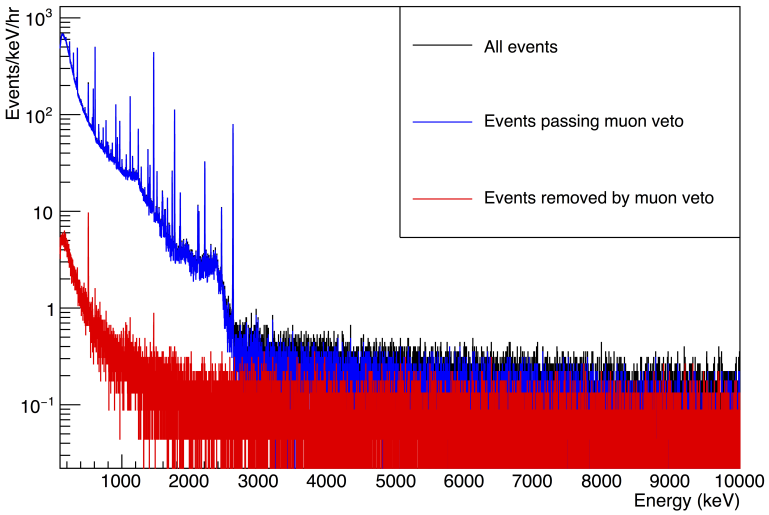

Figure 4.9: The Ge energy spectrum, before and after the muon veto is applied (in black and blue, respectively), and the Ge spectrum of vetoed events (in red). Note that the largest peak in the veto spectrum is seen at 511 keV, as is expected from true coincidence events due to pair production in materials near the detector, with a second small peak appearing at 1022 keV. An additional small peak is seen at 1460 keV, due to the high random coincidence rate of ^{40}K events, potentially from the PMT itself.

4.5.7 Live Time Analysis

The dead time induced by the germanium detector and veto system are comparable to one another. The P-PC detector triggers at approximately 60 Hz with a trigger window of 30 μs,

and the muon veto system triggers at approximately 90 Hz with a trigger window of 20 μs. Each system contributes an expected dead time fraction of 0.18%, leaving a total expected live time fraction of 99.64 %.

In the the average data set used in this analysis, which is 22 hours long, the live time reduction gives 0.08 hours (or less than 5 minutes) of dead time.

Given the smallness of this effect compared to the statistical uncertainties in this analysis, the second-order effect of accidental coincidences is negligible, and is neglected.

4.6 Alpha Event Rate

As a result of the as-built misalignment of the scanning and fixed IR shield axes (see Sec. 4.3.1), the alpha event rate varies with scanning position. Since the degree of misalignment is not known *a priori*, it is estimated from the data.

The fits to the energy spectra described in Sec. 5.1.1 are used to find the mean energy and width of the alpha peak, and a sideband region is selected as described in App. A. Using the sideband region, the alpha-source and a source-free spectrum are normalized to one another, and a count of the Poisson excess above the alpha-source-free runs in a 5σ window around the peak energy is used to calculate the rate at each position.

The assumption of a Gaussian-shaped peak in the energy spectrum is a poor one at low-magnitude scanning radii (as discussed in Sec. 5.1.1), but the rate may be estimated at larger radii on either side of these near-point contact positions, where the Gaussian assumption is a good one. These results may then be extrapolated to find the rate at the remaining positions.

As seen in Fig. 4.10, the source beam is not measurably obstructed between radii of -15 mm and 30 mm, and falls approximately linearly at larger-magnitude negative radii. This observation and the total reduction in rate at the largest magnitude radii lead us to derive an as-built misalignment of less than 2°. The horizontal misalignment must be less than 1 mm, since no scanning positions have a completely obstructed source beam. The exact values cannot be derived, since they are degenerate with one another.

Scanning radii between -15 mm and 30 mm are used to calculate the observed alpha

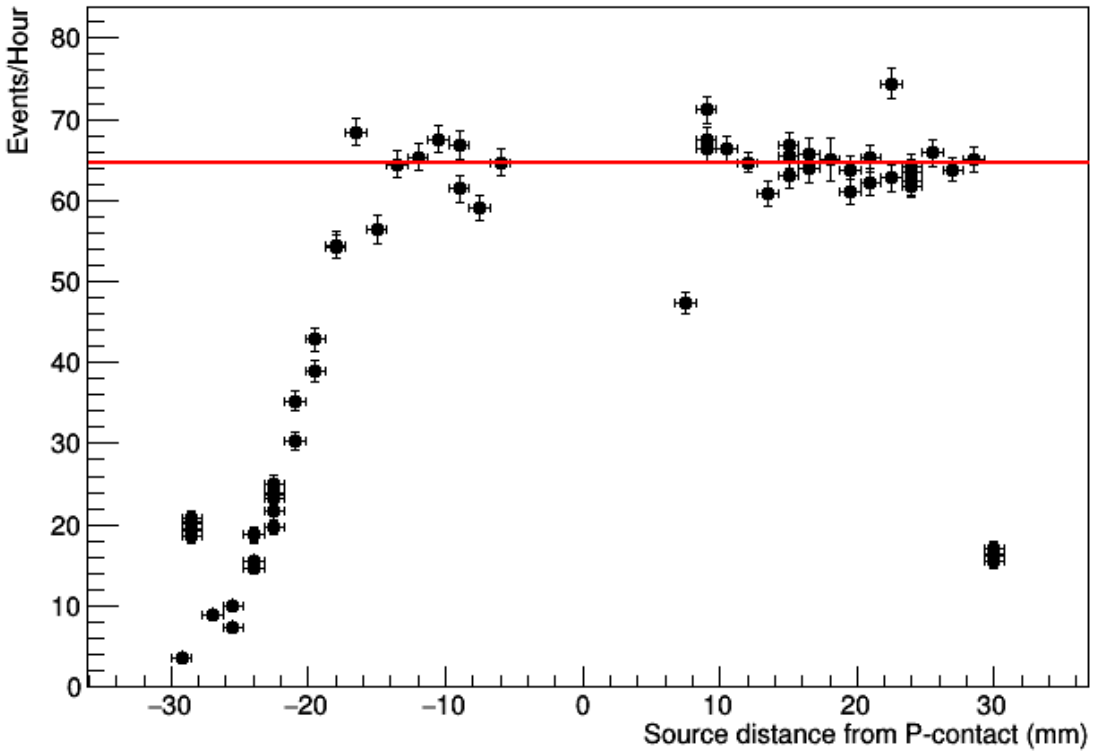

Figure 4.10: Observed alpha event rates in each data set, following background subtraction. The red line indicates the average value, calculated as described in Sec. 4.6. The rate is reduced at positions with $r < -15\,\text{mm}$ because of the misalignment of the scanning and IR cup axes. The rate at $r = 7.5\,\text{mm}$ is reduced by the partial obstruction of the passivated surface by the contact-pin holder, and the rate at $r = 30\,\text{mm}$ is low because the source beam is partially incident on the bevel, which is insensitive to alphas. The errors indicated here assume Poisson statistics.

source rate. The point at $r = 7.5\,\text{mm}$ is not included, since the source beam is partially obstructed by the contact-pin support at this position. The points at $r = 30\,\text{mm}$ are also not included, since at this position, part of the source beam falls on the bevel, rather than on the passivated surface. The bevel is part of the n+ contact of the detector, which is insensitive to alpha interactions. Using the remaining the 32 measurements, the observed source rate is $64.6 \pm 0.5\,\text{events/hr}$, or $18\,\text{mBq}$.

Given that the FWHM of the alpha event peaks (see Fig. 5.4) is larger than the $43\,\text{keV}$ energy difference between the two ^{241}Am alpha decay peaks, nearly the full activity of the source is expected to appear in the peak. Therefore, the observed activity is in excellent agreement with that expected from the source specifications and collimator geometry.

Chapter 5

CHARACTERIZING SURFACE ALPHA INTERACTIONS WITH THE TUBE SCANNER

5.1 Alpha Energy and Spectral Shape

5.1.1 Observations

In the energy spectra for each data set, it is clear that for large-magnitude radii, compared to source-free runs, there is an excess of events falling in a Gaussian peak, as in the examples in Fig 5.1. The energy and width of the peak varies with radius. For positions with radii larger than 6.75 mm in magnitude, the mean alpha energy is larger than 2614 keV, limiting the gamma-interaction background contribution in the peak region. See Figs. 5.1a and 5.1b for examples. Therefore, despite the low alpha interaction rate, the peak can be clearly identified and fit.

A tail of events at low energy is expected to occur along with the peak, due to variation in the alpha penetration depth. However, in practice, adding an exponentially modified Gaussian component to the peak fitting function does not improve the goodness of fit for high-radius data. The low alpha rate and large standard deviation of the Gaussian peak often lead the preferred fit of the tail function to accommodate the background, rather than improving the fit to the peak.

In the fit, the background is modeled by a linear function, which accounts for the gamma pile-up and muon background remaining after muon veto, single-site, and pile-up cuts. No other event cuts are used to produce these spectra. The results of these fits in each data set are shown in Figs 5.3a and 5.3b.

At radii smaller than 6 mm, the alpha peak falls in a region of high gamma backgrounds. Due to the low alpha rate, it can not be fit without applying a pulse-shape cut to select

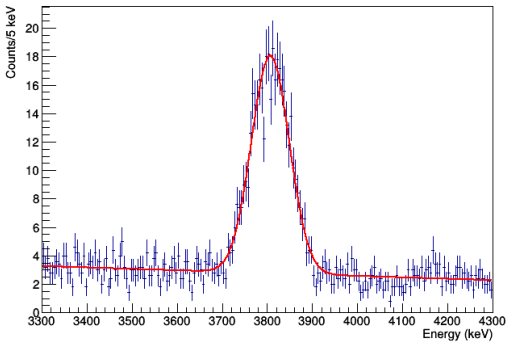

(a) The energy spectrum of a data set taken at 11 turns ($r = -13.5\,\text{mm}$), a total of 25.1 hrs of runtime.

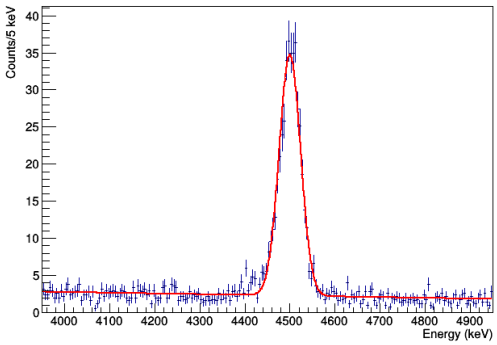

(b) The energy spectrum of a data set taken at 36 turns ($r = 24\,\text{mm}$), with 30.1 hrs of runtime.

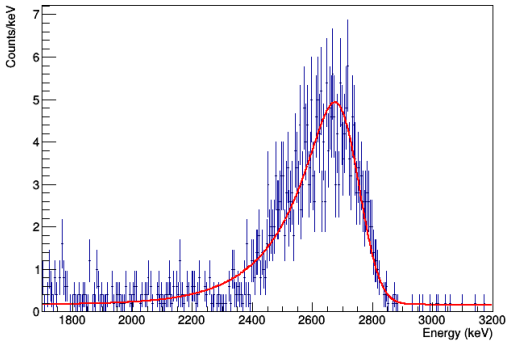

(c) The energy spectrum of a data set taken at 17 turns ($r = -4.5\,\text{mm}$), a total of 19.1 hrs of runtime, with a cut selecting near-point-contact events (`aenorm` > 1.5). At small radii ($r < 6\,\text{mm}$), the peaks become highly non-Gaussian, but fit well to an exponentially-modified Gaussian low-energy tail. In addition to the fit results in Table 5.1, energy ranges for these small-radius positions are given in Table 5.2.

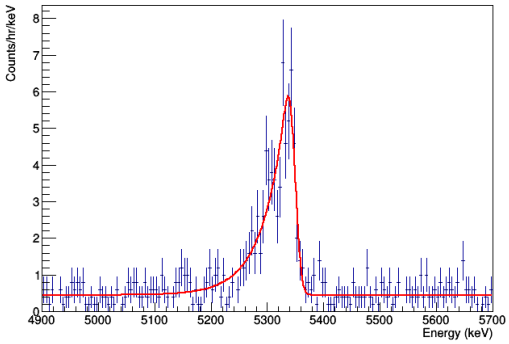

(d) The sum energy spectrum of all runs taken at 19.5 turns ($r = -0.75\,\text{mm}$), a total of 82.4 hrs of runtime, with a cut selecting near-point-contact events (`aenorm` > 1.5). Alphas incident on the point-contact have nearly the full incident energy, a narrower peak width, and visible low-energy tailing due to charge loss in the dead layer of the point-contact. Fit results are given in Table 5.3.

Figure 5.1: The energy spectra and peak fits for various scanning positions.

Data Set	α Pos. (mm)	μ (keV)	σ (keV)	f_τ	τ (keV^{-1})	χ^2/N_{df}
DS170	-4.5	2741±39	59±6	1.0±0.7	147±15	453/294
DS180	-3.0	2436±9	56±7	1.00±0.01	607±43	282/264

Table 5.1: The results of a Gaussian+low energy tail peak shape fit to the energy of alphas incident at small radii. A cut selecting near-point-contact events (aenorm > 1.5) is used to reduce the gamma background rate.

the source events. A cut of aenorm > 1.5 selects near-point contact events while rejecting 99.8% of background events. The peak is highly non-Gaussian, as in Fig. 5.1c, because of the wide range of weighting potential values sampled by the source beam at small radii. In these peaks, there is significant low-energy tailing, and an exponentially-modified Gaussian tail is included in the fit. The results of the fits are given in Table 5.1, where $\frac{1}{\tau}$ is the tailing constant (in keV) and f_τ is the fractional contribution of the low-energy tail component to the peak area. As seen in these results, the tail component dominates the fit to the peak.

Due to the significant low-energy tail at these small radii, the Gaussian peak width does not give an accurate energy range for the alpha events observed. For the smallest radii ($|r| < 3\,\text{mm}$), the Gaussian+tail model fit fails completely. For scans with $|r| \leq 4.5\,\text{mm}$, we have given the estimated energy range of the observed alpha events, in Table 5.2, either in lieu of or to supplement the description of the alpha energy spectra given by the fit results. These ranges were determined by eye – they are the upper and lower energy bounds of the contiguous overdense region of high-A/E events that appear in the alpha-source runs, as in the boxed region of Fig. 5.2.

At scanning positions that are partially or entirely incident on the point-contact, an additional alpha peak in the spectrum appears at nearly the full energy of the emitted alpha. Again, an A/E cut selecting near-point-contact events ($A/E > 1.5$) is applied to reduce the muon background. The peak shape is well-approximated by the sum of a Gaussian and

Data Set	α Pos. (mm)	E_{min} (keV)	E_{max} (keV)
DS170	-4.5	2300	2850
DS180	-3.0	1200	2600
DS185	-2.25	700	2600
DS190	-1.5	800	2800

Table 5.2: Estimated energy range of alpha interactions for source scans at small radii. At these positions, the peak is highly non-Gaussian. All data sets taken at each position are combined to determine these results.

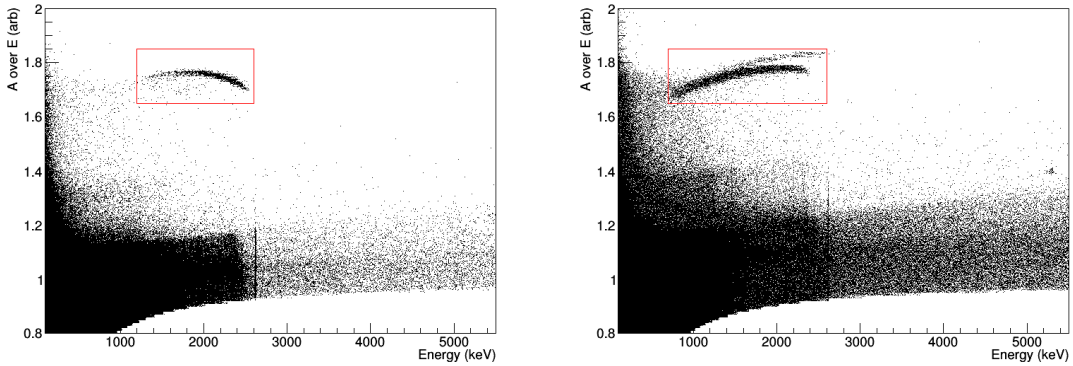

Figure 5.2: At small radii, (*left:* $r = -3.0\,\text{mm}$, *right:* $r = -2.25\,\text{mm}$) the alpha peak becomes highly non-Gaussian and becomes impossible to fit with a Gaussian+low energy tail model. Depending on the scanning position, the energy ranges of the high-A/E alpha events (indicated by the boxed regions above and listed in Table 5.2) are given to supplement or stand in place of the fit result information.

Data Set	α Pos. (mm)	μ (keV)	σ (keV)	f_τ	τ (keV^{-1})	χ^2/N_{df}
DS185	-2.25	5303±8	16±4	1.0±.9	12±11	314/274
DS190	-1.5	5298±5	31±4	0.3±.2	31±4	332/274
DS195	-0.75	5345±4	9±2	0.9±.1	41±6	335/274

Table 5.3: The results of a Gaussian+low energy tail peak shape fit to the energy of alphas incident on the point-contact. All data sets taken at each position are combined to determine these results.

an exponentially-modified Gaussian, as is expected from energy loss in the point-contact itself. See Fig 5.1d. The results of these fits are given in Table 5.3. In DS195, the source beam is entirely incident upon the point-contact, instead of being partially incident on the passivated surface. In this data set, the mean of the Gaussian component of the alpha peak falls at 5345 keV, 141 keV below the full 5.486 MeV alpha energy. The amplitude of this peak indicates a far lower alpha event rate than at nearby positions on the passivated surface. This reflects the fact that the p+ contact is partially obscured by the contact pin, but may also indicate that some alphas may not be penetrating to the active region of the contact, as discussed in Sec. 6.7.1.

All of the peak energies of the fits to the alpha energy spectra are depicted in Fig. 5.3a, and the standard deviations of the gaussian components are depicted in Fig. 5.3b. Plotting these results as a function of the magnitude of the radius, as in Fig. 5.4, the results at the positive- and negative-radii scanning positions appear to have a very small discrepancy. We believe this to be due to a small offset of the true center of the detector from the spindle position assigned to $r = 0$ mm in Sec. 4.3.1, with an additional potential contribution from the hysteresis of the source position. We consider the two sets of scans consistent with one another.

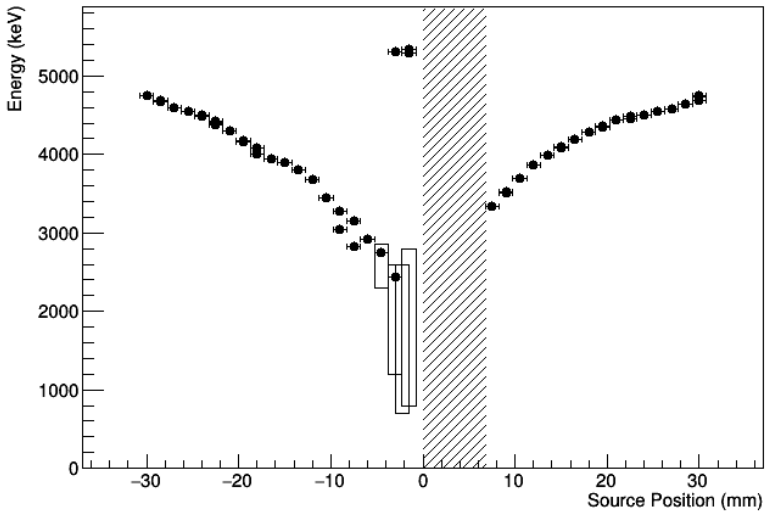

(a) The centroids of the alpha energy peaks in each data set. For scanning positions with significant low-energy tailing, the black box depicts the estimated full energy range of alpha events, as given in Table 5.2. At positions that are partially or completely incident on the point-contact, an additional peak appears at nearly the full incident alpha energy.

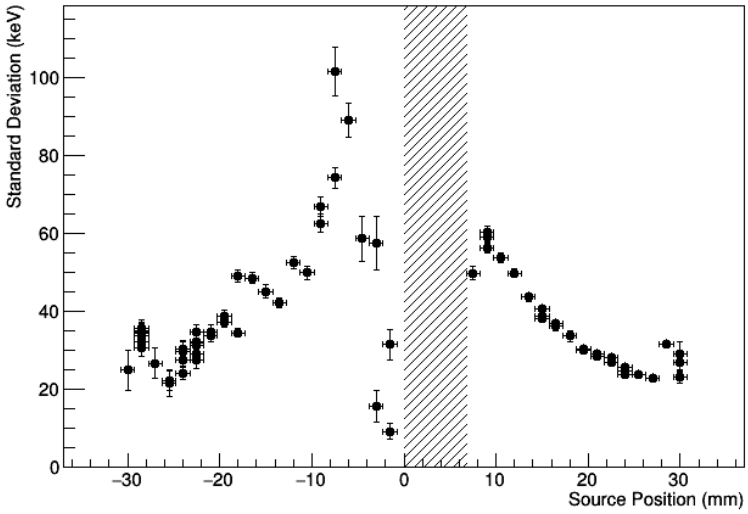

(b) The standard deviation of the gaussian component of the alpha energy peaks in each data set.

Figure 5.3: The results of Gaussian fits to the alpha energy peaks. The hashed box indicates the region on the detector surface that is obscured by the contact pin and contact pin support.

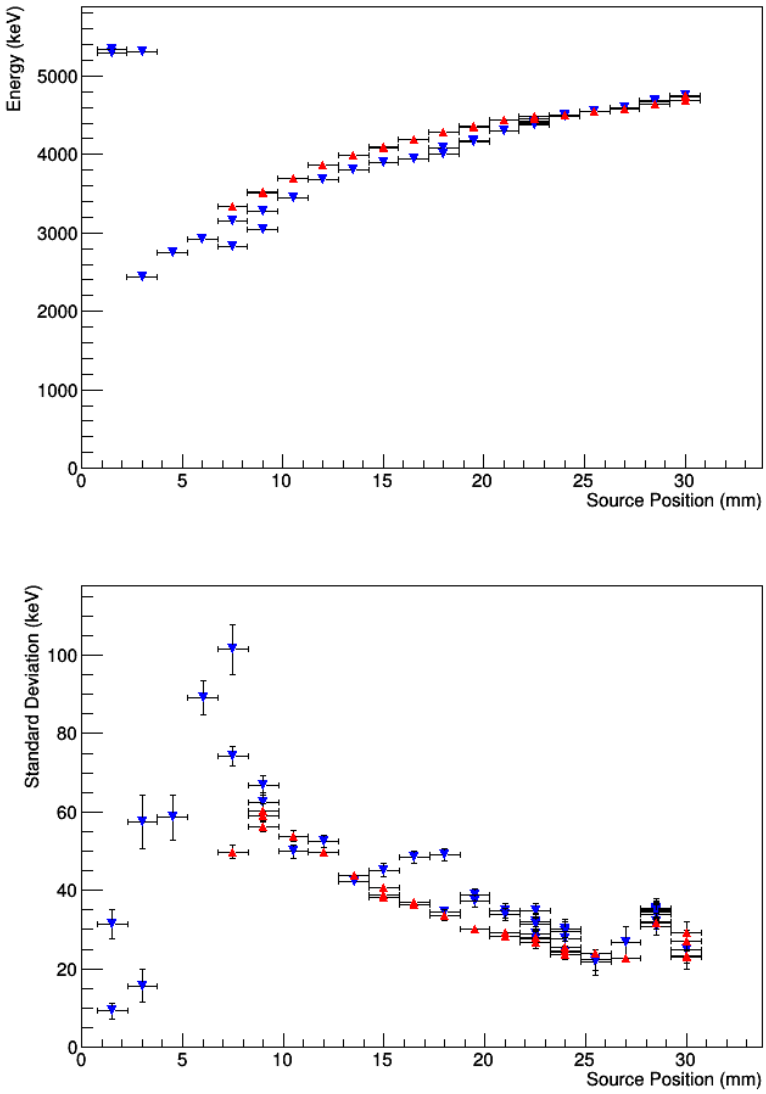

Figure 5.4: The centroids *(top)* and standard deviations *(bottom)* of the alpha energy peaks in each data set, given as a function of the radial distract from the point contact. Negative-radius source positions appear as blue downward-pointing triangles, and positive-radius positions as red upward-pointing triangles. The results of the 0° and 180° scans appear to be consistent.

5.1.2 Radial Dependence of Energy

Using the mean energies at each position found in Sec. 5.1.1, a spectral model describing the energy contributions of alpha contamination at a given position on the passivated surface can be constructed. Though it is slightly unnatural to consider the radial dependence on energy, rather than the inverse, it will simplify the derivation of a full alpha energy spectrum for a given radial contamination model (see Sec. 6.7.1). Therefore we proceed with the former approach.

Plotting the radii of the measurements in which the source was incident on the passivated surface with respect to the centroid energies found at those radii, as in Fig. 5.5, and fitting to the fourth-order polynomial

$$r = aE^4 + 1.6\,\text{mm}$$

where r is the source position radius, in mm, and E is the energy of the resulting event, we find that the fit parameter $a = (5.50 \pm .03) \times 10^{-14}\,\text{mm/keV}^{1/4}$, and the χ^2/N_{df} of the fit is 2.50. The goodness-of-fit is poor due to the discrepancy between the positive- and negative-radii scans.

The constant component is set to be 1.6 mm because this is the outer radius of the point-contact of PONaMa-1; the passivated surface energy function should not exhibit a radial dependence below this value. When the constant component is allowed to float in the fit, it fits to a value of $1.4 \pm .2$ mm, consistent with a radius of 1.6 mm. Therefore, we fix this parameter to the model-driven value.

The choice of a fourth order polynomial was an empirical choice based on the observed spectral shape, and is not driven by any theoretical model. The goodness-of-fit is not improved by the addition of a quadratic component to the fitting function. If the exponent of the energy-dependent term is allowed to float, it fits to a value of 4.2 ± 0.1, and the χ^2/N_{df} of the fit is 2.44, only slightly improved from its previous value. Therefore, for the sake of simplicity, we fix the exponent to a value of 4.

Though the energy spans of events at the lowest scanning radii (where a peak could not

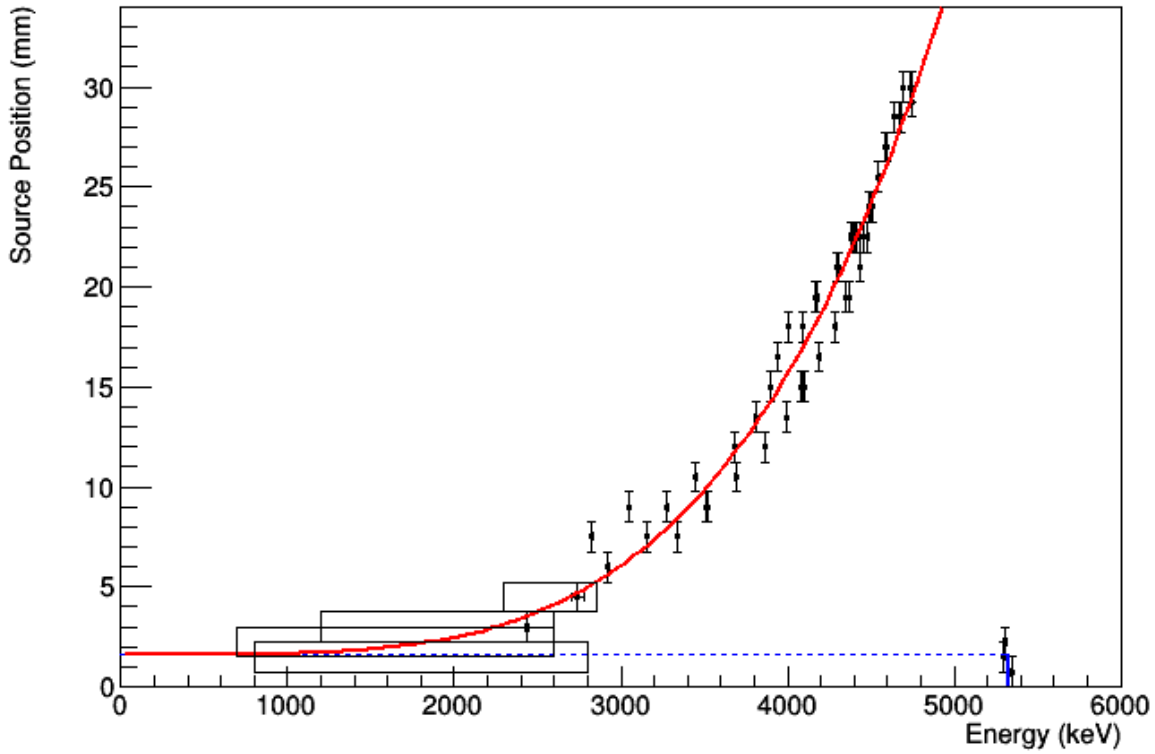

Figure 5.5: Radii of the source incidence position, plotted with respect to the energy of the resulting alpha peak. Only data sets for which a Gaussian (or Gaussian+low-energy tail) peak shape could be fit to the alpha peak are included in the radial dependence fit. The boxes represent the range of energies for the data sets that could not be fit, given in Table 5.2. The passivated-surface radii (scans with $r \geq 3\,\mathrm{mm}$), are fit with a fourth-order polynomial in energy (in red), and the energies of the point-contact positions are averaged (in blue). The discontinuity shown by the dashed line indicates the sudden transition between the behavior of the passivated surface and p+ contact.

be fit to the spectrum) were not included in the fit, their range of values roughly agrees with those given by the fitting function. The increase in the width of the energy peak at low radii found from the derived spectral shape is not as dramatic as that seen in the data; if they matched exactly, the red line in Fig. 5.5 would traverse the full length (in the energy-axis) of each box. This, and the imperfect goodness-of-fit, indicates that there is additional energy-broadening that is not captured by the derived spectral shape function. However, this simple model captures most of the relevant energy information.

To model the energies of alpha events on the point contact itself (at $r < 1.6\,\mathrm{mm}$), the mean energies of the 3 fits to the point-contact alpha peaks are averaged. Their average energy is $5323 \pm 3\,\mathrm{keV}$. The energy at these radii is assumed to be independent of radius.

5.1.3 Discussion

The energy of alpha events from the collimated source incident on the passivated surface of the detector is degraded at all radii, and is reduced far beyond the expected energy loss to a thin dead layer. Furthermore, the energy varies by up to a factor of 5 with the incident radius of the alpha interaction.

Both of these observations indicate that charge loss, whether to slow surface charge collection, charge trapping, or a combination of the two factors, is occurring. Additionally, the radial dependence of energy indicates that positive and negative charge carrier contributions are affected differently, as would be expected from their differing mobilities in germanium.

At positions near the point-contact of the detector, the relative contributions of electrons and electron-holes vary drastically over small distances. For instance, at radii less than 5 mm, the weighting potential at the passivated surface of a detector similar to PONaMa-1 (see Fig. 5.6) varies by over 15% over the diameter of the alpha source beam (1.8 mm). At radii larger than 10 mm, on the other hand, the weighting potential varies by less than 3% over the diameter of the alpha source beam. Based on this difference in the weighting potential, the observed broadening of alpha peak shape is not unexpected.

The weighting potential also allows us to infer that both positive and negative charges

must be affected by the charge loss mechanism in the detector. If only the energy of the electrons were being lost, the alpha peak energy would be reduced by at most 10% at radii larger than 13 mm. Instead, we see, in Fig. 5.3a, the energy is reduced by up to 31% of the full incident alpha energy for these radii. Overall, the energy dependence on radius is larger than the radial dependence of the weighting potential for all radii, with a difference that is particularly dramatic for large radii. If only the energy from the electron-holes were being affected, on the other hand, we would expect the energy of the alpha peak to increase dramatically at radii less than 5 mm, where a large fraction of the signal is generated by electron motion. This is also not observed; the alpha peak falls steeply in energy until the source beam is incident on the point contact itself, with peak energies below 50% of the full alpha energy.

Therefore, we must conclude that both positive and negative charges are being trapped and/or slowed for interactions near the passivated surface, regardless of the radial position of the interaction. Conclusions concerning possible charge-loss mechanisms are discussed in Sec. 5.4.

Events incident on the p-contact, on the other hand, do not show indications of significant charge-trapping. The average energy loss observed is consistent with the loss seen in scans of the point contact of BEGe-type PPC detectors [12]. In BEGe measurements, the energy loss was found to indicate a dead layer thickness of 519 ± 15 nm, larger than the manufacturer-cited Boron implantation depth of approximately 300 nm. This could indicate the presence of additional material on the surface of the point-contact or deadness extending beyond the cited boron-implantation depth.

5.2 DCR Parameter Values and Peak Shape

5.2.1 Observations

In the DCR distribution for each data set, almost all alpha events fall in a Gaussian peak. Fits to the alpha peaks in the DCR distributions are calculated for three of the parameters,

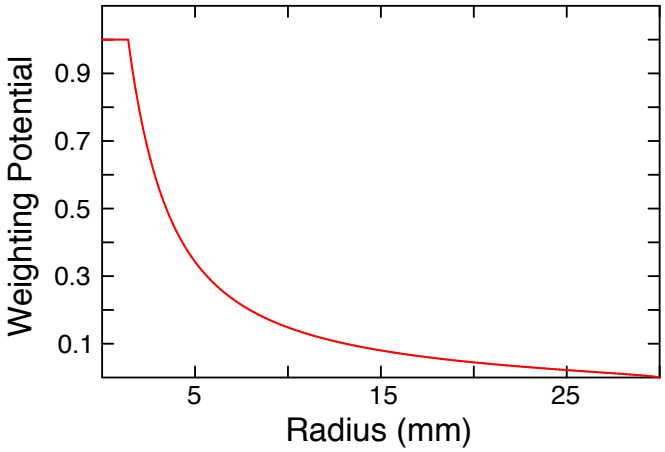

Figure 5.6: The electron weighting potential at the passivated surface of a PPC detector similar to PONaMa-1. Calculated using the `fieldgen` software package [1].

`dcr90`, `dcrpzc90`, and `dcrpzc99norm`. Deriving the results for alternate acceptance levels of the first two simply require a shift of the results, with no rescaling. The final version is provided to correct for the effects of gain shifts or changes in the pole-zero decay constant of the signal pulses, but is sensitive to changes in the noise of the system.

A full model-driven fitting function would include both a Gaussian and exponentially-modified Gaussian that accounts for the tail of low-DCR alpha events, seen in the plots of DCR vs. energy, in the fit to the peak. The background, which is the tail of the background-event Gaussian at DCR ~ 0, would be most appropriately modeled by a quadratic function. In practice, however, the fraction of events occurring in the low-DCR tail of the alpha peak is small, the relaxation constant of the tail is long, and the alpha rate is low. Therefore, when a low-DCR tail is included, it is degenerate with the background function. Similarly, the inclusion of linear and quadratic components does not improve the fit to the background events. Instead, the combination of the low-DCR tail of the signal and the low-DCR rise in

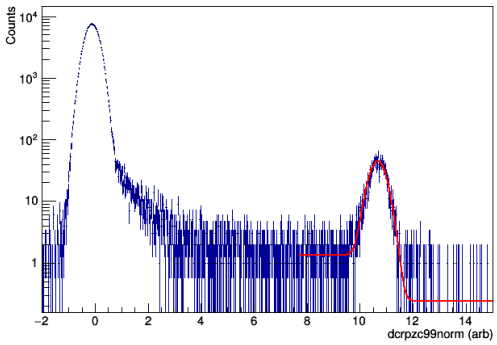

(a) The `dcrpzc99norm` distribution of a data set taken at 11 turns ($r = -13.5\,\text{mm}$), a total of 25.1 hrs of runtime.

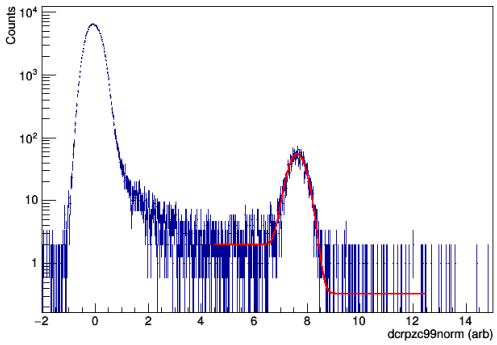

(b) The `dcrpzc99norm` distribution of a data set taken at 36 turns ($r = 24\,\text{mm}$), with 30.1 hrs of runtime.

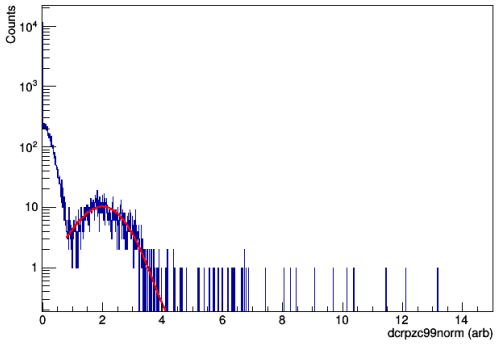

(c) The `dcrpzc99norm` distribution of a data set taken at 18.5 turns ($r = -2.25\,\text{mm}$), a total of 25.0 hrs of runtime, with a cut selecting near-point-contact events (`aenorm` > 1.5). At small radii ($|r| < 3\,\text{mm}$), the DCR parameter values for alpha events become similar to those of gamma background events.

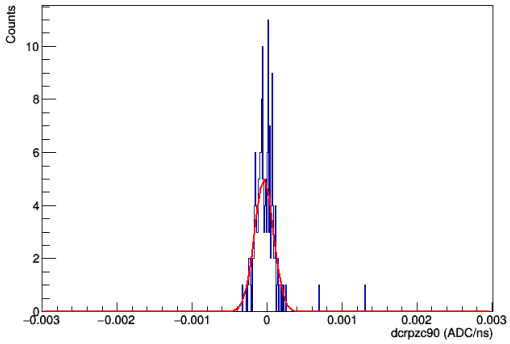

(d) The sum `dcrpzc90` distribution of all runs taken at 19.5 turns ($= -0.75\,\text{mm}$), a total of 82.4 hrs of runtime, with a cut selecting near-point-contact events (`aenorm` > 1.5) in a 5σ energy window centered at the full-energy alpha peak position. Alphas incident on the point-contact do not show elevated DCR values.

Figure 5.7: DCR parameter distributions and Gaussian fits for various peak positions. The different varieties of DCR parameters generally have similarly-shaped distributions, save for peaks near 0 in `dcrpzc99norm`, which are distorted by scaling effects. Fit results are given in Figs 5.8 and 5.9.

the background can be fit effectively by including a step function (centered at the mean of the alpha peak Gaussian) in the background function and limiting the fit window appropriately. Since the peak integral is not used for analysis, it is irrelevant that a fraction of the alpha peak is being fit with the background component of the fit. Ultimately, it is the mean value and width of the DCR peak that is of interest to us, and not the details of the peak shape.

The DCR spectra used for scans with $|r| > 3\,\text{mm}$ include all non-muon single-site events with energies between 1 and 6 MeV. For $|r| > 3\,\text{mm}$, the energies of all observed alpha events fall entirely in this range (see Table 5.2). Furthermore, the DCR value in the peak is sufficiently above the DCR distribution for normal events that the peaks can be clearly distinguished, and the high-DCR peak can be fit to a single Gaussian (see Figs 5.7a and 5.7b for examples).

For data sets with $|r| < 3\,\text{mm}$, the relevant energy range extends below 1 MeV and the DCR values approach those of gamma background events, making the alpha event peak difficult to distinguish. As in the fits to the energy spectra, a pulse shape cut selecting near-point contact (`aenorm` > 1.5) events is applied to reduce the background rate and allow a fit to the alpha events (see Fig 5.7c).

Events incident on the point contact itself do not have a distinct peak in DCR when the broad energy range of 1 to 6 MeV is used. Instead, the peak must be fit using an energy window in which the alpha events dominate the spectrum; a 5σ window around the peak energy (taken from the fits described in Sec. 5.1.1) is used. Due to the low event and background rate after these cuts are applied, the peak is fit using only a Gaussian distribution. This approach is used only for the summed data sets with $r = -0.75\,\text{mm}$, the source position at which the beam is entirely incident on the point contact (see Fig 5.7d).

All three of the DCR parameters are fit with the same procedure. The peak shapes in all three parameters are similar, save for at small radii ($|r| < 6\,\text{mm}$), where the DCR parameter values are small and pole-zero corrected DCR parameters retain better alpha separation from the gamma and muon background events than the `dcr90` value does. At very small DCR values, the `dcrpzc99norm` peak shapes are distorted by the effects of the scaling on negative

tail slope values.

Results are given in Figs. 5.8 and 5.9. It is clear, both there and in the plots of the DCR values with respect to the magnitude of the radius (Figs. 5.10 and 5.11), that unlike the energy, the DCR parameter values of the alpha peaks do not appear to be azimuthally symmetric. At positions with $|r| > 6\,\text{mm}$, the DCR values of alpha events are consistently much higher than those of background events; however, the values differ by up to a factor of 2 at the 0° and 180° scanning positions.

Additionally, the positive and negative radius positions show different qualitative behavior for $|r| > 12\,\text{mm}$. At the negative-radius positions, the DCR parameters values rise as the radius increases, and at positive-radius positions, their values fall with increasing radius.

At positions with $r \leq 12\,\text{mm}$, the 0° and 180° scans are in greater agreement, though their values of `dcr90` and `dcrpzc90` are still offset from one another, as in Fig. 5.10. Correcting for changes in the gain and noise of the system, as in 5.11, brings the values at these radii into closer agreement. In this plot, it can also be seen that the DCR's functional dependence on radius is in agreement for these near-point contact positions.

A discussion of the potential causes of the observed azimuthal dependence, along with further discussion of the DCR parameter significance, is given below.

5.2.2 DCR as an Alpha Rejection Parameter

At almost all scanning radii, alpha events incident on the passivated surface show significant slow charge components, and therefore highly elevated values of the DCR parameters. Therefore, the DCR pulse shape parameters provide a powerful tool by which external alpha events can be identified in PPC detectors.

The amount of energy being collected as slow charge in the first 20 μs of the pulse tail can be calculated directly from the `dcrpzc90` parameter and the calibration constants for the electronics system. A `dcrpzc90` value of 4×10^{-3} ADC/ns, for instance (similar to that found for many source positions), is divided by 0.74 ADC/keV, the average value of the linear term of the energy calibration curve, to give an average rate of delayed charge recovery

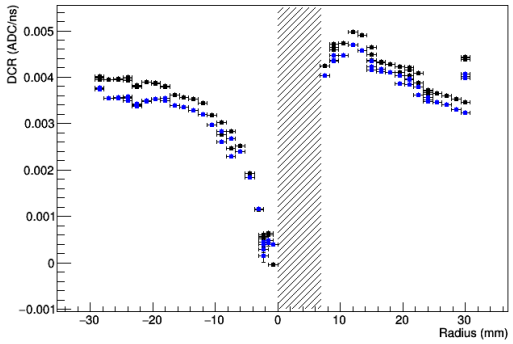

(a) The centroids of the alpha peaks in each data set.

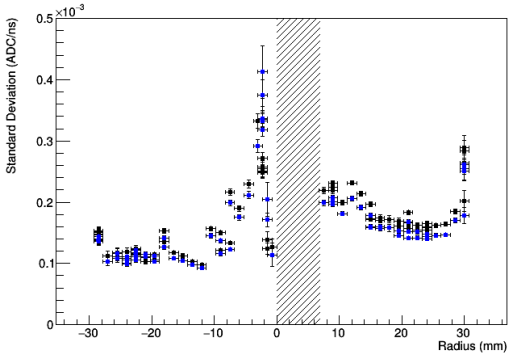

(b) The standard deviation of the alpha peaks in each data set.

Figure 5.8: The results of Gaussian fits to the alpha peaks in `dcrpzc90`, in black, and `dcr90`, in blue. All values are in units of ADC/ns. The hashed box indicates the region on the detector surface that is obscured by the contact pin and contact pin support.

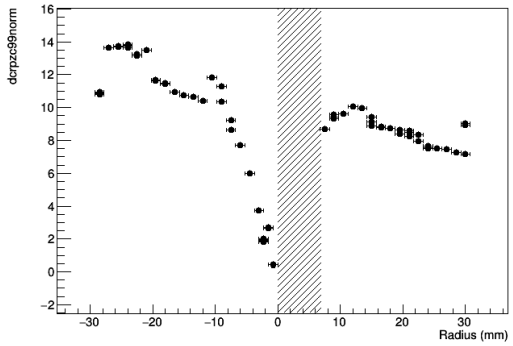

(a) The centroids of the alpha peaks in each data set.

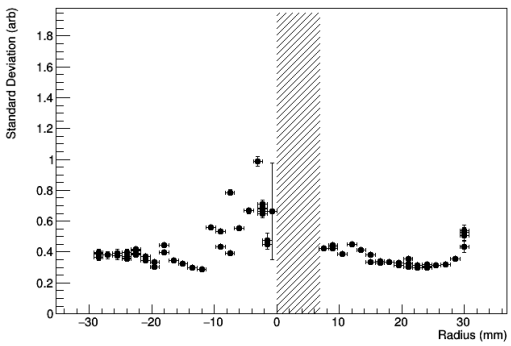

(b) The standard deviation of the alpha peaks in each data set.

Figure 5.9: The results of Gaussian fits to the alpha peaks in `dcrpzc99norm`, in arbitrary units. The hashed box indicates the region on the detector surface that is obscured by the contact pin and contact pin support.

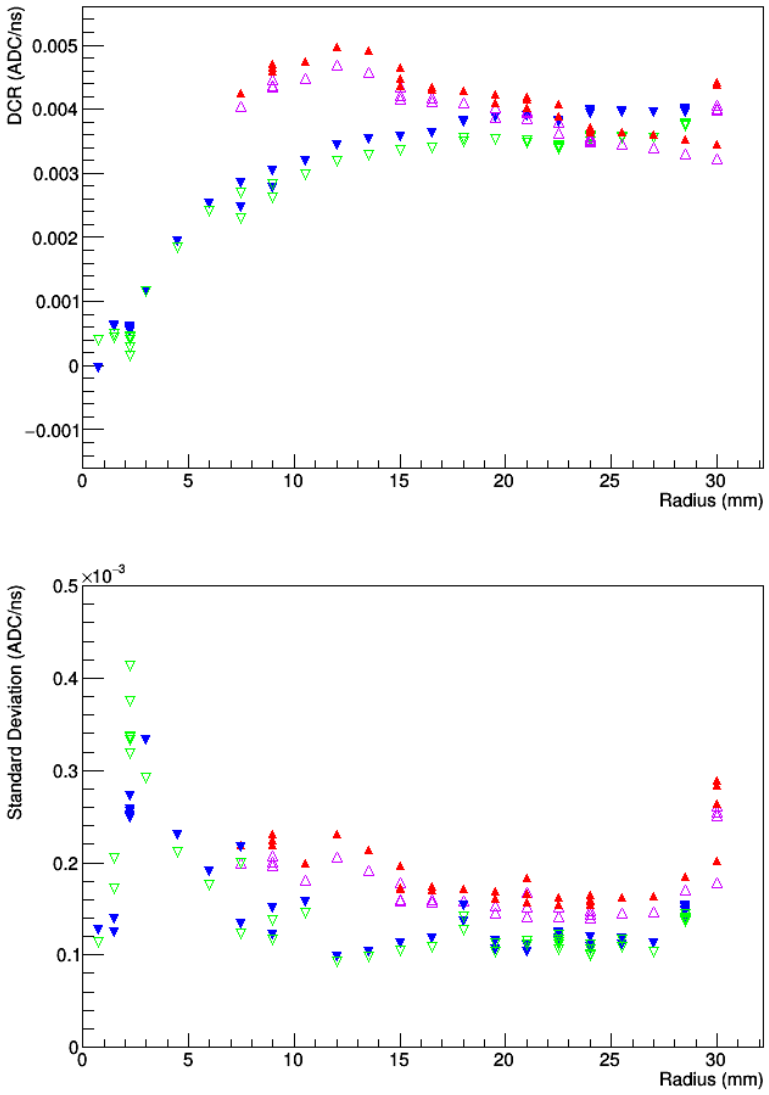

Figure 5.10: The centroids *(left)* and standard deviations *(right)* of the alpha DCR peaks in each data set, given as a function of the radial distract from the point contact. Both `dcrpzc90` and `dcr90` values are shown, in filled and open triangles, respectively. Error bars are suppressed for clarity. Negative-radius source positions appear as blue (`dcrpzc90`) or green (`dcr90`) downward-pointing triangles, and positive-radius positions as red (`dcrpzc90`) or violet (`dcr90`) upward-pointing triangles. The centroids of the 0° and 180° scans are not consistent with other another, but the peak widths appear relatively consistent. See 5.2.2 for discussion.

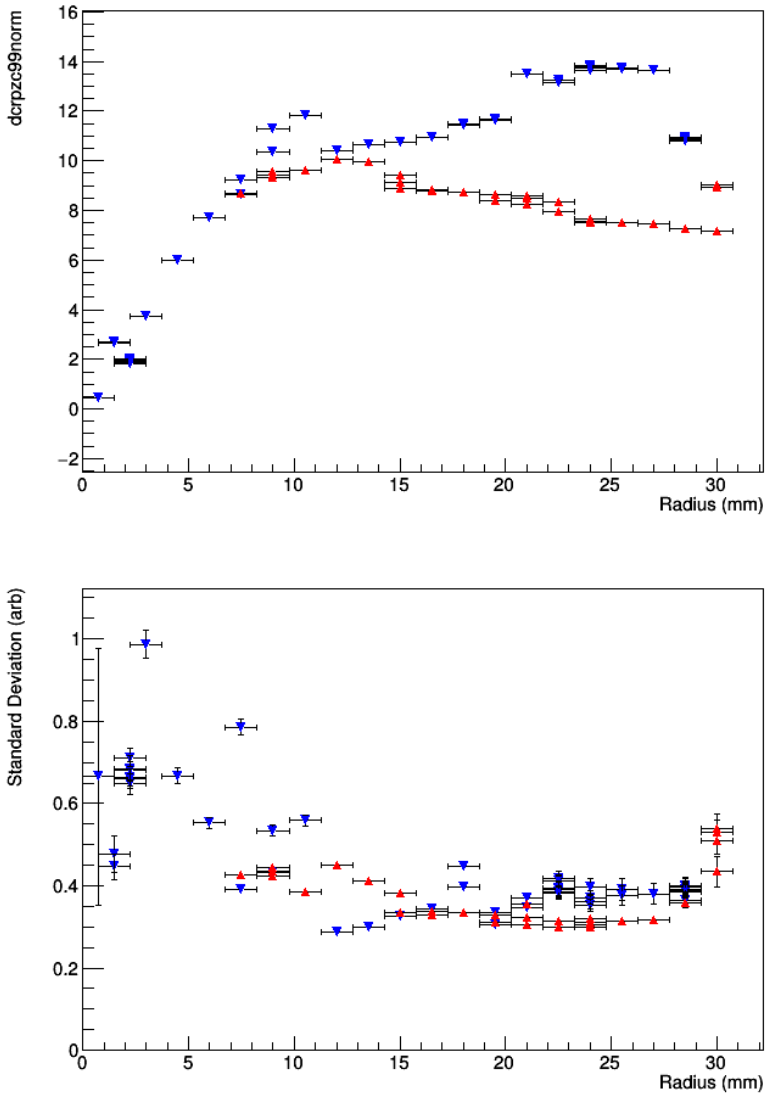

Figure 5.11: The centroids *(top)* and standard deviations *(bottom)* of the alpha `dcrpzc99norm` peaks in each data set, given as a function of the radial distract from the point contact. The centroids of the 0° and 180° scans are not consistent with other another at $r > 12\,\text{mm}$, but the peak widths appear relatively consistent. See 5.2.2 for discussion.

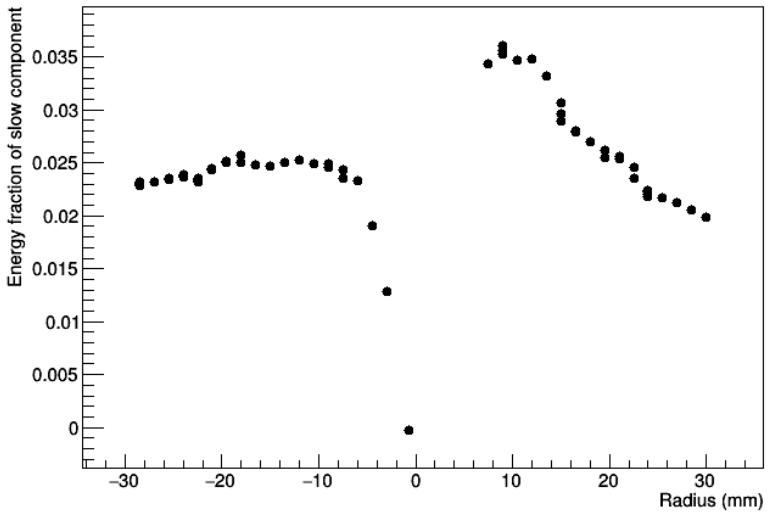

Figure 5.12: The energy of the collected delayed charge, as a fraction of the prompt alpha energy at that scanning position. The uncertainties, which correspond to the uncertainty in the DCR peak position fit, are so small as to not be visible here.

in the pulse of 5.4 keV/ns. The other terms of the calibration curve are small, and are neglected. Therefore, in the 20 μs of waveform tail that are digitized in these measurements, approximately 110 keV of energy is collected.

For each scanning position, we can find the slow component energy as a fraction of the prompt alpha peak energy at that position, as in Fig. 5.12. The delayed charge energy fraction falls quickly at small scanning radii. At radii larger than 6 mm, between 2.0% and 3.6% of the total energy is collected as delayed charge, with an average delayed fraction of 2.5%.

The alpha background events of interest to $0\nu\beta\beta$ searches like the MAJORANA DEMONSTRATOR are those with energies of over 1 MeV. Given the typical PPC detector energy resolution of less than 5 keV at these energies, a 2% delayed charge effect, corresponding to 20 keV, is easily observable. This implies that regardless of the source of the alpha back-

ground, whether or not the alpha particle is degraded in energy before reaching the passivated surface, any event that has high enough energy to be a problematic background event also demonstrates a detectable delayed charge signature, provided its point of incidence is at at a radius greater than 6 mm.

5.2.3 Outlier Events

In plots of a given alpha scan data set in the DCR vs. energy parameter space, as in Fig. 5.13, some fraction of outlier events that do not fall either in the alpha energy or DCR peak also appear. This implies that the Gaussian model of the peak position and shape (in both energy and DCR) does not fully describe all of the observed alpha events. Some events have both degraded energies and DCR values.

Significantly for our purposes, the fraction of the prompt energy that is collected as slow charge (i.e. the ratio of `dcrpzc90` in keV/ns, integrated over the duration of the waveform tail, to the energy) in these events appears to be constant, and is 2.9%, identical to that of the undegraded events. This means that, as discussed in Sec. 5.2.2, these events can still be efficiently identified in the $0\nu\beta\beta$ ROI.

The fraction of events that appear as outliers in both parameters is impossible to calculate precisely, since they become indistinguishable from background events at low energies and DCR values. Based on the numbers of events at higher-than-usual DCR values, we estimate that approxoimately 10% of events are outliers.

It is difficult to speak to the physics of these outlier events, since we do not know their origin. There are two board categories of possibilities, with different implications for our understanding of the passivated surface behavior:

- The degraded outlier events could be caused by a dead layer or shallow angle scattering in the passivated surface itself. Therefore, events such as these could be useful in understanding further aspects of charge collection from surface events, and in measuring the dead-layer associated with the passivated surface.

- The energy degradation could be occurring before the alpha particle reaches the detector surface. Though the source manufacturer cites a 20 keV expected line-width for the ^{241}Am source, that does not preclude the possibility of some small fraction of events being highly degraded in energy upon leaving the source. Another possibility is that these events are scattering in the collimator before arriving at the detector surface. In this case, these events do not reflect the behavior of the detector, and are less relevant.

Given their consistent DCR energy fraction, it seems unlikely that these events are demonstrating substantively different behavior than those in the peak. Therefore, the latter category of explanations seems more likely. Scattering in the collimator could be confirmed as the source of the outlier events with a Monte Carlo simulation of the collimator geometry.

Without knowing the origin of the outlier events, however, we cannot draw conclusions based on them. Future passivated-surface studies with the TUBE cryostat will employ source beams with shallower angles of incidence; based on the results of those studies, we should be able to determine the cause of these events and the thickness of the dead and charge-trapping regions associated with the passivated surface.

5.2.4 Radial Dependence of DCR

The azimuthal dependence (or, we believe, the instability, see below) of the DCR parameters makes it difficult to draw definitive conclusions about their radial dependence. This is particularly the case at large radii ($|r| > 12$ mm). In positive-radius scanning positions, `dcrpzc90` falls with increasing radius, at a rate of $(-4.8 \pm 1.2) \times 10^{-5}$ ADC/ns/mm, found using a linear fit to all data sets in this position range. In negative-radius scanning positions, `dcrpzc90` instead rises with increasing radius, at a rate of $(2.8 \pm 0.3) \times 10^{-5}$ ADC/ns/mm.

Compared to this, the radial dependence of the DCR parameters at positions with $|r| < 12$ mm is dramatic, and occurs with similar functional form in both the positive- and negative-radius scans, as seen in Figs. 5.10 and 5.11. Unfortunately, the source beam is obstructed at small positive-radii positions, so the similarity of the results cannot be tested directly for

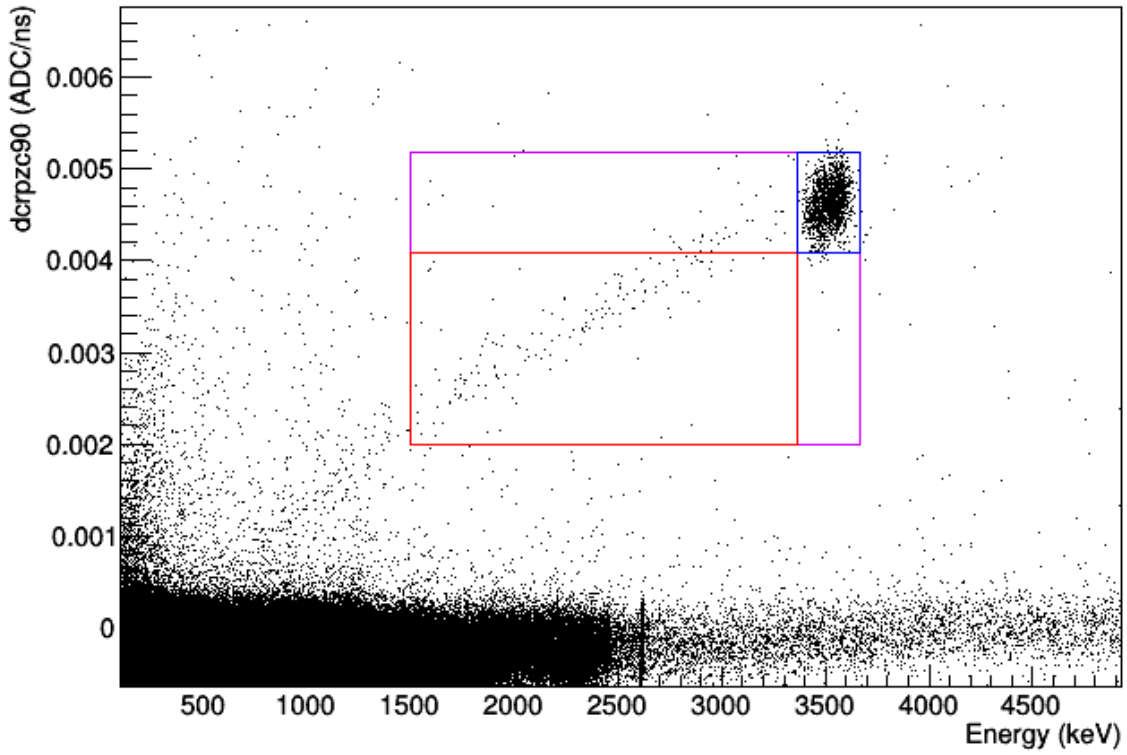

Figure 5.13: A plot of all single-site events in a data set taken at $r = 9\,\text{mm}$, in `dcrpzc90` vs. energy. The blue box shows the region that lies within 5σ of the energy and DCR peaks, and the red box indicates some of the events that are outliers from both peaks. Events that are in the violet box but not in the red or blue boxes are outliers in either the energy or DCR peaks. The red-outlined region shows a clear excess of events over a source-free data set. 8.2% of the events in the violet box (including the red and blue-boxed regions) are outliers from both peaks; 89.2% fall within the 5σ windows of both the energy and DCR peaks.

all radii.

Over the range that can be scanned, though, the positive-radius positions show an increase in `dcrpzc90` with increasing radius with a rate of $(1.4 \pm 0.3) \times 10^{-4}$ ADC/ns/mm, and the negative-radius positions show an increase with a rate of $(3.2 \pm 0.2) \times 10^{-4}$ ADC/ns/mm. If, instead of using all negative-radius data sets, we use only those for which a positive-radius equivalent exists, we derive a rate of change for the `dcrpzc90` value of $(1.8 \pm 0.4) \times 10^{-4}$ ADC/ns/mm, which agrees with the rate found at positive-radius positions to within the uncertainty of the fit.

Most significantly, we find that at incidence positions very close to the point-contact ($|r| < 6$ mm), the DCR parameters cannot be used to reliably identify alpha events while retaining high bulk-event efficiency. Alphas incident on the point-contact itself are completely indistinguishable by their DCR parameters. In these types of events, the A/E or drift time of the signal can be used to maintain the alpha rejection efficiency, as discussed in Sec. 5.3.2.

5.2.5 Stability of the DCR Value

The apparent azimuthal dependence of the DCR value is thought to be a problem of instability in the process by which delayed charge is collected.

The leading candidate for the cause of the shift in the DCR parameters is charging of the detector surface by the alpha particles themselves and the resulting interactions in the detector surface. Passivated surface charge build-up over time has been observed in other PPC detectors [61], and our own measurements of the observed energy indicate that significant charge is being lost on or near the surface.

In studies of the stability, data sets with $|r| < 12$ mm are excluded. Based on the observations of the radial dependence of DCR (above) and the DCR value over time (as in Fig. 5.14, it appears that at these positions, changes in the DCR value are dominated by the radial effects in the detector, and are unaffected by the azimuthal effect or instability, whatever its source.

Plotting `dcrpzc90` in each data set with respect to the data set order (which corresponds,

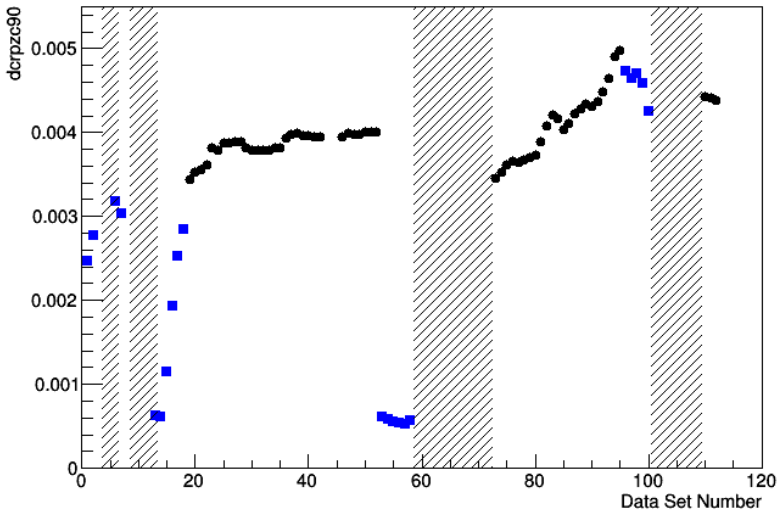

Figure 5.14: The `dcrpzc90` mean value of the alpha peak, as a function of data set order. One data set corresponds, almost exactly, to one day of run time. The hashed boxes indicates stretches of time during which the alpha source was not incident on the detector surface. The color scale indicates the alpha event rate, in events/hr. Results from scanning positions with $|r| > 12\,\text{mm}$ are shown as black circles, with results from those with $|r| < 12\,\text{mm}$ displayed as blue squares.

almost exactly, to days of run time), as in Fig. 5.15, shows a pattern in which the DCR parameter values rise over the time during which the source is incident on the passivated surface, "resetting" to lower values after the source beam is removed from the surface for some time. Furthermore, the rate at which the DCR value increases appears to be correlated with the observed alpha rate, as would be expected if surface charge build-up were the cause of the change.

Additional evidence for this theory is provided by the changes in DCR values in the positions that were repeated non-consecutively, with several days of scanning at other positions occurring between the two scans at that location. This was done for 5 positions, at r = -15,

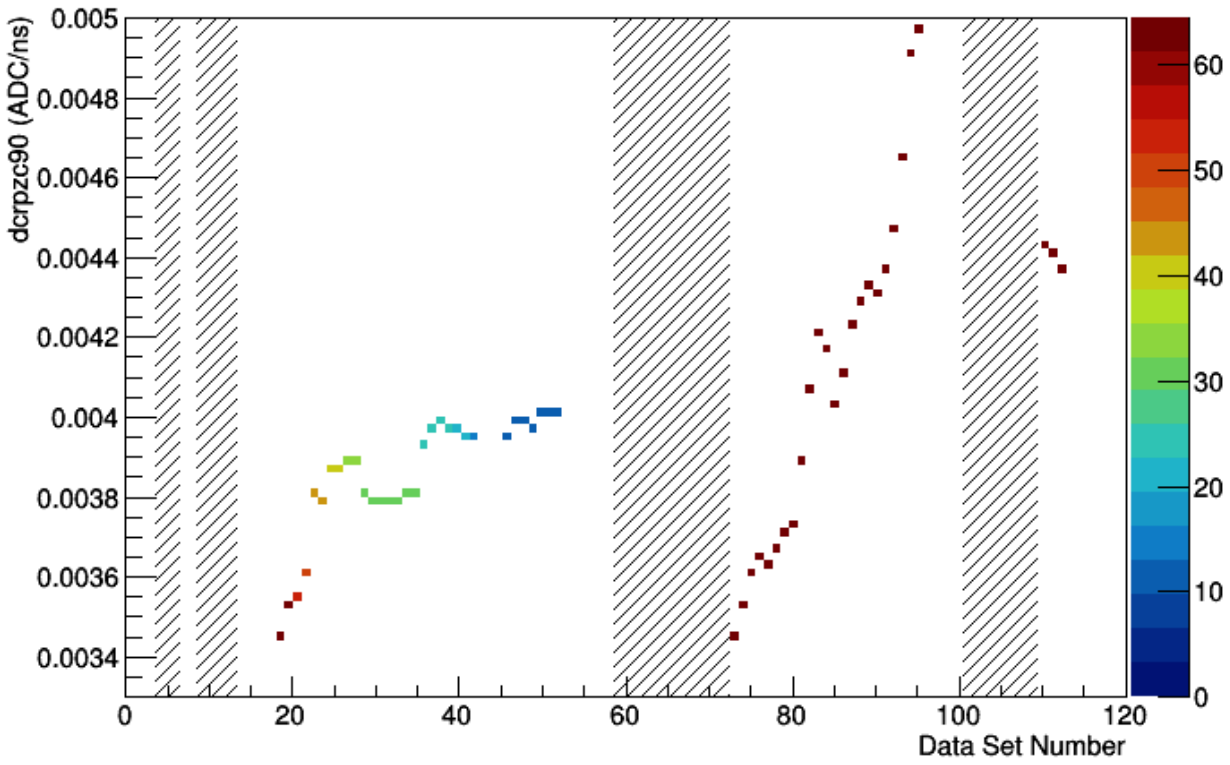

Figure 5.15: The `dcrpzc90` mean value of the alpha peak, as a function of data set order. One data set corresponds, almost exactly, to one day of run time. The hashed boxes indicates stretches of time during which the alpha source was not incident on the detector surface. The color scale indicates the alpha event rate, in events/hr.

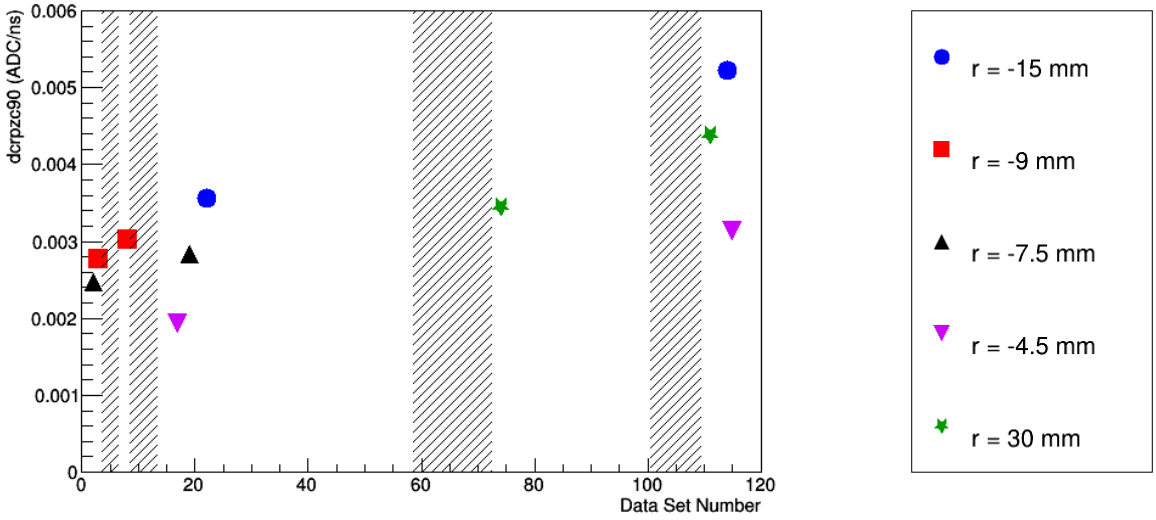

Figure 5.16: The `dcrpzc90` mean value of the alpha peak as a function of data set order for the non-consecutively repeated measurements. The point shape and color indicate the position of the source, as given by the legend. The hashed boxes indicates stretches of time during which the alpha source was not incident on the detector surface.

-9, -7.5, -4.5, and 30 mm. In all three cases, shown in Fig. 5.16, the second measurement shows a higher DCR value than the first measurement.

In spite of the observed instability, the DCR value at smallest re-measured radius ($r = -4.5$ mm) remains smaller than those of the larger-radius positions scanned soon before and after it. This is a good indication that there is radial variation in DCR along with the variation over time.

There are two leading candidate theories as to the cause of the long-term DCR instability, which can be distinguished from one another by a series of planned studies (see Sec. 7.3).

One theory is that the rising DCR values reflect the filling of deep trapping centers in the region of the crystal near the passivated surface. As the surface is bombarded with charge, the deepest potential-well sites will begin to fill and remain filled, leaving only shallower

traps available for charges trapped in later measurements. Charges are released from these shallow traps more easily and quickly, leading to higher values of DCR. This behavior would depend on the detector temperature, with operation at warmer temperatures leading to less DCR instability. Additionally, temperature cycling the detector would reset the DCR at each position to its original value.

Another theory is that the charge lost in the alpha events, particularly the electrons, are creating charged surface channels on the passivated surface layer or even damaging the passivation itself. If this is the case, the direction of scanning (whether one scans from large- to small-magnitude radii, or the reverse) could have an effect on the instability observed. This would also lead to a rise in the detector's leakage current over time, particularly if the surface were being damaged.

Regardless of the cause of the DCR instability, the effect is not relevant for low-background operation of P-PC detectors. In experiments like the MAJORANA DEMONSTRATOR, the alpha event rate per detector is at least 6 orders of magnitude smaller than the rate in the TUBE scans. Therefore, the effects of charge build-up are negligible, as has also been shown in the case of gamma-induced charging of the passivated surface [61].

5.3 A/E and DCR: Complementary Pulse-Shape Discriminators

5.3.1 A/E of Surface Alpha Events

As expected from the calculated drift paths of PPC detectors, the rate of the initial rise of pulses strongly depends on the event incidence radius, particularly near the passivated surface. The high-A/E peak of events associated with the alpha source was fit using a Gaussian function, and its centroid μ_{AE} was taken as the characteristic A/E value of the scanning location. Since the precise peak shapes of the A/E distributions are not of interest for this work, we use a simple fitting model, with only a Gaussian component to identify the peak centroid and width.

For runs in which the energy of the alpha peak is well over 2630 keV ($|r| > 7.5$ mm),

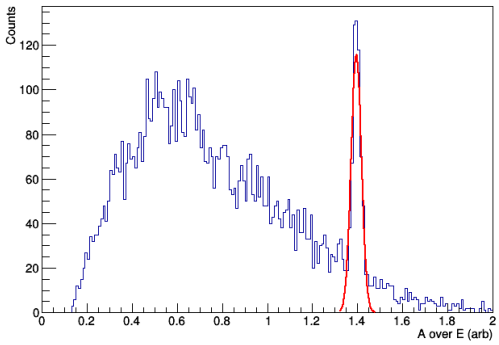

(a) A data set taken at 1 turn ($r = -28.5\,\text{mm}$), a total of 24.9 hrs of runtime, with a cut selecting events with energy between 2630 keV and 6 MeV.

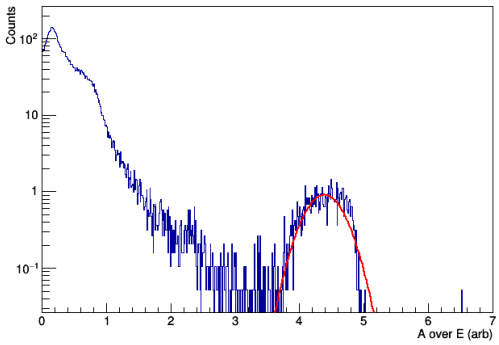

(b) A data set taken at 17 turns ($r = -4.5\,\text{mm}$), a total of 19.1 hrs of runtime, with a cut selecting events with energy between 1 MeV and 6 MeV.

Figure 5.17: Sample A/E distributions and rough Gaussian peak fits to alpha events.

only events with energies between 2630 keV and 6 MeV are included. For data sets with $|r| < 7.5\,\text{mm}$, where all or some of the alpha peak may fall outside this energy window, events with energies between 1 and 6 MeV are included. See Fig. 5.17 for sample A/E distributions and fits.

For most data sets, the peak in A/E is approximately Gaussian in shape. As in the case of energy, the peak becomes non-Gaussian at small radii, where the variation with radius of the drift time of charges becomes large over the diameter of the source beam. At these small radii, however, the A/E values are well above those of 99% of background events in the bulk.

Anomalously low values of A/E occur for events incident on the point-contact itself, as seen in Fig. 5.18. Though these events have very fast rising edges, they also have a substantial slow electron fraction, which reduces the A/E value. To correctly identify events like these from the shape of their rising edge, a drift-time parameter, measuring time over which the pulse rises from the start of the prompt signal to a given fraction of its total amplitude

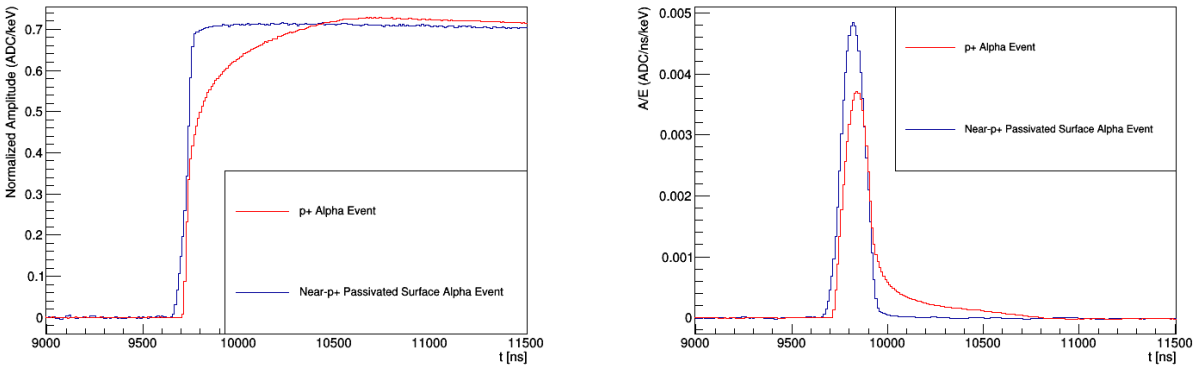

Figure 5.18: Sample waveforms *(left)* and current traces *(right)* for a p+ alpha event with energy of 5336 keV, in red, and a near-p+ passivated surface alpha event with energy of 2639 keV, in blue. The waveforms and currents are both normalized by the event energy. Note that the slow electron contribution of the p+ event (seen in the slow turnover at the end of the drift) leads to an anomalously low current maximum, despite the fast initial drift speed.

(for instance, 50% of the maximum pulse height), would be more appropriate than the A/E parameter used in this analysis. The MAJORANA Collaboration plans to implement such a drift-time-based pulse-shape discriminator, in addition to the `avse` parameter that is currently used to reject multi-site events.

The fit results are displayed in Fig. 5.19. These results indicate that the high-A/E cut applied to find energy and DCR fit results, as in Sec. 5.1.1, is appropriate.

5.3.2 Demonstrating Complementarity of High-A/E and DCR Cuts

The distributions of alpha events incident at various radii in the A/E vs. DCR parameter space (see Fig. 5.20) suggest that the two pulse-shape analyses are highly complementary. This implies that by using both the A/E (or drift time) and DCR pulse shape discriminators, we should be able to achieve excellent alpha event discrimination with only minimal sacrifice

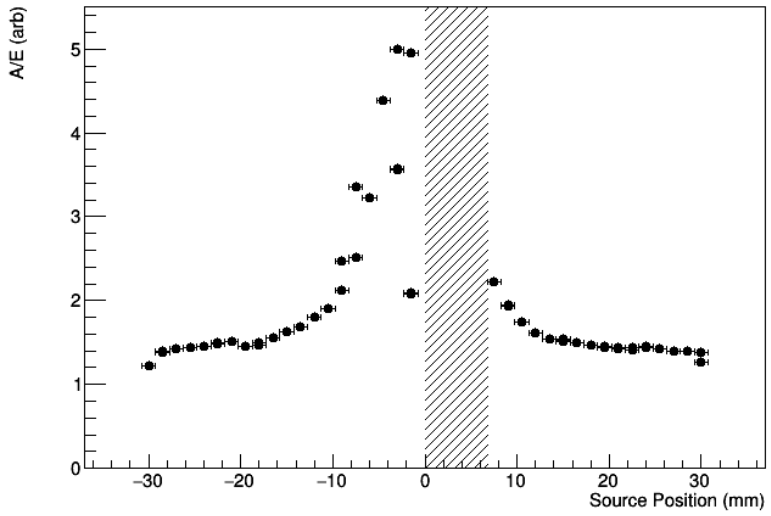

Figure 5.19: The centroids of the alpha peaks in A/E in each data set. The relatively low value of A/E for data sets with $r = -0.75\,\text{mm}$ occurs because the large (relatively slow) electron component of the signal reduces the A/E value for these events.

of bulk events.

Examining the fit results to the DCR and A/E peaks supports this conclusion. The 5σ windows around each alpha peak should include 99% of the events, assuming normally distributed values; by using an equivalent normalization for the A/E and DCR values, we can compare them directly, as in Fig. 5.21. The y-axis in this figure indicates the alpha events' separation from bulk events– 99% of bulk events fall below 1, whether the relevant discrimination parameter is A/E or DCR. Also indicated are the 99.9% acceptance points in each parameter, which occur at different values for A/E and DCR, indicating that the DCR distribution is more heavily-tailed than the A/E distribution.

For each position measured, we find that either or both of the DCR and A/E discriminator parameters are well above the 99.9% acceptance line for that parameter. This indicates that by applying 99.9% bulk-acceptance cuts in both parameters, we can effectively identify alpha

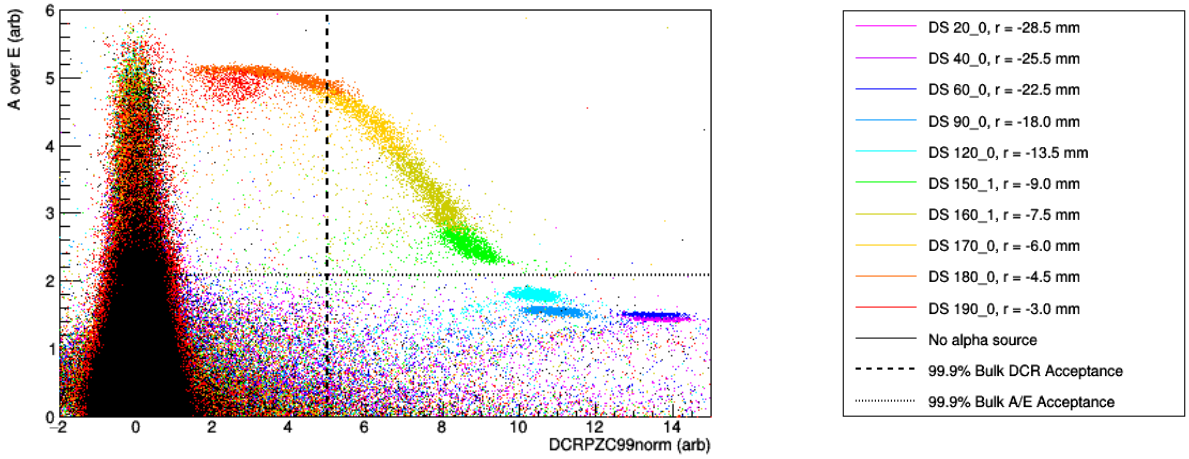

Figure 5.20: The A/E vs. normalized DCR distribution for all single-site events with energies between 100 keV and 10 MeV, at various scanning radii. The points in black are from a data set without the alpha source incident on the detector surface, and the scan data sets are shown in rainbow order, with red representing the smallest-radius scan. 99% of calibration events with energies between 1000 and 2630 keV fall below an A/E value of 1, and 99% of calibration events with energies between 1000 and 2380 keV fall below a `dcrpzc99norm` value of 1.

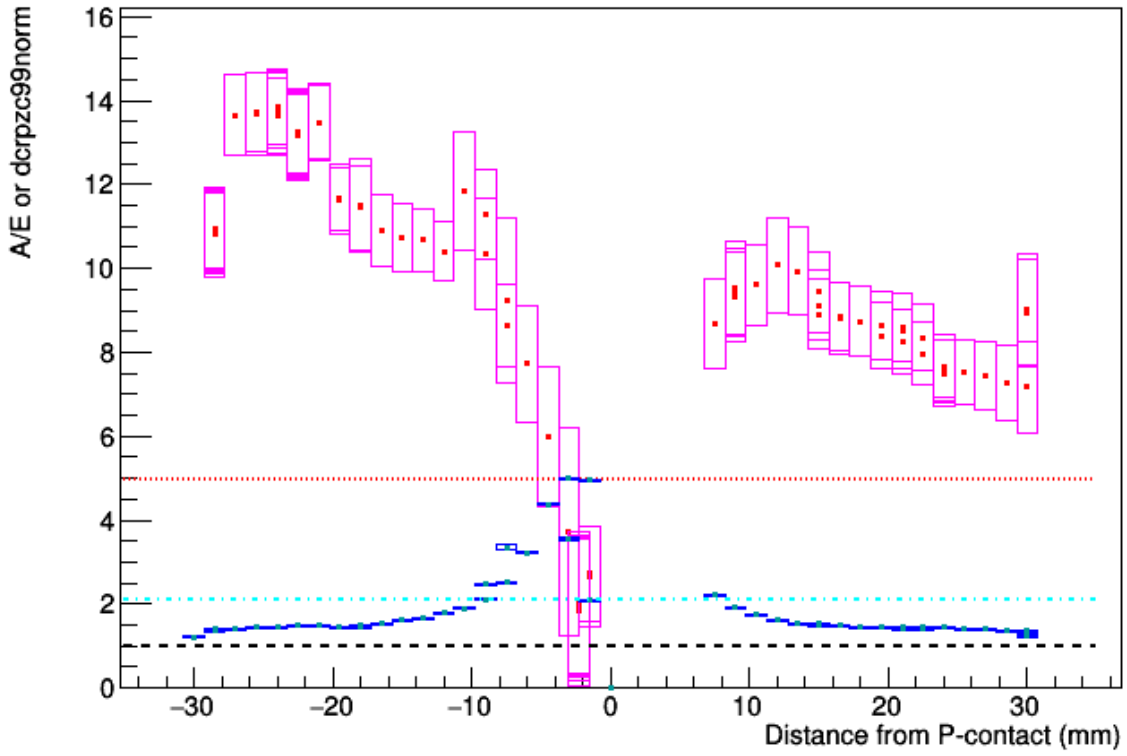

Figure 5.21: The 5σ window containing the A/E and DCR alpha peak positions at each position, normalized to 99% bulk acceptance of both cuts. The red points and magenta boxes indicate the centroids and $\pm 2.5\sigma$ values of the peaks in `dcrpzc99norm`, and the green points and blue boxes indicate the same in `aenorm`. The red dotted line and cyan dotted-dashed line are the 99.9% acceptance points in DCR and A/E, respectively. The black dashed line indicates the 99% acceptance point in both parameters.

events occurring anywhere on the passivated surface. Ergo, total or nearly-total rejection of ^{210}Po alpha events that reach the passivated surface with the full energy of the decay should be possible in PPC detectors with only 0.2% sacrifice of bulk events.

Another advantage of this method of alpha removal is that it is equally effective at all energies of the alpha events, save for the requirement that the energy of the event be high enough that the DCR signal (of approximately 2-3% of the prompt event energy, see above) is detectable (i.e. above the DCR cut threshold). In a low-noise high-resolution environment like the DEMONSTRATOR, this should be the case for all events that could fall in the $0\nu\beta\beta$ ROI when using the 99.9%-bulk acceptance DCR cut. In the TUBE measurements, which have higher noise and poorer resolution, the most degraded events would be retained by such a cut, but removed by a slightly higher-sacrifice cut, with 99% bulk-acceptance. See the outlier events of Fig. 5.20.

Therefore, this purely pulse-shape-based method is as effective for energy-degraded alpha events as it is for undegraded events originating from alpha contamination on the surface itself, assuming that the DCR cut has been set to the appropriate sacrifice level for the system. Waveform simulations incorporating the DCR effect and noise should allow us to directly probe the impact of noise at different frequencies, and, as discussed in Sec. 3.4.2, improvements are planned that would make the DCR parameter less sensitive to noise.

The only exception to this highly efficient alpha event removal occurs for events directly incident on the point-contact itself, at the smallest-radius position. Given that these events do not experience charge trapping, their energies are much higher than that of the $0\nu\beta\beta$ region-of-interest, so they are not a particularly problematic background. If alpha energy is degraded before reaching the point-contact, though, they could have any energy below the full energy of the alpha peak. As discussed above, these events would be effectively tagged with high efficiency if a drift-time parameter were substituted for the A/E parameter, as is planned in the MAJORANA DEMONSTRATOR analysis.

Fig. 5.21 also shows that at positions with $|r| \leq 6\,\text{mm}$, the A/E-based rejection of alpha events dominates in effectiveness, and that for $|r| \leq 9\,\text{mm}$, an 99.9%-acceptance cut in

A/E suffices to tag all alpha events. This is why the previous study of alpha backgrounds in a PPC detector [12], found no need for an additional pulse-shape discriminator beyond A/E. BEGe-type detectors, like the one measured in that work, have the entirety of their passivated surface lying within $|r| = 10\,\text{mm}$, so the use of the DCR discriminator would not measurably improve their background rejection capabilities.

The DCR discriminator is needed, though, in ORTEC-type detectors, which have a passivated surface along the entire bottom plane of the detector. In this detector design, which is that of the detector measured in this work, and used for all of the MAJORANA DEMONSTRATOR's enriched detectors, the DCR discriminator is a powerful way to reject alpha events occurring far from the point-contact, where A/E is relatively insensitive.

5.3.3 Alpha-Identification Efficiency using DCR Techniques

Given that the DCR pulse-shape discrimination technique is less effective than the A/E technique at $|r| \leq 6\,\text{mm}$, we focus our attention on evaluating the alpha-rejection efficiency of the various DCR parameters at scanning positions with $|r| > 6\,\text{mm}$.

To calculate an alpha rejection fraction, we must first find the predicted number of background events in the alpha peak region of the data set, with no DCR cut applied. We use both the right-hand sideband in the data set and the spectral shape in the sideband and peak regions, measured in a source-free run, to find the expected number of background events. The calculation of the efficiency and the associated statistical uncertainty proceeds as described in App. A.

At positions with radii below 6 mm for which the source is incident on the passivated surface, the alpha peak appears in a region of the energy spectrum that is dominated by gamma background events from environmental radioactivity and the materials of the cryostat itself. The alpha event rate is low, and these backgrounds are both high and highly variable. An additional complication comes from the broad energy distribution of the alpha events at these positions, as discussed in Sec. 5.1.1; to find an expected alpha event rate, we must understand the spectral shape over the entire range of relevant energies with high accuracy.

This implies that our approach of normalizing the background spectra to one another is of limited utility. The resulting uncertainties from the estimate of the backgrounds dominate our expected alpha event rate. Without an accurate calculation of the expected number of alpha events, we cannot accurately cite a rejection fraction for the events. Therefore, measurements at these radii are not included in the average efficiency values for each DCR parameter.

Events incident on the point-contact itself are not expected to exhibit slow charge release, and are therefore expected to be relatively unaffected by the DCR cut. Data sets with the source beam incident on the point-contact are therefore also excluded from the average efficiency calculations.

The rejection efficiencies are calculated for each data set using the `dcr90`, `mjddcr90`, and `dcrpzc90`, and `dcrpzc99norm` parameters. The first three of these are set to retain 90% of single-site calibration events, and the final cut is set to retain 99% of calibration events. The results for each data set are shown in Fig. 5.22, and the average rejection efficiency values for each parameter are given in Table 5.4.

The errors for the efficiency of each data set are large, due to the low alpha rate. They are particularly large at positions with large-magnitude negative radii, where the source beam is partially obscured. The calculation of the efficiency involves background subtraction, which results in fluctuations and uncertainties extending above 1.

Averaging the efficiency at all scanning positions, however, reduces the error sufficiently to show that the rejection efficiencies of the various DCR parameters, save for `dcrpzc99norm`, are consistent with 99%. This implies that 1% of alpha events with the full expected energy (indicating that significant charge trapping has occurred) are not measurably re-releasing that charge on the time scale of digitization. The higher average efficiency of the normalized DCR parameter (`dcrpzc99norm`), which is consistent with 100%, suggests that the culprit may be varying noise in the system, which is corrected for by the use of this parameter. This is unsurprising, given the high noise (and particularly the high and varying levels of microphonic noise, due to the vacuum pump operation) in the TUBE scanning setup.

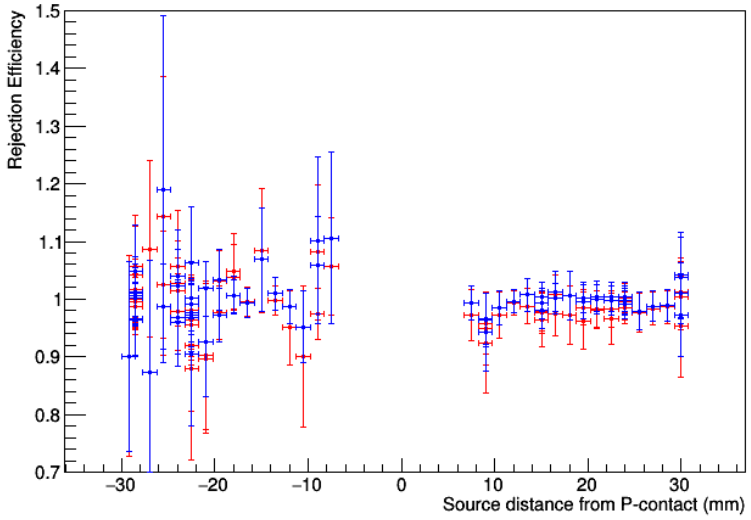

(a) The DCR parameters that employ event-by-event pole-zero correction. Values for `dcrpzc90` are in red, and those for `dcrpzc99norm` are in blue.

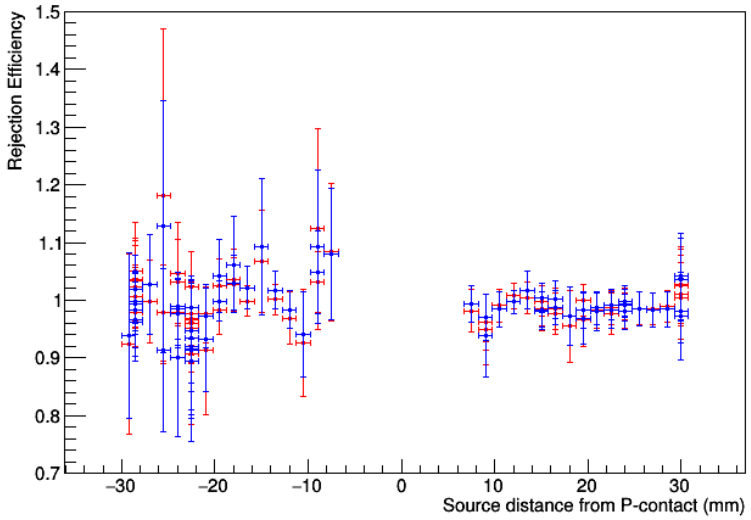

(b) The DCR parameters that employ the linear projection method of pole-zero correction. Values for `dcr90` are in red, and those for `mjddcr90` are in blue.

Figure 5.22: The alpha rejection efficiency of each DCR parameter, calculated for each data set with a source beam incidence position with $r > 6\,\mathrm{mm}$.

DCR Param.	ε (%), $\lvert r\rvert > 6\,\text{mm}$
`dcr90`	99.2±0.5
`dcrpzc90`	98.9±0.5
`mjddcr90`	99.1±0.5
`dcrpzc99norm`	99.7±0.4

Table 5.4: Average alpha rejection efficiencies for all evaluated DCR parameters.

Given that the noise in the MAJORANA DEMONSTRATOR is lower than in the TUBE system, and that the resolution is better, the DCR alpha rejection efficiency is expected to be over 99%.

5.4 Comparison to Models of Surface-Charge Collection

5.4.1 Surface Drift of Electrons

The original theoretical model for the DCR effect posited that slow surface-drift of electrons was responsible for the slow charge component, with holes being collected normally through the bulk, as described in Sec. 3.1. Charge transport models in germanium [57] suggest that charge carrier mobilities are 10 to 100 times slower for surface transport than for bulk transport. Given the overall lower mobility of electrons, and the lower weighting potential they experience over much of the detector surface (as in Fig. 5.6), we would expect that electrons would be much more susceptible to surface transport than electron holes.

This effect can be modeled using the `fieldgen` and `siggen` software packages [1] by generating the fields in the detector with the addition of a small amount of charge deposited on the passivated surface. This creates drift paths that run perpendicular to the passivated surface in a narrow region near the surface. Events that occur in this skin depth, like alpha interactions, will have degraded energies and a DCR contribution (see Fig. 5.23a). Electrons

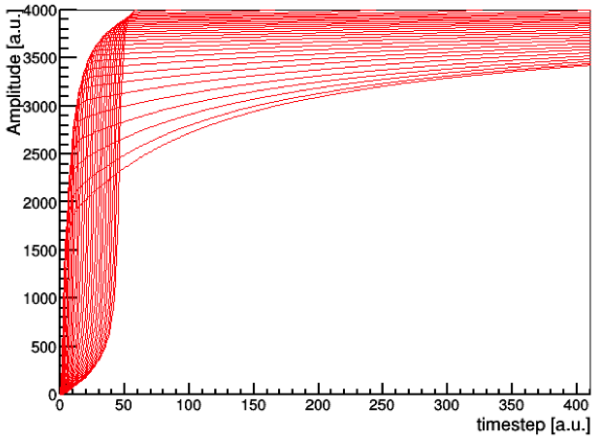

(a) Simulated waveforms for the case of surface drift of electrons. The electron drift speed is set to 2% of the bulk drift speed.

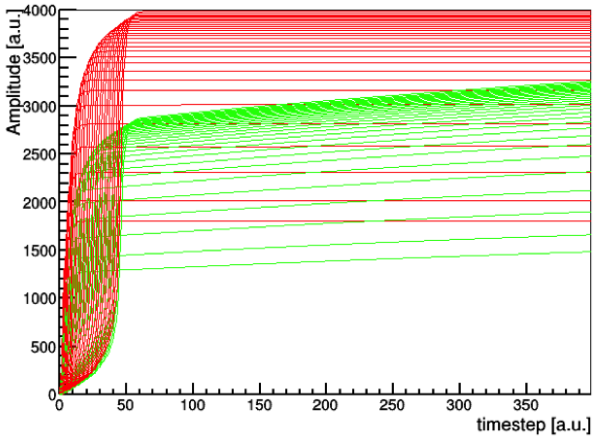

(b) Simulated waveforms for the case of electron loss and hole trapping. The waveforms in red show how the signal would appear with no hole trapping, and only the electron component missing. The waveforms in green show the result of convolving the red waveforms with a delta function and exponential decay (with $\tau = 10\,\mu$s) to emulate the effect of partial hole-trapping and subsequent diffusion into the bulk.

Figure 5.23: Simulated waveforms under each of the two DCR models. In both cases, the lower-amplitude waveforms correspond to smaller alpha incidence radii. Simulations were created using `siggen`, and are courtesy of Susanne Mertens.

that reach the surface are assigned a slower drift speed, in this case a factor of 2% of the bulk drift speed.

The radial dependence of energy, in this case, mimics the inverse of the electron weighting potential exactly, since the fraction of the signal carried by the electrons is missing at all radii (see Fig. 5.24a). Because the electron component of the pulse shape (which is the origin of the DCR signal, in this case) increases in strength at small radii, we would expect that the DCR effect would be particularly large at radii very near to the point-contact radius. In general, it would be expected to decrease with increasing radius, as in Fig. 5.24c.

Given the observed radial dependence of energy and DCR, this model is not confirmed by the TUBE measurements. The values of DCR increase with increasing radius, instead of decreasing as this model predicts. Though the change in energy with radius has the correct qualitative behavior, the observed variation is larger and steeper (as a function of radius) than this model predicts. Though slow surface drift of electrons may be occurring, it is not the dominant effect observed.

5.4.2 Passivated-Surface Trapping of Holes

In response to the TUBE data's conflicts with the electron surface drift model, an alternative model was developed. In this model, the collection of the electron-holes is also impeded by the passivated surface layer effects. If there is a high concentration of bulk trapping centers in a thin layer near the passivated surface, as suggested by the direct measurements of trapping made in segmented germanium detectors [9], then some fraction of the electron-holes will be trapped in the bulk of the detector. Slow rerelease of these charges would lead to a DCR effect, in addition to the prompt signal from untrapped electron-holes. The rate of this rerelease would be temperature-dependent. Additionally, the electron fraction is completely or almost completely lost to trapping or slow surface transport in this model, which as in the surface-electron model, is likely given electrons' lower mobility.

Again, we model the resulting radial dependence of energy and the DCR parameter using `siggen`. The electron contribution to the signal is completely turned off (assigned a drift

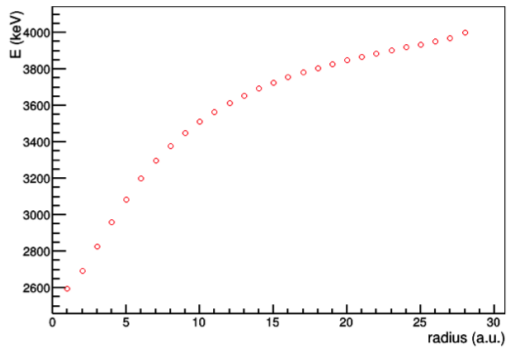

(a) Energy dependence on radius for the case of surface drift of electrons.

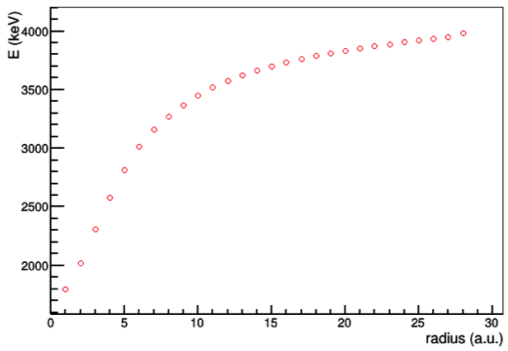

(b) Energy dependence on radius for the case of partial hole trapping and total electron loss.

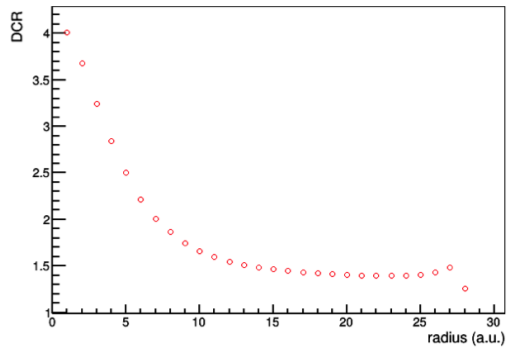

(c) DCR dependence on radius for the case of surface drift of electrons.

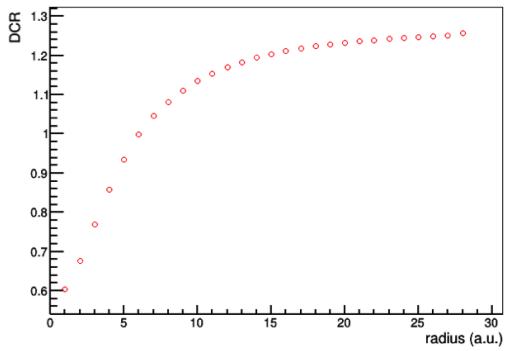

(d) DCR dependence on radius for the case of partial hole trapping and total electron loss.

Figure 5.24: Simulation of the energy *(top)* and DCR *(bottom)* dependence on radius for the two charge loss models. Simulations were created using `siggen`, and are courtesy of Susanne Mertens.

speed of 10^{-4} of the bulk speed), and a given fraction of the electron holes is delayed by convolving their signal with an exponential function with a time constant of $10\,\mu$s.

As in the surface transport model, the energy falls with decreasing radius, but a larger fraction of the incident energy is lost at all radii, as seen in Fig. 5.24b. The radial dependence of the DCR, on the other hand, exhibits the opposite behavior as in the surface-electron model, decreasing dramatically at small radii (see Fig. 5.24d). The electron-hole contribution to the signal drops dramatically at small radii (as seen in the weighting potential, Fig 5.6); since the DCR effect in this case scales with that fraction, it also disappears at small radii.

The energies observed in the TUBE scan of PONaMa-1, and the radial dependence of the DCR parameters at near-point-contact positions (where instability effects are reduced), support this model for the surface alpha charge collection. Further `siggen` simulations should answer the question of whether a constant trapping fraction is sufficient to give the observed radial dependence of energy, or if a radial dependence of the charge trapping is needed to reproduce the effect observed in these measurements.

Chapter 6

ALPHA BACKGROUNDS IN THE MAJORANA DEMONSTRATOR

6.1 Introduction

The MAJORANA DEMONSTRATOR has been taking data with its low-background cryostats since June 2015. Using the open data, we can estimate the background rate of alpha decays in the system and attempt to determine their source. We can evaluate the effectiveness of the DCR pulse-shape discriminator in reducing the background rates, both in the $0\nu\beta\beta$ ROI and at energies over 2.7 MeV, where we expect alpha particle backgrounds to dominate the spectrum.

In particular, we focus on the background rates in the enriched detectors, which were produced by ORTEC. These detectors have similar geometries to the PONaMa-1 detector studied with the TUBE scanner (see Chp. 4 and 5); we expect them to respond similarly to the DCR analysis, with the pulse-shape parameter efficiently identifying passivated-surface alpha events occurring on over 97% of the surface. These detectors also dominate our sensitivity to $0\nu\beta\beta$, given their 88% ^{76}Ge abundance.

In the natural-abundance BEGe-type detectors, the background reduction effect of the DCR analysis is expected to be less than that of a (still-to-be-implemented) near-point-contact event cut, such as an upper limit on the accepted A/E values or a lower limit on the accepted drift times. See Sec. 5.3.2 for further discussion.

6.2 Standard MAJORANA Analysis

Prior to evaluating the effect of the DCR analysis, we apply all of the standard MAJORANA analysis steps. In the event-building stage of processing, the baseline of each waveform is removed and the digitizer non-linearity is corrected [30]. Using the run selection criteria

given in Table 6.1, silver- and gold-ranked runs are used to create the data sets. The data sets used in this analysis, listed in Table 6.2, are composed of silver-ranked runs. since the polyethylene shielding was not yet complete during this period of operations. Detectors that are being operated at full bias, have stable gain, and have stable A vs. E are selected, as described in [38]. Some of the other biased detectors can be used to veto background events that pass through multiple detectors, though their energy information is not used in the spectral analysis.

As suggested by the notes in Table 6.2, there was some variation in the data-taking conditions during Data Sets 0-4. In DS0, the inner copper shield, made from underground electroformed copper, was not in place, and Kalrez® o-rings were used to seal the cryostat, instead of the lower-background PTFE seals in use during later data sets. Therefore, DS0 is expected to have higher gamma background rates than the other data sets. In Data Set 2, waveform multi-sampling, in which 4 consecutive samples (taken at 100 MHz) are summed to create a single stored ADC value, is applied to the the tail of the waveforms. This allows the digitization window to be extended in time, including 30 μs of the waveform tail instead of the 10 μs recorded in the singly-sampled data. Additional shadow shielding to prevent external gamma events from shining down the cryostat cross-arm was added between the end of DS2 and the start of DS3. This should further reduce the gamma background rates in DS3 and DS4, but the effect is expected to be minimal at these low statistics, and is therefore disregarded in this analysis.

A series of data cleaning cuts, described in [58], is applied to remove non-physics waveforms, and pulser events are removed. Since the liquid nitrogen (LN)-filling of the modules creates high noise and subsequent high dead-time due to the elevated trigger rate, all events occurring between 15 minutes before and 5 minutes after an LN-fill are removed. Cosmogenic-induced muon background events are removed by vetoing all events that occur between 50 μs before (to allow for the delay between the muon veto and germanium DAQ systems) and 1 s after a muon event. These cuts, and the dead-time they induce, are described in [68].

The gamma background rate in the DEMONSTRATOR is reduced by applying two analyses

Bit	Silver	Bronze	Bad	Cal	Definition
0			1		Run length: shorter than 3 minutes (1 min for cal)
1			1		Run end: due to ORCA crash -StopTime must be non-zero
2		1			Radon purge: sufficient - average below 5 slpm during run
3	1				Pulser monitor channels are not running (after run 4549)
4			1		Run initialization: issues at run start
5		1			Veto not running: "It does not match expected rate"
6			1		Builder: events not able to be built
7	1				Rate: too high and may affect live-time
8				1	Source present: thus a calibration run
9			1		Trigger Card: Master Trigger card reported lost lock.
10		1			Maintenance/disruptive work
11	1				Shield: not present or incomplete
12			1		Slow control DB is not "available for run"
13			1		Data production logs - bad errors
14		1			One or more Orca bits set: 0 (DAQExpertMode),16 (Transition), 17 (NonStandard), 18 (PulserCal), 19 (ElectronicsCal)

Table 6.1: MJD run quality bit definitions are applied to a run after processing. The result is a 16-bit word that encodes run quality conditions into a number. If the bit is zero, the condition is satisfied. It the bit is one, the condition is not satisfied. The bits are grouped into ranks of gold, silver, bronze, bad, and calibration. The combinations of bits are checked from right to left in the table. If no bits are set, a gold run rank is assigned.

targeted at multiple-scatter gamma events: granularity and A vs. E. In the granularity, or multiplicity, cut, an event is removed if signals occur in two or more detectors within a 4 μs window. This eliminates "true coincidence" events, in which a single physics process occurs in multiple detectors, with the minimal sacrifice of single-site events accounted for in the cited exposure of each data set [68]. An A vs. E cut, as discussed in Sec. 2.2.1, is applied to reduce the backgrounds due to gamma events that scatter multiple times within the same detector [37].

In many of the studies conducted here, we consider only the enriched, ORTEC-geometry detectors, and not the natural-abundance BEGe detectors. The DCR analysis is expected to be most effective and is best-understood in these detectors, since their geometry matches that of PONaMa-1. Since these detectors provide most of the DEMONSTRATOR's $0\nu\beta\beta$-sensitive exposure, the background rates in these detectors are our primary concern.

6.3 DCR Cut Background Reduction

The background rates with and without the DCR cut applied to the data were evaluated in Data Sets 0-4. The data sets are summarized in Table 6.2. The exposures listed here do not exactly match the standard MAJORANA analysis; several detectors in each official data set were disregarded due to incomplete analysis at the time of writing. The runs used The runs used (and the criteria used to select runs) are exactly those in [68] and [38]. The rates are evaluated separately in each data set, so they may be compared across the two modules and, in Module 1, studied over time.

From the summed high-energy spectrum (see Fig. 6.1), we observe a peak near 5.3 MeV, the full energy of the alpha decay of ^{210}Po. This indicates that there is a significant background contribution from the ^{222}Ra decay chain, though the question of whether the decay chain is in equilibrium remains. ^{210}Po has a half-life of 138 days, several times shorter than the accumulated run time of the DEMONSTRATOR; if the decay is unsupported by the long-lived (22 years) ^{210}Pb isotope, we will observe a falling alpha event rate over the course of these data sets.

DS	Dates	Modules	Exposure (kg days)	Enr. Exposure (kg days)	Notes
0	6/26 - 10/7/15	1	509.428	324.220	No inner shield
1	12/31/15 - 5/24/16	1	692.845	626.779	
2	5/24 - 7/14/16	1	114.368	103.520	Multi-sampling enabled
3	8/25 - 9/27/16	1	425.78	342.571	
4	8/25 - 9/27/16	2	223.282	93.615	

Table 6.2: A summary of open data used from the MAJORANA DEMONSTRATOR data sets.

Measurements with the TUBE scanner allow us to conclude that in the enriched detectors, the peak near 5.3 MeV is due to alpha particles incident on the point-contact itself, since little energy is being lost to charge-trapping in these events. The peak is broader and reaches higher energies than we would expect from the measurement of PONaMa-1, but this is likely due to detector-to-detector variation of the point contact dead layer thickness.

To evaluate the rate of alpha background events and the effectiveness of the DCR cut, it is appropriate to study three energy regions. At energies between 2.7 and 4.5 MeV, we expect the dominant background contribution to be alpha particles incident on the passivated surface (or, for BEGe detectors, in the ditch region). The DCR parameter should identify these events as alpha background events with high efficiency, particularly in the enriched detectors.

We take the energy region from 4.5 to 5.5 MeV as a generous estimate of the energy range in which alphas incident on the point contact may appear. The DCR parameter is expected to be insensitive to these events. The use of this large energy window, however, may lead to a contribution from the highest-energy passivated surface events, which the DCR parameter should identify as alpha background events.

The combined energy window of 2.7 to 5.5 MeV is used to study the level of ^{210}Po con-

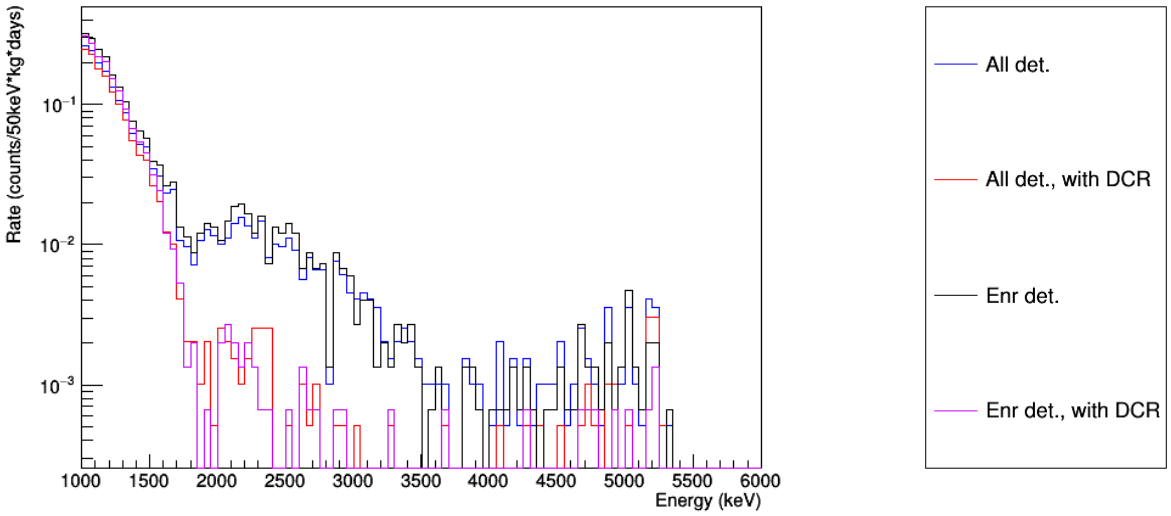

Figure 6.1: Sum spectrum of data sets 0-4. The blue and red lines give the spectra in all detectors with and without the DCR cut, respectively, and the black and violet lines give the same in only the enriched detectors.

tamination, the alpha rate over time, and the variation in alpha backgrounds from detector to detector.

Finally, we also study the energy window used to determine the background in the $0\nu\beta\beta$ region-of-interest, a disjoint 350 keV window around the $0\nu\beta\beta$ Q-value (2039 keV) that excises expected gamma background peak regions. The event energies included in this analysis are those from 1950 to 2350 keV, with the exception of the regions from 2094 to 2127 and 2195 to 2212 keV. In this region, we expect the source of the background events to be a mixture of gamma Compton continuum events and passivated surface alpha events. Data Set 0, in particular, is expected to have a higher rate of gamma background events in this region, since the inner copper shield and additional cross-arm shielding were not yet in place during these runs. Higher background rates are also expected because Kalrez seals were used in the cryostat during these runs, rather than the low-background PTFE seals that were later

installed. Data Sets 1 and 2 may also show slightly higher gamma background rates than Data Sets 3 and 4, since additional shadow shielding was installed between the periods of Data Sets 2 and 3.

Given the TUBE scan results, we expect the alpha events in this energy window to originate from a mixture of small radius and large incidence angle events. High incidence angle events are expected to remain at the DCR parameter values that are characteristic of their incidence radii, and will therefore be identified effectively. For the small radius events, the DCR analysis begins to lose power in identifying alpha events at these energies, due to the falling hole-fraction contribution to the signal. These remaining alpha events are expected to be identifiable with high efficiency by a pulse shape discriminator that identifies near-point-contact events, like the high-A/E analysis used in the TUBE analysis.

In addition to being accepted by channel and run selection steps and having the appropriate energy, events must pass muon veto, data cleaning, granularity, and single-site (A vs. E) event cuts, and must not occur during the LN-fill veto period. Rates are presented for the sum of all detectors and for only enriched (ORTEC-type) detectors, both with and without the 99% bulk-acceptance DCR cut applied to the events. For results, see Table 6.3 and Fig. 6.2.

From these results, there is little indication of a change in the alpha event rate over the course of the data sets. As expected, the DCR analysis reduces the background rate quite effectively in the passivated surface and ROI energy windows, but has little effect in the energy region of the full-energy ^{210}Po events.

6.4 Rate Analysis

To evaluate the rate over time, we use the energy window from 2.7 to 5.5 MeV. Given the low alpha event rates, we average over each data set. As the date of the integrated rate in each data set, we use the exponentially-weighted average date:

$$\bar{t} = \frac{\sum_{i=0}^{n} t e^{\frac{-(t_i+\Delta t/2-t_0)}{\tau}} \Delta t}{\sum_{i=0}^{n} e^{\frac{-(t_i+\Delta t/2-t_0)}{\tau}} \Delta t} \tag{6.1}$$

DS	Energy (MeV)	Rate (cnts/(keV kg d))	Rate after DCR (cnts/(keV kg d))	Enr. Rate (cnts/(keV kg d))	Enr. Rate after DCR (cnts/(keV kg d))
0	$2.7-4.5$	$(4.35^{+0.60}_{-0.60})\times10^{-5}$	$(7.53^{+5.27}_{-3.88})\times10^{-6}$	$(3.71^{+0.66}_{-0.66})\times10^{-5}$	$(8.12^{+6.42}_{-3.98})\times10^{-6}$
	$4.5-5.5$	$(1.20^{+0.90}_{-0.61})\times10^{-5}$	$(1.20^{+0.90}_{-0.61})\times10^{-5}$	$(0^{+5.09}_{-0})\times10^{-6}$	$(0^{+5.09}_{-0})\times10^{-6}$
	ROI	$(3.40^{+0.38}_{-0.32})\times10^{-4}$	$(6.45^{+3.24}_{-2.37})\times10^{-5}$	$(4.11^{+0.50}_{-0.50})\times10^{-4}$	$(6.56^{+4.06}_{-3.03})\times10^{-5}$
1	$2.7-4.5$	$(3.28^{+0.50}_{-0.50})\times10^{-5}$	$(7.63^{+25.7}_{-6.79})\times10^{-7}$	$(3.44^{+0.54}_{-0.54})\times10^{-5}$	$(8.40^{+28.2}_{-7.47})\times10^{-7}$
	$4.5-5.5$	$(4.26^{+0.77}_{-0.77})\times10^{-5}$	$(1.65^{+0.96}_{-0.69})\times10^{-5}$	$(3.63^{+1.44}_{-1.13})\times10^{-5}$	$(9.07^{+8.27}_{-5.73})\times10^{-6}$
	ROI	$(1.88^{+0.27}_{-0.27})\times10^{-4}$	$(2.36^{+2.15}_{-1.49})\times10^{-5}$	$(1.94^{+0.29}_{-0.29})\times10^{-4}$	$(1.30^{+1.91}_{-0.82})\times10^{-5}$
2	$2.7-4.5$	$(3.24^{+2.56}_{-1.59})\times10^{-5}$	$(0^{+1.13}_{-0})\times10^{-5}$	$(3.56^{+2.81}_{-1.75})\times10^{-5}$	$(0^{+1.24}_{-0})\times10^{-5}$
	$4.5-5.5$	$(2.50^{+3.69}_{-1.58})\times10^{-5}$	$(8.33^{+28.0}_{-7.41})\times10^{-6}$	$(1.83^{+3.58}_{-1.34})\times10^{-5}$	$(0^{+2.23}_{-0})\times10^{-5}$
	ROI	$(1.67^{+1.32}_{-0.82})\times10^{-4}$	$(0^{+5.81}_{-0})\times10^{-5}$	$(1.57^{+1.43}_{-0.99})\times10^{-4}$	$(0^{+6.38}_{-0})\times10^{-5}$
3	$2.7-4.5$	$(4.51^{+0.75}_{-0.75})\times10^{-5}$	$(3.76^{+5.54}_{-2.37})\times10^{-6}$	$(3.39^{+1.39}_{-1.07})\times10^{-5}$	$(3.08^{+6.04}_{-2.26})\times10^{-6}$
	$4.5-5.5$	$(2.48^{+1.54}_{-1.15})\times10^{-5}$	$(1.13^{+1.13}_{-0.71})\times10^{-5}$	$(2.22^{+1.66}_{-1.12})\times10^{-5}$	$(8.33^{+12.3}_{-5.26})\times10^{-6}$
	ROI	$(1.61^{+0.61}_{-0.48})\times10^{-4}$	$(1.29^{+2.52}_{-0.94})\times10^{-5}$	$(1.67^{+0.71}_{-0.56})\times10^{-4}$	$(0^{+1.94}_{-0})\times10^{-5}$
4	$2.7-4.5$	$(2.24^{+1.57}_{-1.15})\times10^{-5}$	$(2.49^{+8.36}_{-2.21})\times10^{-6}$	$(2.37^{+2.73}_{-1.50})\times10^{-5}$	$(0^{+1.45}_{-0})\times10^{-5}$
	$4.5-5.5$	$(0^{+1.09}_{-0})\times10^{-5}$	$(0^{+1.09}_{-0})\times10^{-5}$	$(0^{+2.61}_{-0})\times10^{-5}$	$(0^{+2.61}_{-0})\times10^{-5}$
	ROI	$(2.18^{+1.03}_{-0.76})\times10^{-4}$	$(1.28^{+4.30}_{-1.14})\times10^{-5}$	$(4.88^{+2.44}_{-1.83})\times10^{-4}$	$(0^{+7.45}_{-0})\times10^{-5}$
0-4	$2.7-4.5$	$(3.75^{+0.31}_{-0.31})\times10^{-5}$	$(3.57^{+1.91}_{-1.40})\times10^{-6}$	$(3.46^{+0.34}_{-0.34})\times10^{-5}$	$(3.26^{+2.12}_{-1.47})\times10^{-6}$
	$4.5-5.5$	$(2.43^{+0.33}_{-0.33})\times10^{-5}$	$(1.19^{+0.44}_{-0.35})\times10^{-5}$	$(2.00^{+0.65}_{-0.53})\times10^{-5}$	$(5.28^{+3.70}_{-2.72})\times10^{-6}$
	ROI	$(2.31^{+0.17}_{-0.17})\times10^{-4}$	$(3.15^{+1.25}_{-0.98})\times10^{-5}$	$(2.63^{+0.21}_{-0.21})\times10^{-4}$	$(2.35^{+1.26}_{-0.92})\times10^{-5}$
0-4	$2.7-4.5$	$(3.48^{+0.36}_{-0.36})\times10^{-5}$	$(1.83^{+1.83}_{-1.16})\times10^{-6}$	$(3.36^{+0.39}_{-0.39})\times10^{-5}$	$(1.36^{+2.01}_{-0.86})\times10^{-6}$
	$4.5-5.5$	$(2.97^{+0.44}_{-0.44})\times10^{-5}$	$(1.19^{+0.54}_{-0.43})\times10^{-5}$	$(2.78^{+0.90}_{-0.73})\times10^{-5}$	$(7.35^{+5.14}_{-3.79})\times10^{-6}$
	ROI	$(1.83^{+0.19}_{-0.19})\times10^{-4}$	$(1.70^{+1.19}_{-0.88})\times10^{-5}$	$(2.05^{+0.22}_{-0.22})\times10^{-4}$	$(7.00^{+10.3}_{-4.42})\times10^{-6}$

Table 6.3: Background rate results in MAJORANA DEMONSTRATOR Data Sets 0-4, with and without the 99% bulk-acceptance DCR cut applied to the data. The uncertainties given are the 90% Feldman-Cousins statistical confidence intervals [43]. These results to not reflect the finalized MAJORANA analysis.

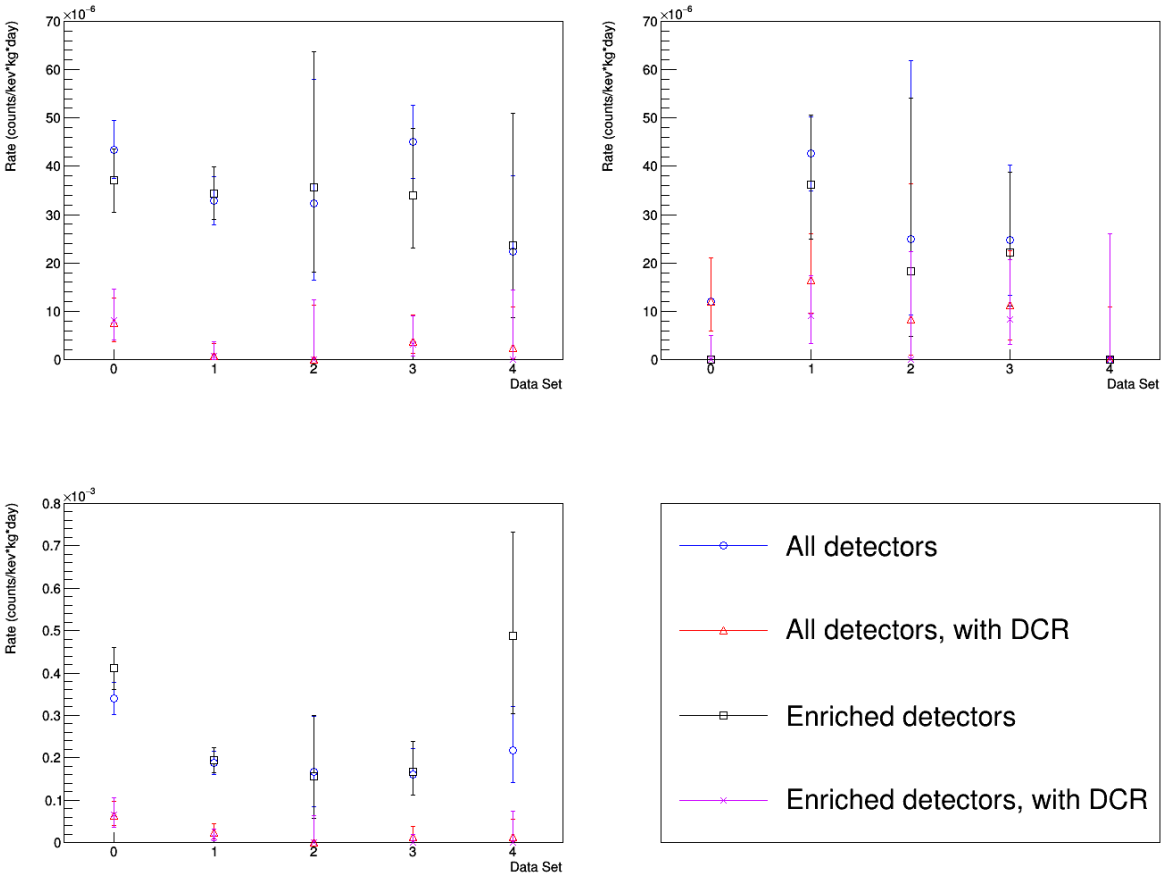

Figure 6.2: Rates in the 2.7 to 4.5 MeV *(upper left)*, 4.5 to 5.5 MeV *(upper right)*, and ROI *(bottom left)* energy windows. Blue circles and and red triangles represent the rates in all detectors with and without the DCR cut, respectively, and black squares and violet crosses give the same in only the enriched detectors.

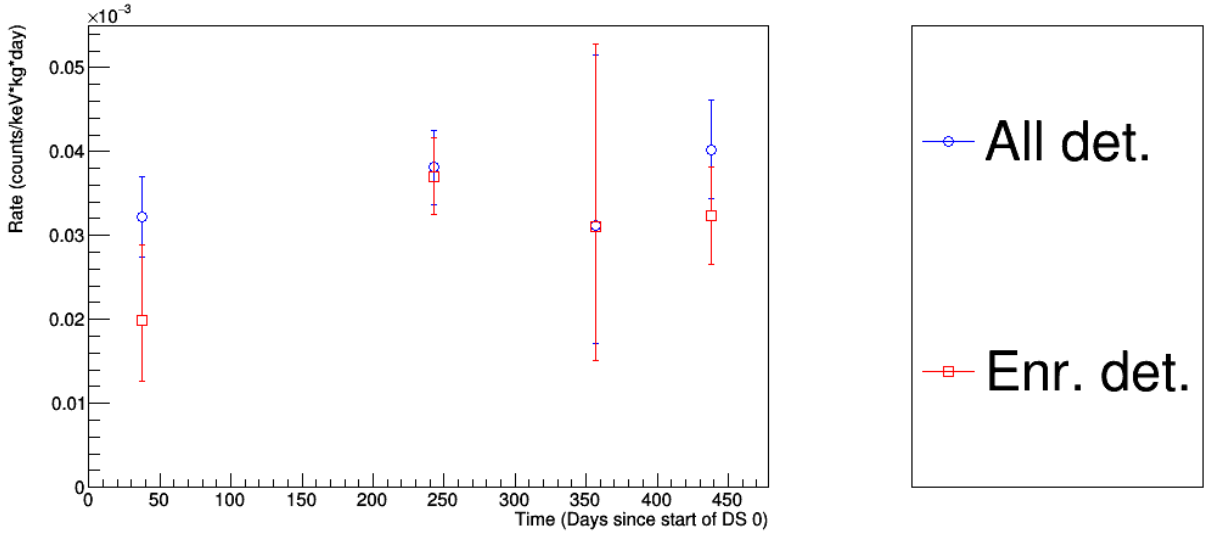

Figure 6.3: M1 alpha background rates in the 2.7 to 5.5 MeV energy window of each data set, given as a function of time. The time given for each data set is the exponentially-weighted average date, as in Eqn. 6.1. Blue circles indicate the rates in all detectors, and red squares are the rates in only enriched detectors. The DCR cut is not applied, but single-site, muon, granularity, and data cleaning cuts are applied to the data. The error bars indicate the 90% Feldman-Cousins statistical confidence intervals [43].

where $\tau = t_{1/2}/\ln(2) = 199.7$ days is the decay constant of ^{210}Po and the sums are taken over each of the n runs of the data set. t_i and Δt are the start times of each run, and t_0 is the start time of the data set, taken as the number of days since the beginning of DS0 data-taking.

As seen in Fig. 6.3, there is no hint of decay in the alpha background rates over time. All of the data set rates are in agreement except for the rate in the DS 0 enriched detectors, which is in tension with the rate in DS1 and in slight tension with that from DS3. In spite of the high statistical errors associated with the rates, the decay would be clearly detectable if the entirety of the alpha background contribution were due to unsupported ^{210}Po decay; the

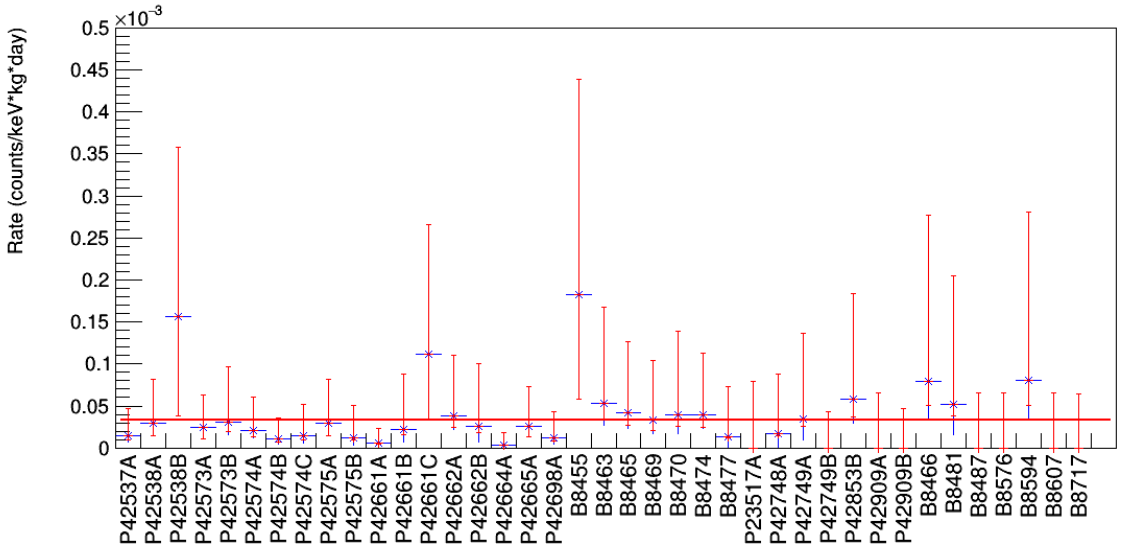

Figure 6.4: Rates in the 2.7 to 5.5 MeV energy window for each detector. Blue error bars indicate the Poisson error bounds, and red error bars indicate the Feldman-Cousins intervals. The average for all detectors is indicated by the red line.

expected rate after 350 days is less than 20% of the starting rate, well outside the statistical uncertainties of the rates. Therefore we must conclude that at least the majority of the alpha backgrounds are supported by ^{210}Pb decay.

The total observed incident ^{210}Po activity in the 2.7 to 5.5 MeV window is 13.1±1.0 μBq, and the total in this energy range in the enriched detectors is 8.8±0.8μBq. These values should be considered to be lower limits on the ^{210}Po activity, since an unknown fraction of events occur at energies below 2.7 MeV.

6.5 Detector-by-detector Backgrounds

The MAJORANA Collaboration is very interested in discovering the source of the alpha background contamination, so that it may, if possible, be removed. To this end, it is also of interest to examine the alpha background rates observed on a detector-by-detector basis, to

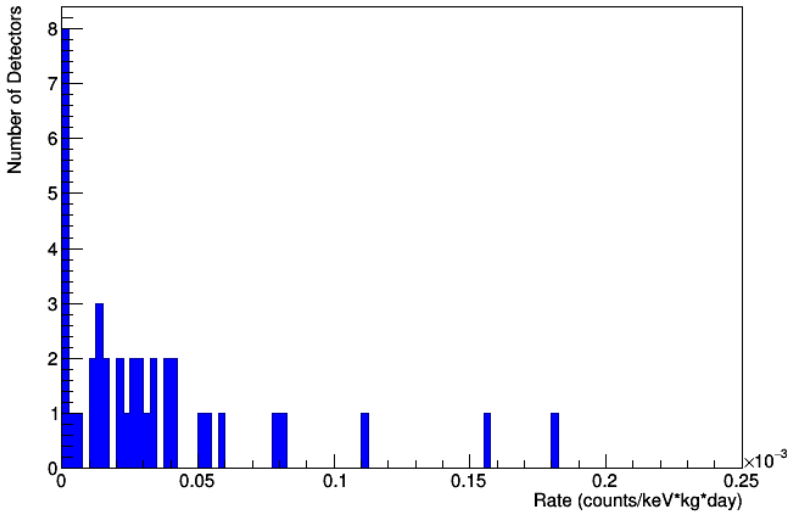

Figure 6.5: The distribution of the number of detectors with a given alpha background rate. 7 of the 8 detectors with rates over 5×10^{-5} cnts/(keVkgd) appear on the list in Table 6.4. The remaining detector is B8463, a BEGe-type (natural) detector with a high uncertainty in its rate due to its small exposure.

find whether some detectors are particularly contaminated. Even if the alpha background cannot be eliminated in during the life of the MAJORANA DEMONSTRATOR, understanding its source will allow future low-background HPGe-based experiments to limit this problematic background.

Again, we integrate the single-site, non-muon events with energies between 2.7 and 5.5 MeV following granularity, LN fill, and data cleaning cuts. The error associated with each detector varies, as their both their masses and operating times vary.

The integral rates for each of the detectors (including Data Sets 0-4) can be seen in Fig. 6.4. In addition to the Poisson errors for these rates, we give the Feldman-Cousins (FC) [43] upper and lower bounds for an expected background of 0. Since the rates are very close to 0, the FC procedure allows us to present rates that transition smoothly to upper limits

Det.	Type	All	Enr.	Rate
P42538B	Enr.	✓	✓	$(1.6^{+0.4}_{-0.4}) \times 10^{-4}$
P42661C	Enr.		✓	$(1.1^{+0.4}_{-0.3}) \times 10^{-4}$
B8455	Nat.	✓	✓	$(1.8^{+0.8}_{-0.6}) \times 10^{-4}$
P42853B	Enr.	✓	✓	$(5.8^{+6.7}_{-3.7}) \times 10^{-5}$
B8466	Nat.	✓	✓	$(8.0^{+12}_{-5.0}) \times 10^{-5}$
B8481	Nat.	✓	✓	$(5.2^{+10}_{-3.8}) \times 10^{-5}$
B8594	Nat.	✓	✓	$(8.1^{+12}_{-5.1}) \times 10^{-5}$

Table 6.4: 7 detectors were found to have alpha rates inconsistent with the average rates. A checked box in the "All" column indicates that the rate is inconsistent with the average rate across all detectors, and a checked box in the "Enr." column indicates that it it inconsistent with the (lower) average rate in the enriched detectors.

when a rate of 0 is measured, without under-coverage.

The average rate, when taken among all the detectors, is $(3.4 \pm 0.4) \times 10^{-5}$ cnts/(keV kg d). When taken among only the enriched detectors, it is $(2.7 \pm 0.4) \times 10^{-5}$cnts/(keV kg d). The difference in these averages does not necessarily imply that the ^{210}Po average activity level differs between the enriched and natural-abundance detectors, since only the alpha spectrum above 2.7 MeV is used to find this rate. If the BEGe-type detector design leads to fewer highly energy-degraded events (with energies less than 2.7 MeV) than the ORTEC geometry, these rates would be brought into closer agreement.

Using these two averages, we find the detectors that are inconsistent with the average rate, as defined by their FC limits (i.e. their lower FC bound is above one or both of the averages). These high-alpha rate detectors are given in Table 6.4. These detectors also appear as outliers in the distribution of detector alpha rates, seen in Fig. 6.5.

The potential origins of the elevated alpha background rates in these detectors are cur-

rently being investigated. The MAJORANA Collaboration has carefully tracked the manufacturing, cleaning, storage, and assembly history of all the detectors and parts [6], and is now studying these records to find the shared elements in these detectors' histories.

6.6 DCR Effect on $0\nu\beta\beta$ Sensitivity

The half-life sensitivity to $0\nu\beta\beta$ is given by:

$$T_{1/2}^{0\nu} > \ln 2 \frac{N_a t \varepsilon}{\langle \mathrm{UL}(B(t)) \rangle},$$

where N_a is the number ^{76}Ge atoms, t is the live time, ε is the efficiency, and $B(mt)$ is the predicted number of background events after the integrated exposure mt. Without the DCR cut applied, $\varepsilon = \varepsilon_0$, the combined efficiency of all other cuts. With the 99% bulk-acceptance DCR cut applied, $\varepsilon = 0.99\varepsilon_0$. $\langle \mathrm{UL}(B) \rangle$ denotes the average upper limit an ensemble of identical experiments would place in the absence of a signal given B background counts [40]. In the nearly background-free regime, the Feldman-Cousins method [43] provides an appropriate means to calculate this value for a given observed background level. At high background levels, $\langle \mathrm{UL}(B) \rangle = \sqrt{B}$.

To calculate the expected background level in the $0\nu\beta\beta$ ROI, we assume that the background spectrum is flat in the region around the 2039 keV Q-value, and is the same as in the 350 keV ROI background estimate window described above. Since the enriched detectors drive the MAJORANA DEMONSTRATOR's sensitivity, we are most interested in the decrease in the backgrounds due to the DCR cut in these detectors. We do not consider Data Set 0 in this analysis, since it was taken with incomplete shielding and is known to have higher gamma backgrounds than the final configuration of the DEMONSTRATOR.

In Data Sets 1 through 4, the use of the 99% bulk-acceptance DCR cut reduces the enriched detector event rate in the $0\nu\beta\beta$ ROI background-estimate window from from 88 counts to 3 counts, a factor of 29 reduction. As seen in Table 6.3, this corresponds to a reduction in the rate from $(2.1 \pm 0.2) \times 10^{-4}$ cnts/(keV kg d) to $(7^{+10}_{-4}) \times 10^{-5}$ cnts/(keV kg d).

To calculate $\langle \mathrm{UL}(B) \rangle$ we must first find B, the expected number of background events in the ROI in time t. For the purposes of this calculation, we take mt to be the accumulated enriched exposure of Data Sets 1-4, 1166.505 kg days. The background index given above must be multiplied by the width of the ROI in keV. Given small changes in the detector resolution between data sets, the optimal width of the ROI has changed slightly over the course of the experiment; we take it to be the exposure-weighted average of the ROI widths in each of the data sets, 2.99 keV.

Multiplying by these values, we find an expected number of background events of 0.73±0.08 without the DCR cut, and $(2^{+4}_{-2}) \times 10^{-2}$ with the DCR cut. Since no events are observed in the ROI, the sensitivity $\langle \mathrm{UL}(B) \rangle$, defined as the average upper limit that would be obtained by an ensemble of experiments with the expected background and no true signal, with 90% confidence, is 3.06 without the DCR cut, or 2.46 with it. The sensitivity without the DCR cut is:

$$T^{0\nu}_{1/2} > \ln 2 \frac{N_a t \varepsilon_0}{3.06},$$

and with the DCR cut it is:

$$T^{0\nu\prime}_{1/2} > \ln 2 \frac{N_a t 0.99 \varepsilon_0}{2.46} = 1.23\, T^{0\nu}_{1/2}.$$

We conclude that the addition of the DCR cut improves the $0\nu\beta\beta$ sensitivity of the MAJORANA DEMONSTRATOR at its current exposure by 23%.

Another calculation of interest is the expected increase in sensitivity after 5 years of operation. To calculate the total expected enriched exposure, we can assume that the operating active mass is the sum of M1's active mass in DS3 and M2's active mass in DS4, giving a total of 18.1 kg. As an estimate of the livetime fraction and duty cycle, we use the values found for DS3, 99.0% and 92.4%, respectively [68] [38]. Therefore, over 5 years of operations, the expected active enriched exposure of the DEMONSTRATOR is 3.02e4 kg days (or 82.8 kg yrs).

Assuming the background rates found in DS 1 - 4 remain constant through the life of the experiment, 19±2 background events would be expected in the ROI over the lifetime of the experiment without the DCR cut, and $0.6^{+0.9}_{-0.4}$ events would be expected with the DCR cut.

Therefore $\langle \mathrm{UL}(B) \rangle$ is 8.81 without the DCR cut, and 2.93 with it. Therefore, over the life of the DEMONSTRATOR, the DCR cut improves the experiment's sensitivity by a factor of 3.

To get a better sense of the value of this increased sensitivity, we can convert it to an increased effective ^{76}Ge mass, and to a monetary value of the increased effective mass of the experiment. With both Modules 1 and 2 taking data, the DEMONSTRATOR has approximately 18 kg of enriched active mass of fully operating detectors that contribute to the $0\nu\beta\beta$ limit. These detectors have an average total mass per detector of 0.85 kg, and an active mass fraction of 92.6%. The approximate costs associated with them are a price of $100 per gram of enriched germanium, and $100,000 per detector of manufacturing costs.

The increase in sensitivity by a factor of 3 corresponds to an additional 36 kg of enriched active mass, which would require the addition of 39 kg of total enriched mass, in 46 additional detectors. At current prices, this would have represented an additional cost of $8.5 million.

6.7 Identifying the Source of Alpha Events in the MAJORANA DEMONSTRATOR

6.7.1 Projected Alpha Energy Spectrum

To create a realistic alpha energy spectrum, the radial dependence of the energy found with the TUBE scan derived in Sec. 5.1.2 must be integrated with respect to position for a given model of the alpha contamination, and corrected for the alpha particle incidence angle energy-dependence. Below, we derive the expected energy spectra for two potential models of contamination: a uniform-distribution model, and a point-source contamination model.

Also needed is the fraction describing the relative rate in the point-contact region, compared to the passivated surface, which characterizes the obstruction of the p+ contact. In the TUBE measurements, the alpha rate at unobscured scanning positions incident on the passivated surface, found in Sec. 4.6 is constant, with an average of 64.6 events/hr. The peak in the data sets with the source fully incident on the point-contact, on the other hand, shows a substantially reduced event rate of $3.9 \pm .3$ events/hr, giving an obstruction fraction f_{obs} of 0.06. This likely due to the partial obstruction of the p+ contact by the contact pin and

contact pin support. Some unknown fraction of the alpha source beam is also falling on the nearby passivated surface, resulting in low-energy ($< 1\,\mathrm{MeV}$) events that are not being taken into account.

This should be considered a lower bound for the detectors in the DEMONSTRATOR, since only the effect of the contact pin obstruction could be relevant for alpha background events in the DEMONSTRATOR. If the source of the events is the tin coating of the contact pin or the detector surface itself, there will be no obstruction ($f_{obs} = 1$). If some other source is responsible for the events, the p+ contact would be partially obscured as in the TUBE measurements ($0.06 < f_{obs} < 1$). For this simplified model we will set $f_{obs} = 1$. In future simulations incorporating the full geometry of the p+ contact and contact pin, this parameter will not be needed.

Uniform-distribution Model, without Incidence Angle Dependence

The uniform-distribution model of alpha contamination assumes a constant distribution σ of alpha-emitters across the entire detector surface, including the point-contact region. This model mimics the distribution that would be expected if, for instance, the detector were exposed to ^{222}Rn during fabrication or construction, leading to a uniform distribution of ^{210}Po decays on the surface. This model would also be appropriate for the case of a uniform distribution of alpha emitters on the surfaces of copper parts, since the crystal mounting plate, the copper part that is closest to the passivated surface in the MAJORANA detector mount design, is roughly equidistant from all points on the passivated surface and point contact.

Beginning with the contamination model:

$$\mathrm{d}n(r, \phi) = \sigma r \mathrm{d}r \mathrm{d}\phi,$$

where ϕ is the azimuthal angle, we split it into point-contact and passivated surface terms. The point-contact component is integrated over the entire point contact region to derive a rate for this contribution, since the energy is independent of radius in this region.

The passivated surface term has a one-to-one correspondence of energy to radius, so one can integrate in the azimuthal angle dimension and transform from the radius to the energy variable to give a rate in terms of energy, i.e., an energy spectrum:

$$\begin{aligned} \mathrm{d}n(E) = &\pi {r_p}^2 f_{obs}\sigma\delta(E-E_{pk})\mathrm{d}E \\ &+\Theta(E_{max}-E)2\pi\sigma r(E)\frac{\mathrm{d}r(E)}{\mathrm{d}E}\mathrm{d}E \end{aligned} \tag{6.2}$$

where $E_{pk} = 5323\,\mathrm{keV}$ is the average energy of the point-contact alpha events, $E_{max} = \sqrt[4]{\frac{r_{max}-r_p}{a}} = 4746\mathrm{keV}$ is passivated-surface energy at the maximum radius of PONaMa-1, and $r_p = 1.6\,\mathrm{mm}$ is the point contact radius.

The radial dependence on energy (found in Sec 5.1.2) is:

$$r(E) = aE^4 + r_p \tag{6.3}$$

where $a = 5.50\times10^{-14}\,\mathrm{mm/keV^{1/4}}$ is the scaling parameter from the fit. Substituting it into Eqn.6.2:

$$\begin{aligned} \mathrm{d}n(E) =&\pi r_p^2 f_{obs}\sigma\delta(E-E_{pk})\mathrm{d}E \\ &+\Theta(E_{max}-E)8\pi\sigma a(aE^7+r_pE^3)\mathrm{d}E. \end{aligned} \tag{6.4}$$

Finally, this energy spectrum should be convolved with the spectral peak shape function at each energy. Since the distribution of passivated surface events is very broad compared to the resolution of the energy peaks, this will have little effect on the shape of the passivated surface contribution. The delta function of the point-contact events, on the other hand, will become a Gaussian+low-energy tail peak like that found in the fit to the energy spectrum of point-contact events. We apply the convolution to only the point-contact events, and set f_{obs} and σ both to 1, to plot the spectrum in Fig. 6.6.

Point-contact Contamination Model, without Incidence Angle Dependence

The other contamination model studied is one in which the alpha events originate in a point source some height h above the center of the p+ contact, and the event rate falls as $\frac{1}{r^2+h^2}$

across the passivated surface of the detector. Possible sources of such a distribution in the MAJORANA DEMONSTRATOR would be contamination of the point-contact region of the detector itself, or of the contact pin, the tin coating of that pin, or the PTFE bushing that holds it in place.

To avoid a divergence at $r = 0$, we assume the contamination on the point-contact itself is uniform, and matches the contamination at the boundary of the point-contact region.

In this case, the contamination model is:

$$\mathrm{d}n(r,\phi) = \begin{cases} \frac{\sigma}{r_p^2} r(E)\mathrm{d}r\mathrm{d}\phi, r < r_p \\ \frac{\sigma}{r(E)^2+h^2} r(E)\mathrm{d}r\mathrm{d}\phi, r > r_p \end{cases}$$

Proceeding as before, the spectral shape is:

$$\begin{aligned} \mathrm{d}n(E) &= \pi f_{obs}\sigma\delta(E - E_{pk})\mathrm{d}E \\ &+ \Theta(E_{max} - E)8\pi\sigma a\frac{(aE^3)(aE^4 + r_p)}{(aE^4 + r_p)^2 + h^2}\mathrm{d}E \end{aligned} \tag{6.5}$$

Note that the point-contact contribution is identical as in the uniform contamination model, save for the numerical factor of $1/r_p^2$. Again, we convolve the delta function with the appropriate peak shape and set f_{obs} and σ both to 1 to plot the predicted spectrum, in Fig. 6.6.

Uniform-distribution Model, with Incidence Angle Dependence

The predicted spectral shape derived above does not account for the radial dependence of the alpha particle's incidence angle. Large incidence angle events would have less energy at a given radius than those measured with the TUBE scanner, since they would traverse more of the high charge-trapping near-surface region. This would create a large enhancement in the low energy portion of the spectrum, and a corresponding reduction at the high energy portion.

To incorporate the incidence angle energy dependence into the polynomial spectral shape model, we assume that charge-trapping occurs over some constant depth of the region below the passivated surface, and that the amount of energy lost to trapping depends linearly on

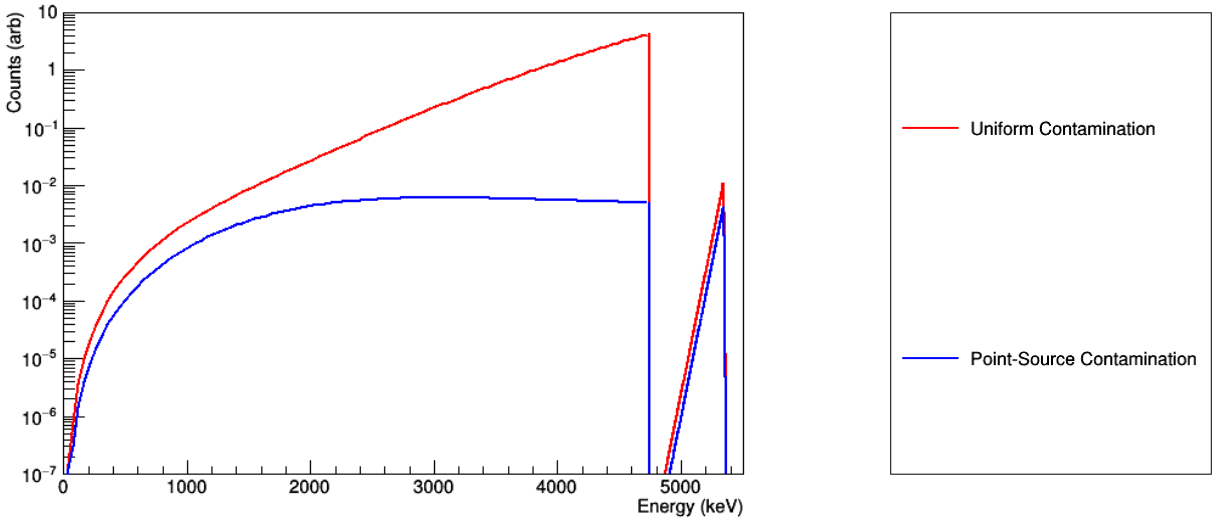

Figure 6.6: The predicted energy spectra for the uniform (in red) and point-contact (in blue) contamination models, without angle-of-incidence correction.

the path length in this region. Therefore the energy at a given incidence angle θ, where θ is measured with respect to the horizontal passivated surface, is:

$$E(r,\theta) = E_0 - \frac{\sin\theta_0}{\sin\theta}(E_0 - E_t(r,\theta_0)) \tag{6.6}$$

where $\theta_0 = 65°$ is the incidence angle of the TUBE scan measurements, E_0 is the alpha decay energy, and $E_t(r,\theta_0)$ is the measured spectral shape in the TUBE measurements.

To correct the energy spectrum for incidence angle dependence, we integrate over all allowed incidence angles to find the corrected energy E_f:

$$E_f(r) = \int_{\rho}^{\pi/2} \left(E_0 - \frac{\sin\theta_0}{\sin\theta}(E_0 - E_t(r,\theta_0))\right)(2\pi\cos\theta)\mathrm{d}\theta$$

where ρ is the minimum incidence angle for which the particle has non-zero energy at some radius r that corresponds to an energy $E_t(r,\theta_0)$:

$$\rho(r) = \arcsin\left(\sin\theta_0\left(1 - \frac{E_t(r,\theta_0)}{E_0}\right)\right)$$

Taking the integral,

$$E_f(r) = 2\pi E_0(1-\cos\rho) + 2\pi \sin\theta_0(E_0 - E_t(r,\theta_0))\ln(\sin\rho)$$

Substituting ρ and using the second-order approximation of $\cos\rho$ in the first term (writing $E_t(r,\theta_0)$ as E_t for the sake of concision),

$$E_f(r) = 2\pi E_0 \sin^2\theta_0 \left(1-\frac{E_t}{E_0}\right)^2 + 2\pi\sin\theta_0(E_0-E_t)\ln\left(\sin\theta_0\left(1-\frac{E_t}{E_0}\right)\right)$$

and

$$\begin{aligned} \mathrm{d}E_f = \Bigg(& 2\pi\sin^2\theta_0\left(1-\frac{E_t}{E_0}\right) - \frac{1}{1-\frac{E_t}{E_0}} \\ & - \sin\theta_0 \ln\left(\sin\theta_0\left(1-\frac{E_t}{E_0}\right)\right) + \frac{E_t}{E_0\left(1-\frac{E_t}{E_0}\right)}\Bigg)\mathrm{d}E_t \end{aligned} \tag{6.7}$$

Substituting these equations into Eqn 6.2, we find the spectral shape shown in Fig. 6.7. Introducing the incidence angle dependence has a drastic effect on the spectral shape, with most alpha events having very low energies of interaction.

Point-contact Contamination Model, with Incidence Angle Dependence

In this case, the incidence angle θ has a one-to-one correspondence with the radius r. Given a point-source of alpha particles at height h, $\theta = \tan\left(\frac{h}{r}\right)$. Then the corrected energy E_f, using Eqn 6.6, is given by:

$$E_f(r) = \frac{\sin\theta_0}{h}\sqrt{h^2+r^2}(E_0 - E_t(r,\theta_0)).$$

where E_t is the measured energy in TUBE.

We can put this in the form of a linear transformation of E_t:

$$\begin{aligned} E_f(r) &= u(r)E_t + v(r) \\ u(r) &= \frac{\sin\theta_0}{h}\sqrt{h^2+r^2} \\ v(r) &= E_0\left(1-\frac{\sin\theta_0}{h}\sqrt{h^2+r^2}\right) \end{aligned} \tag{6.8}$$

As before,

$$r(E_t) = aE_t^4 + r_p.$$

Again, the spectral shape can be found by transforming variables to re-scale the energy axis of the spectrum given in Eqn. 6.5. In this case, the transformation is from the E_t coordinate to the incidence-angle weighted E_f. In other words, these two equations are substituted into the spectrum, along with the Jacobean of the transformation from E_t to E_f. Making the substitution explicit:

$$\begin{aligned} \mathrm{d}n(E_f) &= \pi f_{obs}\sigma\delta(E - E_{pk})\mathrm{d}E \\ &\quad + \Theta(E_{max} - E)8\pi\sigma a\frac{(E_f(r(E_t))^3)(aE_f(r(E_t))^4 + r_p)}{(aE_f(r(E_t))^4 + r_p)^2 + h^2}\mathrm{d}E_f \end{aligned} \tag{6.9}$$

where, writing r rather than $r(E_t)$ for the sake of concision:

$$\begin{aligned} \mathrm{d}E_f &= E_t\mathrm{d}u(r) + u(r)\mathrm{d}E_t - \mathrm{d}v \\ &= \left(r\left(\frac{\sin\theta_0}{h}\right)\left(\frac{E_0 + E_t}{\sqrt{h^2 + r^2}}\right)(4aE_t^3) + \frac{\sin\theta_0}{h}\sqrt{h^2 + r^2}\right)\mathrm{d}E_t \end{aligned} \tag{6.10}$$

For varying heights h of the source, this gives the spectrum pictured in Fig. 6.8. The passivated surface spectrum with $h = 5\,\mathrm{mm}$ is compared to the uniform distribution spectrum in Fig. 6.7

^{210}Po Modifications to the Spectral Model

The projected alpha spectra are scaled to the energy of the ^{241}Am alpha decay. To apply them to the MAJORANA DEMONSTRATOR data, we must rescale it to match the energy of the particle emitted by ^{210}Po, our most significant observed alpha peak. The energy of that decay is 5.304 MeV, as opposed to ^{241}Am's most probable decay of 5.485 MeV.

Given the charge-trapping model for alpha interactions that we have developed, it is most appropriate to simply rescale the energy in the passivated surface spectral shape function by the ratio of the two energies, so $E_i' = \frac{5.305}{5.485}E_i$.

The point-contact energy function, on the other hand, is best understood as charge loss to a dead layer, which reduces the peak energy by a fixed quantity. This loss is independent of

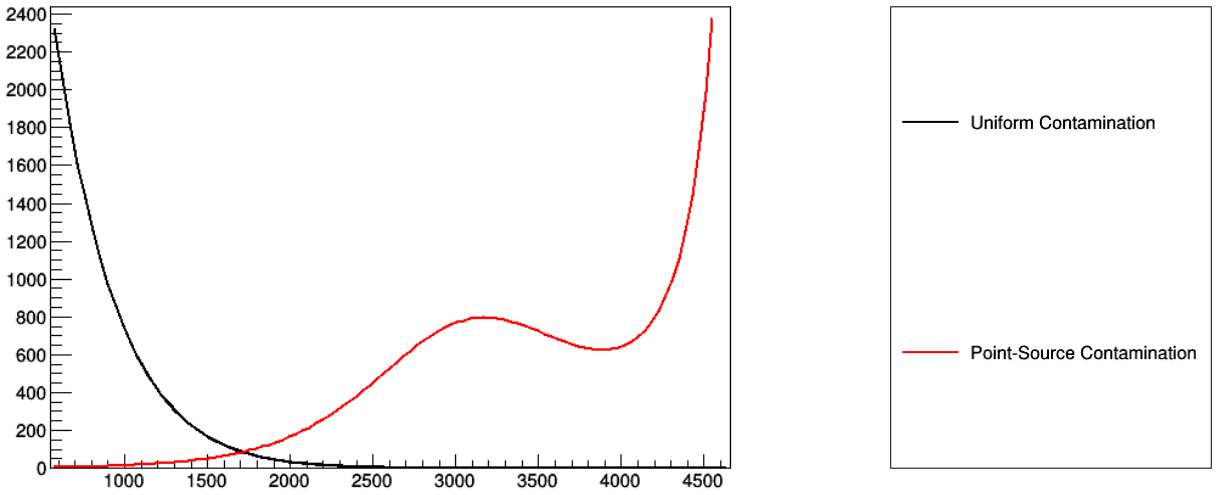

Figure 6.7: The predicted energy spectra for the uniform distribution contamination model, in black, and the point-contact contamination model with $h = 5\,\mathrm{mm}$, in red. Both curves include the incidence angle dependence for the model, and are scaled to the appropriate energies for ^{210}Po decay.

the incident alpha energy, since the energy loss rate $\mathrm{d}E/\mathrm{d}x$ is almost completely independent of energy at these alpha energies. Therefore we shift this function by the difference in the energies (180 keV), rather than applying a scaling factor.

An important caveat is that this spectral shape has a dependence on the radii of the detector and the point contact. Though PONaMa-1 is a typical detector in these respects, the detectors operating in the MAJORANA DEMONSTRATOR vary in both of these dimensions. Similarly, the point-contact dead layers may vary from one detector to another.

6.8 Fitting to the MAJORANA DEMONSTRATOR *Spectrum*

Comparing the projected alpha spectral models to the high-energy spectra in the MAJORANA DEMONSTRATOR we find several things of note. The uniform contamination model

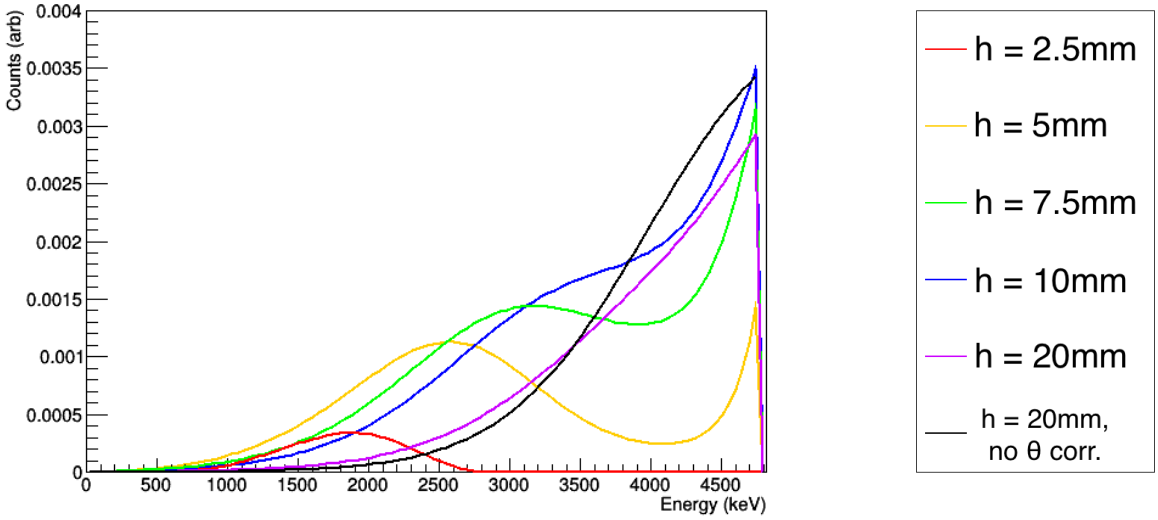

Figure 6.8: The predicted energy spectra for the point-contact contamination model, as h varies. The black curve does not include the incidence angle correction. The alpha source rate σ is set to 1 for all curves.

is immediately disfavored. As seen in Fig. 6.9, its fit to the observed spectrum is poor, and is far worse than that of the point-contact contamination model.

Using the spectral shape model given by Eqns. 6.9 and 6.10, we fit the MAJORANA spectrum in the enriched detectors, with the parameters σ and h determined by the fit. All events in Data Sets 1-4 are used, following data cleaning, LN-fill veto, muon veto, granularity, and A vs. E cuts. The DCR cut is not used, since the goal of this analysis is to pinpoint the source of the alpha events. The energy range used for the fit is from 1900 keV to E_{max}, the endpoint of the PONaMa-1 passivated surface spectrum, scaled to adjust for the ^{210}Po decay energy, 4611 keV. The lower energy bound is chosen to avoid a large contribution from $2\nu\beta\beta$ decay.

The p+ contact event contribution is not used to fit the spectrum; it is simply drawn with the amplitude determined by the passivated surface fit. The background level for the

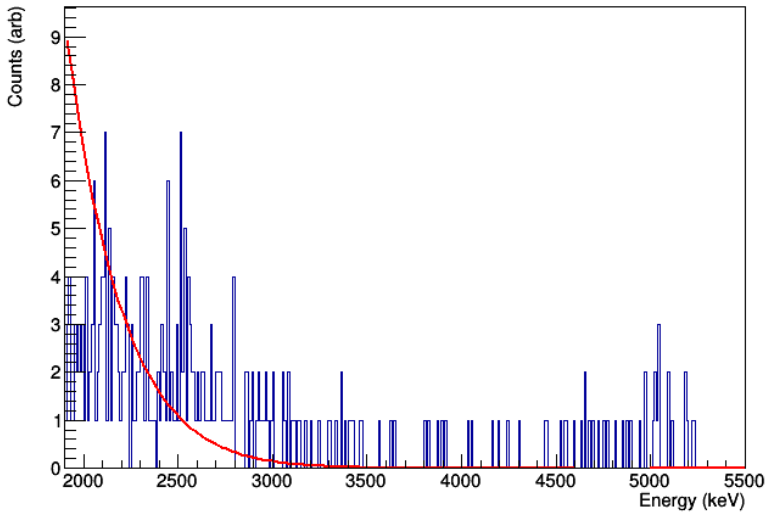

Figure 6.9: The high-energy spectrum from the MAJORANA DEMONSTRATOR Data Sets 1-4, with muon, data cleaning, single-site, and multiplicity cuts applied, is in blue. Bins are 10 keV wide. The constant contamination model for passivated surface events (the red line) was fit to the data, and the predicted scaling was applied to the point-contact peak shape model. In this case, f_{obs} is at its maximum value of 1, and the p+ event peak is so low in amplitude that it is not visible.

peak is set to 0.

The alpha activity parameter σ fits to a value of $430\pm30\,\mathrm{mm}^{-1}$, and the height h fits to a value of 3.75 ± 0.03 mm. The fit is done using the MINUIT log-likelihood fitting algorithm, given the low count rates in the high-energy data. The predicted spectrum fit the data quite well, as seen in Fig. 6.10, giving a χ^2/N_{DF} of $378/269 = 1.40$.

In the highest-energy cluster of events, we that the energy distribution is broader than the single peak observed in PONaMa-1. In Fig. 6.10, we have adjusted the Gaussian peak parameters of the p+ distribution to match (by eye) the observed peak. The centroid μ has been set 100 keV lower in energy than predicted from the TUBE measurements, and the

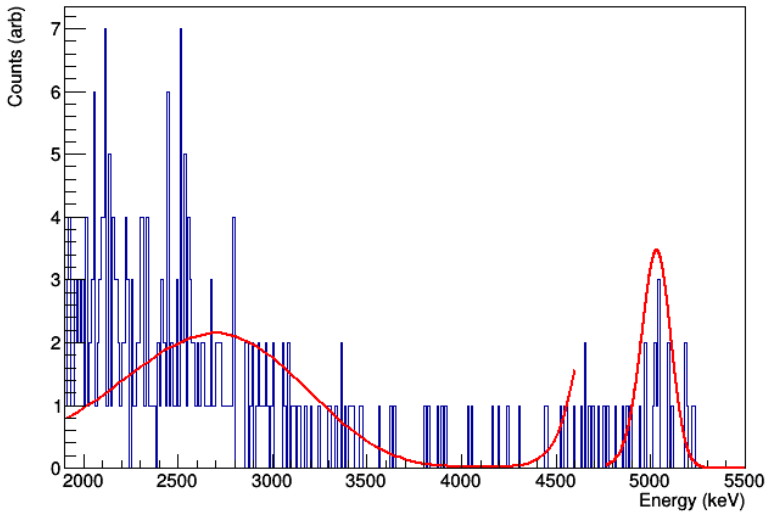

Figure 6.10: The high-energy spectrum from the MAJORANA DEMONSTRATOR Data Sets 1-4, with muon, data cleaning, single-site, and multiplicity cuts applied, is in blue. Bins are 10 keV wide. The point-contact contamination model for passivated surface events (in red) was fit to the data. f_{obs} was set to 0.5. Changes were also made to the p+ Gaussian distribution to account for the impact of including multiple detectors. The Gaussian peak position was shifted downwards in energy by an additional 100 keV, and the width σ was set to 70 keV (instead of the 9 keV measured in TUBE).

width σ has been set to 70 keV, instead of the predicted 9 keV. f_{obs} has been set 0.5.

Since we have modeled the point-contact events as having no incidence angle dependence, and the surface of the dimple has a dramatic curve to it, some energy broadening is expected based on the varying path lengths through the dead region. Given the complicated geometry of this region, a simple analytical model cannot correctly model this behavior, and a full simulation would be needed to reproduce the peak shape. There is also the possibility of variation in the dead layer of different detectors, which are being summed together here.

These results suggest that the alpha background events seen in the MAJORANA DEMON-

STRATOR are likely associated with the plastic bushing that holds the contact pin. This part, with a 6.35 mm diameter, is 3.65 mm above the passivated surface, centered on the contact pin position. Given the simple point-source contamination model used to create the spectral function, this agreement, to within 5% of the bushing position, is extremely suggestive.

That said, the point source approximation used in this model fails for small h. Additionally, other plastic parts in the vicinity of the passivated surface, like the crystal insulators, are not correctly approximated by the centered point-source model used here. To definitively identify the source of the alpha background events, a full simulation is needed, as discussed in Sec. 7.3.

Chapter 7
CONCLUSIONS

7.1 Summary of Results

In this work, we have demonstrated one possible implementation of an algorithm to identify passivated-surface alpha events in P-PC HPGe detectors. By studying alpha events directly using the TUBE scanner, we have characterized the response of the entire alpha-sensitive surface of a detector like those used in the MAJORANA DEMONSTRATOR, describing both the charge trapping/loss and delayed charge recovery (DCR) effect on the passivated and p+ contact surfaces.

This study has allowed us to identify the phenomenon responsible for the DCR effect: near-surface trapping of holes in the semiconductor crystal. This effect has been shown to be highly significant, leading to loss of over 50% of the incident alpha energy at some locations on the detector surface. It has also been shown to be highly dependent on the radial distance from the p+ contact of the alpha's incidence position. Using a combination of the newly-developed DCR pulse-shape parameter and the previously-implemented A/E parameter (or an alternative measure of pulse drift time), alpha events on all sensitive surfaces can be reliably identified with less than 0.2% sacrifice of $0\nu\beta\beta$ signal events.

By applying the DCR analysis to the MAJORANA DEMONSTRATOR low-background data, backgrounds in the $0\nu\beta\beta$ region-of-interest have been reduced by a factor of 29, improving the expected sensitivity of the experiment by a factor of 3.

The measurements taken with TUBE have also allowed us to model the expected alpha background spectral shape in the DEMONSTRATOR. Using an analytic approach, we have

studied two models describing the distribution of alpha-emitting radioactive contaminants in the experiment – one in which the entire passivated surface of each detector has been contaminated, and one in which the background events originate in a point source located some distance above the p+ contact of each detector. We have found that the first model does not match the observed spectrum, and that the second model predicts the spectral features observed in the DEMONSTRATOR quite accurately.

In spite of the many simplifying assumptions used in this study, a two-parameter fit of the model spectrum to the data indicates that the plastics used in the MAJORANA detector unit are likely responsible for the alpha background observed. Though further work is needed to confirm that this is the case, the removal and replacement of these contaminated parts in already being considered.

7.2 Proposed Improvements to the DCR Analysis

Several improvements can still be made to further improve the DCR analysis parameter algorithm, and particularly to reduce the uncertainties associated with its bulk acceptance. The two main contributions to the uncertainty of this value are the pulse shape uncertainty σ_{PS} and the stability $\sigma_{stab.}$.

The pulse-shape uncertainty currently appears to be dominated by the effect of charge trapping. Though one implementation of a charge trapping correction has been described in this work, it relies on very precise calibration of a pulse-maximum energy estimator, and has proven impractical to implement in the DEMONSTRATOR. An alternative approach currently being studied by the MAJORANA Collaboration suggests that a direct measure of the trapping on a waveform-by-waveform basis, based on the drift time of the pulse, can provide a far more accurate measurement of the degeneracy of the bulk trapping and DCR effects. We can subsequently corrected for this effect, reducing the width of the bulk-event DCR distribution and allowing reduced signal sacrifice without a reduction in alpha-identification power.

Multi-site events that evade identification by the A vs. E analysis are also contributing to the measured σ_{PS}. This effect could be reduced by implementing additional single-site

event selection, like a waveform-library-based pulse shape analysis.

The stability-related uncertainty also has two main contributions, both of which can be addressed by future improvements to this analysis: changing pole-zero decay constants and changing noise conditions. The first of these can be addressed by implementing a true pole-zero correction in the MAJORANA analysis, rather than the effective correction used here. Such a correction can be re-calculated based on physics events from weekly energy calibrations, or even more frequently using the onboard pulsers. This would eliminate the effect of small instabilities over months of data-taking seen using the current strategy, in which pole-zero decay constants are calculated once per data set for each channel, and re-calculated when major instabilities are observed.

The latter can be addressed by implementing waveform filtering prior to the DCR parameter evaluation. Since it is high-frequency noise that causes bulk DCR distribution broadening, and the low-frequency components of the waveform that indicate that delayed charge recovery is occurring, the use of notch, wavelet, or bandpass filtering should limit the impact of noise quite effectively.

7.3 Future Studies of Alpha Backgrounds

In the near future, studies with the TUBE scanner will attempt to identify the origin of the observed DCR instability observed in the system. By bias- and temperature-cycling the system, we should be able to distinguish the effects of the two leading hypotheses: surface-channel formation and deep trap filling. Another near-term study will focus on taking alpha data with a longer digitization window– over 100 μs instead of the 30 μs used in this work. This will allow us to further characterize the rate of charge re-release. Other studies with the TUBE scanner will focus on characterizing the thickness of the charge trapping region associated with the passivated surface, whether by varying the incidence angle of an alpha source or by measuring the energy-dependent efficiency of various low-energy gamma peaks with a multi-line gamma source like ^{133}Ba.

Further work should also be done to study the DCR effect in other detector geometries,

like Canberra's BEGe P-PC, and new inverted-coax geometries being considered by the LEGEND Collaboration. To this purpose, a re-analysis of the TUBE BEGe scan data is being considered, and the MAJORANA group at the University of Washington is proceeding in the design and eventual construction of a scanner that will allow surface measurements of larger-diameter detectors with variable angle-of-incidence.

Upcoming efforts by the MAJORANA Collaboration will also focus on incorporating the observed passivated-surface behavior into simulations of alpha backgrounds. This will allow a more accurate background model for the experiment to be constructed, and will lead to a more precise identification of contaminated elements in the DEMONSTRATOR than can be provided by the simplified analytical model used in this work.

7.4 The Future of Double-Beta Decay Searches

The search for $0\nu\beta\beta$ decay stands at an exciting crossroads. The current generation of experiments, like the DEMONSTRATOR, GERDA, CUORE, EXO-200, KamLAND-Zen and others, have released or will be releasing new results in the coming few years. These experiments have used a wide range of techniques, whether in their choice of isotope, detection technique, or background reduction strategies.

To move to the tonne scale, and to achieve the low backgrounds needed to be sensitive to the entire inverted hierarchy range of $m_{\beta\beta}$, future experiments will have to draw on a variety of these techniques. This is the approach taken by the LEGEND Collaboration, which is drawing on the techniques developed by both the GERDA and the MAJORANA Collaborations.

One strategy that can make a major impact on an experiment's background rejection capability is particle identification, distinguishing beta decay events from alpha and gamma events. Though it is not typically described in those terms, multi-site event rejection in P-PC detectors is a sort of gamma particle identification; in this work, we have shown that the DCR analysis can provide a similar tool to identify alpha events with very little signal event sacrifice. These capabilities, as well as the extremely low ROI background rates seen

in the current ^{76}Ge experiments, provide an exciting path forward for the field.

This work also demonstrates the power that having a complete description of the physics of detectors can have in rare event searches. When studying more common processes, "fringe cases" like the passivated surface behavior studied here can be disregarded. In studies of exceedingly rare physics, like $0\nu\beta\beta$, however, these cases have to be as completely understood as possible, even if the fraction of the detector affected is far less than 1%.

In fact, understanding the phenomena behind these anomalous behaviors can actually serve as a powerful tool, as it has in the case studied here. This is an important lesson to retain in developing new low-background techniques. This work and other efforts by the MAJORANA Collaboration have shown that far more information still remains to be extracted from our HPGe signals; by leveraging it, we can reach new levels of sensitivity even with the same, currently-operating experiment. A similar campaign of simulations and relatively simply-accomplished dedicated measurements could lead to further improvements in other experiments as well.

BIBLIOGRAPHY

[1] Software developed by i-yang lee (lbnl), karin lagergren and david radford (ornl).

[2] C.E. Aalseth, M. Amman, F.T. Avignone III, H.O. Back, A.S. Barabash, P.S. Barbeau, M. Bergevin, F.E. Bertrand, M. Boswell, V. Brudanin, W. Bugg, T.H. Burritt, M. Busch, G. Capps, Y.-D. Chan, J.I. Collar, R.J. Cooper, R. Creswick, J.A. Detwiler, J. Diaz, P.J. Doe, Yu. Efremenko, V. Egorov, H. Ejiri, S.R. Elliott, J. Ely, J. Esterline, H. Farach, J.E. Fast, N. Fields, P. Finnerty, B. Fujikawa, E. Fuller, V.M. Gehman, G.K. Giovanetti, V.E. Guiseppe, K. Gusey, A.L. Hallin, G.C. Harper, R. Hazama, R. Henning, A. Hime, E.W. Hoppe, T.W. Hossbach, M.A. Howe, R.A. Johnson, K.J. Keeter, M. Keillor, C. Keller, J.D. Kephart, M.F. Kidd, A. Knecht, O. Kochetov, S.I. Konovalov, R.T. Kouzes, L. Leviner, J.C. Loach, P.N. Luke, S. MacMullin, M.G. Marino, R.D. Martin, D.-M. Mei, H.S. Miley, M.L. Miller, L. Mizouni, A.W. Meyers, M. Nomachi, J.L. Orrell, D. Peterson, D.G. Phillips II, A.W.P. Poon, G. Prior, J. Qian, D.C. Radford, K. Rielage, R.G.H. Robertson, L. Rodriguez, K.P. Rykaczewski, H. Salazar, A.G. Schubert, T. Shima, M. Shirchenko, D. Steele, J. Strain, G. Swift, K. Thomas, V. Timkin, W. Tornow, T.D. Van Wechel, I. Vanyushin, R.L. Varner, K. Vetter, J.F. Wilkerson, B.A. Wolfe, W. Xiang, E. Yakushev, H. Yaver, A.R. Young, C.-H. Yu, V. Yumatov, C. Zhang, and S. Zimmerman. Astroparticle physics with a customized low-background broad energy germanium detector. *Nuclear Instruments and Methods in Physics Research Section A: Accelerators, Spectrometers, Detectors and Associated Equipment*, 652(1):692 – 695, 2011. Symposium on Radiation Measurements and Applications (SORMA) {XII} 2010.

[3] K. Abe, J. Amey, C. Andreopoulos, M. Antonova, S. Aoki, A. Ariga, D. Autiero, S. Ban, M. Barbi, G. J. Barker, G. Barr, C. Barry, P. Bartet-Friburg, M. Batkiewicz, V. Berardi, S. Berkman, S. Bhadra, S. Bienstock, A. Blondel, S. Bolognesi, S. Bordoni, S. B. Boyd, D. Brailsford, A. Bravar, C. Bronner, M. Buizza Avanzini, R. G. Calland, T. Campbell, S. Cao, S. L. Cartwright, M. G. Catanesi, A. Cervera, C. Checchia, D. Cherdack, N. Chikuma, G. Christodoulou, A. Clifton, J. Coleman, G. Collazuol, D. Coplowe, A. Cudd, A. Dabrowska, G. De Rosa, T. Dealtry, P. F. Denner, S. R. Dennis, C. Densham, D. Dewhurst, F. Di Lodovico, S. Di Luise, S. Dolan, O. Drapier, K. E. Duffy, J. Dumarchez, M. Dziewiecki, S. Emery-Schrenk, A. Ereditato, T. Feusels, A. J. Finch, G. A. Fiorentini, M. Friend, Y. Fujii, D. Fukuda, Y. Fukuda, V. Galymov, A. Garcia, C. Giganti, F. Gizzarelli, T. Golan, M. Gonin, D. R. Hadley, L. Haegel, M. D. Haigh, D. Hansen, J. Harada, M. Hartz, T. Hasegawa, N. C. Hastings, T. Hayashino, Y. Hayato, R. L. Helmer, A. Hillairet, T. Hiraki, A. Hiramoto, S. Hirota, M. Hogan,

J. Holeczek, F. Hosomi, K. Huang, A. K. Ichikawa, M. Ikeda, J. Imber, J. Insler, R. A. Intonti, T. Ishida, T. Ishii, E. Iwai, K. Iwamoto, A. Izmaylov, B. Jamieson, M. Jiang, S. Johnson, P. Jonsson, C. K. Jung, M. Kabirnezhad, A. C. Kaboth, T. Kajita, H. Kakuno, J. Kameda, D. Karlen, T. Katori, E. Kearns, M. Khabibullin, A. Khotjantsev, H. Kim, J. Kim, S. King, J. Kisiel, A. Knight, A. Knox, T. Kobayashi, L. Koch, T. Koga, A. Konaka, K. Kondo, L. L. Kormos, A. Korzenev, Y. Koshio, K. Kowalik, W. Kropp, Y. Kudenko, R. Kurjata, T. Kutter, J. Lagoda, I. Lamont, M. Lamoureux, E. Larkin, P. Lasorak, M. Laveder, M. Lawe, M. Licciardi, T. Lindner, Z. J. Liptak, R. P. Litchfield, X. Li, A. Longhin, J. P. Lopez, T. Lou, L. Ludovici, X. Lu, L. Magaletti, K. Mahn, M. Malek, S. Manly, A. D. Marino, J. F. Martin, P. Martins, S. Martynenko, T. Maruyama, V. Matveev, K. Mavrokoridis, W. Y. Ma, E. Mazzucato, M. McCarthy, N. McCauley, K. S. McFarland, C. McGrew, A. Mefodiev, C. Metelko, M. Mezzetto, P. Mijakowski, A. Minamino, O. Mineev, S. Mine, A. Missert, M. Miura, S. Moriyama, Th. A. Mueller, J. Myslik, T. Nakadaira, M. Nakahata, K. G. Nakamura, K. Nakamura, K. D. Nakamura, Y. Nakanishi, S. Nakayama, T. Nakaya, K. Nakayoshi, C. Nantais, C. Nielsen, M. Nirkko, K. Nishikawa, Y. Nishimura, P. Novella, J. Nowak, H. M. O'Keeffe, K. Okumura, T. Okusawa, W. Oryszczak, S. M. Oser, T. Ovsyannikova, R. A. Owen, Y. Oyama, V. Palladino, J. L. Palomino, V. Paolone, N. D. Patel, P. Paudyal, M. Pavin, D. Payne, J. D. Perkin, Y. Petrov, L. Pickard, L. Pickering, E. S. Pinzon Guerra, C. Pistillo, B. Popov, M. Posiadala-Zezula, J.-M. Poutissou, R. Poutissou, P. Przewlocki, B. Quilain, T. Radermacher, E. Radicioni, P. N. Ratoff, M. Ravonel, M. A. Rayner, A. Redij, E. Reinherz-Aronis, C. Riccio, P. A. Rodrigues, E. Rondio, B. Rossi, S. Roth, A. Rubbia, A. Rychter, K. Sakashita, F. Sánchez, E. Scantamburlo, K. Scholberg, J. Schwehr, M. Scott, Y. Seiya, T. Sekiguchi, H. Sekiya, D. Sgalaberna, R. Shah, A. Shaikhiev, F. Shaker, D. Shaw, M. Shiozawa, T. Shirahige, S. Short, M. Smy, J. T. Sobczyk, H. Sobel, M. Sorel, L. Southwell, J. Steinmann, T. Stewart, P. Stowell, Y. Suda, S. Suvorov, A. Suzuki, S. Y. Suzuki, Y. Suzuki, R. Tacik, M. Tada, A. Takeda, Y. Takeuchi, H. K. Tanaka, H. A. Tanaka, D. Terhorst, R. Terri, T. Thakore, L. F. Thompson, S. Tobayama, W. Toki, T. Tomura, C. Touramanis, T. Tsukamoto, M. Tzanov, Y. Uchida, M. Vagins, Z. Vallari, G. Vasseur, T. Vladisavljevic, T. Wachala, C. W. Walter, D. Wark, M. O. Wascko, A. Weber, R. Wendell, R. J. Wilkes, M. J. Wilking, C. Wilkinson, J. R. Wilson, R. J. Wilson, C. Wret, Y. Yamada, K. Yamamoto, M. Yamamoto, C. Yanagisawa, T. Yano, S. Yen, N. Yershov, M. Yokoyama, K. Yoshida, T. Yuan, M. Yu, A. Zalewska, J. Zalipska, L. Zambelli, K. Zaremba, M. Ziembicki, E. D. Zimmerman, M. Zito, and J. Żmuda. Combined analysis of neutrino and antineutrino oscillations at t2k. *Phys. Rev. Lett.*, 118:151801, Apr 2017.

[4] K. Abe et al. Letter of Intent: The Hyper-Kamiokande Experiment — Detector Design and Physics Potential —. 2011.

[5] N. Abgrall, E. Aguayo, F. T. Avignone, A. S. Barabash, F. E. Bertrand, M. Boswell, V. Brudanin, M. Busch, A. S. Caldwell, Y.-D. Chan, C. D. Christofferson, D. C. Combs,

J. A. Detwiler, P. J. Doe, Yu. Efremenko, V. Egorov, H. Ejiri, S. R. Elliott, J. Esterline, J. E. Fast, P. Finnerty, F. M. Fraenkle, A. Galindo-Uribarri, G. K. Giovanetti, J. Goett, M. P. Green, J. Gruszko, V. E. Guiseppe, K. Gusev, A. L. Hallin, R. Hazama, A. Hegai, R. Henning, E. W. Hoppe, S. Howard, M. A. Howe, K. J. Keeter, M. F. Kidd, A. Knecht, O. Kochetov, S. I. Konovalov, R. T. Kouzes, B. D. LaFerriere, J. Leon, L. E. Leviner, J. C. Loach, P. N. Luke, S. MacMullin, R. D. Martin, S. Mertens, L. Mizouni, M. Nomachi, J. L. Orrell, C. O'Shaughnessy, N. R. Overman, David Phillips, A. W. P. Poon, K. Pushkin, D. C. Radford, K. Rielage, R. G. H. Robertson, M. C. Ronquest, A. G. Schubert, B. Shanks, T. Shima, M. Shirchenko, K. J. Snavely, N. Snyder, D. Steele, J. Strain, A. M. Suriano, J. Thompson, V. Timkin, W. Tornow, R. L. Varner, S. Vasilyev, K. Vetter, K. Vorren, B. R. White, J. F. Wilkerson, T. Williams, W. Xu, E. Yakushev, A. R. Young, C.-H. Yu, and V. Yumatov. The majorana demonstrator neutrinoless double-beta decay experiment. *Advances in High Energy Physics*, 2014:18, 2014.

[6] N. Abgrall, E. Aguayo, F.T. Avignone III, A.S. Barabash, F.E. Bertrand, V. Brudanin, M. Busch, D. Byram, A.S. Caldwell, Y-D. Chan, C.D. Christofferson, D.C. Combs, C. Cuesta, J.A. Detwiler, P.J. Doe, Yu. Efremenko, V. Egorov, H. Ejiri, S.R. Elliott, J. Esterline, J.E. Fast, P. Finnerty, F.M. Fraenkle, A. Galindo-Uribarri, G.K. Giovanetti, J. Goett, M.P. Green, J. Gruszko, V.E. Guiseppe, K. Gusev, A.L. Hallin, R. Hazama, A. Hegai, R. Henning, E.W. Hoppe, S. Howard, M.A. Howe, K.J. Keeter, M.F. Kidd, O. Kochetov, S.I. Konovalov, R.T. Kouzes, B.D. LaFerriere, J. Diaz Leon, L.E. Leviner, J.C. Loach, J. MacMullin, R.D. Martin, S.J. Meijer, S. Mertens, M.L. Miller, L. Mizouni, M. Nomachi, J.L. Orrell, C. OShaughnessy, N.R. Overman, R. Petersburg, D.G. Phillips II, A.W.P. Poon, K. Pushkin, D.C. Radford, J. Rager, K. Rielage, R.G.H. Robertson, E. Romero-Romero, M.C. Ronquest, B. Shanks, T. Shima, M. Shirchenko, K.J. Snavely, N. Snyder, A. Soin, A.M. Suriano, D. Tedeschi, J. Thompson, V. Timkin, W. Tornow, J.E. Trimble, R.L. Varner, S. Vasilyev, K. Vetter, K. Vorren, B.R. White, J.F. Wilkerson, C. Wiseman, W. Xu, E. Yakushev, A.R. Young, C.-H. Yu, V. Yumatov, and I. Zhitnikov. The majorana parts tracking database. *Nuclear Instruments and Methods in Physics Research Section A: Accelerators, Spectrometers, Detectors and Associated Equipment*, 779:52 – 62, 2015.

[7] N. Abgrall, I. J. Arnquist, F. T. Avignone, A. S. Barabash, F. E. Bertrand, A. W. Bradley, V. Brudanin, M. Busch, M. Buuck, T. S. Caldwell, Y.-D. Chan, C. D. Christofferson, P.-H. Chu, C. Cuesta, J. A. Detwiler, C. Dunagan, Y. Efremenko, H. Ejiri, S. R. Elliott, T. Gilliss, G. K. Giovanetti, J. Goett, M. P. Green, J. Gruszko, I. S. Guinn, V. E. Guiseppe, C. R. S. Haufe, R. Henning, E. W. Hoppe, S. Howard, M. A. Howe, B. R. Jasinski, K. J. Keeter, M. F. Kidd, S. I. Konovalov, R. T. Kouzes, A. M. Lopez, J. MacMullin, R. D. Martin, R. Massarczyk, S. J. Meijer, S. Mertens, C. O'Shaughnessy, A. W. P. Poon, D. C. Radford, J. Rager, A. L. Reine, K. Rielage, R. G. H. Robertson, B. Shanks, M. Shirchenko, A. M. Suriano, D. Tedeschi, J. E. Trimble, R. L. Varner,

S. Vasilyev, K. Vetter, K. Vorren, B. R. White, J. F. Wilkerson, C. Wiseman, W. Xu, E. Yakushev, C.-H. Yu, V. Yumatov, I. Zhitnikov, B. X. Zhu, and MAJORANA Collaboration. New Limits on Bosonic Dark Matter, Solar Axions, Pauli Exclusion Principle Violation, and Electron Decay from the Majorana Demonstrator. *Physical Review Letters*, 118(16):161801, April 2017.

[8] N. Abgrall, I.J. Arnquist, F.T. Avignone III, H.O. Back, A.S. Barabash, F.E. Bertrand, M. Boswell, A.W. Bradley, V. Brudanin, M. Busch, M. Buuck, D. Byram, A.S. Caldwell, Y.-D. Chan, C.D. Christofferson, P.-H. Chu, C. Cuesta, J.A. Detwiler, J.A. Dunmore, Yu. Efremenko, H. Ejiri, S.R. Elliott, P. Finnerty, A. Galindo-Uribarri, V.M. Gehman, T. Gilliss, G.K. Giovanetti, J. Goett, M.P. Green, J. Gruszko, I.S. Guinn, V.E. Guiseppe, R. Henning, E.W. Hoppe, S. Howard, M.A. Howe, B.R. Jasinski, R.A. Johnson, K.J. Keeter, M.F. Kidd, O. Kochetov, S.I. Konovalov, R.T. Kouzes, B.D. LaFerriere, J. Leon, J.C. Loach, J. MacMullin, S. MacMullin, R.D. Martin, R. Massarczyk, S. Meijer, S. Mertens, M.L. Miller, J.L. Orrell, C. O'Shaughnessy, N.R. Overman, A.W.P. Poon, K. Pushkin, D.C. Radford, J. Rager, K. Rielage, R.G.H. Robertson, E. Romero-Romero, M.C. Ronquest, A.G. Schubert, B. Shanks, M. Shirchenko, K.J. Snavely, N. Snyder, D. Steele, A.M. Suriano, D. Tedeschi, J.E. Trimble, R.L. Varner, S. Vasilyev, K. Vetter, K. Vorren, B.R. White, J.F. Wilkerson, C. Wiseman, W. Xu, E. Yakushev, C.-H. Yu, V. Yumatov, and I. Zhitnikov. The majorana demonstrator radioassay program. *Nuclear Instruments and Methods in Physics Research Section A: Accelerators, Spectrometers, Detectors and Associated Equipment*, 828:22 – 36, 2016.

[9] I. Abt, L. Garbini, C. Gooch, S. Irlbeck, X. Liu, M. Palermo, and O. Schulz. Alpha-event and surface characterisation in segmented true-coaxial {HPGe} detectors. *Nuclear Instruments and Methods in Physics Research Section A: Accelerators, Spectrometers, Detectors and Associated Equipment*, 858:80 – 89, 2017.

[10] R. Acciarri et al. Long-Baseline Neutrino Facility (LBNF) and Deep Underground Neutrino Experiment (DUNE). 2016.

[11] K.-H. Ackermann, M. Agostini, M. Allardt, M. Altmann, E. Andreotti, A. M. Bakalyarov, M. Balata, I. Barabanov, M. Barnabé Heider, N. Barros, L. Baudis, C. Bauer, N. Becerici-Schmidt, E. Bellotti, S. Belogurov, S. T. Belyaev, G. Benato, A. Bettini, L. Bezrukov, T. Bode, V. Brudanin, R. Brugnera, D. Budjáš, A. Caldwell, C. Cattadori, A. Chernogorov, O. Chkvorets, F. Cossavella, A. D'Andragora, E. V. Demidova, A. Denisov, A. di Vacri, A. Domula, V. Egorov, R. Falkenstein, A. Ferella, K. Freund, F. Froborg, N. Frodyma, A. Gangapshev, A. Garfagnini, J. Gasparro, S. Gazzana, R. Gonzalez de Orduna, P. Grabmayr, V. Gurentsov, K. Gusev, K. K. Guthikonda, W. Hampel, A. Hegai, M. Heisel, S. Hemmer, G. Heusser, W. Hofmann, M. Hult, L. V. Inzhechik, L. Ioannucci, J. Janicskó Csáthy, J. Jochum, M. Junker,

R. Kankanyan, S. Kianovsky, T. Kihm, J. Kiko, I. V. Kirpichnikov, A. Kirsch, A. Klimenko, M. Knapp, K. T. Knöpfle, O. Kochetov, V. N. Kornoukhov, K. Kröninger, V. Kusminov, M. Laubenstein, A. Lazzaro, V. I. Lebedev, B. Lehnert, D. Lenz, H. Liao, M. Lindner, I. Lippi, J. Liu, X. Liu, A. Lubashevskiy, B. Lubsandorzhiev, A. A. Machado, B. Majorovits, W. Maneschg, G. Marissens, S. Mayer, G. Meierhofer, I. Nemchenok, L. Niedermeier, S. Nisi, J. Oehm, C. O'Shaughnessy, L. Pandola, P. Peiffer, K. Pelczar, A. Pullia, S. Riboldi, F. Ritter, C. Rossi Alvarez, C. Sada, M. Salathe, C. Schmitt, S. Schönert, J. Schreiner, J. Schubert, O. Schulz, U. Schwan, B. Schwingenheuer, H. Seitz, E. Shevchik, M. Shirchenko, H. Simgen, A. Smolnikov, L. Stanco, F. Stelzer, H. Strecker, M. Tarka, U. Trunk, C. A. Ur, A. A. Vasenko, S. Vogt, O. Volynets, K. von Sturm, V. Wagner, M. Walter, A. Wegmann, M. Wojcik, E. Yanovich, P. Zavarise, I. Zhitnikov, S. V. Zhukov, D. Zinatulina, K. Zuber, and G. Zuzel. The Gerda experiment for the search of 0 $\nu\beta\beta$ decay in ^{76}Ge. *European Physical Journal C*, 73:2330, March 2013.

[12] M. Agostini. *Signal and background studies for the search of neutrinoless double beta decay in GERDA*. PhD thesis, Technische Unversitat Munchen, 2013.

[13] M. Agostini, M. Allardt, E. Andreotti, A. M. Bakalyarov, M. Balata, I. Barabanov, M. Barnabé Heider, N. Barros, L. Baudis, C. Bauer, N. Becerici-Schmidt, E. Bellotti, S. Belogurov, S. T. Belyaev, G. Benato, A. Bettini, L. Bezrukov, T. Bode, V. Brudanin, R. Brugnera, D. Budjáš, A. Caldwell, C. Cattadori, A. Chernogorov, F. Cossavella, E. V. Demidova, A. Domula, V. Egorov, R. Falkenstein, A. Ferella, K. Freund, N. Frodyma, A. Gangapshev, A. Garfagnini, C. Gotti, P. Grabmayr, V. Gurentsov, K. Gusev, K. K. Guthikonda, W. Hampel, A. Hegai, M. Heisel, S. Hemmer, G. Heusser, W. Hofmann, M. Hult, L. V. Inzhechik, L. Ioannucci, J. Janicskó Csáthy, J. Jochum, M. Junker, T. Kihm, I. V. Kirpichnikov, A. Kirsch, A. Klimenko, K. T. Knöpfle, O. Kochetov, V. N. Kornoukhov, V. V. Kuzminov, M. Laubenstein, A. Lazzaro, V. I. Lebedev, B. Lehnert, H. Y. Liao, M. Lindner, I. Lippi, X. Liu, A. Lubashevskiy, B. Lubsandorzhiev, G. Lutter, C. Macolino, A. A. Machado, B. Majorovits, W. Maneschg, M. Misiaszek, I. Nemchenok, S. Nisi, C. O'Shaughnessy, L. Pandola, K. Pelczar, G. Pessina, A. Pullia, S. Riboldi, N. Rumyantseva, C. Sada, M. Salathe, C. Schmitt, J. Schreiner, O. Schulz, B. Schwingenheuer, S. Schönert, E. Shevchik, M. Shirchenko, H. Simgen, A. Smolnikov, L. Stanco, H. Strecker, M. Tarka, C. A. Ur, A. A. Vasenko, O. Volynets, K. von Sturm, V. Wagner, M. Walter, A. Wegmann, T. Wester, M. Wojcik, E. Yanovich, P. Zavarise, I. Zhitnikov, S. V. Zhukov, D. Zinatulina, K. Zuber, and G. Zuzel. Pulse shape discrimination for gerda phase i data. *The European Physical Journal C*, 73(10):2583, Oct 2013.

[14] M. Agostini, M. Barnabe-Heider, T. Bode, D. Budjáš, A. Lazzaro, and S. Schönert. Bege detector response to alpha-induced energy depositions on the p+ electrode and groove

surfaces. bege detector response to alpha-induced energy depositions on the p+ electrode and groove surfaces. GERDA Scientific/Technical Report GSTR-13-006, Physik Department E15, Technische Universität München, July 2013.

[15] M. Agostini, G. Benato, and J. Detwiler. Discovery probability of next-generation neutrinoless double-β decay experiments. *ArXiv e-prints*, May 2017.

[16] M. Agostini et al. The background in the $0\nu\beta\beta$ experiment GERDA. *Eur. Phys. J.*, C74(4):2764, 2014.

[17] E. Aguayo, M. Amman, F.T. Avignone, A.S. Barabash, P.J. Barton, J.R. Beene, F.E. Bertrand, M. Boswell, V. Brudanin, M. Busch, Y.-D. Chan, C.D. Christofferson, J.I. Collar, D.C. Combs, R.J. Cooper, J.A. Detwiler, P.J. Doe, Yu. Efremenko, V. Egorov, H. Ejiri, S.R. Elliott, J. Esterline, J.E. Fast, N. Fields, P. Finnerty, F.M. Fraenkle, A. Galindo-Uribarri, V.M. Gehman, G.K. Giovanetti, M.P. Green, V.E. Guiseppe, K. Gusey, A.L. Hallin, R. Hazama, R. Henning, E.W. Hoppe, M. Horton, S. Howard, M.A. Howe, R.A. Johnson, K.J. Keeter, M.F. Kidd, A. Knecht, O. Kochetov, S.I. Konovalov, R.T. Kouzes, B.D. LaFerriere, J. Leon, L.E. Leviner, J.C. Loach, Q. Looker, P.N. Luke, S. MacMullin, M.G. Marino, R.D. Martin, J.H. Merriman, M.L. Miller, L. Mizouni, M. Nomachi, J.L. Orrell, N.R. Overman, G. Perumpilly, D.G. Phillips, A.W.P. Poon, D.C. Radford, K. Rielage, R.G.H. Robertson, M.C. Ronquest, A.G. Schubert, T. Shima, M. Shirchenko, K.J. Snavely, D. Steele, J. Strain, V. Timkin, W. Tornow, R.L. Varner, K. Vetter, K. Vorren, J.F. Wilkerson, E. Yakushev, H. Yaver, A.R. Young, C.-H. Yu, and V. Yumatov. Characteristics of signals originating near the lithium-diffused n+ contact of high purity germanium p-type point contact detectors. *Nuclear Instruments and Methods in Physics Research Section A: Accelerators, Spectrometers, Detectors and Associated Equipment*, 701:176 – 185, 2013.

[18] Q. R. Ahmad, R. C. Allen, T. C. Andersen, J. D. Anglin, G. Bühler, J. C. Barton, E. W. Beier, M. Bercovitch, J. Bigu, S. Biller, R. A. Black, I. Blevis, R. J. Boardman, J. Boger, E. Bonvin, M. G. Boulay, M. G. Bowler, T. J. Bowles, S. J. Brice, M. C. Browne, T. V. Bullard, T. H. Burritt, K. Cameron, J. Cameron, Y. D. Chan, M. Chen, H. H. Chen, X. Chen, M. C. Chon, B. T. Cleveland, E. T. Clifford, J. H. Cowan, D. F. Cowen, G. A. Cox, Y. Dai, X. Dai, F. Dalnoki-Veress, W. F. Davidson, P. J. Doe, G. Doucas, M. R. Dragowsky, C. A. Duba, F. A. Duncan, J. Dunmore, E. D. Earle, S. R. Elliott, H. C. Evans, G. T. Ewan, J. Farine, H. Fergani, A. P. Ferraris, R. J. Ford, M. M. Fowler, K. Frame, E. D. Frank, W. Frati, J. V. Germani, S. Gil, A. Goldschmidt, D. R. Grant, R. L. Hahn, A. L. Hallin, E. D. Hallman, A. Hamer, A. A. Hamian, R. U. Haq, C. K. Hargrove, P. J. Harvey, R. Hazama, R. Heaton, K. M. Heeger, W. J. Heintzelman, J. Heise, R. L. Helmer, J. D. Hepburn, H. Heron, J. Hewett, A. Hime, M. Howe, J. G. Hykawy, M. C. Isaac, P. Jagam, N. A. Jelley, C. Jillings, G. Jonkmans, J. Karn, P. T. Keener, K. Kirch, J. R. Klein, A. B. Knox,

R. J. Komar, R. Kouzes, T. Kutter, C. C. Kyba, J. Law, I. T. Lawson, M. Lay, H. W. Lee, K. T. Lesko, J. R. Leslie, I. Levine, W. Locke, M. M. Lowry, S. Luoma, J. Lyon, S. Majerus, H. B. Mak, A. D. Marino, N. McCauley, A. B. McDonald, D. S. McDonald, K. McFarlane, G. McGregor, W. McLatchie, R. M. Drees, H. Mes, C. Mifflin, G. G. Miller, G. Milton, B. A. Moffat, M. Moorhead, C. W. Nally, M. S. Neubauer, F. M. Newcomer, H. S. Ng, A. J. Noble, E. B. Norman, V. M. Novikov, M. O'Neill, C. E. Okada, R. W. Ollerhead, M. Omori, J. L. Orrell, S. M. Oser, A. W. Poon, T. J. Radcliffe, A. Roberge, B. C. Robertson, R. G. Robertson, J. K. Rowley, V. L. Rusu, E. Saettler, K. K. Schaffer, A. Schuelke, M. H. Schwendener, H. Seifert, M. Shatkay, J. J. Simpson, D. Sinclair, P. Skensved, A. R. Smith, M. W. Smith, N. Starinsky, T. D. Steiger, R. G. Stokstad, R. S. Storey, B. Sur, R. Tafirout, N. Tagg, N. W. Tanner, R. K. Taplin, M. Thorman, P. Thornewell, P. T. Trent, Y. I. Tserkovnyak, R. van Berg, R. G. van de Water, C. J. Virtue, C. E. Waltham, J.-X. Wang, D. L. Wark, N. West, J. B. Wilhelmy, J. F. Wilkerson, J. Wilson, P. Wittich, J. M. Wouters, and M. Yeh. Measurement of the Rate of $\nu_e + \mathrm{d} \rightarrow \mathrm{p} + \mathrm{p} + \mathrm{e}^-$ Interactions Produced by ^{8}B Solar Neutrinos at the Sudbury Neutrino Observatory. *Physical Review Letters*, 87(7):071301, August 2001.

[19] Fengpeng An et al. Neutrino Physics with JUNO. *J. Phys.*, G43(3):030401, 2016.

[20] V. N. Aseev, A. I. Belesev, A. I. Berlev, E. V. Geraskin, A. A. Golubev, N. A. Likhovid, V. M. Lobashev, A. A. Nozik, V. S. Pantuev, V. I. Parfenov, A. K. Skasyrskaya, F. V. Tkachov, and S. V. Zadorozhny. Upper limit on the electron antineutrino mass from the troitsk experiment. *Phys. Rev. D*, 84:112003, Dec 2011.

[21] John N. Bahcall, M. H. Pinsonneault, and G. J. Wasserburg. Solar models with helium and heavy-element diffusion. *Rev. Mod. Phys.*, 67:781–808, Oct 1995.

[22] A. S. Barabash. Precise half-life values for two-neutrino double-β decay. *Phys. Rev. C*, 81:035501, Mar 2010.

[23] P S Barbeau, J I Collar, and O Tench. Large-mass ultralow noise germanium detectors: performance and applications in neutrino and astroparticle physics. *Journal of Cosmology and Astroparticle Physics*, 2007(09):009, 2007.

[24] Pasquale Di Bari. An introduction to leptogenesis and neutrino properties. *Contemporary Physics*, 53(4):315–338, 2012.

[25] M. S. Basunia. Nuclear data sheets. *107*, (3323), 2006.

[26] G. Bertolini and A. Coche, editors. *Semiconductor Detectors*. Elsevier-North Holland, Amsterdam, 1968.

[27] Dušan Budjáš, Marik Barnabé Heider, Oleg Chkvorets, Nikita Khanbekov, and Stefan Schönert. Pulse shape discrimination studies with a broad-energy germanium detector for signal identification and background suppression in the gerda double beta decay experiment. *Journal of Instrumentation*, 4(10):P10007, 2009.

[28] R. N. Cahn, D. A. Dwyer, S. J. Freedman, W. C. Haxton, R. W. Kadel, Yu. G. Kolomensky, K. B. Luk, P. McDonald, G. D. Orebi Gann, and A. W. P. Poon. White Paper: Measuring the Neutrino Mass Hierarchy. In *Proceedings, 2013 Community Summer Study on the Future of U.S. Particle Physics: Snowmass on the Mississippi (CSS2013): Minneapolis, MN, USA, July 29-August 6, 2013*, 2013.

[29] A. Caldwell, A. Merle, O. Schulz, and M. Totzauer. A Global Bayesian Analysis of Neutrino Mass Data. *ArXiv e-prints*, May 2017.

[30] P. H. Chu, J. A. Detwiler, T. Gilliss, I. Guinn, S. Mertens, D. Radford, R. Varner, and B. Zhu. Energy performance of the majorana demonstrator. Technical Report M-TECHDOCPHYS-2017-012, Majorana Technical Report, 2017.

[31] Bruce T. Cleveland, Timothy Daily, Jr. Raymond Davis, James R. Distel, Kenneth Lande, C. K. Lee, Paul S. Wildenhain, and Jack Ullman. Measurement of the solar electron neutrino flux with the homestake chlorine detector. *The Astrophysical Journal*, 496(1):505, 1998.

[32] The EXO-200 Collaboration. Search for majorana neutrinos with the first two years of exo-200 data. *Nature*, 510(7504):229–234, 06 2014.

[33] The GERDA Collaboration. Background-free search for neutrinoless double-decay of 76ge with gerda. *Nature*, 544(7648):47–52, 04 2017.

[34] R.J. Cooper, D.C. Radford, K. Lagergren, James F. Colaresi, Larry Darken, R. Henning, M.G. Marino, and K. Michael Yocum. A pulse shape analysis technique for the majorana experiment. *Nuclear Instruments and Methods in Physics Research Section A: Accelerators, Spectrometers, Detectors and Associated Equipment*, 629(1):303 – 310, 2011.

[35] C. L. Cowan, F. Reines, F. B. Harrison, H. W. Kruse, and A. D. McGuire. Detection of the free neutrino: a confirmation. *Science*, 124(3212):103–104, 1956.

[36] G. Adam Cox, Charles A. Duba, Mark A. Howe, Sean McGee, Alan W. Myers, Keith Rielage, R. G Hamish Robertson, Laura C. Stonehill, Brandon L. Wall, John F. Wilkerson, and Tim D. Van Wechel. Sudbury neutrino observatory neutral current detectors signal readout system. *IEEE Transactions on Nuclear Science*, 51(5 I):2227–2230, 10 2004.

[37] C. Cuesta. Multi-site event discrimination for the MAJORANA DEMONSTRATOR; draft. Technical Report M-TECHDOCUNIDOC-2017-014, Majorana Technical Report, Apr 2017.

[38] C. Cuesta and M. Buuck. Run selection and data cleaning of ds3 (m1). Technical Report M-TECHDOCUNIDOC-2017-008, Majorana Technical Report, 2017.

[39] DES Collaboration, T. M. C. Abbott, F. B. Abdalla, A. Alarcon, J. Aleksić, S. Allam, S. Allen, A. Amara, J. Annis, J. Asorey, S. Avila, D. Bacon, E. Balbinot, M. Banerji, N. Banik, W. Barkhouse, M. Baumer, E. Baxter, K. Bechtol, M. R. Becker, A. Benoit-Lévy, B. A. Benson, G. M. Bernstein, E. Bertin, J. Blazek, S. L. Bridle, D. Brooks, D. Brout, E. Buckley-Geer, D. L. Burke, M. T. Busha, D. Capozzi, A. Carnero Rosell, M. Carrasco Kind, J. Carretero, F. J. Castander, R. Cawthon, C. Chang, N. Chen, M. Childress, A. Choi, C. Conselice, R. Crittenden, M. Crocce, C. E. Cunha, C. B. D'Andrea, L. N. da Costa, R. Das, T. M. Davis, C. Davis, J. De Vicente, D. L. DePoy, J. DeRose, S. Desai, H. T. Diehl, J. P. Dietrich, S. Dodelson, P. Doel, A. Drlica-Wagner, T. F. Eifler, A. E. Elliott, F. Elsner, J. Elvin-Poole, J. Estrada, A. E. Evrard, Y. Fang, E. Fernandez, A. Ferté, D. A. Finley, B. Flaugher, P. Fosalba, O. Friedrich, J. Frieman, J. García-Bellido, M. Garcia-Fernandez, M. Gatti, E. Gaztanaga, D. W. Gerdes, T. Giannantonio, M. S. S. Gill, K. Glazebrook, D. A. Goldstein, D. Gruen, R. A. Gruendl, J. Gschwend, G. Gutierrez, S. Hamilton, W. G. Hartley, S. R. Hinton, K. Honscheid, B. Hoyle, D. Huterer, B. Jain, D. J. James, M. Jarvis, T. Jeltema, M. D. Johnson, M. W. G. Johnson, T. Kacprzak, S. Kent, A. G. Kim, A. King, D. Kirk, N. Kokron, A. Kovacs, E. Krause, C. Krawiec, A. Kremin, K. Kuehn, S. Kuhlmann, N. Kuropatkin, F. Lacasa, O. Lahav, T. S. Li, A. R. Liddle, C. Lidman, M. Lima, H. Lin, N. MacCrann, M. A. G. Maia, M. Makler, M. Manera, M. March, J. L. Marshall, P. Martini, R. G. McMahon, P. Melchior, F. Menanteau, R. Miquel, V. Miranda, D. Mudd, J. Muir, A. Möller, E. Neilsen, R. C. Nichol, B. Nord, P. Nugent, R. L. C. Ogando, A. Palmese, J. Peacock, H. V. Peiris, J. Peoples, W. J. Percival, D. Petravick, A. A. Plazas, A. Porredon, J. Prat, A. Pujol, M. M. Rau, A. Refregier, P. M. Ricker, N. Roe, R. P. Rollins, A. K. Romer, A. Roodman, R. Rosenfeld, A. J. Ross, E. Rozo, E. S. Rykoff, M. Sako, A. I. Salvador, S. Samuroff, C. Sánchez, E. Sanchez, B. Santiago, V. Scarpine, R. Schindler, D. Scolnic, L. F. Secco, S. Serrano, I. Sevilla-Noarbe, E. Sheldon, R. C. Smith, M. Smith, J. Smith, M. Soares-Santos, F. Sobreira, E. Suchyta, G. Tarle, D. Thomas, M. A. Troxel, D. L. Tucker, B. E. Tucker, S. A. Uddin, T. N. Varga, P. Vielzeuf, V. Vikram, A. K. Vivas, A. R. Walker, M. Wang, R. H. Wechsler, J. Weller, W. Wester, R. C. Wolf, B. Yanny, F. Yuan, A. Zenteno, B. Zhang, Y. Zhang, and J. Zuntz. Dark Energy Survey Year 1 Results: Cosmological Constraints from Galaxy Clustering and Weak Lensing. *ArXiv e-prints*, August 2017.

[40] J. A. Detwiler. MJD 0nbb Decay Sensitivity Calculations; final. Technical Report M-TECHDOCPHYS-2011-043, Majorana Technical Report, Sep 2011.

[41] K. Eguchi, S. Enomoto, K. Furuno, J. Goldman, H. Hanada, H. Ikeda, K. Ikeda, K. Inoue, K. Ishihara, W. Itoh, T. Iwamoto, T. Kawaguchi, T. Kawashima, H. Kinoshita, Y. Kishimoto, M. Koga, Y. Koseki, T. Maeda, T. Mitsui, M. Motoki, K. Nakajima, M. Nakajima, T. Nakajima, H. Ogawa, K. Owada, T. Sakabe, I. Shimizu, J. Shirai, F. Suekane, A. Suzuki, K. Tada, O. Tajima, T. Takayama, K. Tamae, H. Watanabe, J. Busenitz, Z. Djurcic, K. McKinny, D.-M. Mei, A. Piepke, E. Yakushev, B. E. Berger, Y. D. Chan, M. P. Decowski, D. A. Dwyer, S. J. Freedman, Y. Fu, B. K. Fujikawa, K. M. Heeger, K. T. Lesko, K.-B. Luk, H. Murayama, D. R. Nygren, C. E. Okada, A. W. P. Poon, H. M. Steiner, L. A. Winslow, G. A. Horton-Smith, R. D. McKeown, J. Ritter, B. Tipton, P. Vogel, C. E. Lane, T. Miletic, P. W. Gorham, G. Guillian, J. G. Learned, J. Maricic, S. Matsuno, S. Pakvasa, S. Dazeley, S. Hatakeyama, M. Murakami, R. C. Svoboda, B. D. Dieterle, M. DiMauro, J. Detwiler, G. Gratta, K. Ishii, N. Tolich, Y. Uchida, M. Batygov, W. Bugg, H. Cohn, Y. Efremenko, Y. Kamyshkov, A. Kozlov, Y. Nakamura, L. De Braeckeleer, C. R. Gould, H. J. Karwowski, D. M. Markoff, J. A. Messimore, K. Nakamura, R. M. Rohm, W. Tornow, A. R. Young, and Y.-F. Wang. First results from kamland: Evidence for reactor antineutrino disappearance. *Phys. Rev. Lett.*, 90:021802, Jan 2003.

[42] S. R. Elliott et al. Initial Results from the MAJORANA DEMONSTRATOR. 2016.

[43] G. J. Feldman and R. D. Cousins. Unified approach to the classical statistical analysis of small signals. *Phys. Rev. D*, 57:3873–3889, April 1998.

[44] Y. Fukuda, T. Hayakawa, E. Ichihara, K. Inoue, K. Ishihara, H. Ishino, Y. Itow, T. Kajita, J. Kameda, S. Kasuga, K. Kobayashi, Y. Kobayashi, Y. Koshio, M. Miura, M. Nakahata, S. Nakayama, A. Okada, K. Okumura, N. Sakurai, M. Shiozawa, Y. Suzuki, Y. Takeuchi, Y. Totsuka, S. Yamada, M. Earl, A. Habig, E. Kearns, M. D. Messier, K. Scholberg, J. L. Stone, L. R. Sulak, C. W. Walter, M. Goldhaber, T. Barszczxak, D. Casper, W. Gajewski, P. G. Halverson, J. Hsu, W. R. Kropp, L. R. Price, F. Reines, M. Smy, H. W. Sobel, M. R. Vagins, K. S. Ganezer, W. E. Keig, R. W. Ellsworth, S. Tasaka, J. W. Flanagan, A. Kibayashi, J. G. Learned, S. Matsuno, V. J. Stenger, D. Takemori, T. Ishii, J. Kanzaki, T. Kobayashi, S. Mine, K. Nakamura, K. Nishikawa, Y. Oyama, A. Sakai, M. Sakuda, O. Sasaki, S. Echigo, M. Kohama, A. T. Suzuki, T. J. Haines, E. Blaufuss, B. K. Kim, R. Sanford, R. Svoboda, M. L. Chen, Z. Conner, J. A. Goodman, G. W. Sullivan, J. Hill, C. K. Jung, K. Martens, C. Mauger, C. McGrew, E. Sharkey, B. Viren, C. Yanagisawa, W. Doki, K. Miyano, H. Okazawa, C. Saji, M. Takahata, Y. Nagashima, M. Takita, T. Yamaguchi, M. Yoshida, S. B. Kim, M. Etoh, K. Fujita, A. Hasegawa, T. Hasegawa, S. Hatakeyama, T. Iwamoto, M. Koga, T. Maruyama, H. Ogawa, J. Shirai, A. Suzuki, F. Tsushima, M. Koshiba, M. Nemoto, K. Nishijima, T. Futagami, Y. Hayato, Y. Kanaya, K. Kaneyuki, Y. Watanabe, D. Kielczewska, R. A. Doyle, J. S. George, A. L. Stachyra, L. L. Wai, R. J. Wilkes, and K. K.

Young. Evidence for Oscillation of Atmospheric Neutrinos. *Physical Review Letters*, 81:1562–1567, August 1998.

[45] L. L. Gadeken and B. C. Robertson. The influence of Ge(Li) detector pulse shape variations on constant fraction and snap-off timing discriminators. *Nuclear Instruments and Methods*, 136:255–259, July 1976.

[46] G. K. Giovanetti, N. Abgrall, E. Aguayo, F. T. Avignone, A. S. Barabash, F. E. Bertrand, M. Boswell, V. Brudanin, M. Busch, D. Byram, A. S. Caldwell, Y.-D. Chan, C. D. Christofferson, D. C. Combs, C. Cuesta, J. A. Detwiler, P. J. Doe, Y. Efremenko, V. Egorov, H. Ejiri, S. R. Elliott, J. E. Fast, P. Finnerty, F. M. Fraenkle, A. Galindo-Uribarri, J. Goett, M. P. Green, J. Gruszko, V. E. Guiseppe, K. Gusev, A. L. Hallin, R. Hazama, A. Hegai, R. Henning, E. W. Hoppe, S. Howard, M. A. Howe, K. J. Keeter, M. F. Kidd, O. Kochetov, S. I. Konovalov, R. T. Kouzes, B. D. LaFerriere, J. Leon, L. E. Leviner, J. C. Loach, J. MacMullin, S. MacMullin, R. D. Martin, S. Meijer, S. Mertens, M. Nomachi, J. L. Orrell, C. O'Shaughnessy, N. R. Overman, D. G. Phillips, A. W. P. Poon, K. Pushkin, D. C. Radford, J. Rager, K. Rielage, R. G. H. Robertson, E. Romero-Romero, M. C. Ronquest, A. G. Schubert, B. Shanks, T. Shima, M. Shirchenko, K. J. Snavely, N. Snyder, A. M. Suriano, J. Thompson, V. Timkin, W. Tornow, J. E. Trimble, R. L. Varner, S. Vasilyev, K. Vetter, K. Vorren, B. R. White, J. F. Wilkerson, C. Wiseman, W. Xu, E. Yakushev, A. R. Young, C.-H. Yu, and V. Yumatov. A Dark Matter Search with MALBEK. *Physics Procedia*, 61:77–84, 2015.

[47] V. E. Guiseppe, S. R. Elliott, A. Hime, K. Rielage, and S. Westerdale. A Radon Progeny Deposition Model. *AIP Conf. Proc.*, 1338:95–100, 2011.

[48] J. L. Hewett, H. Weerts, R. Brock, J. N. Butler, B. C. K. Casey, J. Collar, A. de Gouvea, R. Essig, Y. Grossman, W. Haxton, and et al. Fundamental Physics at the Intensity Frontier. *ArXiv e-prints*, May 2012.

[49] E. W. Hoppe, A. Seifert, C. E. Aalseth, P. P. Bachelor, A. R. Day, D. J. Edwards, T. W. Hossbach, K. E. Litke, J. I. McIntyre, H. S. Miley, S. M. Schulte, J. E. Smart, and G. A. Warren. Cleaning and passivation of copper surfaces to remove surface radioactivity and prevent oxide formation. *Nuclear Instruments and Methods in Physics Research Section A, Accelerators, Spectrometers, Detectors and Associated Equipment*, 579(1):486–489, Aug 2007.

[50] Fedor Šimkovic, Amand Faessler, Herbert Müther, Vadim Rodin, and Markus Stauf. $0\nu\beta\beta$-decay nuclear matrix elements with self-consistent short-range correlations. *Phys. Rev. C*, 79:055501, May 2009.

[51] Soo-Bong Kim. New results from RENO and prospects with RENO-50. *Nucl. Part. Phys. Proc.*, 265-266:93–98, 2015.

[52] H.V. Klapdor-Kleingrothaus, A. Dietz, L. Baudis, G. Heusser, I.V. Krivosheina, B. Majorovits, H. Paes, H. Strecker, V. Alexeev, A. Balysh, A. Bakalyarov, S.T. Belyaev, V.I. Lebedev, and S. Zhukov. Latest results from the heidelberg-moscow double beta decay experiment. *The European Physical Journal A - Hadrons and Nuclei*, 12(2):147–154, 2001.

[53] G. F. Knoll. *Radiation Detector and Measurement*. John Wiley and Sons, Inc., Hoboken, NJ, 3rd edition, 2000.

[54] Ch Kraus, B. Bornschein, L. Bornschein, J. Bonn, B. Flatt, A. Kovalik, B. Ostrick, E. W. Otten, J. P. Schall, Th Thümmler, and Ch Weinheimer. Final results from phase ii of the mainz neutrino mass search in tritium β decay. *The European Physical Journal C - Particles and Fields*, 40(4):447–468, Apr 2005.

[55] P.N. Luke, F.S. Goulding, N.W. Madden, and R.H. Pehl. Low capacitance large volume shaped-field germanium detector. *Nuclear Science, IEEE Transactions on*, 36(1):926–930, Feb 1989.

[56] M.D. Messier. First neutrino oscillation measurements in nova. *Nuclear Physics B*, 908:151 – 160, 2016. Neutrino Oscillations: Celebrating the Nobel Prize in Physics 2015.

[57] P. Mullowney, M.-C. Lin, K. Paul, C. Ahrens, M. Loh, R. J. Cooper, D. C. Radford, and E. Hull. Computational models of germanium point contact detectors. *Nuclear Instruments and Methods in Physics Research A*, 662:33–44, January 2012.

[58] J. Myslik. Data Cleaning in DS0-DS5 for $0\nu\beta\beta$-decay analysis; draft. Technical Report M-TECHDOCUNIDOC-2017-018, Majorana Technical Report, Aug 2017.

[59] K.A. Olive et al. Review of Particle Physics. *Chin.Phys.*, C38:090001, 2014.

[60] N. R. Overman, E. W. Hoppe, and R. S. Addleman. Surface cleaning techniques: ultra-trace icp-ms sample preparation and assay of hdpe. *Journal of Radioanalytical and Nuclear Chemistry*, 296(3):1303–1310, Jun 2013.

[61] Dimitrios Palioselitis and GERDA collaboration. Experience from operating germanium detectors in gerda. *Journal of Physics: Conference Series*, 606(1):012007, 2015.

[62] W. Pauli. Letter to attendees at a physics conference in tubingen, 1930.

[63] Florian Priester, Michael Sturm, and Beate Bornschein. Commissioning and detailed results of {KATRIN} inner loop tritium processing system at tritium laboratory karlsruhe. *Vacuum*, 116(0):42 – 47, 2015.

[64] R. G. H. Robertson. Empirical Survey of Neutrinoless Double Beta Decay Matrix Elements. *Mod. Phys. Lett.*, A28:1350021, 2013.

[65] J. Schechter and J. W. F. Valle. Neutrinoless double-β decay in su(2)xu(1) theories. *Phys. Rev. D*, 25:2951–2954, Jun 1982.

[66] S. Turck-Chieze and I. Lopes. Toward a unified classical model of the sun - On the sensitivity of neutrinos and helioseismology to the microscopic physics. *Astrophysical Journal*, 408:347–367, May 1993.

[67] Walter Winter. Neutrino mass hierarchy determination with IceCube-PINGU. *Phys. Rev.*, D88(1):013013, 2013.

[68] C. Wiseman, T. S. Caldwell, T. Gilliss, C. R. S. Haufe, A. L. Reine, S. Meijer, and P.-H. Chu. Livetime and exposure for majorana demonstrator data sets 0-5. Technical Report M-TECHDOCPHYS-2017-016, Majorana Technical Report, 2017.

[69] J. F. Ziegler, M. D. Ziegler, and J. P. Biersack. SRIM - The stopping and range of ions in matter (2010). *Nuclear Instruments and Methods in Physics Research B*, 268:1818–1823, June 2010.

[70] K. Zuber. Double beta decay experiments. Neutrino Astrophysics and Fundamental Properties Seminar, Institute for Nuclear Theory, June 2015.

[71] G. Zuzel and M. Wójcik. Removal of the long-lived ^{222}Rn daughters from copper and stainless steel surfaces. *Nuclear Instruments and Methods in Physics Research A*, 676:140–148, June 2012.

Appendix A

BACKGROUND-SUBTRACTED EFFICIENCY

A.1 Calculating Efficiency

The alpha rejection efficiency of the DCR cut is evaluated using information from both a sideband and a source-free data set to estimate the background in the signal peak region. This method allows for both a non-flat background spectrum and for a varying background level over the course of the measurements. Both of these corrections are used to account for the presence of muon background events in the alpha peak regions.

The energy regions used in the calculation are depicted in Fig. A.1. The signal region S, determined using the Gaussian fit to the alpha energy peak, is taken to be a 5σ window centered at the peak centroid. The background sideband region B is taken to be a 500 keV window starting 5σ above the centroid of the alpha peak. Only a right-hand-side sideband window is used, since outlier alpha events (see Sec. 5.2.3) contribute to the left-hand sideband. The background spectrum energy windows C and D have identical energy ranges as S and B, respectively. In each window, the event count with and without the DCR cut applied is measured.

Of these eight measurements, only six are used to calculate the efficiency, since the DCR acceptance rate of background events in regions B and D is irrelevant for the computation of the background in the signal region. Using the labels for the regions, and indicating counts without the DCR cut applied with the subscript u and those with the cut applied with the subscript c, the DCR alpha acceptance rate is given by:

$$\epsilon_A = \frac{S_c - \frac{B_u C_c}{D_u}}{S_u - \frac{B_u C_u}{D_u}} = f(S_c, C_c, S_u, C_u, B_u, D_u) \tag{A.1}$$

where the A indicates the "true," background-subtracted, alpha events. The measurements

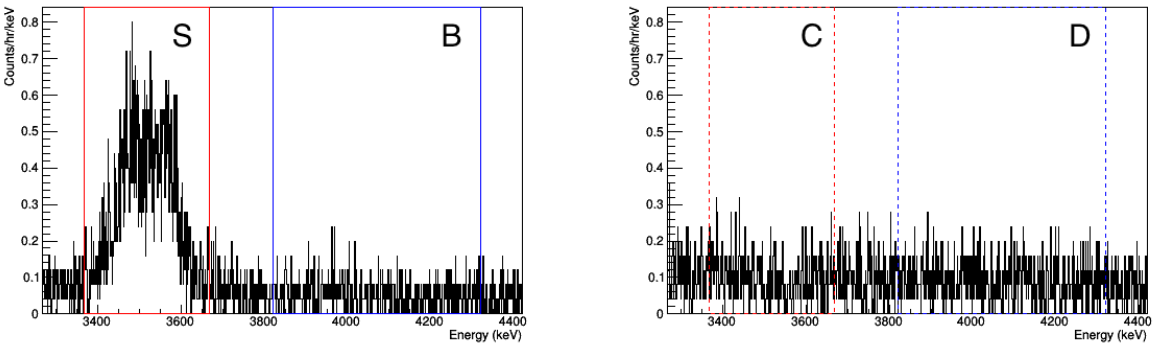

Figure A.1: An example of the energy regions used to calculate the alpha rejection efficiency. The spectrum with the alpha source incident on the detector surface *(left)* is used to define the location and width of the signal region S and the location of the sideband window B. The same energy regions in the background spectrum *(right)*, C and D, are used to determine the underlying background spectrum shape.

in different regions are independent of one another, and given the low statistics, they are assumed to be Poisson-distributed.

A.2 Uncertainty of Efficiency

The uncertainty of a generic non-linear function is found by Taylor expanding it to first order:

$$f(x_1, x_2, ..., x_n) \approx f^0 + \sum_i^n \frac{\partial f}{\partial x_i} x_i$$

where the sum is over all independent variables, and $\frac{\partial f}{\partial x_i}$ is the partial derivative of f, evaluated at the mean value of all measured x_i. Since f^0 is constant, it does not contribute to the uncertainty, and the variance is:

$$\sigma_f^2 = \sum_i^n \frac{\partial f}{\partial x_i}^2 \sigma_i^2 + \sum_i^n \sum_{j(j\neq i)}^n \frac{\partial f}{\partial x_i} \frac{\partial f}{\partial x_j} Cov.(x_i, x_j) \tag{A.2}$$

This derivation assumes that the relative uncertainties of the measurements σ_i/x_i are small, a safe assumption in this case. The numbers of counts in each measurement window are Poisson-distributed variables, so $\sigma_i = \sqrt{x}_i$.

The covariance between measurements in difference regions is 0, since these measurements are independent. The covariance between S_u and S_c, or between C_u and C_c, on the other hand, is non-zero and must be calculated.

The counts in a given region with and without the DCR cut applied are binomial-distributed. Therefore, in region S, for example, where $\epsilon = \frac{S_c}{S_u}$,

$$\sigma_\epsilon^2 = \frac{\epsilon(1-\epsilon)}{N} = \frac{S_c(S_u - S_c)}{S_u^3}.$$

Again using the linearized propagation of uncertainty formula,

$$\sigma_\epsilon^2 = \frac{\partial\epsilon}{\partial S_c}^2 \sigma_{S_c}^2 + \frac{\partial\epsilon}{\partial S_u}^2 \sigma_{S_u}^2 + 2\frac{\partial\epsilon}{\partial S_c}\frac{\partial\epsilon}{\partial S_u} Cov.(S_c, S_u)$$

and substituting the appropriate expressions

$$\frac{S_c(S_u - S_c)}{S_u^3} = \frac{S_c}{S_u^2} + \frac{S_c^2}{S_u^3} - 2\frac{S_c}{S_u^3} Cov.(S_c, S_u)$$

allows us to solve for the covariance:

$$Cov.(S_c, S_u) = S_c$$

The same holds in region C.

Substituting Eqn. A.1 in Eqn. A.2 and writing only non-zero terms,

$$\begin{aligned}\sigma_\epsilon^2 =& \frac{\partial\epsilon}{\partial S_c}^2 \sigma_{S_c}^2 + \frac{\partial\epsilon}{\partial S_u}^2 \sigma_{S_u}^2 + 2\frac{\partial\epsilon}{\partial S_c}\frac{\partial\epsilon}{\partial S_u} Cov.(S_c, S_u) \\ &+ \frac{\partial\epsilon}{\partial C_c}^2 \sigma_{C_c}^2 + \frac{\partial\epsilon}{\partial C_u}^2 \sigma_{C_u}^2 + 2\frac{\partial\epsilon}{\partial C_c}\frac{\partial\epsilon}{\partial C_u} Cov.(C_c, C_u) \\ &+ \frac{\partial\epsilon}{\partial B_u}^2 \sigma_{B_u}^2 + \frac{\partial\epsilon}{\partial D_u}^2 \sigma_{D_u}^2\end{aligned} \tag{A.3}$$

where $\epsilon = \epsilon_A$. Substituting the partial derivatives, Poisson uncertainties, and expressions for the covariances found above, results, after some manipulation, in the expression:

$$\begin{aligned}\sigma_\epsilon^2 = \frac{1}{A_u^2}\Bigg[&\left(S_c + \frac{{B_u}^2}{D_u} C_c\right)(1-2\epsilon) \\ &+ \left(S_u + \frac{{B_u}^2}{D_u} C_u\right)\epsilon^2 \\ &+ \frac{B_u}{D_u^2}\left(1 + \frac{B_u}{D_u}\right)(\epsilon C_u - C_c)^2 \Bigg]\end{aligned} \tag{A.4}$$

where $A_u = S_u - \frac{B_u C_u}{D_u}$ and $\epsilon = \epsilon_A$ is as given in Eqn. A.1.